OBSERVATIONS OF Z-PINCHES DRIVEN BY A HIGH VOLTAGE, PULSED POWER SOURCE

by

E.S. Figura

March, 1989

This thesis is submitted in partial fulfilment of the requirements for the degree of Ph.D. and D.I.C.

Plasma Physics Group,
Blackett Laboratory,
Imperial College,
London.

This thesis is dedicated to my mother
and the memory of my father, without
whose faith and encouragement this
work would not have been completed.

ABSTRACT

Experimental observations of two Z−pinch configurations are described: (a) a gas−embedded Z−pinch and (b) a fibre Z−pinch. Both pinches are driven by a high voltage, pulsed power source which gives a current of *150* kA over *100* ns with a risetime of *50* ns.

In the gas−embedded experiment a ruby laser is used to initiate a small diameter discharge in typically *1* atm. hydrogen. The plasma is preheated by a current of about *7* kA for *50* ns during which time it expands radially. It is then Joule heated by the main fast rising current. For the first *10* − *30* ns the pinch is in radial equilibrium after which it is transformed into an expanding helix by an $m=1$ instability. The onset of this instability is measured by a coil positioned coaxial to the pinch to monitor the axial magnetic field generated by the helical current flow. The results indicate that at this high current (*150* kA) the observed scaling of the $m=1$ instability growth time with pressure is consistent with MHD theory. This scaling was not observed in experiments at lower currents.

In the fibre experiment a Z−pinch is produced by discharging the generator into an optical glass fibre ranging in diameter from *20* to *125* μm. Optical framing photography shows that $m=0$ instabilities appear within *13* ns of current flow. Some of the instabilities are seen to move axially and this movement is in either direction. Shadowgraphs taken with a ruby laser pulse show that the plasma is optically thick. Assuming blackbody emission a temperature of *10* − *30* eV is inferred from the optical photographs.

Time−integrated X−ray measurements reveal a number of dense, bright localised X−ray emitting sources along the length of the fibre together with a background plasma emitting X−rays with energies of about *1* − *2* keV. The data also suggests that there is incomplete ionisation of the fibre. Time−resolved measurements show that the plasma emission is dominated by silicon K−shell radiation, indicating a peak temperature of around *1* − *2* keV.

CONTENTS

		page
ABSTRACT		3
LIST OF CONTENTS		4
LIST OF FIGURES		8
LIST OF TABLES		14
CHAPTER ONE: An Introduction to Z−pinches		
1.1.	Introduction	15
1.2.	What is a Z−pinch?	18
1.3.	The Lawson Condition	18
1.4.	Stability of Z−pinches	20
1.5.	The Equilibrium Z−pinch	25
1.6.	Z−pinch Experiments	28
1.7.	Structure of the Thesis	30
1.8.	Units	31
CHAPTER TWO: The Apparatus		
2.1.	Introduction	32
2.2.	The Marx Bank	32
2.3.	The Transmission Line	35
2.4.	The Line Switch	36
2.5.	The Transfer Section	39
2.6.	The Pinch Chamber	44
2.7.	The Voltage Monitors	48
2.8.	The Current Monitor	52
2.9.	The B_z Monitor	56
2.10.	The Laser	61
2.11.	The Timing Sequence	64

CHAPTER THREE: The Gas−embedded Z−pinch

3.1.	Introduction	66
3.1.1.	Stability and Finite Ion Larmor Radius Effects	67
3.2.	The Experimental Arrangement	69
3.3.	The Observations	71
3.4.	Discussion	80
3.4.1.	The Preheat Phase	80
3.4.2.	The Equilibrium Phase	80
3.4.3.	The Unstable Phase	84
3.5.	Conclusions	87

THE FIBRE Z−PINCH

CHAPTER FOUR: Optical Diagnostics

4.1.	Introduction	89
4.2.	The Experimental Arrangement	90
4.3.	The Observations	90
4.4.	Discussion	98
4.4.1.	Streaks and Axial Movement	98
4.4.2.	The Instability	101
4.4.3.	The Internal Fibre Emission	103
4.4.4.	A Determination of T_e from Optical Photographs	110
4.4.5.	Radiation from a Plasma	118
4.4.6.	The Plasma Equilibrium State	120
4.5.	Conclusions	123

CHAPTER FIVE: Laser Diagnostics

5.1.	Introduction	126
5.2.	The Experimental Arrangement	127
5.3.	The Observations	130
5.3.1.	Schlieren Photography	130
5.3.2.	Holographic Interferometry	133
5.4.	Discussion	139

5.4.1.	Schlieren/Shadowgraph Measurements	141
5.4.2.	Estimate of the Electron Number Density	141
5.4.3.	Is the Laser Refracted or Absorbed?	145
5.4.4.	The Streaked Shadowgraphs	146
5.4.5.	Holographic Interferometry Measurements	147
5.4.6.	The Abel Transform and its Inverse	148
5.4.7.	Is the Fibre Fully Ionised?	150
5.4.8.	Instabilities, Refraction and Plasma Evolution	152
5.4.9.	A Further Discussion about Blackbodies	153
5.5.	Conclusions	154

CHAPTER SIX: X−ray Diagnostics

6.1.	Introduction	156
6.2.	The Experimental Arrangement	157
6.2.1.	The X−ray Pinhole Camera	157
6.2.2.	X−ray PIN Diodes	157
6.2.3.	X−ray Film and Filters	161
6.3.	The Observations	166
6.4.	Discussion	177
6.4.1.	The Spatial Extent of the X−ray Emitting Plasma	177
6.4.2.	The X−ray Emission Profile	178
6.4.3.	Modelling the Plasma X−ray emission	180
6.4.4.	The Density and Lifetime of the X−ray Emitting Regions	183
6.4.5.	The Electrode Emission and Electron Beams	188
6.4.6.	Plasma X−rays	193
6.4.7.	Can the Plasma be Hot?	196
6.5.	Conclusions	197

CHAPTER SEVEN: Conclusions

7.1.	Z−pinches and Pulsed Power	199
7.2.	The Gas−embedded Z−pinch	199
7.3.	The Fibre Z−pinch	201
7.3.1.	Simulation of the Fibre Experiment	203

7.3.2. Initial Plasma Formation 214
7.4. Summary and Future Work 216

APPENDIX A: **Transmission Line Simulation**

A.1. BERTHA – A Versatile Transmission Line Code 218
A.2. Description of the Program 220

APPENDIX B: **How to Determine Number Density Profiles**

B.1. Holography and the Abel Transform 227
B.2. Solution of the Inverse Abel Transform 228
B.3. Errors due to Refraction 229
B.4. Other Methods of Solving the Problem 231

REFERENCES 234

ACKNOWLEGEMENTS 239

LIST OF FIGURES

page

CHAPTER ONE: An Introduction to Z−pinches

Figure:	1.1.a	Cross−sections for deuterium fusion reactions	16
	1.1.b	Reaction rates as a function of temperature	17
	1.2	The linear Z−pinch	19
	1.3.a	The $m=0$ (sausage) instability	21
	1.3.b	The $m=1$ (kink) instability	22

CHAPTER TWO: The Apparatus

Figure:	2.1	Schematic of the current generator	33
	2.2	Schematic of the Marx bank	34
	2.3	Schematic cross−section of the line switch	37
	2.4	Charging of the transfer section via the switch capacitance	38
	2.5	Current profiles with and without a transfer section	40
	2.6	Resistive charging of the transfer section	42
	2.7	Discharging of the transfer section into the pinch	42
	2.8.a	Preheat current into a short−circuit	43
	2.8.b	Current profile calculated by BERTHA	43
	2.9.a	Schematic cross−section of the chamber used for the gas−embedded pinch experiment	45
	2.9.b	Photograph of the fibre−pinch chamber	46
	2.10	Schematic cross−section of the fibre−pinch chamber	47
	2.11.a	Schematic of the voltage monitor	49

	2.11.b	Equivalent electrical circuit of the monitor	50
	2.12.a	Calibration of the voltage monitors	51
	2.12.b	Output signals from the monitors	51
	2.13.a	Schematic of the current monitor	53
	2.13.b	Schematic of the B_θ loop	53
	2.14.a	Output from the B_θ loop	55
	2.14.b	Output from the current monitor	55
	2.15.a	Schematic of the B_z monitor	57
	2.15.b	Schematic showing the B_z probe with a helical coil	57
	2.16	A plot of the integrated output of the B_z probe, V_o against $n'a^2I$	58
	2.17.a	Output from the B_z probe on a short−circuit shot	60
	2.17.b	Corresponding current signal	60
	2.18.a	Schematic of ruby laser	62
	2.18.b	The laser pulse profile	62
	2.19.a	Circuit for triggering the laser	63
	2.19.b	Output from the circuit	63
	2.20	The timing sequence for the experiment	65

CHAPTER THREE: **The Gas−embedded Z−pinch**

Figure:	3.1	The experimental set−up	70
	3.2	Streak photographs: (a) with preheat (b) without preheat	72
	3.3	Typical data shot:	
		(a) streak photograph	75
		(b) current	75
		(c) dI/dt	76
		(d) B_z	76
	3.4	Duration of equilibrium as a function of initial filling pressure	77
	3.5	Current at onset of $m=1$ instability versus initial filling pressure	78

CHAPTER FOUR: Optical Diagnostics

Figure:	4.1	Schematic of the streak/framing set–up	91
	4.2.a	Streak photograph of the plasma emission	93
	4.2.b	Corresponding current trace	93
	4.3	Typical data set of streak photographs	94
	4.4	Evolution of pinch diameter for a range of initial fibre diameters	95
	4.5	Variation of the light–up time, t_Q with initial fibre diameter, Φ_i	96
	4.6	Typical data set of framing photographs	97
	4.7.a	Temperature distribution in a cylinder at various times	105
	4.7.b	Centre and average temperatures for an infinite cylinder	105
	4.8.a	Specific heat for silica glass	106
	4.8.b	Thermal conductivity for silica glass	106
	4.9	Transmission of: (a) quartz window, $W(\lambda)$ (b) neutral density filter, $F(\lambda)$	111
	4.10	Spectral sensitivity of the streak camera	112
	4.11	Set–up for determining the constant K	114
	4.12	Microdensitometer scan of a typical plasma image	117

CHAPTER FIVE: Laser Diagnostics

Figure:	5.1	Set–up for schlieren and streaked shadowgraph photography	128
	5.2.a	Set–up for holographic interferometry	129
	5.2.b	Reconstruction of the holograms	129
	5.3	Sequence of schlieren photographs	131
	5.4.a	Schlieren photograph of a reference (undisturbed) fibre	132

5.4.b	Streaked shadowgraph together with a streak of the laser	132
5.5.a	Reconstructed hologram at $t=17$ ns	134
5.5.b	Hologram of a fibre prior to the discharge	134
5.6	Reconstructed holograms at: (a) $t=127$ ns (b) $t=147$ ns	135
5.7	Electron number density profile at $t=17$ ns	137
5.8	Electron number density profiles at $t=147$ ns at axial positions z_1, z_2 and z_3	138
5.9.a	Schlieren set−up showing beam deviation in the plasma	143
5.9.b	Normalised density profiles	144
5.9.c	Deviation angle profiles for the density profiles in figure 5.9.b	144
5.10	Geometry of a ray travelling through a radially symmetric plasma column (assuming no refraction)	149

CHAPTER SIX: X−ray Diagnostics

Figure:	6.1	The pinhole camera	158
	6.2	Schematic of the filtered pinhole arrangement	159
	6.3	Schematic of the PIN diode arrangement	160
	6.4	Sensitivity of Kodak DEF film	162
	6.5	Transmission of *3* μm aluminium and the film layer	163
	6.6	Filter transmissions incorporating PIN diode response	164
	6.7	X−ray pinhole images using *470* μm pinholes	167
	6.8	X−ray pinhole images using: (a) *100* μm pinholes (b) *50* & *20* μm pinholes	169

	6.9	Microdensitometer scans of the image in figure 6.8.b (a) axial scan (b) radial scan	170
	6.10	X−ray pinhole images of an initially curved fibre	171
	6.11	PIN diode signals − no collimation	173
	6.12	PIN diode signals − *3* mm collimation	174
	6.13	PIN diode signals − *35* mm collimation	175
	6.14	Ratios of differently collimated PIN diode signals	176
	6.15	Emission profiles and their Abel transforms	179
	6.16	X−ray film dose (pertaining to figure 6.8) versus temperature	186
	6.17	Charge delivered to anode as a function of beam energy	192
	6.18	X−ray dose versus temperature for the filtered PIN diodes	194
	6.19	Ratios of the X−ray dose for the filtered PIN diodes	195

CHAPTER SEVEN: **Conclusions**

Figure:	7.1	Plasma radius	205
	7.2	Electron temperature	206
	7.3	Mass density	207
	7.4	Average ion charge	208
	7.5	Heating of the centre of the fibre	209
	7.6	Radial electron temperature profile at different times	210

APPENDIX A: Transmission Line Simulation

Figure:	A.1	Definition of the two travelling voltage waves	219
	A.2	An example of a transmission line configuration	222
	A.3	A general three element junction	223
	A.4	Schematic of the general program	226

LIST OF TABLES

page

CHAPTER THREE: The Gas−embedded Z−pinch

Table:	3.1	The timing of B_z wrt the onset of the instability	73
	3.2	Difference in dI/dt between plasma and short−circuit shots	78
	3.3	Equilibrium times for different filling pressures	81
	3.4	Temperature and line density needed to satisfy $\Omega_i \tau_{ii} \gg 1$	82

THE FIBRE Z−PINCH

CHAPTER FOUR: Optical Diagnostics

Table:	4.1	Axial velocity of instabilities for different diameter fibres	99
	4.2	Electron densities needed for LTE to hold for $n=2$	121
	4.3	Equilibration times to achieve LTE in transient plasmas	122

CHAPTER SIX: X−ray Diagnostics

Table:	6.1	K−shell energies for the electrodes and filters	165
	6.2	Important Silicon lines below *40* A	166

CHAPTER ONE

An Introduction to Z−pinches

1.1. Introduction

The basic goal of plasma physics research has been to produce controlled thermonuclear reactions (CTR) in the laboratory, in order to make use of the energy released from them. Its solution will provide an almost inexhaustible supply of energy from the abundant supplies of fuel that exist in nature.

Thermonuclear reactions arise from collisions between fast atomic nuclei in high temperature matter. If these colliding nuclei have sufficient energy to overcome the potential barrier of mutual electrostatic repulsion then they will react, liberating energy in the process. The rate at which such reactions take place is a strong function of the energy of the nuclei and hence a strong function of temperature.

The main thermonuclear reactions involve the fusion of light nuclei and are listed below, together with the energies involved (MeV):

$$D + T \rightarrow He^4\ (3.52) + n\ (14.06) \qquad (1)$$

$$D + He^3 \rightarrow He^4\ (3.67) + p\ (14.67) \qquad (2)$$

$$D + D \rightarrow T\ (1.01) + p\ (3.03) \qquad (3.a)$$

$$D + D \rightarrow He^3\ (0.82) + n\ (2.45) \qquad (3.b)$$

Figure 1.1.a shows how the cross−section, σ, for each reaction varies with the particle energy whilst in figure 1.1.b the variation of the reaction rate, $<\sigma v>$, with temperature is shown (where v is the velocity of the particles and $<...>$ signifies an average value − see e.g. Dolan, 1982). Of all the reactions, the fusion of deuterium and tritium is by far the most favourable (in terms of the cross−section). The reaction rates all peak at very high temperatures ($\approx$ *20* keV or greater) and this presents a problem for any system in how to confine the reacting particles.

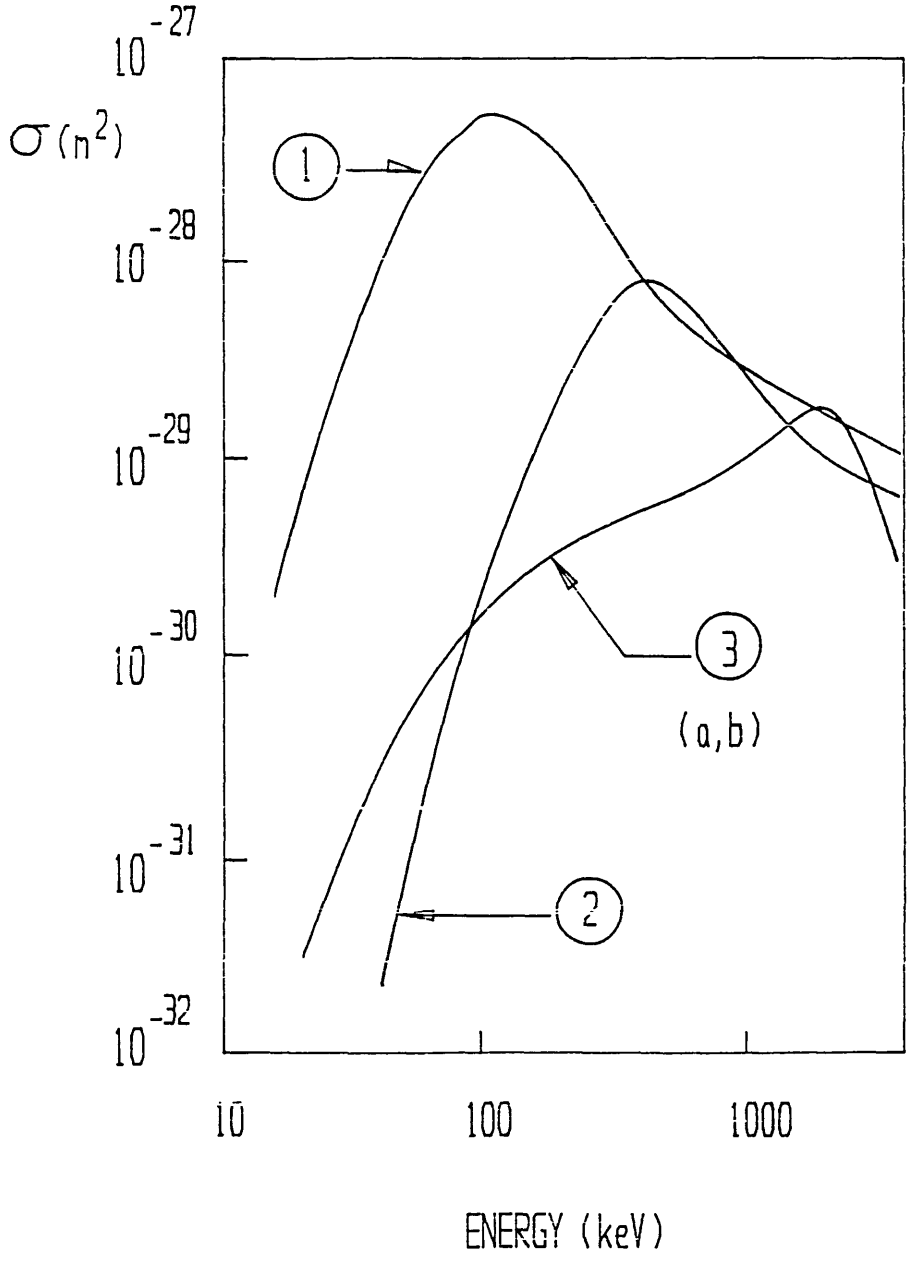


Figure 1.1.a: Cross-sections for deuterium fusion reactions

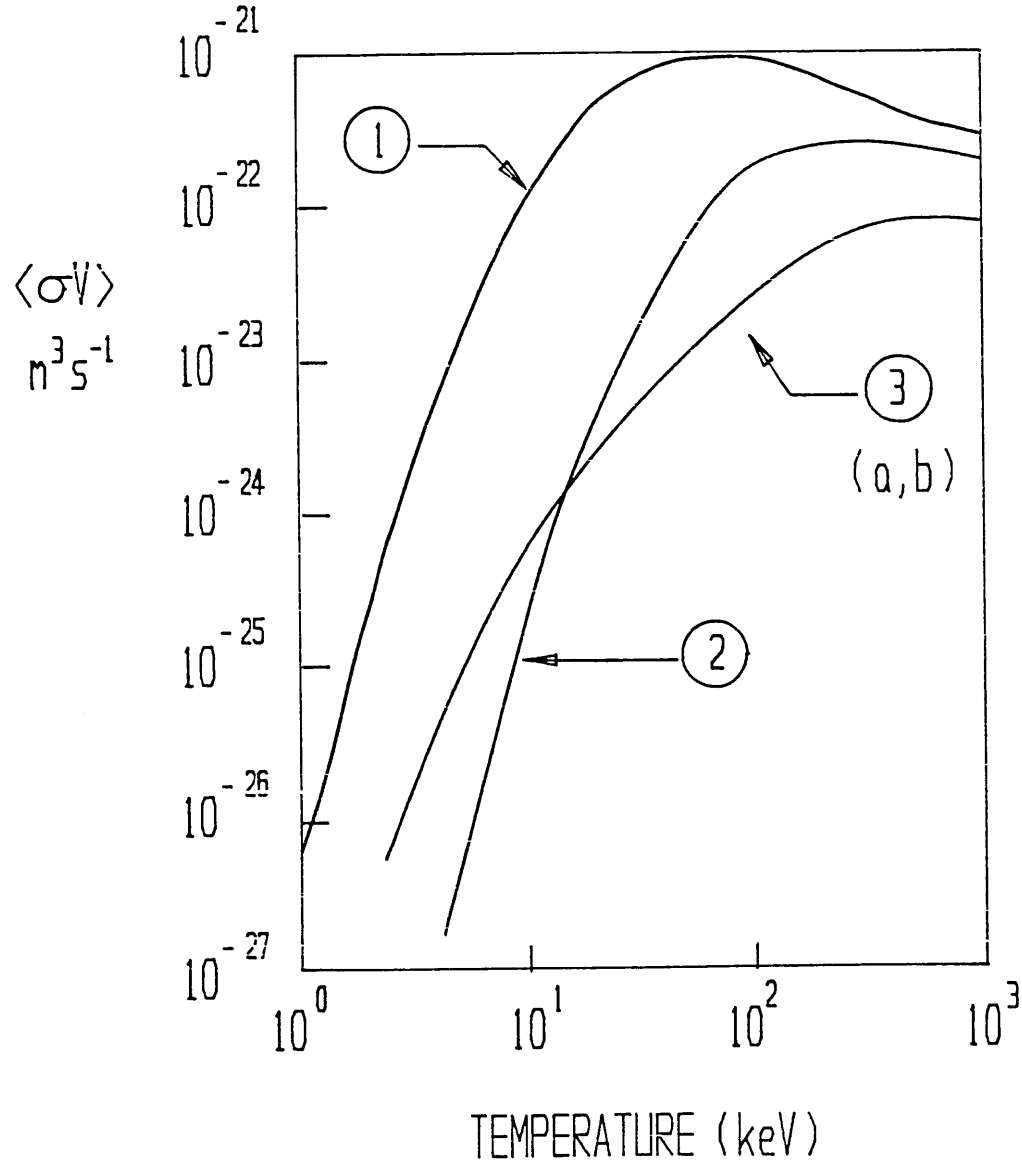


Figure 1.1.b: Reaction rates as a function of temperature

1.2. What is a Z−pinch?

The fundamental problem in CTR requiring solution is how to insulate the very high temperature plasma from the surrounding walls of the containing vessel. The particles which comprise the plasma must be contained for a sufficiently long time to allow a high probability of their reacting with one another before striking the chamber walls.

The simplest plasma confinement device is the linear Z−pinch. This consists of a cylindrical column of plasma which carries a current, J_z, in the axial direction (figure 1.2). Associated with this current is its own self−induced magnetic field, B_θ. In equilibrium, the outward internal pressure of the plasma is balanced by the radially inward $\underline{J} \wedge \underline{B}$ force at the plasma edge. In principle, then, one can confine any plasma at a given density and temperature, in a Z−pinch, simply by passing the appropriate current through it.

1.3. The Lawson Condition

One essential condition must be satisfied by all prospective fusion devices: namely, the energy released by the nuclear fusion reactions must more than compensate for the energy expended from other sources in generating and maintaining a high temperature plasma. This problem was examined by J.D. Lawson (1957). In his paper Lawson considered a general model not dependent on any particular method of confinement. The results are summarised below.

Assuming equal electron and ion number densities and temperatures then the internal energy of the plasma per unit volume is $3nkT$. The energy confinement time, τ, is defined by the equation:

$$P_Q = 3nkT/\tau \qquad (1)$$

where P_Q is the power loss per unit volume (through heat conduction, particle loss etc.), n is the electron density.

The other energy loss mechanism is taken to be bremsstrahlung and the power loss per unit volume is:

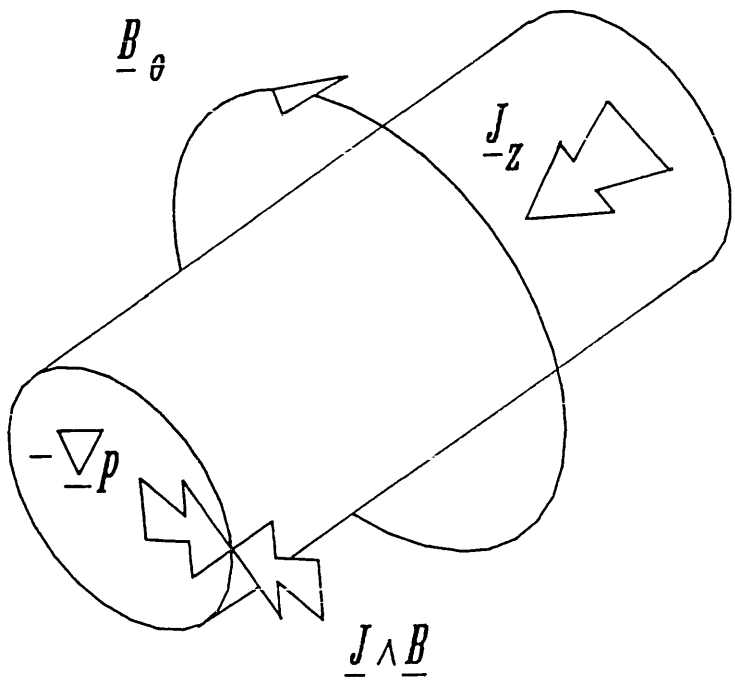


Figure 1.2: The linear Z-pinch

$$P_b = 1.5 \times 10^{-38} Z^2 n^2 (kT/e)^{\frac{1}{2}} \quad \text{[S.I.]} \qquad (2)$$

The output power due to fusion reactions per unit volume of plasma depends on the components of the reaction. For a deuterium/tritium mixture this power is:

$$P_t = (n^2/4)\langle \sigma v \rangle Q_t \qquad (3)$$

where σ is the reaction cross-section

v is the particle velocity

$\langle \ldots \rangle$ denotes an average value

Q_t is the energy released per reaction.

Lawson took into account the efficiency of converting the thermal energy into electrical energy and also the efficiency of heating the plasma; this he denoted by η which he took to be $1/3$. The Lawson condition then states that the energy necessary to maintain the plasma at thermonuclear conditions must be less than η times the energy released from the plasma and from thermonuclear burn i.e.:

$$P_b + P_\ell < \eta(P_b + P_\ell + P_t) \qquad (4)$$

Substituting for the various energy losses and gains, one finds that this imposes a condition on the product $n\tau$:

$$n\tau > \frac{3kT}{\frac{\eta}{1-\eta}\frac{Q_t}{4}\langle \sigma v \rangle} \qquad (5)$$

where it is assumed that the power generated is much greater than bremsstrahlung loss.

So $n\tau$ is a function of temperature only. For the DT reaction, $\langle \sigma v \rangle$ peaks ($\approx 5 \times 10^{-22}$ $m^3 s^{-1}$) at about a temperature of 20 keV and so the Lawson condition becomes (with $Q_t \simeq 3.5$ MeV):

$$n\tau > 3 \times 10^{20} \quad [m^{-3}s]$$

1.4. Stability of Z-pinches

In order to utilise the Z-pinch as a fusion device then the equilibrium state must be stable for at least as long as the energy confinement time, τ. Figures 1.3.a and 1.3.b show the form of two of the simplest perturbations that can occur

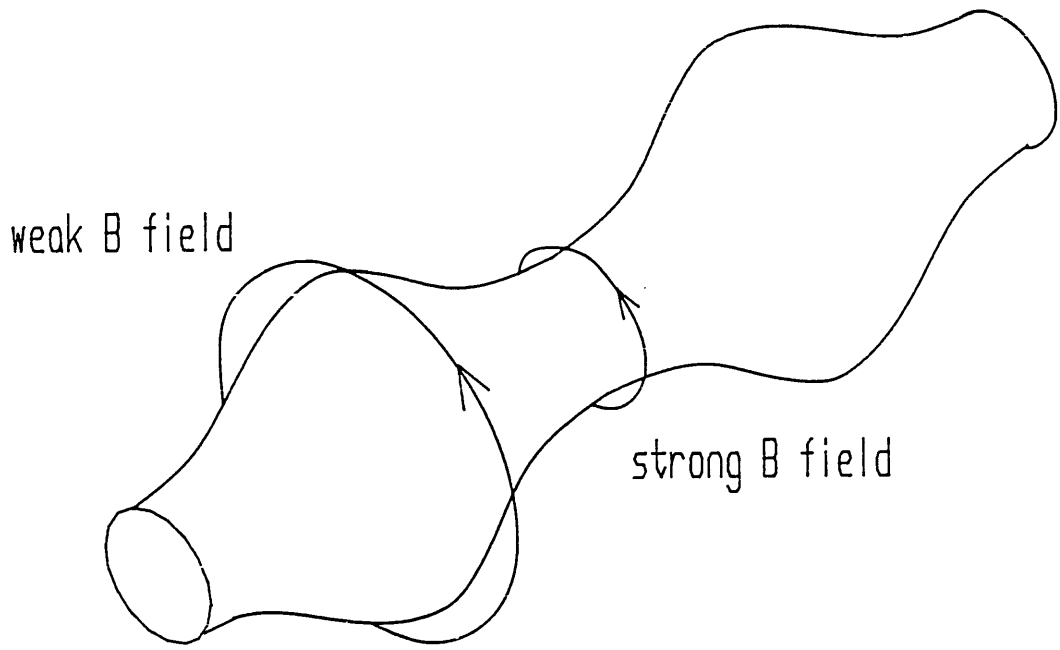


Figure 1.3.a: The m=0 (sausage) instability

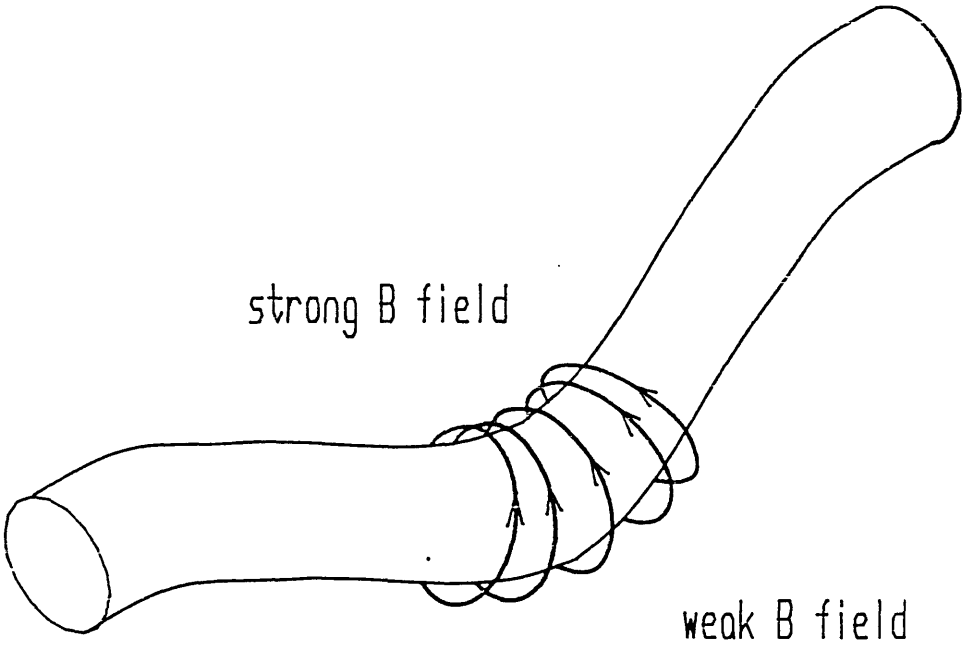


Figure 1.3.b: The m=1 (kink) instability

in a linear pinch. The first consists of local contractions of the plasma along its length. As a result the magnetic pressure in the contracted region is greater than in the neighbouring regions. Since the plasma is free to flow in the axial direction then this rise in magnetic pressure is not offset by an increase in the internal pressure. Hence the deformation carries on growing and disrupts the pinch. From its appearance this instability is frequently referred to as a 'sausage' instability.

The second deformation is known as a 'kink' instability since the plasma axis is displaced in a sinusoidal fashion. In this case the field strength on the outside of the bend is less than that on the inside and so the amplitude of this perturbation also increases in time.

The stability analysis of the Z−pinch has been treated and reviewed in some detail (Tayler 1957, Freidberg 1982). The salient features are summarised below.

If we consider a cylindrical Z−pinch then when a perturbation occurs the surface of the pinch ceases to be cylindrical. The perturbation changes the distance from the surface to the axis by an amount δr. This displacement can be represented as a superposition of Fourier components of the form:

$$\delta r = \xi_o e^{i(m\theta + kz - \omega t)} \qquad (6)$$

where ξ_o is the amplitude of the component

k is the axial wavenumber.

The coefficient m is called the mode number and it determines the azimuthal periodicity of δr. When $m=0$ the displacement is independent of the azimuth. This is just the sausage instability. The $m=1$ mode is the kink instability where the axis of the pinch column is disturbed helically.

The $m=0$ and $m=1$ modes are found to be the most unstable both theoretically and experimentally.

For a Z−pinch plasma to be stable to the $m=0$ MHD mode the pressure profile must satisfy the Kadomtsev criterion (Kadomtsev, 1966):

$$S(r) = - \frac{r}{P_0}\frac{dP_0}{dr} - \frac{2\Gamma}{(1 + \Gamma\beta(r)/2)} < 0 \qquad (7)$$

where $P_0(r)$ is the equilibrium pressure profile

$B_0(r)$ is the equilibrium magnetic field

$\beta(r) = 2\mu_0 P_0 / B_0^2$

Γ is the ratio of specific heats.

A profile in which P_0 falls off more steeply with r at any point is unstable. Also note that since P_0 is finite for all r then any equilibrium where P_0 falls to zero at the edge is unstable to $m=0$ modes. It can also be shown that a profile is Kadomtsev stable only if the current density is slightly peaked on axis.

For modes with $m \neq 0$ the Z−pinch is stable to internal modes if

$$-\frac{r}{P_0}\frac{dP_0}{dr} - \frac{m^2}{\beta(r)} < 0 \qquad (8)$$

is satisfied everywhere. A Z−pinch with a finite current density on axis is always unstable to $m=1$ modes.

A thorough discussion of the stability of Z−pinches with respect to experimental observations at Imperial College can be found in a paper by Coppins (1987).

The conditions under which ideal MHD is valid are discussed in detail by various authors (Freidberg, Coppins). These can be summarised as follows:

Large collisionality is needed to establish Maxwellian distributions amongst the ions and electrons. However, this cannot be too large such as to allow resistive diffusion to be significant i.e. plasma resistivity has to be negligible. Finally, the ion Larmor radii have to be negligible compared to the pinch radius, again such that the scale length for resistive diffusion is much smaller than the typical plasma dimensions. Freidberg (1982) expresses these conditions in terms of two dimensionless variables x and y:

$$x = \sqrt{(m_i / m_e)} v_i^{th} \tau_{ii} / a \qquad (9.a)$$

$$y = a_i / a \qquad (9.b)$$

where:

v_i^{th} is the ion thermal velocity

$$= \sqrt{(kT_i / m_i)} \qquad (9.c)$$

τ_{ii} is the ion collision time

$$= 2.09 \times 10^7 \, T_i^{3/2} \sqrt{\mu} / (Z^2 n_i \ln\Lambda) \text{ [c.g.s.]} \qquad (9.d)$$

a_i is the ion Larmor radius

$$= v_i^{th} / \omega_i \tag{9.e}$$

ω_i is the ion Larmor frequency

$$= ZeB / m_i \tag{9.f}$$

μ is the ratio of the ion to proton mass

$ln\Lambda$ is the Coulomb logarithm.

Thus:

(a)	small gyroradius,	$y \ll 1$
(b)	large collisionality,	$x \ll 1$
(c)	small resistivity,	$y^2 / x \ll 1.$

If any of these three conditions are not fulfilled then ideal MHD has to be modified accordingly.

1.5. The Equilibrium Z−pinch

In a Z−pinch which is in radial equilibrium, plasma heating and confinement are both determined by the pinch current. If the current rises too slowly it allows the plasma to heat up faster than the build−up of the confining magnetic field; as a result the plasma column expands. On the other hand, if the current rises too fast then the heating rate is slow compared to the build−up of the magnetic field and the plasma column pinches. There is a particular current waveform for which the plasma can be heated in radial equilibrium.

This heating process can be characterised by two equations:

(a) the energy balance equation

$$\frac{d}{dt} \left\{ \frac{3}{2} \left[n_e kT_e + n_i kT_i \right] \right\} = \eta J^2 - P_{rad} - P_{cond} \tag{10}$$

where $n_{e,i}$ is the electron, ion number density

$T_{e,i}$ is the electron, ion temperature

η is the plasma resistivity (see Spitzer, 1956)

P_{rad} is the energy loss due to radiation

P_{cond} is the energy loss due to conduction.

(b) the pressure balance equation

$$\underline{J} \wedge \underline{B} = \underline{\nabla} (p_e + p_i) \tag{11}$$

where $\underline{B}$ is the self magnetic field produced by the pinch current

$p_{e,i}$ is the electron, ion pressure $= n_{e,i} k T_{e,i}$.

The magnetic field can be expressed in terms of the pinch current through Ampere's Law:

$$\underline{\nabla} \wedge \underline{B} = \mu_0 \underline{J} \tag{12}$$

Then, assuming $T_e = T_i$ (for simplicity), integration of equation (11) over the pinch cross-section gives the Bennett equation:

$$8\pi N_e k T_e (1 + 1/Z) = \mu_0 I^2 \tag{13}$$

where $n_i = n_e / Z$ (Z is the effective charge of the ion)

$N_e = \int 2\pi r n_e dr$ is the pinch line density

(number of electrons per unit length of plasma)

The analysis of the equilibrium pinch was first carried out (independently) by Pease and Braginskii (1957) where they considered the steady state solution of Joule heating balancing bremsstrahlung radiation losses. The solution contains the result that a steady state pinch is in equilibrium at only one current independent of pinch radius and plasma density. For a hydrogen plasma this current (Pease-Braginskii current) is about 1.7 MA.

If axial losses are taken into account (Haines, 1960) then in the steady state the energy equation (10) becomes:

$$\frac{\partial q_z}{\partial z} + \frac{1}{r} \frac{\partial}{\partial r} (r q_r) + \beta_b n^2 T^{\frac{1}{2}} = J_z E_z \tag{14}$$

where q_z and q_r are the axial and radial heat fluxes, respectively and Bremsstrahlung radiation loss in a hydrogen plasma dominates at high temperatures ($\beta_b = 1.69 \times 10^{-32}$ [W/cm^3]).

Haines neglected the radial heat loss and considered two extreme cases: $\Omega_e\tau_e = 0$ and $\Omega_e\tau_e = \infty$ ($\Omega_e\tau_e$ is the electron Hall parameter). Both cases gave almost identical results. For $\Omega_e\tau_e = \infty$, the steady state temperature is given by:

$$T_m^{2.5} = 1.41 \times 10^{-3} z_0 (\pi a^2)^{-1} I(1 - (I/I_{pb})^2) \qquad (15)$$

where z_0 is the pinch length

a is the pinch radius

$I_{pb} = (4k/\mu_0)(G\ln\Lambda/\beta_b)^{\frac{1}{2}}$ is the Pease–Braginskii current

$G = (4e^2/3\epsilon_0^2)(2\pi m/k^3)^{\frac{1}{2}}$

$\ln\Lambda$ is the Coulomb logarithm.

So, a steady state can exist for any current below I_{pb} with a temperature T_m given by equation (15). Maximum steady state temperature is achieved when

$$I = I_{pb}/\sqrt{3} \simeq 0.97\ MA$$

The full time–dependent energy equation can be solved (again neglecting radial losses – see e.g. Favre–Dominguez 1985, Schlachter 1982). The solution gives the dependence of temperature (and hence current through the Bennett equation) on only number density and line density. Hence one has a set of curves (Haines–Hammel curves, see e.g. Haines 1960) to describe the approach to the Pease–Braginskii current assuming a Bennett equilibrium, ohmic heating and bremsstrahlung losses.

To get an idea of the initial current rate of rise needed to achieve this, we note that at early times, when the plasma is cold, energy losses are not important. Assuming $n_e = n_i = n$ and $T_e = T_i = T$ and using the Bennett relation (equation (13))in equation (10) we find (e.g. Haines, 1960):

$$\frac{dI}{dt} = 3.88 \times 10^{-3} \frac{N^{\frac{1}{2}}}{a^2 T} \qquad (16)$$

For the deuterium discharges of interest for controlled thermonuclear fusion, then one needs:

$$dI/dt \simeq 10^{15} - 10^{16} \qquad [\ As^{-1}\ ]$$

In the gas−embedded pinch, where a laser is used to create a discharge in, typically, one atmosphere of hydrogen, typical parameters are:

channel radius, $a_0 = 100\ \mu m$
initial channel temperature assumed to be $\simeq 3\ eV$
initial line density, $N = 1.7 \times 10^{18}\ m^{-1}$.

Hence, initially one needs:

$$dI/dt = 1.7 \times 10^{14} \qquad [\ As^{-1}\ ]$$

If rate of current rise is smaller than indicated by the above expression then the plasma will expand because the rate of ohmic heating will not be balanced by the rate of increase of magnetic pressure. Conversely, for larger rates of rise the plasma will contract.

1.6. Z−pinch Experiments

It has been shown theoretically that a Z−pinch in radial equilibrium with end losses to electrodes and bremsstrahlung radiation losses balanced by ohmic heating can satisfy the Lawson condition, $n_e\tau \gtrsim 10^{20}\ m^{-3}s$ (Haines, 1978). Conceptual fusion reactor parameters have been calculated for typical number densities, $n_e \simeq 10^{27}\ m^{-3}$ and confinement times, $\tau \simeq 10^{-7}\ s$; these conditions can be achieved in a short ($\ell \simeq 0.1\ m$) and narrow ($r \simeq 20\ \mu m$) deuterium/tritium discharge with a current of $\simeq 1\ MA$.

Alfven and Smars (1960) first proposed that a Z−pinch embedded in a dense neutral gas background may be of interest as a controlled fusion device. The analysis of Manheimer (1972) showed that the embedded Z−pinch could attain enhanced stability. Early experiments were performed by Smars, where a hydrogen discharge between two plane electrodes at atmospheric pressure was driven by a generator producing a current rate of rise of $dI/dt \simeq 10^{11}\ As^{-1}$. Later work involved using high power lasers to create a discharge channel which was subsequently heated by a large current (Pechacek, Jones, Hammel). All these experiments were operated in the regime of relatively slow rising currents: $dI/dt < 10^{12}\ As^{-1}$. Common features of these experiments are:

(i) continuous expansion of the plasma column with no radial equilibrium;

(ii) the absence of $m=0$ MHD instabilities;

(iii) a transformation of the expanding plasma into a helical structure via an $m=1$ MHD instability.

Even with current risetimes of the order of 5×10^{12} As^{-1} these features have still been observed (Hammel *et al*, 1983). However, examination of the requirements for pinch equilibrium shows that current rise rates much larger than those used in the above experiments are required in the initial phase of the channel development.

The initial rate of rise of current needed is inversely proportional to the channel temperature. Thus at early times, when the plasma is cold, a large dI/dt is needed. To overcome this, a small axial current prior to the main current pulse is applied to the pinch (Dangor *et al* 1984, Favre−Dominguez 1985). This then creates the necessary conditions for the main current pulse to heat the pinch under radial pressure balance.

In the preheated pinch there is initially an expansion of the discharge column (during the preheat). However, when the main current is applied a narrow plasma column is formed which is in pressure equilibrium. The duration of this equilibrium phase is of the order of ~ 4 MHD growth times. This equilibrium pinch is finally disrupted by an internal $m=1$ instability which transforms the pinch into an expanding helical structure.

Measurements show that there is an increase in the pinch line density. This accretion of particles is also observed in other experiments (Hammel *et al*, 1983). These observations are consistent with a model in which the column expansion is a result of an increase in plasma at the channel−neutral gas interface. It has also been suggested that accretion plays an important part in establishing the onset of the $m=1$ instability in the preheated Z−pinch (Coppins, 1987).

Two techniques to control accretion have been suggested. The first is to limit the line density by initiating a pinch in a small diameter capillary i.e. to use a physical wall to limit accretion (Sethian *et al* 1984, Hammel *et al* 1984). However, experiments performed at the Naval Research Laboratory show that the walls of the capillary are turned into plasma early on into the current flow. This, together with the internal plasma, expands continuously.

The second approach to eliminate accretion is to use a solid, small diameter, deuterium fibre. Since the fibre is surrounded by vacuum then the line density is determined solely by the amount of fibre material. Recent results from such experiments are encouraging. At the Los Alamos National Laboratory Z−pinch columns have been made from 40 μm diameter fibres of solid deuterium (Scudder, 1985). A high voltage generator produces channels with line density, $N = 6 \times 10^{19}$ m^{-1} carrying a *250* kA peak current.

Although the column expands with velocities ~ 4×10^5 cm s^{-1} it appears to be free from instabilities for ≈ 100 Alfven transit times (~ 50 ns). During this time it is hot ($T \simeq 300$ eV) and dense ($n_e \simeq 2 \times 10^{21}$ cm^{-3}) and producing neutrons. After this time an $m=0$ instability sets in. X−ray diagnostics show that the column, and not the m= 0 instabilities, is the source of neutrons. In addition, none of the instabilities themselves have a temperature $T > 1$ keV.

More recently, Sethian *et al* (1987) have formed dense Z−pinches from deuterium fibres from 80 − 125 μm diameter with peak currents up to 640 kA. Their pinch appears to remain stable during the 130 ns up to the current maximum. This corresponds to ~ 40 MHD growth times. At current peak the pinch is seen to go rapidly $m=0$ unstable and produces a very large neutron pulse (~ 10^{12} neutrons in ~ 30 − 60 ns pulse).

Preliminary theoretical investigations, based on ideal MHD theory (Coppins, Culverwell and Chittenden, 1987), suggest that the fibre is not fully ionised and that the fact that the instability attains observable amplitude at current peak is a coincidence.

1.7. Structure of the Thesis

This thesis describes work done on two experiments:

(a) a gas−embedded Z−pinch;

(b) a quartz fibre Z−pinch.

In the gas−embedded experiment a preheat current is applied to a channel which has been initiated in high pressure hydrogen using a focussed laser. This creates the necessary conditions for the main current (150 kA peak) to heat the pinch under radial pressure equilibrium. At this high current it is expected that the ions will be magnetised and that finite ion Larmor radius effects could lead to enhanced stability. Chapter 3 of this thesis presents the results and discussion pertaining to this experiment.

As a precursor to experiments on solid deuterium fibre pinches an experiment on a pinch produced from a quartz fibre was performed. This has lead to an understanding of the pinch formation and its subsequent development. Optical observations were made to determine the dynamics, stability and evolution of the plasma − these results are presented in Chapter 4. The evolution of the plasma electron density was followed using schlieren photography and holographic interferometry − Chapter 5 discusses the results from these observations. Finally, diagnosis of the X−ray emission from the plasma was performed to determine the

state of ionization and the temperature of the plasma. This is dealt with in Chapter 6.

A description of the apparatus used to perform both experiments is contained in Chapter 2. Both the experiments described in this thesis are reviewed in Chapter 7 and the significance of the results is discussed in the light of current research.

1.8. Units

All units are either S.I. or c.g.s. and are clearly indicated in all equations. All temperatures are quoted in eV. The notation employed for equations is as follows (e.g.):

$$F = ma \qquad [\mathrm{N}, (\mathrm{kg}, \mathrm{ms}^{-2})]$$

Here, the first unit in the square brackets refers to the quantity on the left−hand side of the equation and the units in round brackets refer (in order) to the quantities on the right−hand side of the equation.

CHAPTER TWO

The Apparatus

2.1. Introduction

As can be seen from the requirements on dI/dt (Chapter 1) the fast current risetimes that are needed necessitate the use of pulsed power technology. For that reason a new current generator was designed and built for this work.

The generator consists of a high voltage Marx bank which pulse charges a long section transmission line (see figure 2.1). This voltage is then applied across the load by means of a fast gas switch. The load is isolated from the switch inductance by a short section transmission line, known as the transfer section; this, together with the switch, shapes the current pulse initially.

The generator provides a current pulse of *150* kA, with a *10–90%* risetime of *50* ns, into an inductive (~ *50* nH) short–circuit load. The peak rate of rise of current is 3.0×10^{12} As^{-1}.

The performance of the generator is monitored by various voltage and current probes situated along its length. A resistive voltage divider at the Marx output monitors its behaviour. Two capacitive monitors measure the voltage (a) on the line before the switch and (b) on the transfer section at the load chamber end. The current delivered to the load is measured by a single turn coil situated inside the earth electrode of the chamber.

2.2. The Marx Bank

A Marx bank, which is a class of high voltage generator, consists of multiple capacitors which are charged in parallel and then rapidly switched to provide a series voltage multiplication.

The Marx used in the present experiment was originally loaned from A.W.R.E., Aldermaston by J.C. Martin and his colleagues and was previously used to generate relativistic electron beams. A detailed description of the current Marx is given by VanDevender (Ph.D. Thesis, 1974) whilst the technology employed in the Marx is given in Storr (1969).

Figure 2.2 shows a schematic diagram of the Marx. It is composed of eight

THE GENERATOR

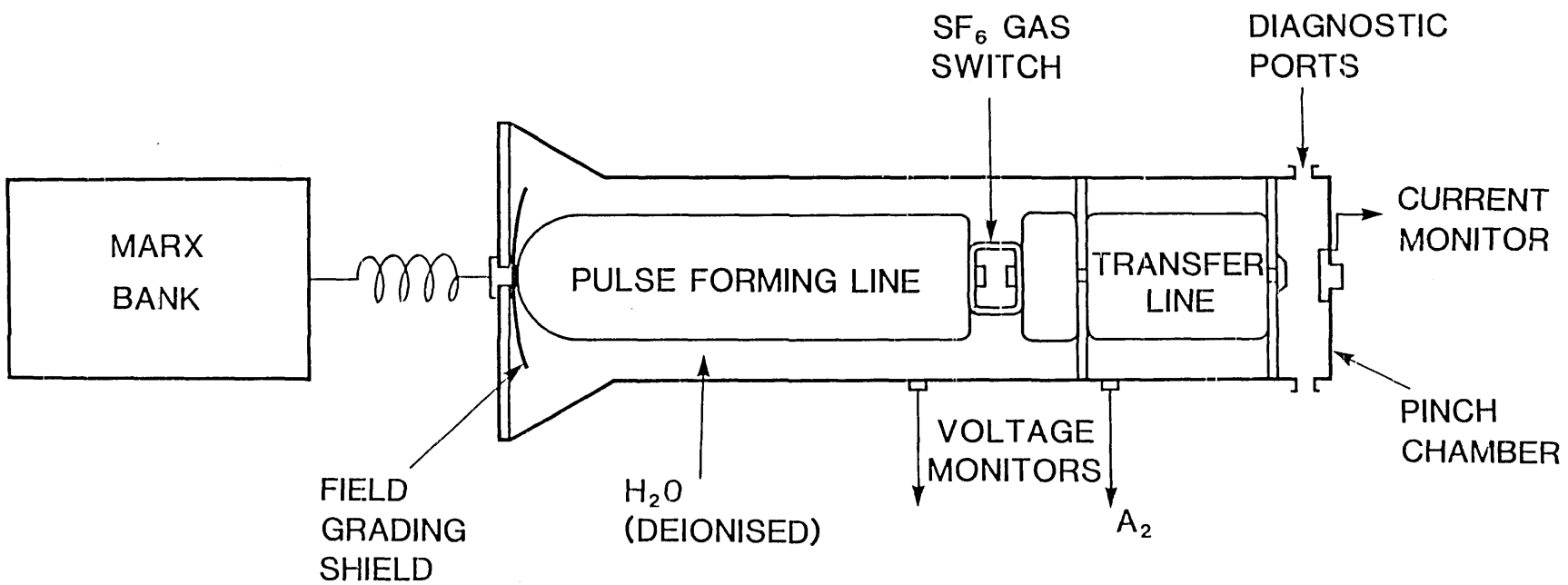


Figure 2.1: Schematic of the current generator

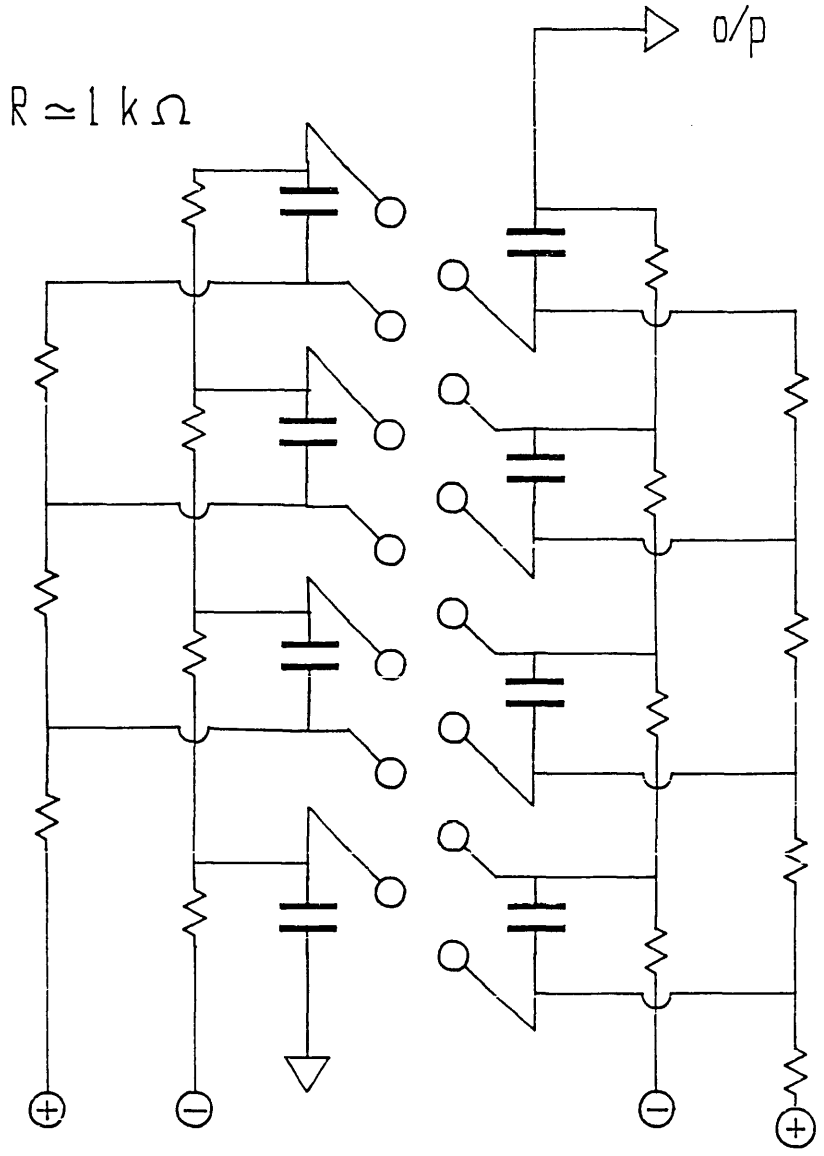


Figure 2.2: Schematic of the Marx bank

0.5 μF, *100* kV capacitors; these were each charged to *50* kV to give *400* kV across a capacitance of *62.5* nF when the Marx was switched to series. The external inductance linking the Marx output to the pulse-forming line was *4.8* μH. A wire cage housed the Marx, thus screening the outside environment from the electrical noise it generated when triggered.

2.3. The Transmission Line

The shape of the current pulse is determined by the transmission line itself. The line consists of a pulse-forming line (PFL) and a transfer section which are separated by a self-breaking switch.

The characteristics of the PFL are as follows:

dielectric	:	H_2O	
impedance	:	*3* Ω	(measured)
capacitance	:	*24* nF	-"-
double transit time	:	*160* ns	-"-

The line is made of dural and consists of a *15"* square section outer conductor with a *10"* diameter circular section inner conductor. The formula for the impedance of a line with such a cross-section is given in an article by Wheeler (1950):

$$Z = 60 \ln(sD/d) \quad [\ \Omega\ ] \tag{1}$$

where d = diameter of inner conductor

D = diameter of outer conductor

s is the measure of how much the outer conductor deviates from a circular cross-section($\simeq 0.70$).

For the present line we find:

$$Z = 3.2 \quad [\ \Omega\ ]$$

Thus the measured value is in close agreement with the calculated value.

The water is continuously circulated through a resin ion exchanger (Elga Products) which maintains the volume resistivity of the water above *1* MΩcm. This provides a self-discharge e-folding time of $\simeq$ *7* μs compared with the line charging time of $\simeq$ *1* μs. Water is chosen as the dielectric for the transmission line because of:

(i) the high energy storage per unit volume;

(ii) a low EM wave velocity and hence smaller physical length compared with oil dielectric;

(iii) its self−healing property after breakdown and last, but not least

(iv) it is very cheap!

Figure 2.1 shows the relevant details. The interface between the inductive feed from the Marx and the line is a *2.5* cm thick, *4'* square sheet of perspex followed by a water dielectric reduction section − this is needed to overcome surface tracking problems at the interface. A voltage grading shield is put on the inside to inhibit flashover across the interface.

2.4. The Line Switch

The switch used for shaping the current pulse is a self−breaking gas gap. Figure 2.3 shows the cross−section of the switch. The insulating body was machined from a solid cast block of perspex which was then annealed to rid it of stresses. The brass electrodes were spring loaded to absorb the breakdown shock. SF_6 was used as the working gas because of its excellent electrical properties − reliable breakdown and high stand−off voltage. The switch was calibrated by measuring the hold−off voltage as a function of filling pressure (the hold−off voltage is the threshold voltage at which the gap self−breaks).

Reliable operation and low temporal jitter was obtained by operating the switch at the *80%* self−break condition i.e. for a given voltage, V_0, the gap pressure is adjusted such that it closes at a voltage $V = 0.8V_0$. For the present transmission line the time at which the switch closed was $\approx$ *720* ns after the Marx had erected.

The design of the switch (figure 2.3) allowed the transfer section to be charged to small fraction of the main charging voltage. Since the plates either side of the switch are of a larger diameter there is a capacitance between the PFL and the transfer section and this allows a small fraction of the main voltage to appear on the transfer section. The capacitance across the switch is thus:

$$C_S = \epsilon_0 \epsilon_r A / d \qquad (2)$$

where A is the effective area of the plates

d is the spacing between the plates.

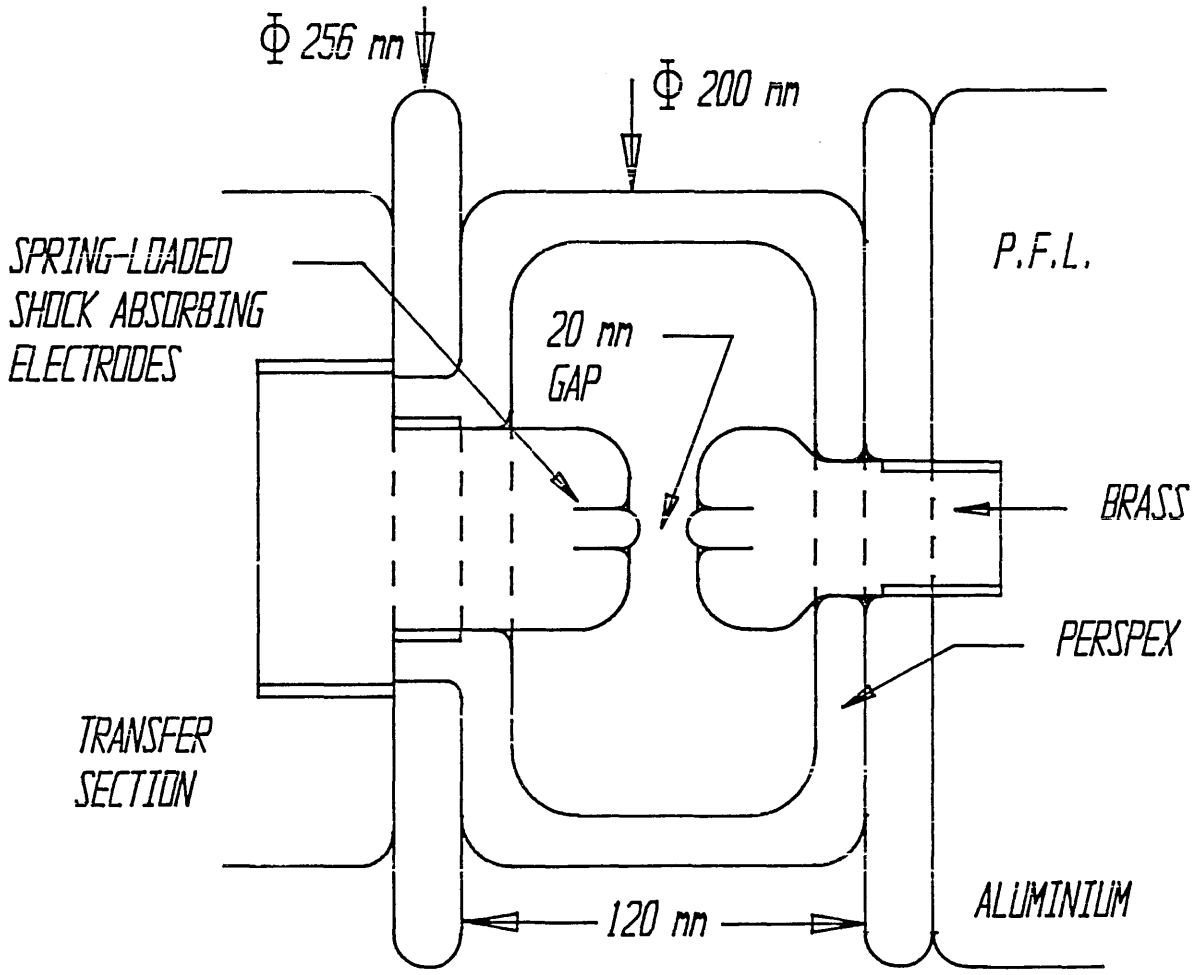
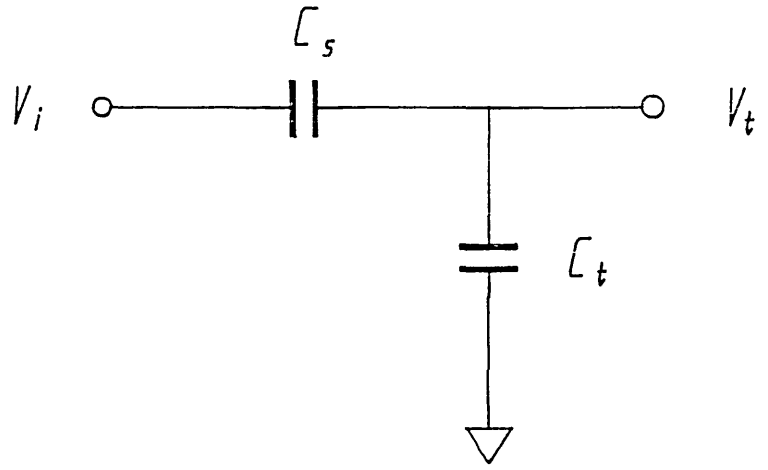


Figure 2.3: Schematic cross-section of the line switch



V_i is the voltage on the PFL

V_t is the voltage on the transfer section

C_s is the capacitance across the switch = 0.15 nF

C_t is the capacitance of the transfer section = 11.4 nF

Figure 2.4: Charging of the transfer section via the switch capacitance

Putting in the values for A and d we find:

$$C_s \simeq 0.15 \qquad \text{[nF]}$$

Since the transit time of the transfer section (and the PFL) is small compared to the charging time then it behaves as a capacitor; the value of this capacitance is $C_t = 11.4$ nF. Hence the equivalent electrical circuit of the charging of the transfer section via the switch capacitance is as shown in figure 2.4.

So the precharge fraction is:

$$\frac{V_t}{V_i} = \frac{C_s}{C_s + C_t} = 0.013$$

For $V_i \simeq 500$ kV the prepulse voltage, $V_t \simeq 6.5$ kV and the measured prepulse current was $\simeq 2$ kA. This current is not large enough to achieve conditions whereby the gas-embedded pinch can be heated under pressure balance.

However, by putting resistors across the gap one can increase this fraction substantially. This was done for the gas-embedded experiment, where the preheat current was provided by discharging the transfer section prior to the gap closing.

2.5. The Transfer Section

The transfer section performs two functions:

(a) it isolates the pinch inductance from the switch inductance and so improves the current risetime;

(b) it provides a small preheat current (when necessary) before the main discharge.

The transfer section is necessary in order to achieve the highest possible rate of rise of current; it can be shown that when the switch inductance is comparable to the load inductance then inclusion of a transfer section significantly increases dI/dt compared to not having a transfer section (Choi, PhD Thesis, 1983). Figure 2.5 shows the current profiles (into a short circuit) with and without a transfer section for the parameters of the present generator. These profiles were calculated using a transmission line code named BERTHA, which is described in Appendix A.

In the gas-embedded experiment a preheat current is required in order for the main current to be able to heat the pinch under pressure balance. This is provided by charging the transfer section to a fraction of the main line voltage via

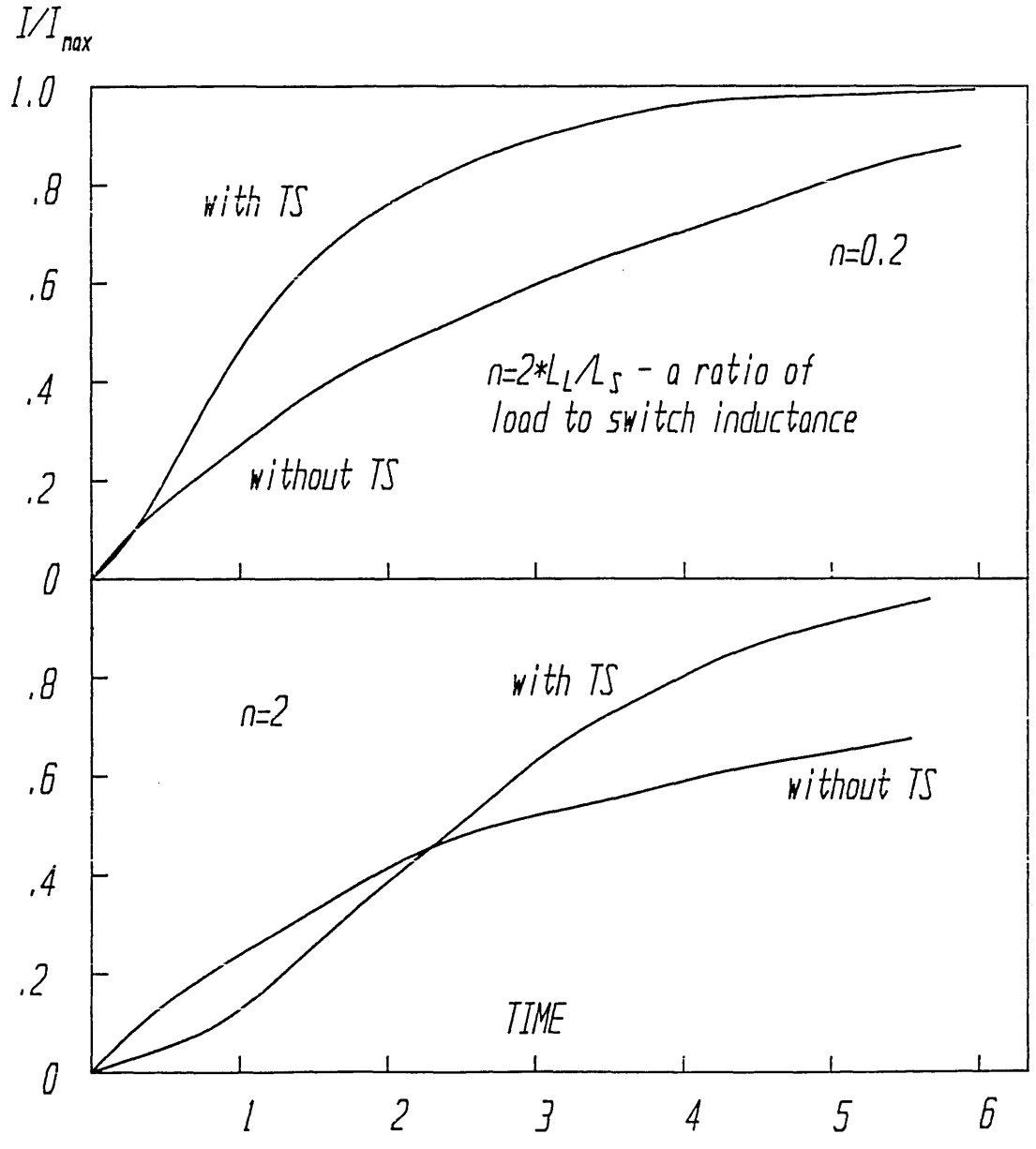


Figure 2.5: Current profiles with and without a transfer section

$CuSO_4$ resistors placed across the line switch. The equivalent charging circuit is shown in figure 2.6.

Here V_i is the voltage on the PFL and can be approximated by:

$$V_i = V'(1 - \cos \omega t) \tag{3}$$

where V' is the peak line voltage = Marx stacked voltage × gain of the PFL.

The circuit equation is:

$$\frac{dV_o}{dt} + \frac{V_o}{RC} = \frac{V_i}{RC} \tag{4}$$

The solution of equation (4) with V_i given by equation (3) at the time $t=T/4$ (T is the PFL charging period) is:

$$V_o = V'[1 - \exp(-T/4\tau)] \tag{5}$$

where $\tau = RC$.

For 5% precharge, $\tau = 9.5$ μs and thus $R \simeq 680\ \Omega$. This is close to the value calculated from the BERTHA program.

The discharging of the transfer section into the pinch can be represented by an LC circuit as shown in figure 2.7. The pinch is represented as an inductive load. The equation describing the current in such a circuit is:

$$\frac{d^2 i}{dt^2} + \frac{1}{LC}\, i = 0 \tag{6}$$

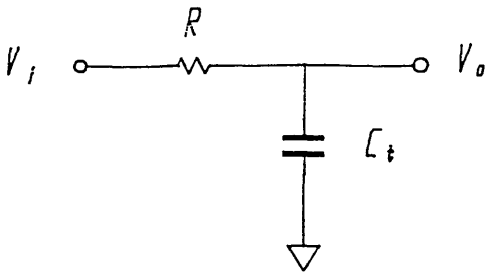
Solving the above equation, one finds that the period is given by:

$$T = 2\pi(LC)^{\frac{1}{2}} \simeq 180 \text{ ns} \qquad \text{(using the line parameters).}$$

The peak current is

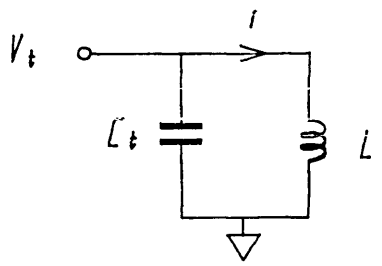
$$I_t = V_t(L/C)^{-\frac{1}{2}} \simeq 8 \text{ kA}$$

Figure 2.8 shows a typical preheat current into a short circuit together with a profile generated by BERTHA; both agree very well with the calculated values.



V_i is the voltage on the PFL
V_o is the voltage on the transfer section
R is the total resistance across the switch
C_t is the capacitance of the transfer section = 11.4 nF

Figure 2.6: Resistive charging of the transfer section



V_t is the voltage on the transfer section $\simeq$ 20 kV
i is the current flowing into the load, L
C_t is the capacitance of the transfer section
L is the inductance of the pinch plus electrodes $\simeq$ 70 nH

Figure 2.7: Discharging of the transfer section into the pinch

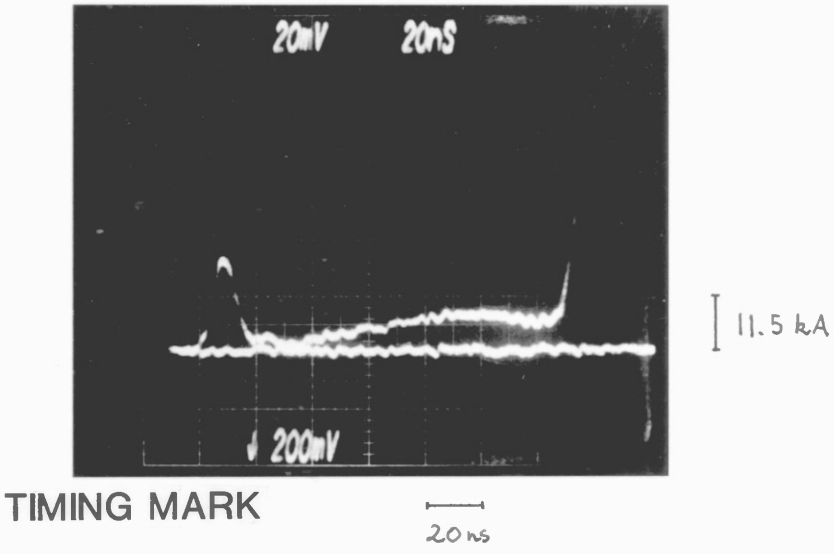


Figure 2.8.a: Preheat current into a short-circuit

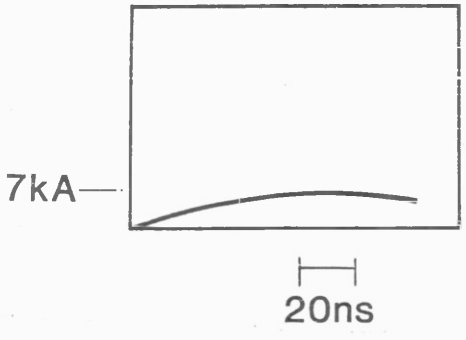


Figure 2.8.b: Current profile calculated by BERTHA

2.6. The Pinch Chamber

Two different chambers were used in the course of this work. Figure 2.9.a is a cross-section diagram of the first chamber which was used for the gas-embedded pinch experiment. The body was machined out of a cast block of dural and the flange was then welded onto it. When the chamber was bolted to the front of the generator it formed a continuation of the outer conductor of the transmission line. The transfer section tapered down to join the live electrode as shown in the diagram. The characteristics of the chamber are:

inner radius	:	*178* mm
external inductance	:	*50* nH
electrode separation	:	*13* mm
operating pressure	:	*0.3 – 2* bar

Since the geometry was coaxial, the external inductance could be calculated with reasonable accuracy by summing

$$L = 2\ell ln(b/a) \qquad \text{[nH, (cm)]} \qquad (7)$$

(where b = chamber inner radius, a = outer radius of electrode) over all the geometry (a more accurate formula is given in Grover, 1946). By placing a short circuit of known dimensions into the chamber, the external inductance could be deduced from the voltage across the electrodes and dI/dt. The resulting value agreed with the above calculation to within *5%*.

An *18* mm diameter quartz window allowed the laser initiating the gas-embedded pinch to be focussed onto the live electrode through a *2.5* mm diameter hole in the earth electrode. The earth electrode was specially shaped to allow the B_z monitor to be placed in a position where it did not perturb the pinch. Four quartz windows located on the circumference of the chamber and at *90°* to each other provide easy access to the pinch for the diagnostics. After each shot the chamber was pumped down to a base pressure of *10* mtorr using a rotary pump.

A current monitor was housed inside the earth electrode whilst a B_θ loop was placed close to the same electrode to act as another current diagnostic. The B_z monitor was placed coaxial to the earth electrode and monitored any axial flux that might be produced by the pinch.

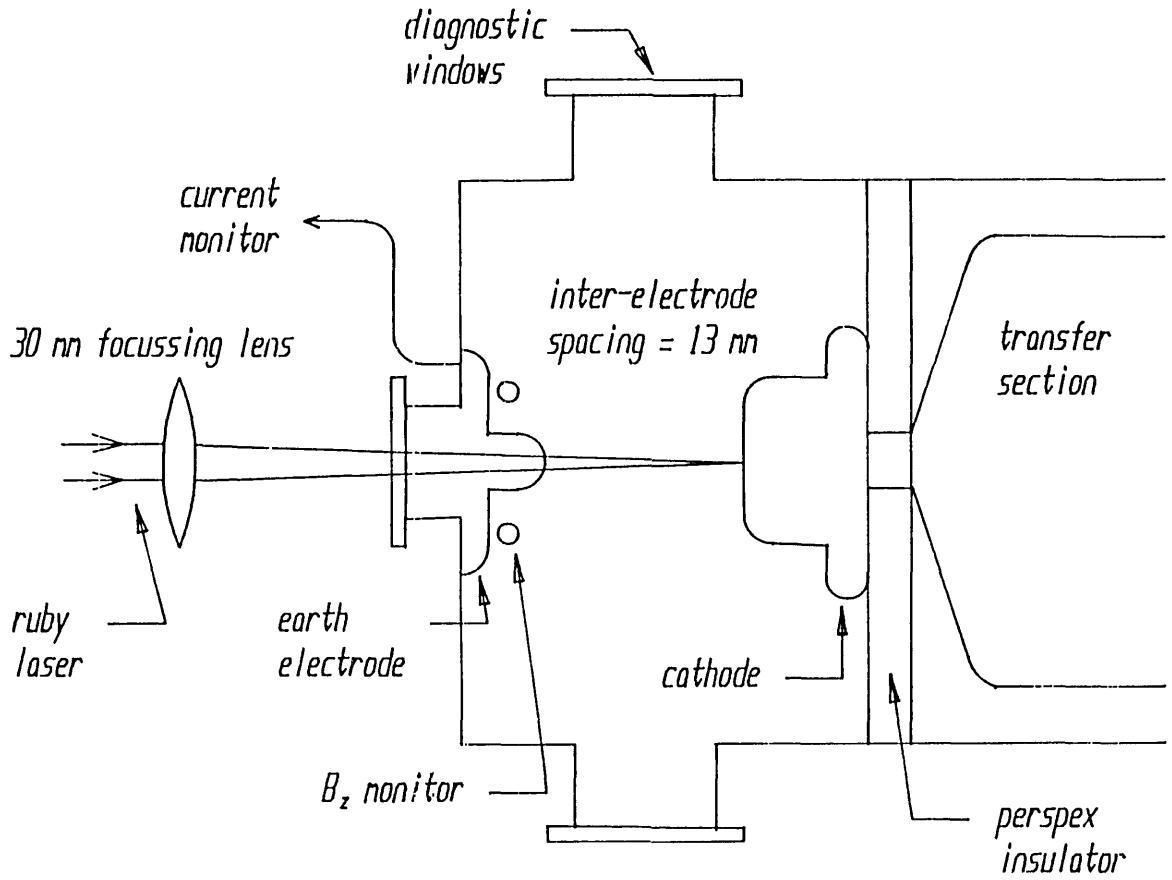


Figure 2.9.a: Schematic cross-section of the chamber used for the gas-embedded pinch experiment

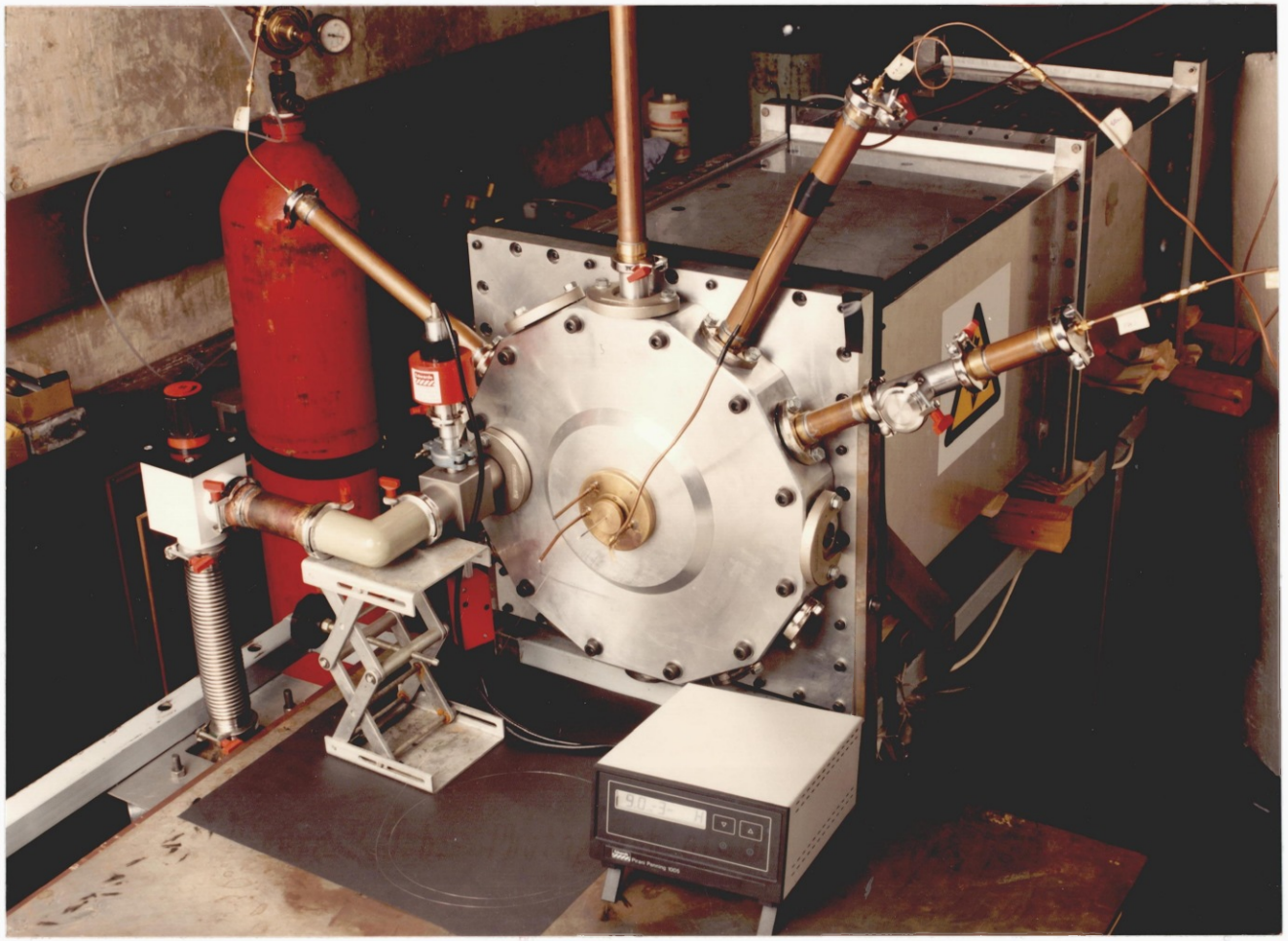


Figure 2.9.b: Photograph of the fibre-pinch chamber

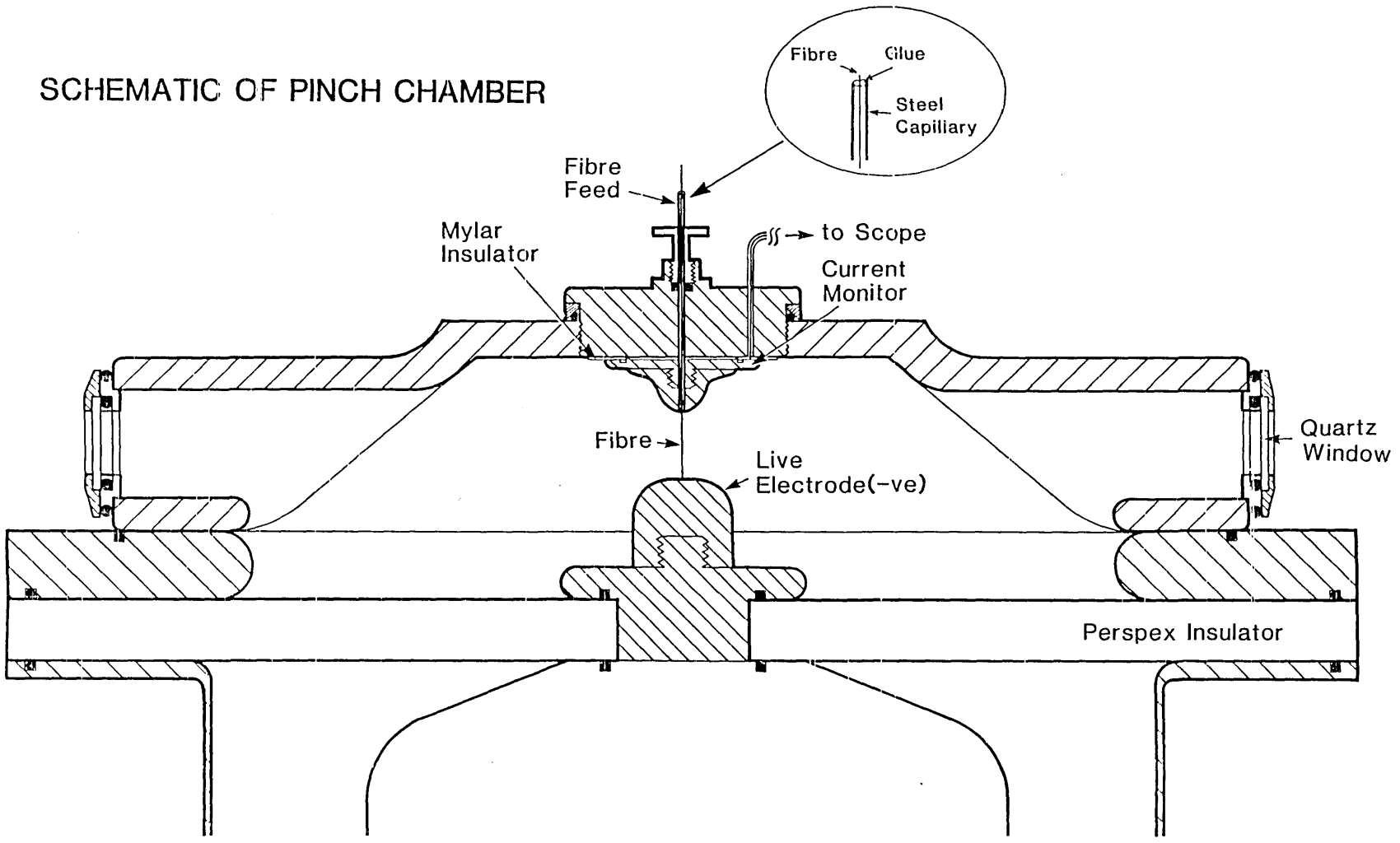


Figure 2.10: Schematic cross-section of the fibre-pinch chamber

For the fibre experiment a new pinch chamber was designed and built. This chamber provided more diagnostic ports and easier access to the pinch. Figure 2.9.b is a photograph of the new pinch chamber. It was machined out of a solid block of dural. There were twelve diagnostics ports; four of these took NW40 flange fittings whilst the rest were *NW25* size – these are a standard for vacuum work. The earth electrode assembly was made from brass and screwed into the chamber body; thus modifications could be made to the earth electrode without unbolting the chamber (a quite laborious process). The chamber was pumped by a rotary/diffusion pump system through a *NW40* port situated next to the earth electrode assembly. The working base pressure was ~ 10^{-4} torr. The chamber was bolted onto the front of the generator so that the body was a continuation of the outer conductor of the transmission line.

Figure 2.10 is a schematic cross–section of the chamber. The electrode separation is *25* mm. The inside was contoured as shown so that probes (specifically pinhole cameras) could be inserted without distorting the field too much. The *NW40* viewing ports allowed the whole pinch to be viewed if necessary. The figure also shows how the fibre was mounted inside the chamber.

2.7. The Voltage Monitors

There are two capacitive voltage monitors along the transmission line: one before the gas switch to monitor the voltage on the PFL and a second one to measure the voltage on the transfer section at the load end. By coupling to the high voltage inner conductor through the water surface breakdowns are eliminated and field distortions reduced. There is no need for precision balanced components. The probes contain a brass disc which couples to the inner conductor of the line and lies flush with the inner surface of the outer conductor, together with a dural shell which couples to the outer conductor via the water (figure 2.11.a). The use of the water as the dielectric for both dividing capacitors offers, in principle, a perfect voltage division ratio for any frequency signal (Choi, PhD Thesis, 1983).

The characteristics of such probes are described in detail in other publications (Favre–Dominguez, PhD Thesis, 1985; Shlachter, PhD Thesis, 1982). Figure 2.11.b shows the equivalent electrical circuit of the voltage monitor. The output voltage, V_o, is related to the input signal, V_i, via:

$$V_0 \frac{R}{\tau_0} + \frac{\tau_2}{\tau_0} \frac{dV_o}{dt} = \frac{V_i}{\tau_1} + \frac{dV_i}{dt} \qquad (8)$$

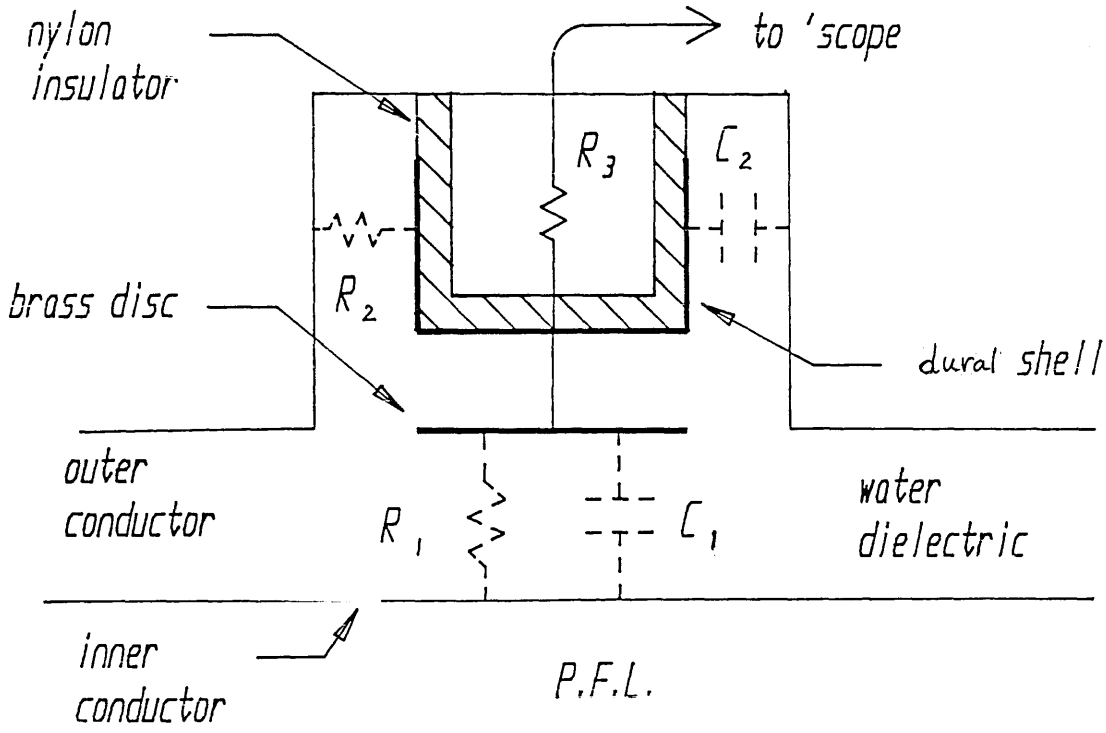
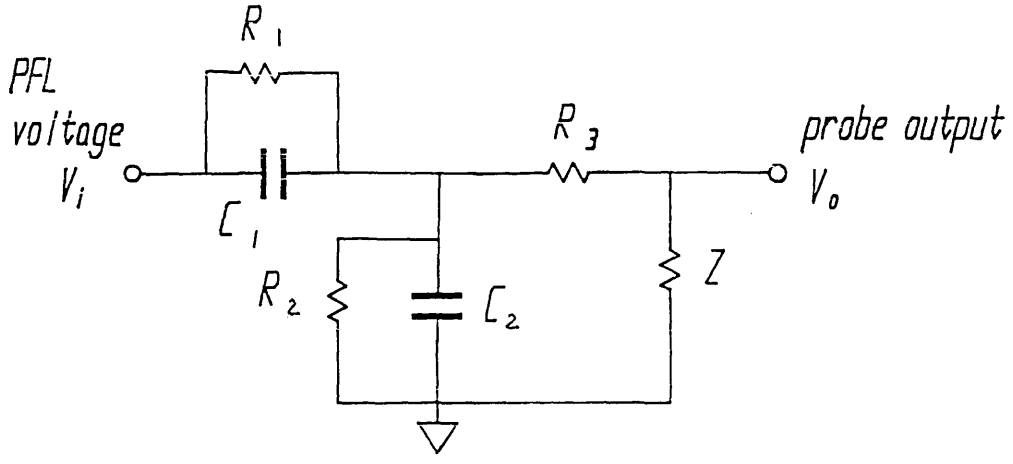


Figure 2.11.a: Schematic of the voltage monitor



C_2 is the capacitance between the probe shell and the PFL outer
C_1 is the capacitance between the probe disc and the PFL inner
R_1, R_2 are stray resistances (due to the water)
R_3 is an integrating resistor
Z is the cable inpedance between probe and 'scope

Figure 2.11.b: Equivalent electrical circuit of the monitor

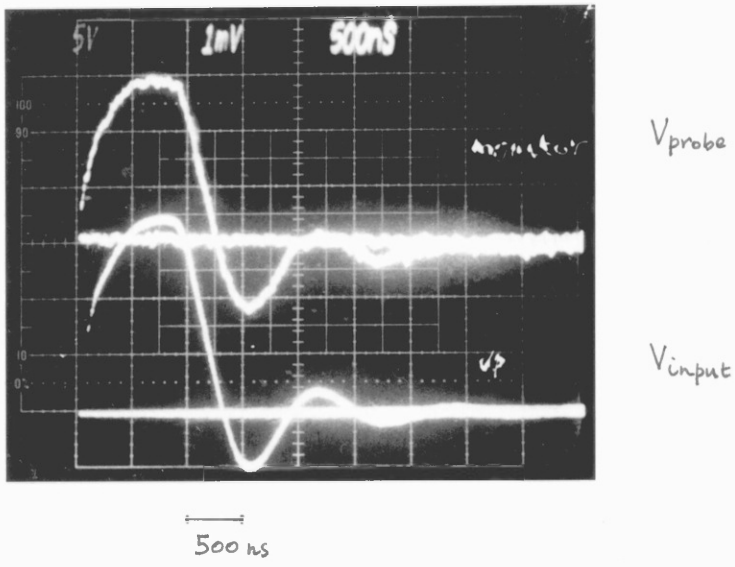


Figure 2.12.a: Calibration of the voltage monitors

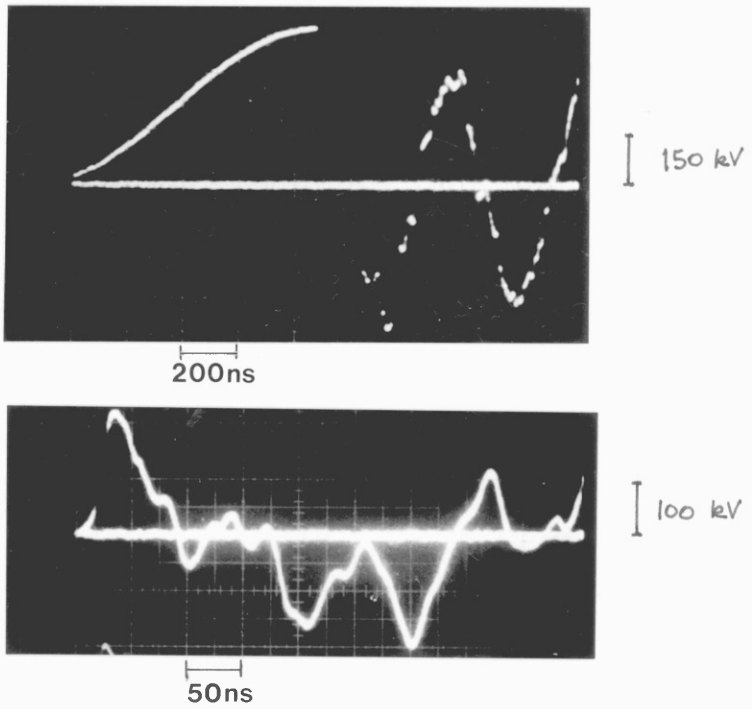


Figure 2.12.b: Output signals from the monitors

where $\tau_0 = ZC_1$

$\tau_1 = R_1C_1$

$\tau_2 = (R_3 + Z)(C_1 + C_2)$

$R = 1 + (R_3 + Z)(1/R_1 + 1/R_2)$

If one arranges for τ_1, $\tau_2/R \gg \Delta t$, the timescale of interest, then

$$\frac{\tau_2}{\tau_0} \frac{dV_o}{dt} \simeq \frac{dV_i}{dt} \tag{9}$$

Thus:

$$V_0 \simeq \frac{\tau_0}{\tau_2} V_i \tag{10}$$

Hence, the output is proportional to the input signal. The above conditions give the minimum values for C_1 and C_2 and the probe was designed to satisfy those values.

Calibration was performed by injecting a voltage pulse into the PFL and comparing the voltage monitor output with the output from a calibrated resistive voltage monitor. Figure 2.12.a shows a calibration shot whilst figure 2.12.b shows typical voltage waveforms before and after the line switch.

Both probes gave an output of *1* volt for an input of *50* kV.

2.8. The Current Monitor

A schematic of the current monitor is shown in figure 2.13.a. The monitor consists of an annular groove machined into the earth electrode assembly. The insulator forces the current to flow around the channel and the variation of magnetic flux inside the channel induces a voltage at the pick−up point A. The probe acts as a one−turn Rogowski coil and is described in detail in the literature (Ekdahl, 1980). The voltage induced at point A is

$$V = -\frac{d\Phi}{dt} = -\frac{\mu_0}{2\pi} \frac{dI}{dt} \int_r \int_z \frac{drdz}{r} \tag{11}$$

where $\Phi = \int \underline{B}.\underline{ds}$ and $\underline{ds}$ is an area element.

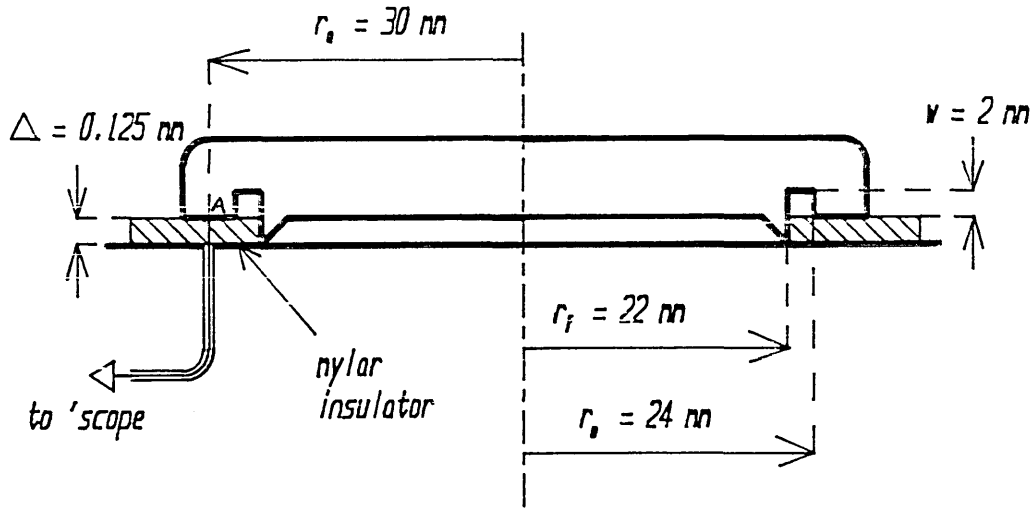


Figure 2.13.a: Schematic of the current monitor

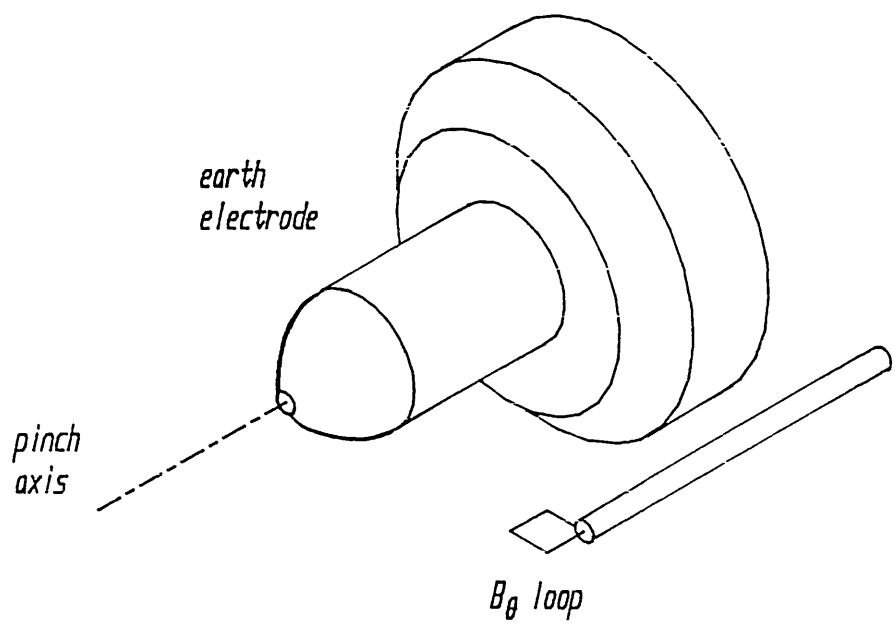


Figure 2.13.b: Schematic of the B_θ loop

Thus:

$$L_{tot} = \frac{\mu_0}{2\pi} \left\{ \int_{r_i}^{r_o} \frac{dr}{r} \int_0^{w+\Delta} dz + \int_{r_o}^{r_a} \frac{dr}{r} \int_0^{\Delta} dz \right\} \qquad (12.a)$$

$$= \frac{\mu_0}{2\pi} \{(w+\Delta) ln(r_o/r_i) + \Delta ln(r_a/r_o)\} \qquad (12.b)$$

$$= 4.3 \times 10^{-11} \quad [H]$$

The monitor was calibrated by discharging a capacitor into a short−circuit. This is an *LC* circuit and so the current delivered can be calculated; the monitor output is then measured and compared with the current delivered by the circuit. The measured value of L_{tot} was 4.5×10^{-11} H − the agreement with the calculated value was within *5%*.

Since the output voltage of the monitor is proportional to dI/dt then this signal has to be integrated to produce a current waveform. Passive integrators using feed−through capacitors (which are low inductance and help to reduce stray pick−up) were employed for this purpose.

The integrated output at the scope is (for $RC \gg \tau$, where τ is the typical frequency of the input signal):

$$V_o = (L_{tot}/RC)I \qquad (13)$$

where *RC* is the time constant of the integrator.

For $RC = 6.5$ μs the probe gave an output of *1* volt for a load current of *144* kA. This sensitivity was also verified by running the BERTHA code and agreement was within a few percent.

The B_θ loop (figure 2.13.b) works on the same principle as the one−turn Rogowski − it measures the flux produced by the axial current flow. Figure 2.14 shows the output of the loop and the corresponding trace from the current monitor. The agreement between both probes is good. It is preferable to use the latter for measuring currents since this measures the actual current through the pinch. The B_θ loop measures the local B_θ field; to deduce the current certain assumptions have to be made (viz. azimuthal symmetry and the geometry needs to be well−defined − loop area etc.). Such assumptions are not neccesary with the other probe.

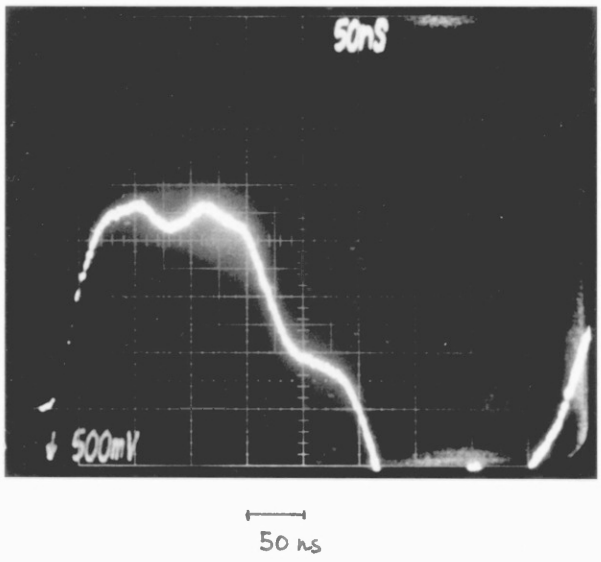


Figure 2.14.a: Output from the B_θ loop

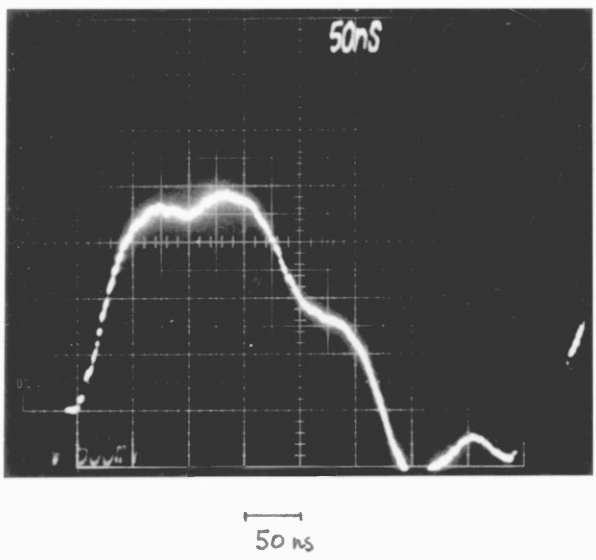


Figure 2.14.b: Output from the current monitor

2.9. The B_z Monitor

Figure 2.15.a is a schematic of the B_z monitor. It was made from a length of solid coaxial cable (*RG141, 50* Ω) which was wound into a coil with the inner conductor soldered to the outside at one point. The probe was placed over the specially shaped earth electrode close to its base and coaxial to the pinch (see figure 2.15.b). Since the brass electrode is a good conductor its skin depth for high frequency fields is very small; thus, any such magnetic fields produced by the pinch would not penetrate into the electrode i.e. the electrode acts as a flux−divertor. So the probe only monitored a fraction of any flux produced by the pinch (or calibration springs).

To check whether the probe was correctly aligned a straight short−circuit was placed coaxially in the chamber and the generator discharged through it. The probe was deemed to be correctly aligned when the output from it was zero.

Figure 2.15.b is a schematic showing the probe and a helical coil (which represents either the spring used for calibration or the pinch after it has been transformed into a helix). The mutual inductance of this system is:

$$M = M_{ld} - M_d \qquad (14)$$

where M_i = mutual inductance of a solenoid of length i with a coil situated in its end plane.

The mutual inductance of a solenoid with a single turn coil in its end plane is given by (Grover, Ch.14, p.111):

$$M = 2\pi^2 a\alpha\rho N Q_0(\alpha,\rho^2) \qquad \text{[nH, (cm)]} \qquad (15)$$

where:

$$\rho^2 = \frac{A^2}{(A^2 + x^2)} , \qquad \alpha = \frac{a}{A}$$

and Q_0 is a tabulated function of α and ρ^2 (see figure 2.15.b for notation).

In both the calibration and the experiment, $\alpha < 0.1$; in this case $Q_0 = 1$. Using the values in figure 2.15.b in equation (15) we get:

$$M = 8.9n'a^2 \qquad \text{[nH]} \qquad (16)$$

where n' is the number of turns per centimetre in the solenoid.

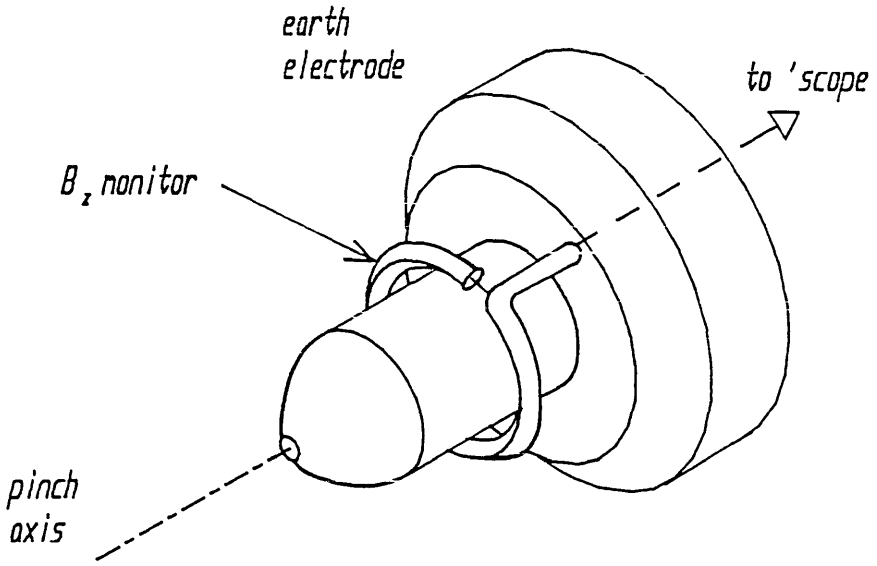


Figure 2.15.a: Schematic of the B_z monitor

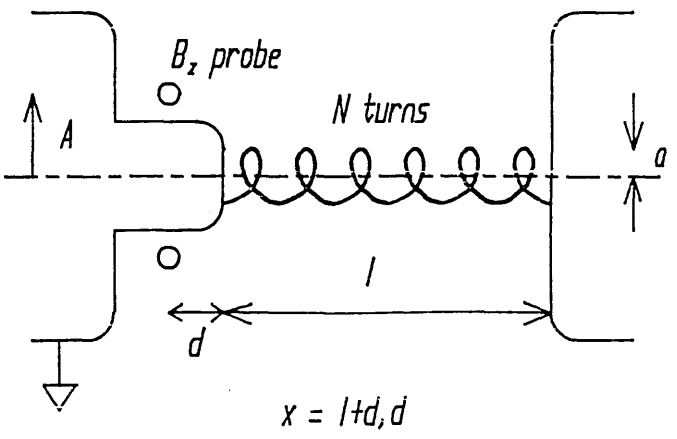


Figure 2.15.b: Schematic showing the B_z probe with a helical coil

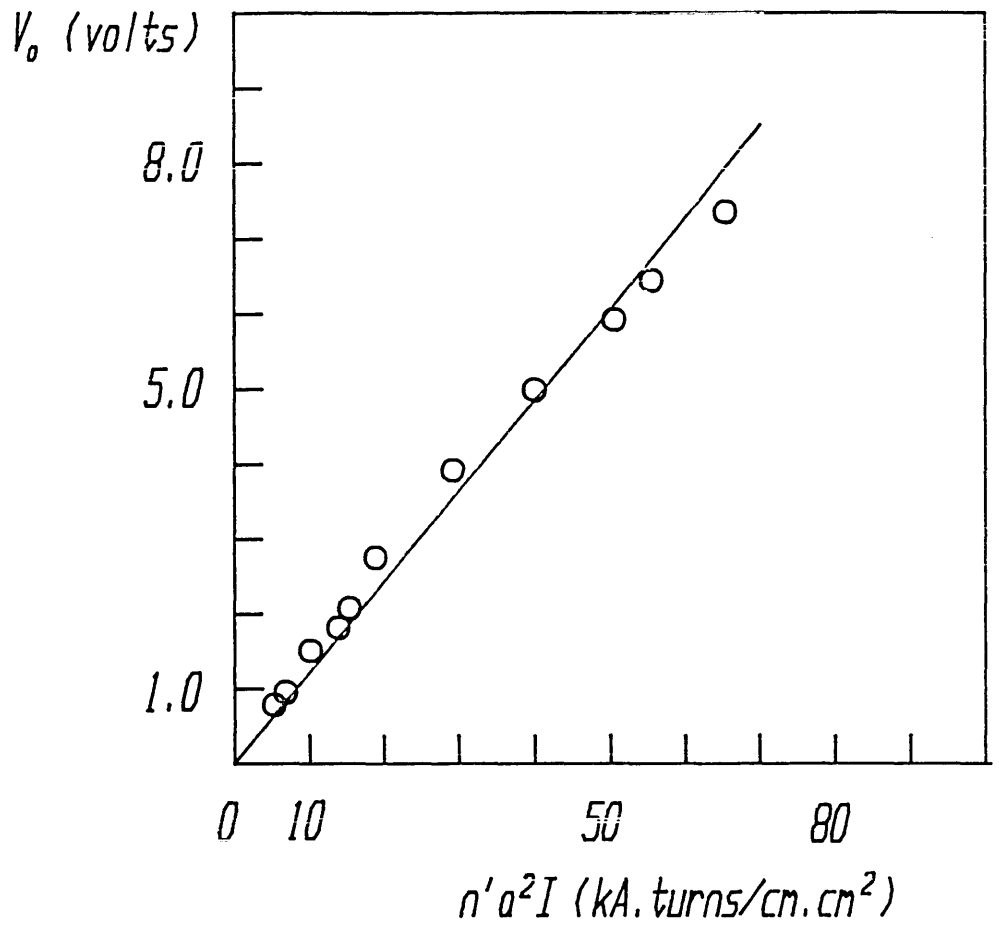


Figure 2.16: A plot of the integrated output of the B_z probe, V_o, against $n'a^2I$

If we assume that the shaped earth electrode diverts a certain amount of axial flux then the output from the probe is:

$$V = fM(dI/dt) \tag{17}$$

where f is the fraction of the axial flux that is intercepted by the probe.

This signal is then integrated using a passive integrator ($RC = 3.75$ μs). Hence the final output at the scope is:

$$V_O = 2.4fn'a^2I \qquad [\text{V, (cm, kA)}] \tag{18}$$

A plot of V_O against $n'a^2I$ should give a straight line with a slope $2.4f$. This plot is shown in figure 2.16. Applying a least-squares fit to the data gives a value for f of 5.1×10^{-2} ; so the shaped earth electrode diverts a lot of flux away from the probe. Knowing the pinch current and the pinch radius (from the streak phototgraphs), then the above graph could be used to deduce the wavelength of the instability.

The probe was calibrated as follows: a spring of known dimensions, number of turns and wound in a specific direction was placed between the electrodes inside the chamber. The chamber was filled with SF_6 gas to prevent breakdown between turns. Then the generator would be discharged into the spring and the output from the monitor measured. This was done for a number of springs of different diameter (the range of diameters was actually quite small – 3 to 6 mm); the number of turns was typically 4 and this could not really be varied since breakdown occurred between turns (even with the SF_6 gas for insulation).

The calibration was assumed to be valid for all springs; however it is not known how the electrode shape influences the amount of flux intercepted by the probe for very small diameter, very tightly wound solenoids (as might be the case for the helical pinch).

The main difference between loosely and tightly wound solenoids is that there is less flux leakage between the turns of the solenoid in the latter case – one might then expect the probe to intercept a larger amount of flux and thus the value of $n'a^2I$ corresponding to the probe output to be smaller than that predicted by the graph in figure 2.16. However, with the diameter of the pinch being an order of magnitude smaller than the springs used in the calibration the effect of the shaped earth electrode might be to divert even more flux than the graph would have one to suppose.

These points must be borne in mind when interpreting the actual values of

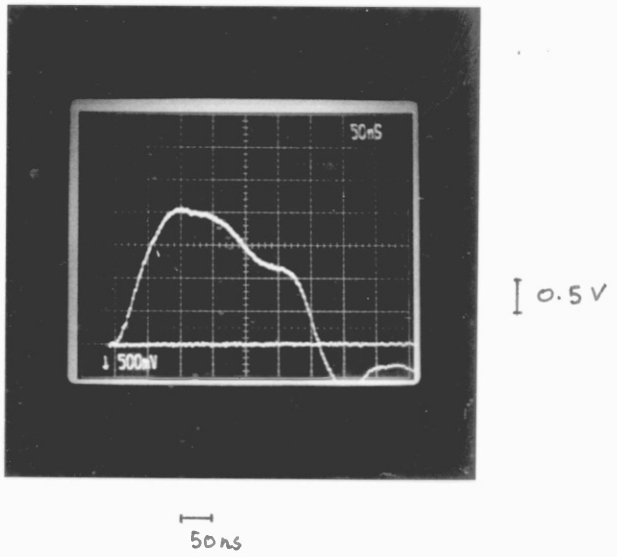


Figure 2.17.a: Output from the B_t probe on a short-circuit shot

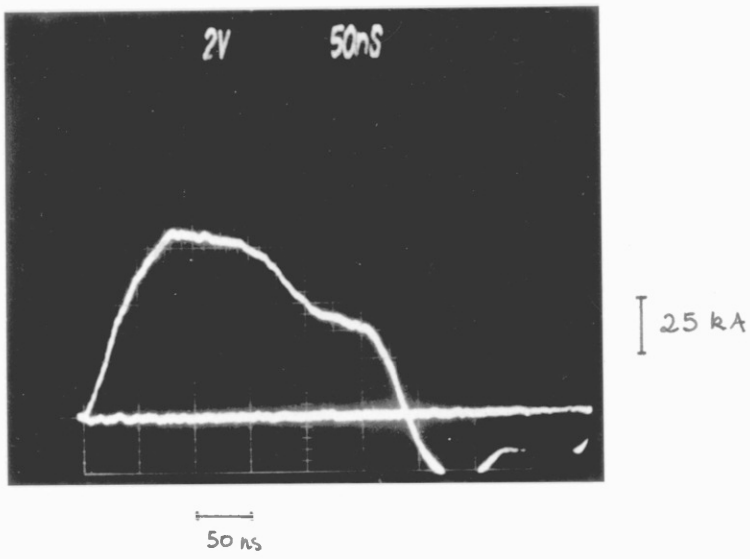


Figure 2.17.b: Corresponding current signal

the output of the probe. Figure 2.17 shows the output from the B_z monitor together with the current signal. As can be seen, both signals have the same profile (as is to be expected).

2.10. The Laser

A ruby laser (Quantel) was used for both initiating the gas−embedded pinch and for diagnostic purposes. Figure 2.18.a is a schematic of the arrangement. The laser consists of ruby oscillator and amplifier. It is Q−switched by means of a Pockel's cell placed between the rear mirror and the oscillator. A Brewster stack situated between the oscillator and the Pockel's cell defines the plane of polarisation of the laser light as being horizontal. Longitudinal modes are selected by a Fabry−Perot resonator placed between the oscillator and the telescope; this also defines the other end of the laser cavity. A *1* mm circular aperture between the quarter−wave plate and the oscillator picks out the transverse modes. The laser light is double−passed through the amplifier, there being a gain of ~ *5* on each pass. A Dove prism allows the beam to utilise different regions of the amplifying rod as it double−passes.

When the laser was operated at full power the output energy from the oscillator was ~ *35* mJ and the final energy after amplification ≃ *1* J. The laser shape was measured by a PIN diode and the result is shown in figure 2.18.b; it fits a Gaussian profile with the $FWHM = 7$ ns.

The system that triggered the laser had to be reliable and to operate with low temporal jitter (otherwise a lot of shots would be necessary to gather the appropriate data). Since the temporal jitter in the erection of the Marx was large, the laser triggering could not be synchronised with it. An electrical circuit had to be developed that would allow the laser to be triggered when voltage first appeared on the PFL. This circuit is shown in figure 2.19.a.

It is a double−differentiating circuit (i.e. the input to this circuit is differentiated twice; since the voltage on the PFL varies as $(1 - \cos\omega t)$ then the circuit will produce an output that varies as $(\cos\omega t)$ − thus intially the output is very fast) which produces a *12* V pulse with a risetime of *50* ns (figure 2.19.b.) as soon as voltage appears on the PFL. The output of this circuit then triggers a delay unit which in turn triggers the Pockel's cell at the appropriate time. The temporal jitter of this circuit is ≃ *10* ns; only the jitter in the gas switch determines the reliability with which the laser is triggered. This is of the order of *10 − 20* ns and so one might expect a total jitter of ≃ *30* ns in the timing of

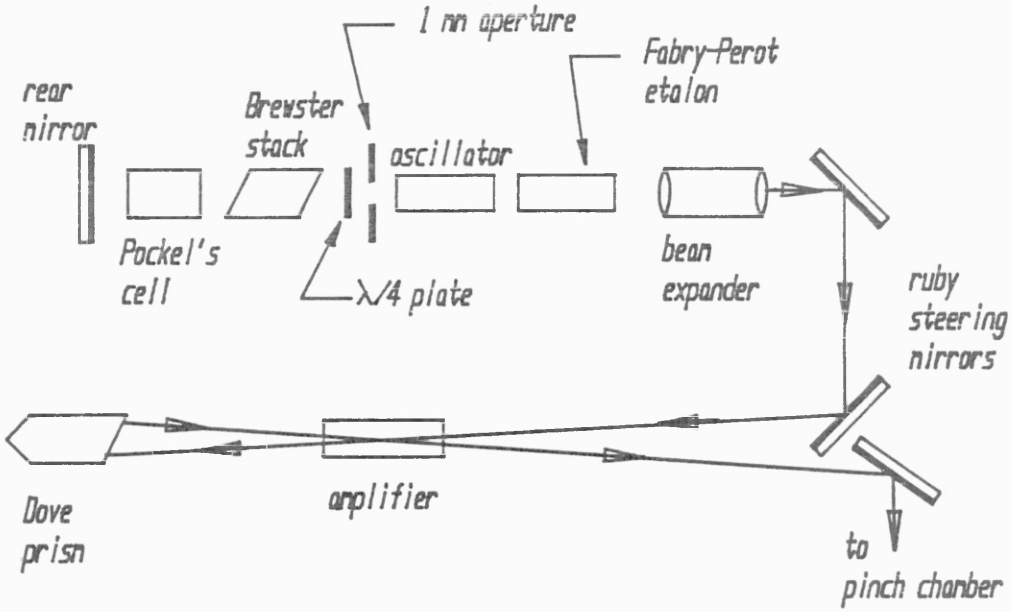


Figure 2.18.a: Schematic of the ruby laser

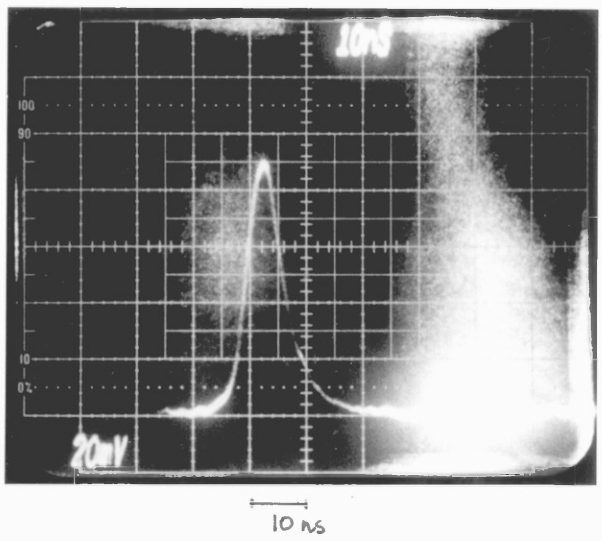


Figure 2.18.b: The laser pulse profile

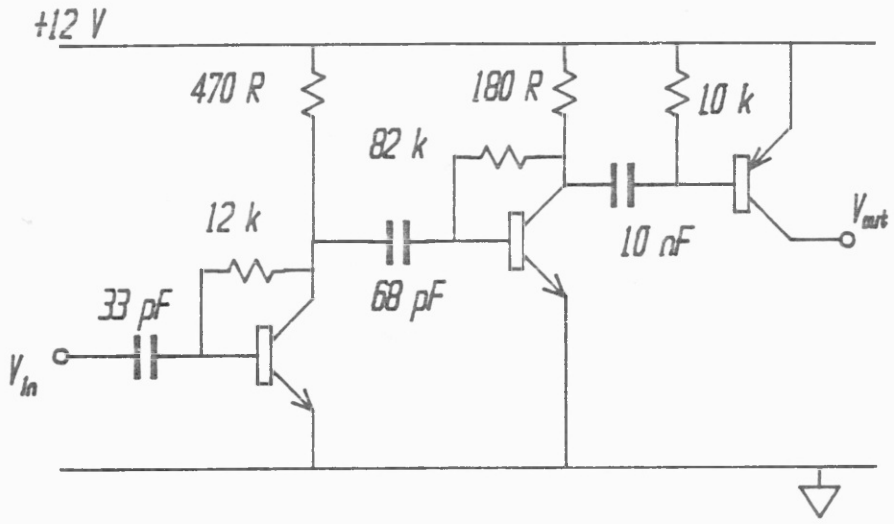


Figure 2.19.a: Circuit for triggering the laser

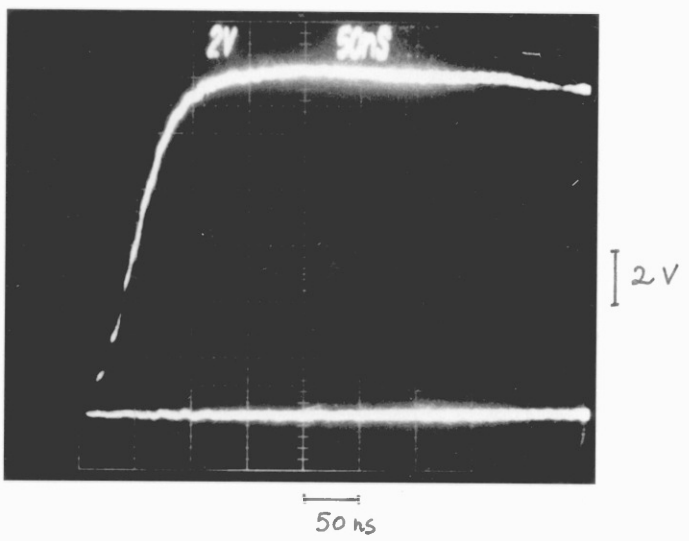


Figure 2.19.b: Output from the circuit

the laser with respect to the start of current flow in the pinch.

2.11. The Timing Sequence

The timing sequence for the experiment is shown in figure 2.20. Initially the laser is charged and fired. A trigger from the oscillator flashlamps then triggers the Marx via a delay unit. When voltage appears on the PFL then the double differentiating circuit Q−switches the laser (again via a delay unit). This same pulse is also used to trigger other diagnostic apparatus via appropriate delay units.

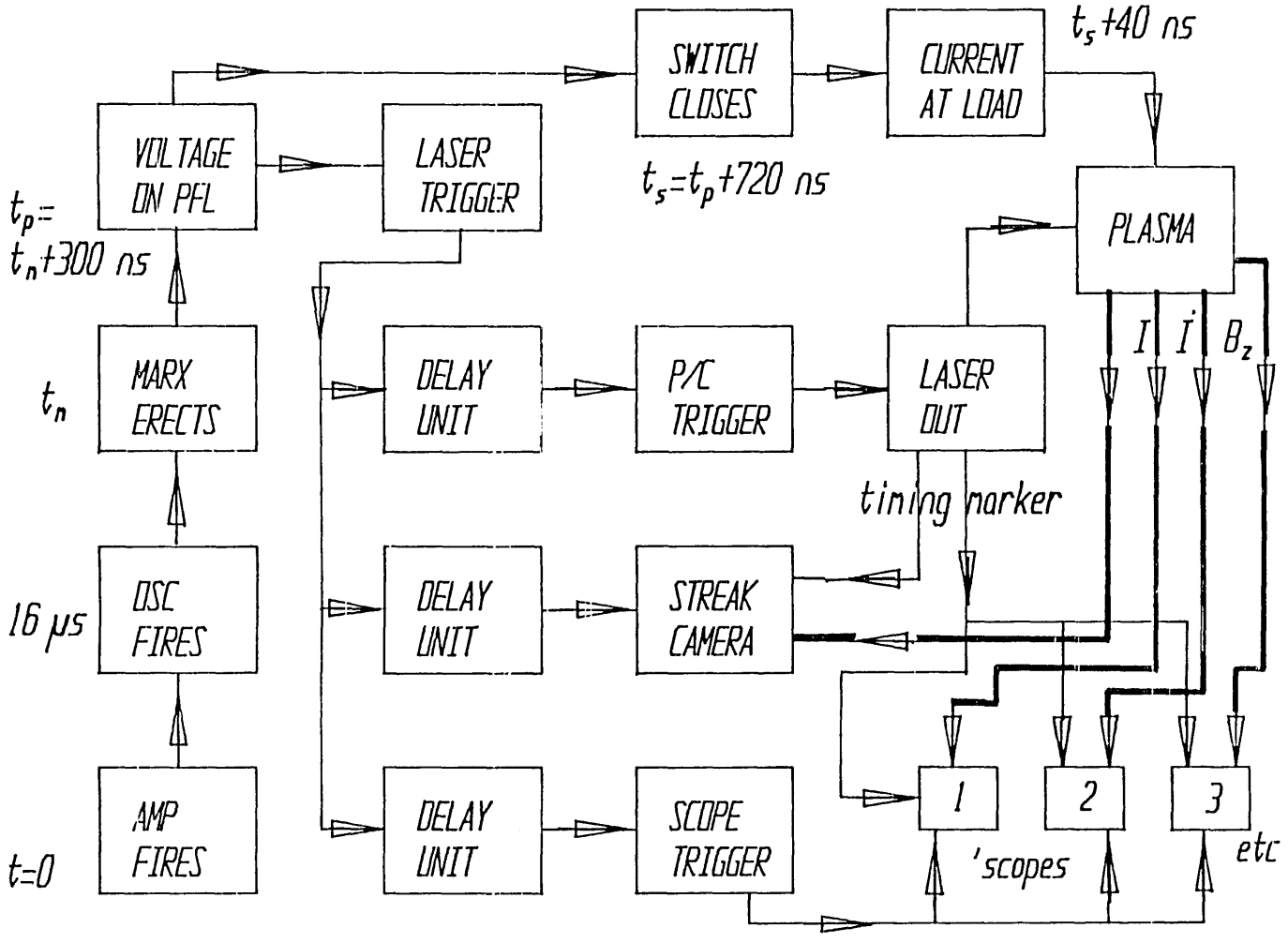


Figure 2.20: The timing sequence for the experiment

CHAPTER THREE

The Gas−Embedded z−pinch

3.1. Introduction

Early work on gas−embedded Z−pinches was performed with rates of rise of current of $\simeq 10^{12}$ As^{-1}. We have seen in Chapter 1 that this is insufficient to heat the pinch under pressure balance and consequently the plasma expands. This expansion leads to an accretion of particles from the surrounding neutral gas into the plasma and an increase in line density. Unless the current is tailored to overcome this then there will be a drop in temperature and it could also lead to MHD instability (since the ratio of ion Larmor radius to pinch radius decreases). So it would seem desirable to avoid this expansion.

The discharge channel is created by focussing a high power ruby laser between two electrodes into (typically) one atmosphere of hydrogen gas. However, in the initial stages of channel development the plasma is cold and there is difficulty in providing an adequate dI/dt to prevent expansion (Chapter 1). To overcome this the channel is heated by a small axial current (known as preheat) of $\simeq 7$ kA for $\simeq 50$ ns prior to the main current. This preheat then establishes the right conditions for the main current to heat the pinch under pressure balance.

There are three phases of the pinch evolution:

(i) preheat

(ii) equilibrium

(iii) instability.

Experiments were initially performed with a peak current of 50 kA (referred to as low current) and $dI/dt \simeq 1.4 \times 10^{12}$ As^{-1} (Favre−Dominguez, 1985). The results are summarised below.

(i) The Preheat Phase

During preheat, the discharge column expands with a velocity

$$v_{exp} \simeq 1.7 \times 10^{6} \quad [\text{cm s}^{-1}]$$

This velocity is greater than the sound speed in the background neutral gas;

thus the expanding column drives a shock into the gas forming a high density neutral layer at the pinch boundary. The density jump is of the order *4* across a thickness of $\approx$ *50* μm. Holographic interferometry measurements show an initially hollow electron density profile which becomes peaked on axis during the equilibrium phase. The preheat is important since in its absence no equilibrium phase is observed (in common with the early gas–embedded experiments outlined in Chapter 1).

(ii) The Equilibrium Phase

When the main current is applied to the expanding channel a pinch in radial equilibrium is established. The radius of the equilibrium pinch is $\approx$ *700* μm. For an initial filling pressure of *0.3* bar the equilibrium lasts for *40* ns whilst at *1* bar the duration of the equilibrium is only *15* ns. The high density neutral layer has slowed down and is expanding with a velocity, $v_{exp} \simeq 5 \times 10^5$ cm s^{-1}. The pinch line density increases by a factor of two – this is explained by accretion due to a flow of neutral particles into the pinch. Time–integrated X–ray pinhole measurements give a temperature of $\simeq$ *60* eV. This is about twice the estimated Bennett temperature and, together with the way the instability develops, would seem to indicate a current profile that is peaked on axis.

(iii) The Unstable Phase

The equilibrium is destroyed by an $m=1$ MHD instability which grows from the axis and transforms the pinch into an expanding helix. The initial expansion of the helix is consistent with the calculated growth time of the MHD $m=1$ instability. However, the scaling of the growth time with initial filling pressure is not consistent with MHD theory. Although the ratio of ion Larmor radius to pinch radius is of the order of *1* the ions are not magnetised ($\Omega_i \tau_{ii} \simeq 0.05 - 0.25$ for a temperature $\simeq 20 - 40$ eV) and so finite ion Larmor radius (FILR) effects are not to be expected.

3.1.1. Stability and Finite Ion Larmor Radius Effects

The characteristic growth time for an $m=1$ MHD instability is the radial Alfven transit time (Tayler, 1957):

$$\tau_{m=1} = \tau_a = r/v_a \qquad (1)$$

where $v_a = 2.18 \times 10^{16} \mu^{-\frac{1}{2}} n_i^{-\frac{1}{2}} B$ [m s^{-1}, (m^{-3}, Tesla)]

μ is the ratio of ion to proton mass.

So the growth time depends on the filling pressure (through n_i); however, the scaling of the growth time with pressure that Favre–Dominguez observed was contrary to that predicted by MHD theory.

One possible regime where MHD modes may be stable occurs when the ion Larmor radius is comparable to the pinch radius and when the ions are magnetised i.e. the conditions for ideal MHD to be valid (section *1.4*, Chapter 1) are not satisfied. In this limit the conventional MHD equations are no longer applicable and more complete theoretical treatments suggest improved stability (Bowers and Haines, 1971; Coppins, 1984; Rosenbluth, Krall and Rostoker, 1962).

The essence of finite ion Larmor radius stability is as follows:

In a perturbed electric field, the ions experience a slightly different mean electric field than the electrons (because their Larmor radii are larger than those of the electrons and also comparable to the pinch radius). Hence their drift velocity across the field is different. This leads to a charge separation in opposite phase to that which is driving the instability. If the former is greater than the latter then a stable oscillation is the result.

The ratio of the ion Larmor radius to the pinch radius is given by:

$$\frac{a}{a}i = \frac{m_i v_i^{\perp}}{eBa} \qquad (2)$$

where $v_i^{\perp}$ is the component of the ion velocity perpendicular to B.

If the ions only possess thermal energy then we get (using the Bennett equation):

$$a_i/a = 2.01 \times 10^{8} N^{-\frac{1}{2}} \qquad (3)$$

for a hydrogen plasma.

Thus, for a Z–pinch in radial equilibrium a_i/a depends only on the line density. In the experiment, typically

$$N = 2.0 \times 10^{18} \qquad [m^{-1}]$$

$$\therefore \quad a_i/a = 0.14$$

So the first condition for FILR effects can be satisfied. But the ions also have to be magnetised. This requires

$$\Omega_i \tau_{ii} \gg 1 \tag{4}$$

where Ω_i is the ion cyclotron frequency and τ_{ii} is the ion collision time.

For hydrogen ($Z = 1$, $m_i = m_p$ = proton mass) we have

$$\Omega_i = eB/m_p \tag{5}$$

$$\tau_{ii} = \frac{3^{\frac{1}{2}}(6\pi\epsilon_0^2)m_p^{\frac{1}{2}}T^{3/2}}{n_i e^4 \ln\Lambda} \qquad [S.I.] \tag{6}$$

where $\ln\Lambda$ is the Coulomb logarithm ($\simeq 7 - 8$). We therefore find:

$$\Omega_i \tau_{ii} = 3.9 \times 10^{31} \frac{aI^4}{N^{5/2}\ln\Lambda} \tag{7}$$

where the Bennett equation has been used to relate T to I for a pinch in radial equilibrium.

To achieve $\Omega_i \tau_{ii} \gg 1$ for $N = 2.0 \times 10^{18}$ m^{-1} and $a = 0.7$ mm we require:

$$I \gg 35 \text{ kA}$$

In the low current experiment, $I_{peak} = 50$ kA and so this condition was not fulfilled (especially since the measured temperature was $\simeq 2.5$ times higher than the Bennett temperature). With the new generator a peak current of 150 kA could be achieved and so this second condition for FILR effects ought to have been satisfied. The aim of the experiment was to investigate the stability of a gas-embedded Z-pinch under conditions for which FILR effects are expected to enhance the stability of the pinch.

3.2. The Experimental Arrangement

Figure 3.1 shows the experimental set-up. The ruby laser was focussed onto the live electrode through a 2.5 mm diameter hole in the ground electrode. Four $CuSO_4$ resistors placed across the gas switch allowed the transfer section to be

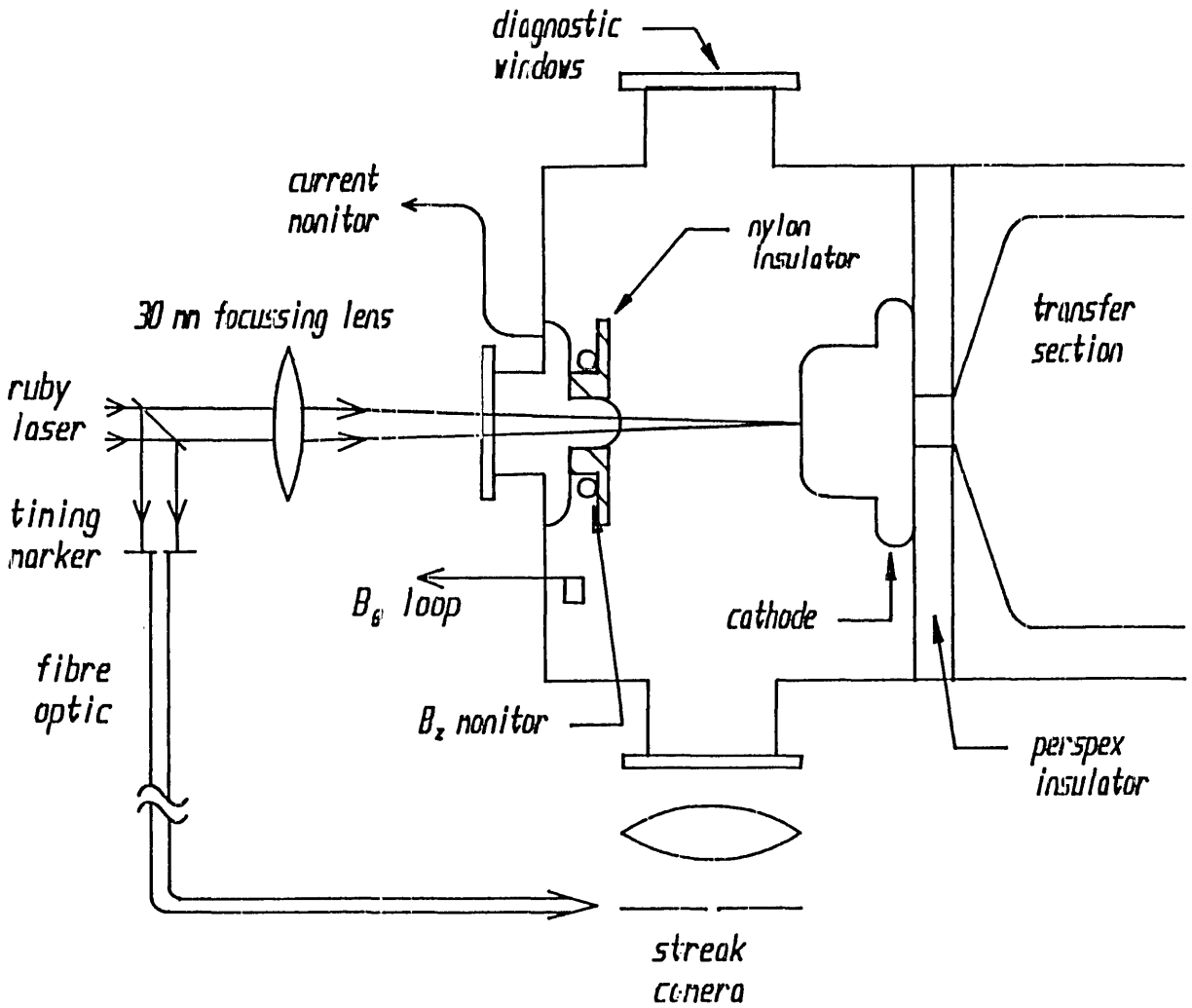


Figure 3.1: The experimental set-up

charged to (typically) *5%* of the main charging voltage. When the laser initiated the discharge, the transfer section discharged into the channel thus providing a preheat current of $\simeq$ *7* kA. Approximately *50* ns after the start of preheat the main current was applied to the discharge, at the peak of the prepulse current.

Optical streak photography was used to study the dynamics of the Z−pinch plasma. The plasma was imaged onto the slit of a Hadland Imacon *675* camera; a sweep speed of *5* ns/mm was used and the magnification was *2.0*. The B_Z monitor was used to detect the appearance of an axial magnetic field which would be associated with helical current flow due to the $m=1$ instability; hence, this provided a measurement of when the instability occurred with respect to the current. A nylon insulating disc shielded the B_Z probe from any X−rays and electrons that might come from the pinch or electrodes and which would create a spurious signal. The main pinch current was measured with a B_θ coil whilst the internal Rogowski groove was used for measuring dI/dt.

A timing marker for all the electrical signals was provided by monitoring a reflection off one of the steering mirrors in the laser housing. This was fed into a PIN diode (via a fibre−optic) and then into the oscilloscopes. In this way the appearance of an axial magnetic field could be accurately timed with respect to the start of the main current and dI/dt. A reflection off a second steering mirror was taken directly into the streak camera slit (again using a fibre−optic) to provide a timing mark for the streak photographs. The relative timing between all the markers was then measured by firing the machine and laser into a short circuit.

3.3. The Observations

As in the low current experiment, there are three phases of the pinch evolution:

(i) preheat

(ii) equilibrium

(iii) instability.

Figure 3.2.a is a typical streak photograph showing all three phases. The initial expansion is the preheat phase (dI/dt is not matched to that needed for heating under pressure balance). The discharge channel expands with a velocity

$$v_{exp} = 1.1 \times 10^6 \qquad [\text{cm s}^{-1}]$$

with the preheat current (in this particular shot) being *2.7* kA.



mag^n = 0.8

23 ns

(a)



mag^n = 0.25

23 ns

(b)

Figure 3.2: Streak photographs:
(a) with preheat
(b) without preheat

Without a preheat current one only observes a continuous expansion – i.e. there is no equilibrium phase (figure 3.2.b).

The equilibrium phase starts as soon as the main current is applied to the pinch. Unfortunately, most of the data was taken using a streak camera without an intensifier and the preheat phase (plus some of the equilibrium phase) was not visible. The duration of the equilibrium was measured by taking the difference between the appearance of the B_z signal and the start of current. The assumption here was that the onset of the instability was accompanied by an axial magnetic field generated by a helical current flow; Table 3.1 shows the timing of B_z with respect to the onset of the instability (as measured from the streak photographs) for different pressures. From the table, one sees that the start of B_z is concurrent with the onset of the instability (within the experimental error) and so the above assumption is valid (a + sign means that the B_z signal occurred *after* the observed start of the instability).

Table 3.1: *The timing of B_z wrt the onset of the instability*

p (atm)	*shot #*	*start of B_z wrt instability (ns)*
0.33	6.070	−1
0.33	7.071	+2
0.33	8.072	−1
0.67	2.122	−3
0.67	2.146	−1
0.67	3.147	+1
1.00	3.132	0
1.00	1.150	+2
1.00	2.152	−1

Figure 3.3 shows a typical data shot with the streak photograph being accompanied by oscilloscope traces of I, dI/dt and B_z. The variation of the duration of the equilibrium with initial filling pressure is shown in figure 3.4. For comparison, t_{eq} for the low current experiment is also shown. As can be seen, the equilibrium times scale in opposite directions for the different experiments. In figure 3.5 the current at the time of the onset of the instability (i.e. at the end of the equilibrium phase) is also plotted against filling pressure. The diameter of the equilibrium column is *0.30* mm compared to the value of *0.7* mm in the low current experiment.

The equilibrium column is finally disrupted by an $m=1$ MHD instability and is transformed into an expanding helix. In the low current experiment the helical instability was observed from holographic interferometry measurements; in the present experiment the observation of an axial magnetic field indicates that there is helical current flow in the pinch when the instability sets in. The onset of this instability appears to be very sudden. If we define a 'growth rate' for the plasma expansion as being

$$\gamma_g \equiv (d\xi_r/dt)/\xi_r \qquad (8)$$

where ξ_r is the radial displacement of the plasma, then from the streak photographs we measure a value of

$$\gamma_g \simeq 1.8 \times 10^8 \quad [s^{-1}]$$

This 'growth rate' is not to be confused with the ideal MHD growth rate although it is a measure of how quickly the instability expands. This rapid expansion is not axisymmetric and though the plasma column is transformed into a helix it is well defined. The typical expansion velocity is

$$v_{exp} \simeq 6.7 \times 10^6 \quad [cm\ s^{-1}]$$

From the B_z measurements one can determine what the value of ka is (k is the wave number $= 2\pi/\lambda$, λ is the wavelength of the instability and a is the equilibrium radius of the pinch) – the quantity ka characterises instabilities in MHD stability theory. In the experiment, one finds that (for the initial pressures, *0.3 – 1* bar)

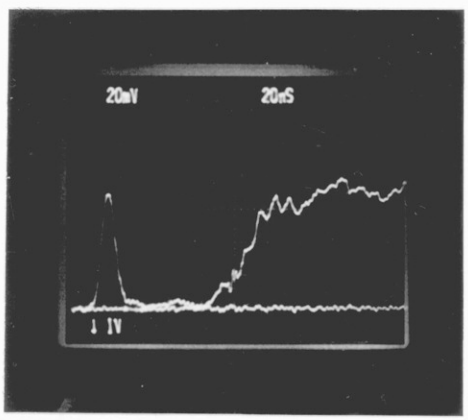
$$ka \simeq 4.2$$



mag^n = 0.8

23 ns

(a)



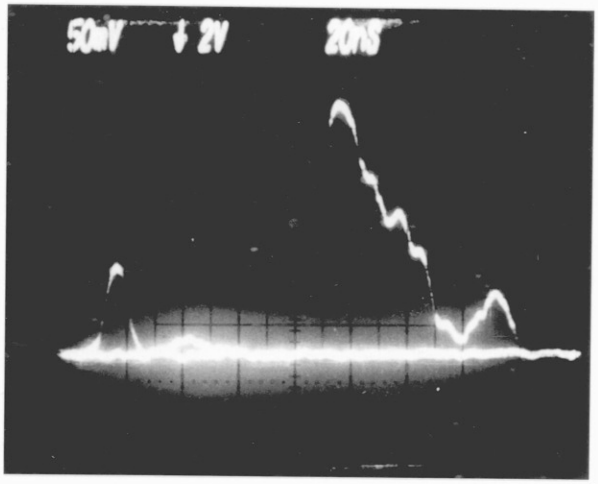
30 kA

TIMING MARK

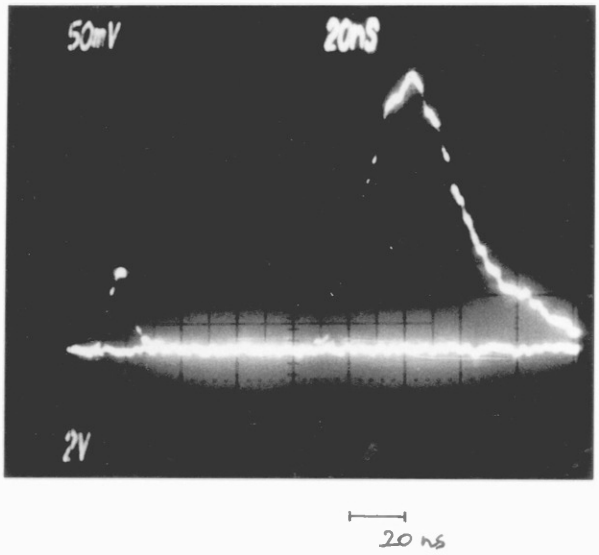
20 ns

(b)

Figure 3.3: Typical data shot
(a) streak photograph
(b) current



(c)



(d)

Figure 3.3 (cont.): (c) dI/dt
(d) B_z

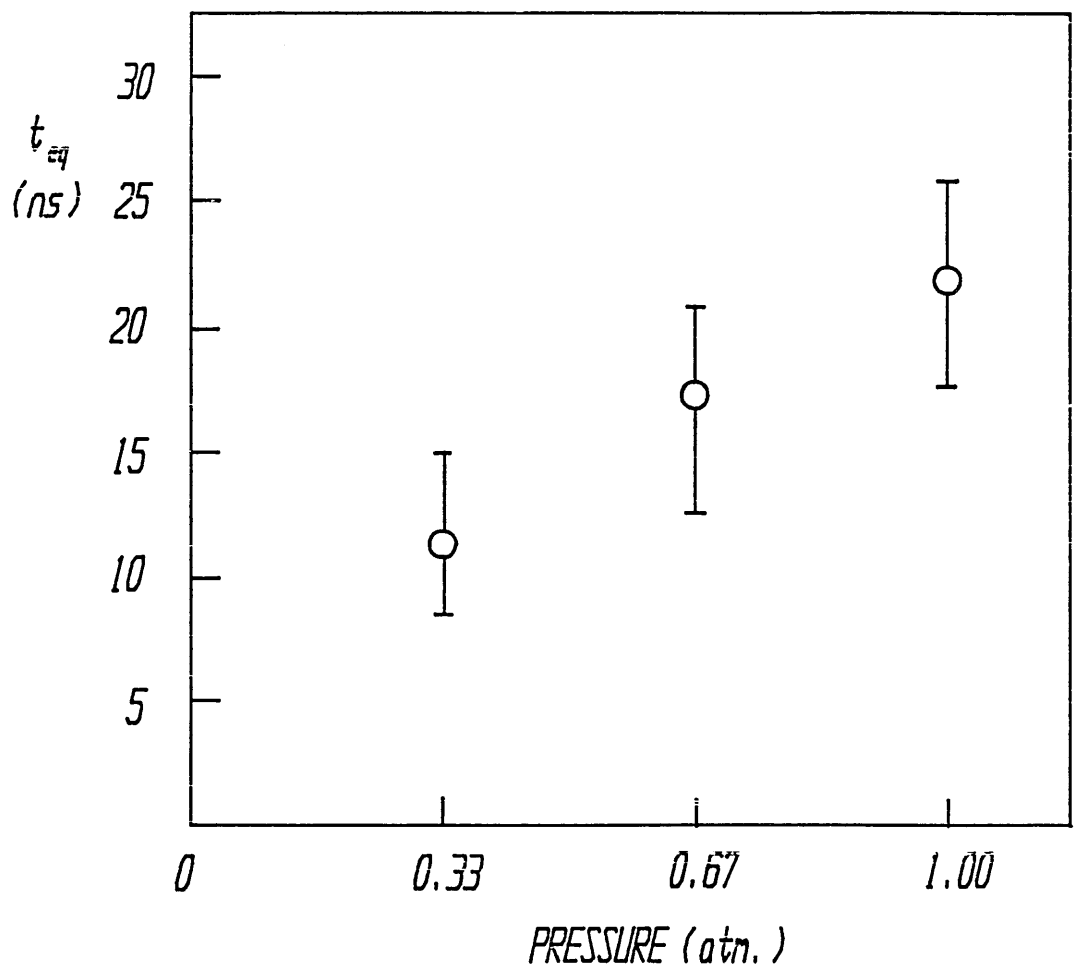


Figure 3.4: Duration of equilibrium as a function of initial filling pressure

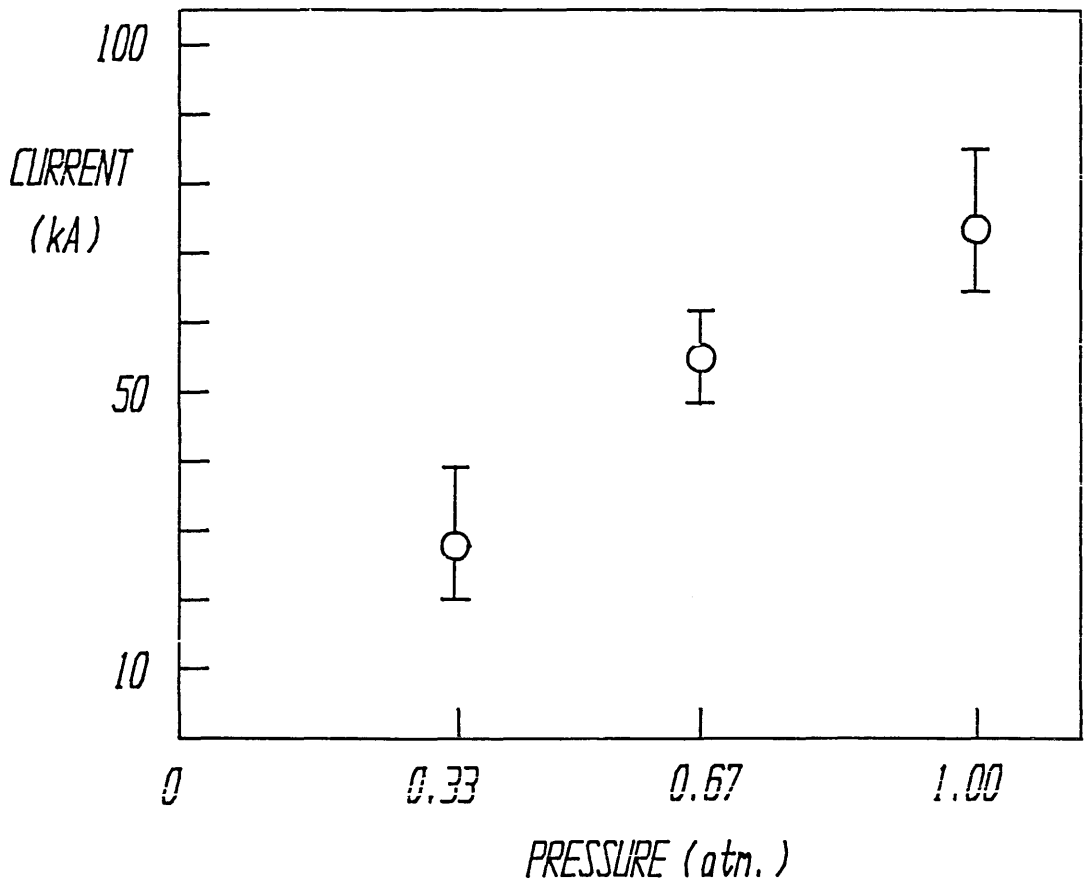


Figure 3.5: Current at onset of m=1 instability versus initial filling pressure

This is good agreement with the value from the low current experiment where $ka = 4.0$.

There are some interesting points to note from the measurements of B_z and dI/dt. The time taken for the peak of dI/dt to be reached in the plasma shots is less than that for a short-circuit current (see Table 3.2). The onset of B_z with respect to peak dI/dt is also shown in the table.

Table 3.2: *Difference in dI/dt between plasma and short-circuit shots*

p (atm)	*10% → peak dI/dt time for plasma shots (ns)*	*10% → peak dI/dt time for s/c shots (ns)*	*onset of B_z wrt peak dI/dt (ns)*
0.33	11.7 ± 1.1		−3.3 ± 1.9
0.67	12.3 ± 2.5	15.8 ± 0.4	−5.2 ± 5.0
1.00	13.2 ± 3.7		−3.0 ± 3.0

In all cases the B_z signal occurs before peak dI/dt is reached. The figures in Table 3.2 suggest that the onset of the instability causes a drop in dI/dt. This ought to be mirrored in the current traces. Indeed, upon the appearance of B_z there appears to be a sudden and quick change in the current waveform and this would suggest a sudden increase in inductance of the pinch.

In every single data shot it was found from the polarity of the B_z measurements that the helical current flow was always left-handed. For all these shots the generator operated in the negative polarity mode. Unfortunately, at the time it was not possible to operate the generator in a positive polarity mode and so investigate whether the current flow would now be right-handed.

In the plasma shots the B_z signals do not mimic the current traces (in contrast to the short-circuit spring shots). It appears that after a certain time the B_z signal is shorted out – this could be due to either the current starting to flow axially again (the helical turns shorting themselves) or the B_z probe shorting itself to earth. All the calibration shots for the probe were made with typical currents of $\simeq 70$ kA and pinch voltages $\simeq 200$ kV such that the typical output of the probe

was $\simeq$ 7 V – no shorting of the probe occurred in these shots. This would seem to preclude the latter as the explanation for the decay of the B_z signal.

3.4. Discussion

3.4.1. The Preheat Phase

In his thesis, Favre–Dominguez discusses the characteristics and dynamics of the preheat phase. From his observations the preheat is characterised by three things:

(i) the electron density remains nearly constant;

(ii) the column expands with a velocity higher than the sound speed in the background gas;

(iii) a high density neutral layer builds up at the edge of the discharge channel.

The picture he proposes for the development of the channel is as follows:

The laser initiates a narrow discharge channel with a high degree of ionisation. Joule heating by the small preheat current is not balanced by a corresponding increase in magnetic pressure and the channel expands. This expansion is faster than the local sound speed and a shock is produced in the surrounding gas. A high density neutral layer is formed; the shock heats the neutral particles and dissociation takes place.

In the present experiment the preheat phase was only observed by optical streak photography. An expansion of the channel similar to that in the low current experiment was observed. Also, no axial magnetic field was detected during this phase. The preheat current in both experiments was the same and so it would seem that the channel develops in the same manner, as discussed above, for both experiments (this is to be expected since there is no difference in how the pinch is initiated or preheated).

3.4.2. The Equilibrium Phase

When the main current is applied to the pinch an equilibrium phase is observed. The radius of the equilibrium pinch is $\simeq$ *0.15* mm – this is about one half of the radius observed in the low current experiment. The difference between the low and high current cases at this stage of the experiment is that dI/dt is a factor of *2 – 3* greater in the latter case. Thus there might be greater pinching

of the discharge channel before pressure balance is established. This can be seen from the equation relating dI/dt to the equilibrium channel radius, temperature and line density (equation (16), Chapter 1):

$$dI/dt \propto \sqrt{N}/(a^2T)$$

Thus, for constant N and T, the ratio of the equilibrium radius in the high current to low current experiments is

$$a^h/a^\ell \simeq 1/\sqrt{3} \simeq 0.6$$

Thus the smaller radius observed in the present experiment is consistent with the higher dI/dt provided by the new generator.

Table 3.3 shows the values of the equilibrium time together with the calculated radial Alfven transit time. For comparison the values for the low current case are also tabulated.

Table 3.3: *Equilibrium times for different filling pressures*

	p (atm)	τ_{ob} (ns)	τ_a (ns)	τ_{ob}/τ_a
low current:	0.33	40	7.5	$\simeq 5$
	1.00	15	9.0	$\simeq 2$
high current	0.33	12	7.2	$\simeq 2$
	0.67	19	5.4	$\simeq 3.5$
	1.00	23	5.7	$\simeq 4$

It has been shown that the first condition for FILR stabilisation can just be satisfied (equation (3)). However, the ions also have to be magnetised. We have from equation (7) and with $ln\Lambda = 7$:

$$\Omega_i \tau_{ii} = 5.6 \times 10^{30} a I^4 N^{-5/2} \gg 1 \qquad (9)$$

For the equilibrium pinch one can express the current in terms of the temperature. One thus finds that:

$$T \gg (I/a)^{2/5} \times 19.6 \qquad \text{[eV, (kA, mm)]} \qquad (10)$$

And from Bennett, the line density to achieve this temperature condition is:

$$N \ll 1.80 \times 10^{17} I^2/T \qquad [\text{m}^{-1}, (\text{kA, eV})] \qquad (11)$$

Equations (10) and (11) have to be satisfied in order for the second condition for FILR stabilisation to be valid. One can take the current and the radius at the end of the equilibrium phase and calculate the minimum and maximum limits on the temperature and line density needed to satisfy $\Omega_i \tau_{ii} \gg 1$. This is shown in Table 3.4.

Table 3.4: *Temperature and line density needed to satisfy* $\Omega_i \tau_{ii} \gg 1$

p	*equilibrium radius*	*current at end of equilibrium*	T^*	N^*
(atm)	*(mm)*	*(kA)*	*(eV)*	(m^{-1})
0.33	0.15	25	152	7.3×10^{17}
0.67	0.15	56	210	2.3×10^{18}
1.00	0.15	71	231	3.5×10^{18}

So to satisfy $\Omega_i \tau_{ii} \gg 1$, we need $T \gg T^*$ (and since the pinch is in equilibrium, to achieve this temperature $N \ll N^*$).

For $p = 0.33$ atm, $r = 0.15$ mm the line density is

$$N_e = 5.63 \times 10^{17} \qquad [\text{m}^{-1}]$$

From equation (3), $a_i / a = 0.38$ and so the first condition for FILR stabilisation is satisfied.

The corresponding Bennett temperature is

$$T = 174 \quad [\text{eV}]$$

at the end of the equilibrium phase (assuming a line density equal to the initial filling density); this marginally fulfils the condition given by equation (10) for $p = 0.33$ atm.

Coppins (1988) calculates the value of Freidberg's dimensionless parameters, x and y, for both the low and the high current gas–embedded pinches. He finds that in the high current case, ideal MHD is valid only at $p = 0.67$ and 1.00 atm. So the conditions in the pinch at $p = 0.33$ atm. can fulfil the requirements for FILR stabilisation.

However, the pinch at this filling pressure is observed to be stable only for about two MHD growth times i.e. it is not anomalously stable. Coppins (1988) has suggested that the stability is a feature of exponential growth; in a situation where the growth rate is increasing with time, the onset of the instability will appear sudden and delayed as is observed experimentally. So it appears that enhanced stability is not observed in the pinch at $p = 0.33$ atm.

There are two reasons why FILR stabilisation might not observed. Firstly, if the electric field is uniform then the drift velocity across the field for both electrons and ions will be the same. So there will be no charge separation and hence no stabilisation. Secondly, the conditions for stabilisation might not be fulfilled! This could happen if the ions are collisional although the Freidberg parameter, x, indicates that this is not the case. However if there is significant accretion then the line density could well increase by a factor of ~ 3 (as in the low current case). In this case the Bennett temperature will decrease down to ~ 60 eV meaning that the ions *will* be collisional and FILR is not applicable.

Although the electron number density or temperature have not been measured it is likely that, as in the low current case, there is accretion of particles into the pinch and hence a corresponding drop in temperature. Thus the second condition for FILR stabilisation is not fulfilled and enhanced stability is not observed.

3.4.3. The Unstable Phase

The equilibrium pinch is disrupted by an $m=1$ MHD instability. The onset of the disruption is accompanied by the appearance of an axial magnetic field, B_z, which thus indicates that there is helical current flow when the MHD instability disrupts the plasma. This instability is characterised by the product $ka = 4.2$ with the typical wavelength being $\simeq 0.2$ mm.

A general feature of ideal MHD linear instabilities is that the maximum growth rate occurs in the limit of zero wavelength ($ka \rightarrow \infty$). Such instabilities are not observed experimentally. For small, finite wavelength instabilities a non-linear study would be required. Coppins (private communication - 1986, 1987) has studied the stability of a gas-embedded Z-pinch using a "shooting code" and assuming that the fastest growing instability is characterised by $ka = 4.0$. In his paper, Coppins (1987) considers the low current gas-embedded pinch; it is suggested that the equilibrium current is centre peaked since the $m=0$ instability is absent and the $m=1$ instability is peaked on axis. Such a current profile is Kadomtsev stable to $m=0$ but unstable to $m=1$ modes. A centre peaked current would also explain the discrepancy between the measured and the Bennett temperature. It is also suggested that a centre peaked temperature profile could arise from a cooling of the outer region of the plasma through accretion or thermal conduction to the surrounding neutrals.

The value of $ka \simeq 4.2$ was deduced from the strength of the B_z signals. This assumed that the helical pinch could be imagined as an ideal spring with the all the current flowing through its turns. The 'number of turns' of such a 'plasma spring' at the start of the instability is ~ 22 (in a length of 13 mm). If one assumes that the axial field produced is similar to that of a long solenoid then:

$$B_z = \mu_0 n' I \qquad [\mathrm{T}] \tag{12}$$

where n' is the number of turns per unit length.

Putting in typical values for $n' = (22 \text{ turns})/(13 \text{ mm})$ and $I = 25$ kA we get:

$$B_z \simeq 53 \qquad [\mathrm{T}]$$

This is comparable to the azimuthal field during the equilibrium phase:

$$B_\theta \simeq 33 \qquad [\mathrm{T}]$$

Measurements of the delay between the occurence of the B_z signal with respect to the dI/dt signal (Table 3.2) suggest that the onset of the instability causes a drop in dI/dt. One also notices that in the current traces, at the time of the appearance of the B_z signal there is a sharp decrease in the current before it starts rising again. This indicates that there is an increase in the pinch inductance. It is possible to calculate the change in the plasma inductance as a result of its transformation into such a 'plasma spring'.

We shall assume that, in the process of the pinch being transformed into a helix, magnetic flux is conserved. This will be true if the 'growth rate' of the expansion, γ_g, is larger than the current growth rate, γ_i, which is defined as:

$$\gamma_i \equiv (dI/dt)/I \tag{13}$$

For $dI/dt \simeq 3$ kA/ns and $I \simeq 25$ kA we find

$$\gamma_i \simeq 1.2 \times 10^8 \quad [s^{-1}]$$

Meanwhile, from section 3.3, the expansion 'growth rate' is

$$\gamma_g \simeq 1.8 \times 10^8 \quad [s^{-1}]$$

and we assume that magnetic flux is conserved during the onset of the instability.

Then the inductance of the helical pinch is:

$$L' = L_0(I_0/I') \tag{14}$$

where $L' = L_h + L_e$ is the sum of the helical pinch and electrode inductances

$L_0 = L_p + L_e$ is the inductance of the equilibrium pinch plus the electrodes

I_0, I' are the currents before and after the onset of the instability.

The inductance of the equilibrium pinch is given by

$$L_p = 2\ell ln(b/a_i) \qquad [nH,(cm)] \tag{15}$$

where ℓ is the pinch length $= 1.3$ cm

b is the chamber wall radius $= 178$ mm

a_i is the equilibrium pinch radius $= 0.15$ mm.

We thus get:

$$L_p = 18.4 \quad \text{[nH]}$$

whilst the measured electrode inductance is *50* nH.

$$\therefore \quad L_0 = 68.4 \quad \text{[nH]}$$

From the current trace we measure the current ratio as:

$$I_0 / I' = 0.6$$

$$\therefore \quad L_h = 66 \quad \text{[nH]}$$

The inductance of a helical spring is given Grover (1949):

$$L_s = 4\pi^2 a^2 b n'^2 K \quad \text{[nH,(cm)]} \tag{16}$$

where a is the radius of the spring = *0.06* cm (measured)

b is the lenght of the spring = *1.3* cm

n' is the number of turns/cm = *22/1.3*

K is a factor taking into account the ends of the spring ($\simeq$ *1*).

We thus find that

$$L_s = 55 \quad \text{[nH]}$$

This is within *20%* of the measured value. However, there are large errors involved: L_s is proportional to n'^2 and n' is proportional to I^2. Thus a *5%* error in I will give a *20%* error in L_s. There is also a *10%* error in the measurement of L_h (through I_0 / I'); we conclude that the agreement between L_s and L_h is good. Thus the increase in the pinch inductance is consistent with it being transformed into a helix as deduced from the B_z probe.

It was also found that the current flow is always left−handed (when the generator provides 'negative' current). This cannot be due to an asymmetric current flow prior to the instability since the pinch geometry is radially symmetric. No satisfactory explanation exists for this phenomenon.

3.5. Conclusions

As in previous low current experiments, three phases (preheat, equilibrium and instability) of the pinch evolution have been observed in this high current experiment. An expanding discharge is created in the preheat and this is observed to be identical in the two experiments. When the main current is applied to the expanding channel a pinch in radial equilibrium is established. The duration of this equilibrium is measured to be consistent with that predicted by MHD theory, in contrast to the low current experiment.

Measurements with an axial magnetic field probe show that the equilibrium is destroyed by an $m=1$ MHD instability which transforms the pinch into an expanding helix. The consequent increase in inductance is reflected in a momentary decrease in current at the time of the transition. This is consistent with the magnetic flux being conserved during the transition.

The current flow during the unstable phase was found to be always left−handed (when the generator provides 'negative' current). The pinch geometry is radially symmetric and one would not expect an asymmetric current flow which might account for this behaviour. No satisfactory explanation exists for this phenomenon.

It has been shown that the conditions under which one might expect to observe enhanced stability due to finite ion Larmor radius effects are marginally fulfilled only at a pressure of *0.33* atm. The observed growth time of the instability in this case is less than twice the ideal MHD time i.e. stability is not 'enhanced'. To achieve conditions where FILR effects would produce enhanced stability it is necessary to heat the pinch to high temperatures and this is limited by accretion of neutral particles into the plasma column (which leads to a reduction of temperature).

THE FIBRE Z-PINCH

CHAPTER FOUR

Optical Diagnostics

4.1. Introduction

In trying to achieve a high density, high temperature plasma conventional Z−pinches such as the gas−embedded pinch have suffered from the problems of accretion of neutral particles into the plasma column, leading to a loss of temperature and from MHD instabilities which disrupt the pinch early in the current flow. With a solid fibre (surrounded by a vacuum) there is no problem with accretion and the density is determined by the fibre mass which can be easily controlled. In a recent experiment reported by Sethian *et al.* (1987), a deuterium fibre Z−pinch plasma was observed to expand and remain stable up to current maximum, corresponding to about *40* MHD growth times. Because of this and also because the deuterium fibre is initially non−conducting, one needs to study and understand the plasma formation, dynamics and stability in an insulating fibre. In our experiment, a Z−pinch plasma was produced by ionisation of an optical quartz fibre.

Observation of the optical emission from a plasma enables one to say something about the state of the plasma and its dynamics. High speed optical streak and framing photography was performed to observe the optical emission from the plasma formed from the optical quartz fibre. The use of the optical fibre also allowed the plasma formation to be investigated by monitoring the light generated *internally* within the fibre. A discussion of the possible mechanisms responsible for the internally emitted light is presented in this chapter. There is evidence (Chapter 5) that the plasma is optically thick. On the basis of this, a method for determining the temperature of the plasma is presented. In the concluding section to this chapter, the validity of the assumptions on which this calculation is based, namely that the radiation is blackbody, is discussed.

4.2. The Experimental Arrangement

The Z−pinch plasma was formed by ionisation of an optical quartz fibre (of the communications type); it was a *125* μm diameter York fibre, with single mode propagation at *1* μm and an inner core diameter of *8* μm. A Hadland Imacon *675* camera with either a streak or framing unit, together with a gated intensifier (Kentech Instruments) was used to observe the optical emission from the plasma. A magnification of $m = 5.5$ was used for the streak photographs. The experimental arrangement is shown schematically in figure 4.1.

When the camera was used in the framing mode an image rotator was placed between the fibre and the imaging lens. The image of the plasma was rotated by *90°* so that its length was imaged onto the slit (the slit actually viewed ~ *45%* of the plasma length) whilst the magnification was changed to $m = 1.4$. The slit width was increased to *2.5* mm to be able to see the whole diameter of the column over the time period of interest.

A *20* metre length of fibre was used in the experiment − one end being fed into the pinch chamber and used to produce the pinch; the other end was placed in the slit plane as shown in figure 4.1. Any light produced in the core of the plasma would then be propagated through the remainder of the fibre and recorded by the camera as it reached the slit.

To correlate the plasma light with the pinch current a timing fiducial was required for the photographs and current traces. The ruby laser provided the timing mark − a reflection off one of the steering prisms was guided onto the camera slit by a standard plastic optical fibre. A reflection off another prism was taken via another optical fibre into a PIN diode, with the resulting signal being used as a timing mark for the current traces. By measuring all the timing delays it was then possible to correlate the pinch light with the current trace.

Streak speeds of *5* ns/mm and framing rates of 75×10^6 fps were used. To prevent the photocathode from being damaged the intensifier gain was set to maximum and the light filtered when necessary by neutral density filters.

4.3. The Observations

Figure 4.2 shows a streak photograph of the plasma emission (referred to as plasma light) together with a current trace. As can be seen, light from the plasma is only visible ~ *10−20* ns after the start of current flow. The plasma expands initially with a velocity ~ 10^6 cm s^{-1}. This continues until peak current

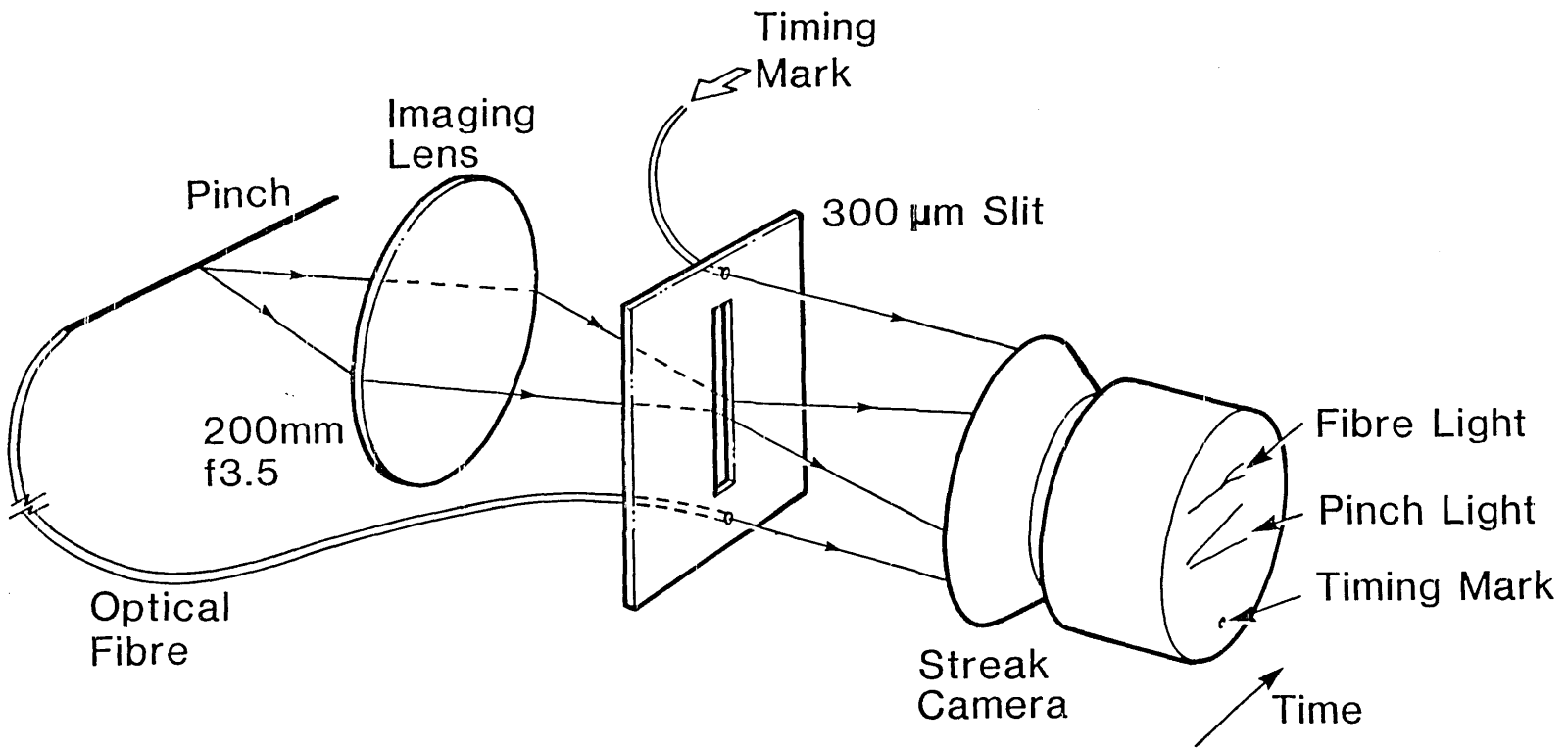


Figure 4.1: Schematic of the streak/framing set-up

is reached (at $t \approx 75$ ns) at which point the plasma expands rapidly with a velocity ~ 5×10^6 cm s^{-1}.

Figure 4.3 shows a typical data set. Again, time $t=0$ corresponds to the start of current flow. The most striking feature of these pictures is the irreproducible behaviour of the plasma. On some shots the plasma is seen to pinch, on others localised regions of plasma are formed and some shots show a stable, non−expanding column for a long period. This behaviour is typical and is irrespective of the initial fibre diameter.

Figure 4.4 shows the evolution of the pinch diameter in time as measured from the streak photographs, for a range of initial fibre diameters. Although the general evolution is similar for all fibres there are significant variations even amongst the same diameter fibres. In general the pinch is not in radial equilibrium − it expands with velocities ~ 10^6 cm s^{-1} up to current peak after which the expansion becomes more rapid, with v_{exp} ~ 5×10^6 cm s^{-1}.

Streaks of the emission from the core of the fibre (referred to as fibre light) can also be seen in the photographs of figure 4.3. This fibre light can be characterised as follows:

(a) low intensity emission, early during current flow, which is modulated with a period of 20−30 ns and

(b) very high intensity emission at approximately peak current.

Characteristic (a) does not seem to be reproducible; sometimes there is no modulation of the fibre light prior to light−up and at other times there is more than one modulation of the light. The time taken, from the start of current flow, to reach stage (b) is referred to as the light−up time. Figure 4.5 is a graph showing the variation of the light−up time, t_Q with initial fibre diameter, Φ_i. There appears to be no correlation between t_Q and Φ_i.

Figure 4.6 shows a typical data set of framing photographs. Time $t=0$ coincides with the start of current flow. The time between frames is 13 ns. The photographs show what appears to be a $m=0$ instability develop within the first 13 ns of current flow. The spacing between the instabilities varies between 0.4 − 1.1 mm. Some of these instabilities move along the axis, towards either anode or cathode. Since the camera actually streaks between frames this motion is observable and its velocity is measured to be:

$$v_{movement} \simeq 5 \times 10^6 \qquad [\text{cm s}^{-1}]$$

For an accurate measurement of this velocity a grid should be placed at the slit plane. The movement of the instabilities can then be measured against a



Figure 4.2.a: Streak photograph of the plasma emission

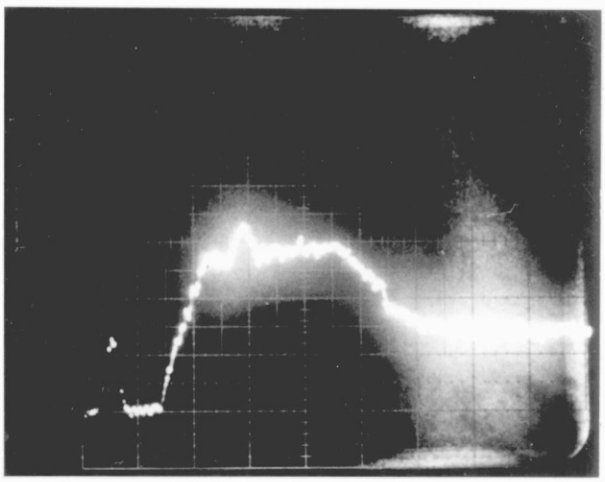


Figure 4.2.b: Corresponding current trace

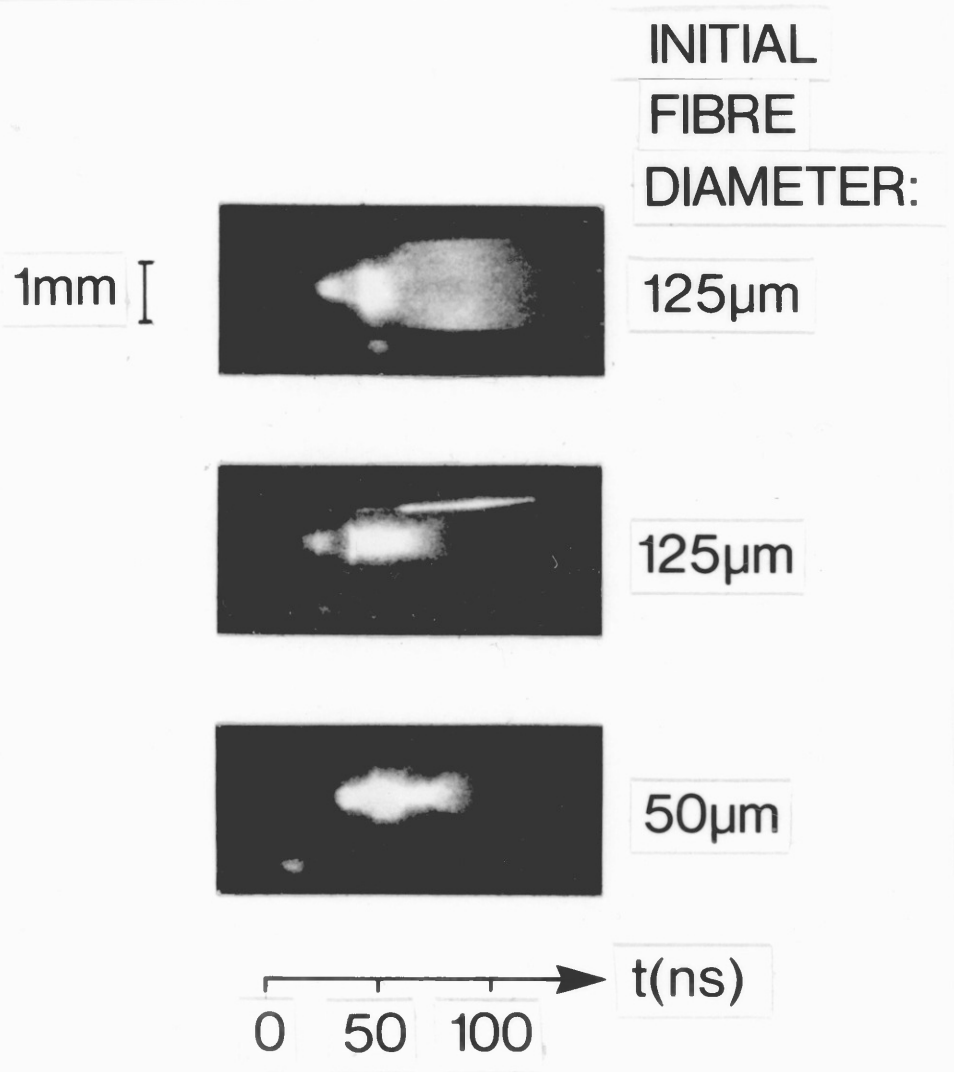


Figure 4.3: Typical data set of streak photographs

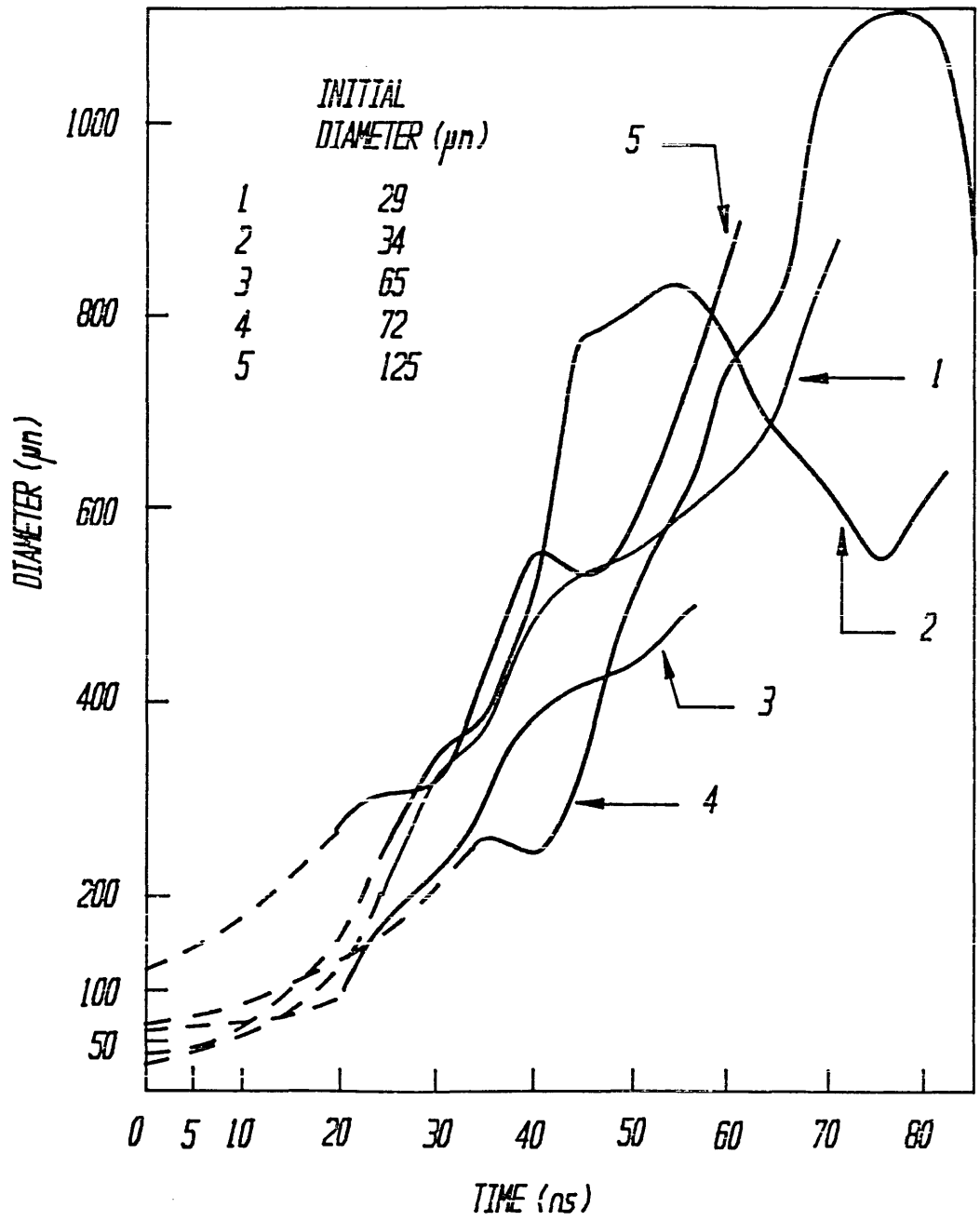


Figure 4.4: Evolution of pinch diameter for a range of initial fibre diameters

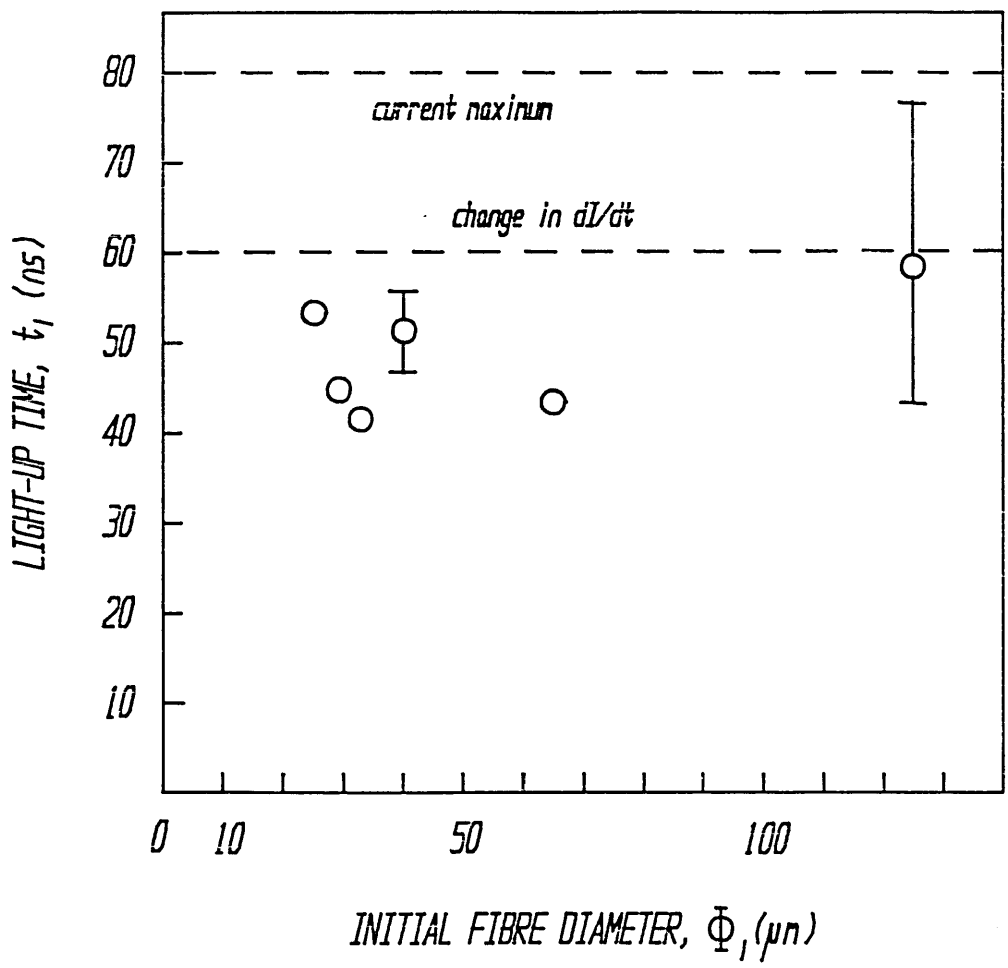


Figure 4.5: Variation of light-up time, t_l with initial fibre diameter, Φ_i

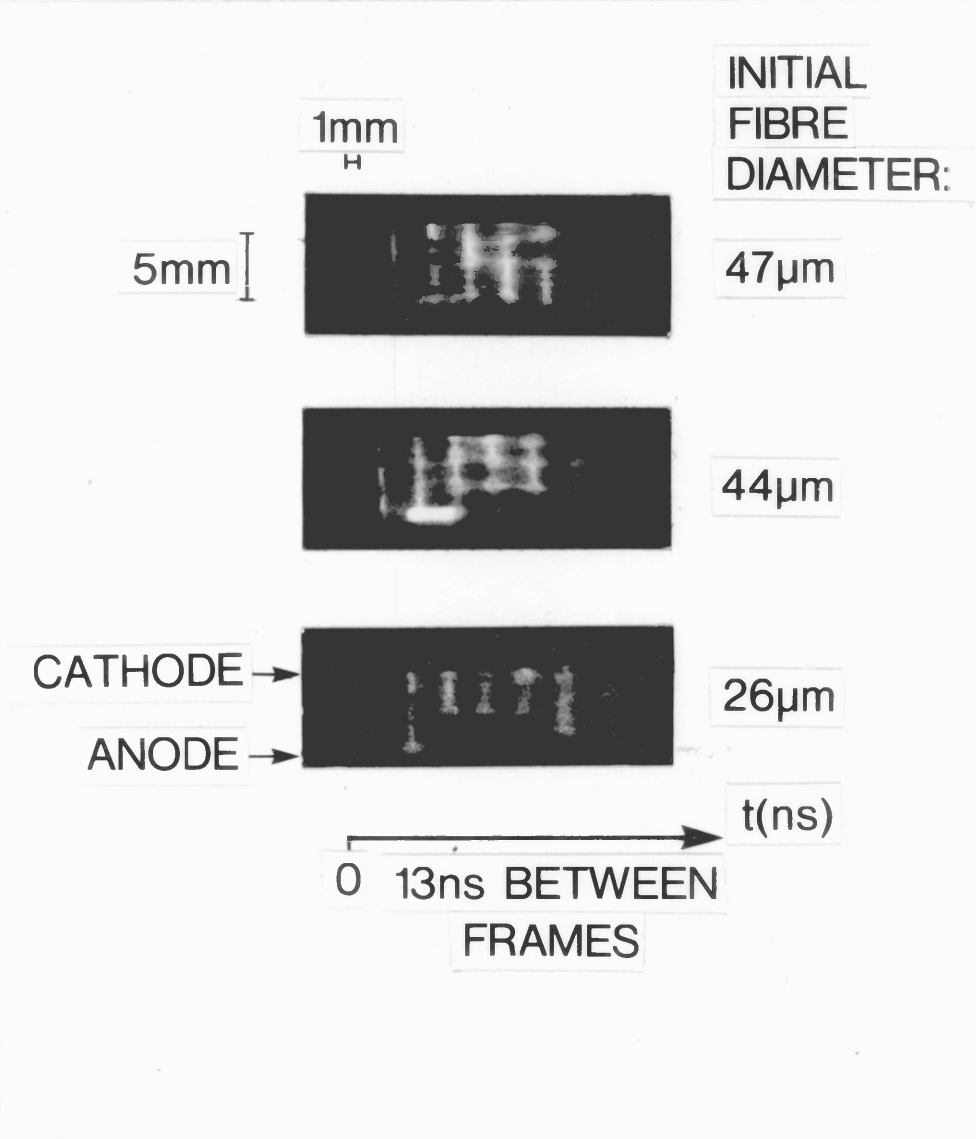


Figure 4.6: Typical data set of framing photographs

background scale. This method also compensates for any artificial movement that the framing unit might introduce (e.g. interference from electrical noise). Such a procedure should be followed in any future such measurements. There is, however, other evidence for the axial motion of the instabilities (see Chapter 5).

These instabilities also expand radially with about the same velocity as the axial movement. They gradually merge together as the current increases towards its peak. At current peak the pinch appears diffuse. Up to this point, although the pinch is unstable it is grossly confined to a well defined column.

The start and subsequent development of the instability is independent of the initial fibre diameter.

4.4. Discussion

4.4.1. Streaks and Axial Movement

To understand the irreproducible behaviour seen on the streak photographs one must examine the optical framing photographs. These show an instability developing within *13* ns of current flow (figure 4.6). Not only that, the instabilities are seen to move along the axis of the fibre. Thus we have the explanation for the streak photographs. In the streak set−up only a small section of the plasma is imaged onto the slit. If there is no axial movement of the plasma then the streak photograph gives a true picture of the temporal history of the plasma radius at a particular point along its length. As soon as there is axial movement of plasma then the streak photograph is a convolution of both radial and axial motion of the plasma and this has to be taken into account in the interpretation of such pictures. Hence the rapid expansion and then apparent pinching seen on some photographs (e.g. figure 4.3.b) is just the motion of one of the instabilities across the field of view of the slit. Since the pinch is not stable there is no reason why from shot to shot one should observe the same behaviour (even if no instability moves across the slit's field of view).

Table 4.1 shows typical axial velocities for different diameter fibres and as one can see, there is a large range of values. If one assumes that, for example, in the streak in figure 4.3.b the apparent expansion at $t=65$ ns is due to an instability moving along the fibre axis then its velocity is:

$$v_{axial} = 1.15\ mm/20\ ns = 5.8 \times 10^6 \quad [\text{cm s}^{-1}]$$

which fits in well with the values in table 4.1.

Table 4.1: *Axial velocity of instabilities for different diameter fibres*

shot #	Φ_i *(μm)*	v_{axial} *(cm* s^{-1}*)*
2.014	26	1.5×10^6
2.011	47	3.8×10^6
9.009	49	3.8×10^6
6.006	61	1.7×10^6
2.003	63	7.1×10^6
4.005	125	2.6×10^6

Axial motion of instabilities has been observed by other workers (Aglitskii, Antsiferov and Panin 1985, Aranchuk *et al* 1986). Aglitskii *et al* observed hot spot motion in a vacuum arc with axial velocities:

$$v_{axial} \simeq 10^7 \qquad [\text{cm s}^{-1}]$$

These velocities were inferred from measurements of the Doppler shift of the K−shell emission of the He−like ions. However, no explanation for the observed hot spot movement is offered.

Aranchuk *et al* experimented with pinches made from exploding copper wires. Again, instabilities were observed which moved with velocities:

$$v_{axial} \sim 1 - 4 \times 10^7 \qquad [\text{cm s}^{-1}]$$

These velocities were measured from the blurring in the images of the instabilities as observed in schlieren photography (see Chapter 5). The axial movement was assumed to arise because of local contractions of the plasma.

It is difficult to explain the axial movement of the instabilities if they are an

ideal $m=0$ MHD instability. This is because the ideal $m=0$ MHD instability is symmetric; although there is a flow of plasma out of the necked regions into the expanding instabilities, this flow is the same in both axial directions and the unstable region itself experiences no motion axially. The non-linear evolution of the $m=0$ instability, in both the short and long wavelength limit, has been examined by Book, Ott and Lampe (1976) and Garanin and Chernyshev (1987). They found that in both limits the instability develops into a 'spike and bubble' structure (see also Roderick and Hussey, 1984). The evolution of the necked region is such that there is axial plasma flow out of it and into the radially expanding instability. One could argue that the moving regions seen in the framing photographs are the axially flowing jets of plasma – a similar phenemenon has been seen in computer simulations (Dr. A.E. Robson, NRL, private communication)– which are denser than the surrounding plasma and therefore appear brighter than the surrounding lower density plasma.

However, the experimental observations clearly show that it is the instabilities themselves that are moving. It seems that they develop independently of each other; this would happen, for example, if the fibre was axially non-uniform. For the instabilities to develop in this way then the Alfven transit time around the necked region must be shorter than the sonic transit time across the same region i.e. the instabilities do not have time to communicate with each other.

The Alfven velocity is given by (Chapter 3):

$$v_a = 2.18 \times 10^{16} B/\sqrt{(\mu n_i)} \quad [\mathrm{m\ s^{-1}},(\mathrm{T},\mathrm{m^{-3}})]$$

where $\mu = m_{ion}/m_p = 20$ for SiO_2.

Taking the necked region to be of radius 100 μm, length 1 mm, with an ion density of 10^{18} $\mathrm{cm^{-3}}$ and a current of 10 kA flowing at this early time, we get for the Alfven transit time around the necked region:

$$\tau_a \simeq 10 \text{ ns}$$

Meanwhile, the sonic velocity is given by:

$$c_s = 9.79 \times 10^5 (\gamma Z T_e/\mu)^{\frac{1}{2}} \quad [\mathrm{cm\ s^{-1}}] \qquad (1)$$

where γ is the adiabatic index, T_e is in eV and $\mu = m_{ion}/m_p = 20$ for SiO_2.

Thus, the sonic transit time across the necked region is ($Z=2$, $T_e = 10$ eV):

$$\tau_s \simeq 80 \text{ ns}$$

Hence it is possible that the instabilities do indeed develop independent of each other. This would mean that a net force could act on an unstable region because of different axial plasma flows, thus causing the instability to move.

4.4.2. The Instability

From the framing photographs the instability is first observed within the first *13* ns of current flow and its subsequent development shows it to be an $m=0$ instability. This type of instability is characterised by a transport of mass from one region to another. The timescale of this process is determined by the ion transit time across the plasma column. Thus:

$$\tau_{m=0} \simeq \Delta r / v^i_{th} \qquad (2)$$

where v^i_{th} is the ion thermal velocity and Δr is the characteristic plasma size.

The initial velocity of the radial expansion of the instability is $\sim 1.0 \times 10^6$ cm s^{-1}. Taking Δr as *100* μm one finds:

$$\tau_{m=0} \simeq 10.0 \text{ ns}$$

This agrees well with the optical framing photographs.

The plasma expansion will proceed at the ion sound velocity (equation (1)):

$$c_s = 9.79 \times 10^5 \, (\gamma Z T_e / \mu)^{\frac{1}{2}} \qquad [\text{cm s}^{-1}]$$

Taking $c_s = 1.0 \times 10^6$ cm s^{-1} (and assuming $\gamma = 5/3$, $Z = 2$) we get for the electron temperature:

$$T_e = 6.3 \quad [\text{eV}]$$

If we now assume that $T_e = T_i$ and $n_e = n_i / Z_{eff}$ (with $Z_{eff} = 2$) then from the Bennett equation:

$$N_e = \frac{\mu_0 I^2}{8\pi k T_e (1 + 1/Z_{eff})} \qquad (3)$$

If we take the current after *10* ns to be $I = 20$ kA and $T_e = 6.3$ eV then:

$$N_e = 1.3 \times 10^{19} \qquad [\mathrm{m}^{-1}]$$

This is the estimated electron line density at this early time.

The solid line density is $N_s = 9.8 \times 10^{21}$ m^{-1}. This then indicates that only a small fraction of the initial fibre has been ionised at early times. Thus an estimate of how much of the fibre is ionised is given by

$$N_e / N_s = (2\pi r \delta r Z n_s) / (n_s \pi r^2) \qquad (4)$$

where δr is the thickness of the fibre shell which is ionised.
Putting in the values from above, we estimate:

$$\delta r \simeq 2.5 \times 10^{-2} \qquad [\mu\mathrm{m}]$$

This indicates that only a thin surface layer of the fibre is ionised at very early times.

From the framing photographs, the number of instabilities seen along the length of the fibre was typically *6*. These were not always uniformly spaced – however, the typical separation was ~ *1.0* mm. The initial radius of the fibre is *62.5* μm. Thus the instability is characterised by:

$$ka = 2\pi a / \lambda = 0.39$$

Thus, this is a long wavelength instability.

The Kadomtsev criterion (Chapter 1) determines the type of pressure profile needed for a Z–pinch to be stable to the different MHD modes. A current profile that is peaked on axis is stable to the $m=0$ MHD mode but unstable to $m=1$ modes. A flat current profile, on the other hand, is unstable to the $m=0$ mode.

From the estimated line density it appears that at early times there is a surface plasma; current will preferentially flow in this outside plasma which will get hot whilst the core will be much cooler (even though thermal conduction is taking place). Such a profile would not be Kadomtsev stable and thus would be

prone to MHD instabilities, particularly to the $m=0$ mode.

It is a general feature of ideal MHD linear instabilities that the growth rate is largest in the limit of zero wavelength ($ka \rightarrow \infty$). The observed instability, however, is long wavelength ($ka < 0.8$). It has been shown (Coppins, 1988) that for a pinch with a flat current profile, the $m=1$ mode dominates in the limit of long wavelength. That the $m=1$ mode is not seen, and with the observed value of $ka \sim 0.4$, suggests that a flat current profile does not exist. This in turn suggests that a surface current Z−pinch exists at early times. Additionally, since the $m=1$ mode involves local displacements of the pinch axis, then a plasma situated around a solid interior would not be able to support an $m=1$ mode. This picture agrees well with the observed nature of the instability.

4.4.3. The Internal Fibre Emission

Let us now examine the emission from inside the fibre. If the emission is due to some kind of heating process that is taking place inside the fibre the there are three basic processes that could be responsible for this heating:

(a) resistive diffusion of the current through the fibre;

(b) thermal conduction of heat into the fibre;

(c) shock heating of the fibre.

Since the evidence points to the fact that the fibre is far from being fully ion ised then we shall consider a model in which the fibre is still a solid with only a surface plasma on the outside. Resistive diffusion of the current can be neglected − the bulk fibre is non−conducting and the current will flow in the surface plasma. In this case the Bennett equation is not applicable inside the fibre; a constant temperature inside the fibre is assumed, which is not related to the current. On the basis of such a model we shall now examine the processes of thermal conduction and shock heating that might be responsible for the internal fibre emission.

(a) Thermal conduction

The model we are considering is a classical problem of thermal conduction in a solid: we have a cylindrical solid at a temperature, T_0, whose surface is at a temperature, T_S (in our model, the surface plasma maintains T_S) and we wish to know how the temperature will distribute itself inside the solid and on what timescale. The solutions to such a problem are well documented in standard texts

(e.g. Carslaw and Jaeger, 1959).

If we assume that the temperature T_S is far greater than T_0, then we can essentially let $T_0 = 0$. The solution for constant T_S is (Carslaw and Jaeger, p.199):

$$T(r,t) = T_S - \frac{2T_S}{a} \sum_{n=1}^{\infty} exp[-\kappa\alpha_n^2 t] \frac{J_0(r\alpha_n)}{\alpha_n J_1(a\alpha_n)} \qquad (5)$$

where κ is the diffusivity $= K/\rho c$

K is the thermal conductivity

ρ is the density

c is the specific heat

a is the fibre radius

α_n are the positive roots of the Bessel function $J_0(\alpha a) = 0$.

This solution assumes that κ is not a function of temperature or time.

Figure 4.7.a shows values of $T(r,t)/T_S$ for various values of $\kappa t/a^2$ plotted against r/a, whilst figure 4.7.b shows the centre and average temperatures for a cylinder of diameter 2ℓ. These two figures then allow us to estimate the characteristic thermal conduction time for our model.

Before proceeding with that, however, one notices two things about this solution. Firstly, the function $T(r,t)$ increases monotonically in time i.e. there is no modulation of $T(r,t)$ in time. In the experiment, however, one sees a modulation of the internally emitted intensity. This then indicates that either the form of the surface temperature, T_S, is incorrect or that there is another process responsible for this modulation. The second point to note is the variation of the characteristic thermal conduction time with the radial dimensions of the fibre. Figures 4.7.a and 4.7.b show that for a fixed ratio of $T(r,t)/T_S$ the characteristic time scales as the square of the fibre radius. Again, such a dependance is not observed in the experiment.

With these reservations in mind let us proceed to determine the characteristic thermal conduction time. Computer simulations (see Chapter 7) show that we might expect the center of the fibre to reach temperatures of $0.2 - 0.8$ eV. Thus taking the ratio $T(r,t)/T_S = 0.2/10$ we find from figure 4.7.b that

$$\kappa t/\ell^2 = 0.05$$

To estimate the thermal diffusivity we refer to data published by Goldsmith A., Waterman T.E. and Hirschhorn H.J. (1961). The specific heat and

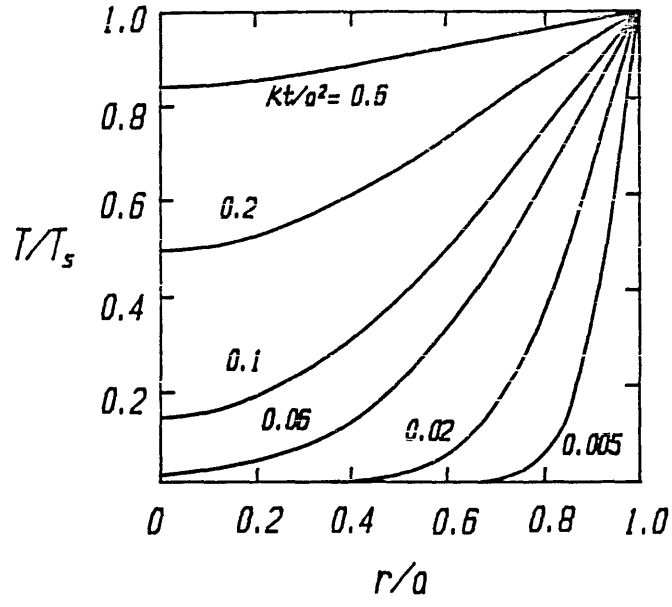


Figure 4.7.a: Temperature distribution in a cylinder at various times

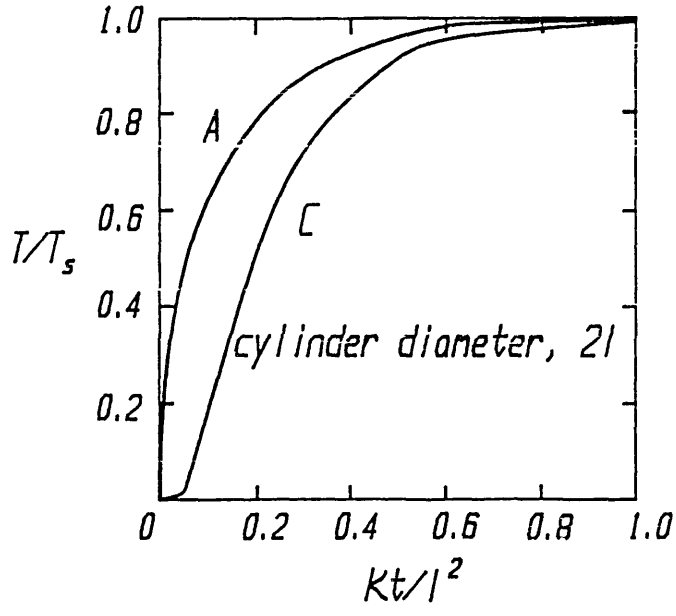


Figure 4.7.b: Centre and average temperatures for an infinite cylinder

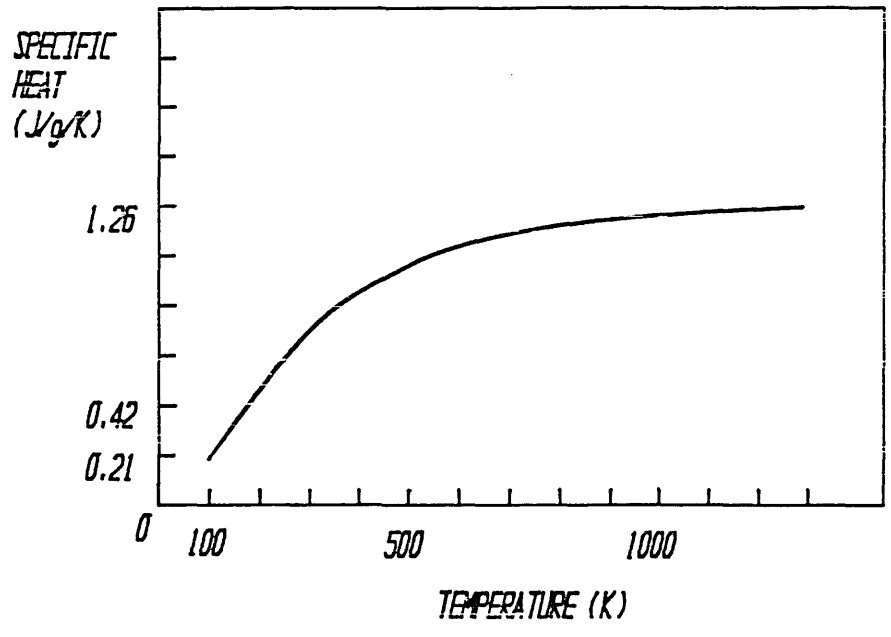


Figure 4.8.a: Specific heat for silica glass

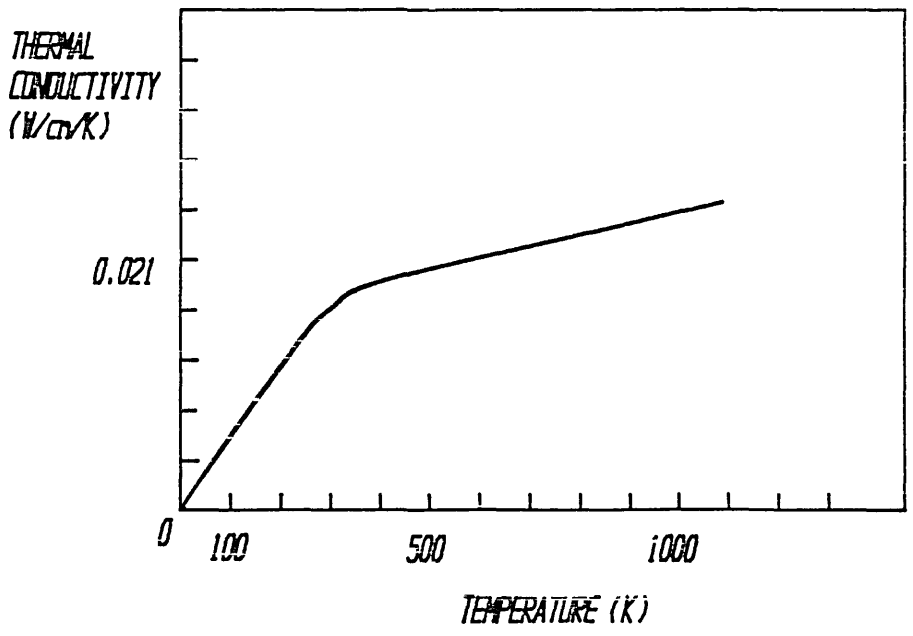


Figure 4.8.b: Thermal conductivity for silica glass

thermal conductivity for silica glass is shown in figures 4.8.a and 4.8.b. We thus find that at $T = T_0 = 300$ K, $\kappa = 1.07 \times 10^{-2}$ cm^2/sec. Using $\ell = 62.5$ μm we find for the characteristic thermal conduction time:

$$\tau_{th} = 183 \times 10^{-6} \quad [s]$$

This is three orders of magnitude larger than the observed timescale (~ 30 ns).

Even if T_s ~ 100 eV, $\kappa t / a^2$ ~ 0.005 and τ_{th} ~ 18 μs which is still far longer than what is observed.

It is interesting to compare this model with one in which the fibre is fully ionised. The radial ion thermal conduction time across the magnetic field is given by (Haines, 1978):

$$\tau_{k\perp}^{i} = (m_e / m_i)^{\frac{1}{2}} \tau_{k\perp}^{e} = 4.09 \times 10^{-2} \tau \qquad (6)$$

where $\tau = 1.71 \times 10^{-11} \pi a^2 T_m^{3/2}$ [s, (m, K)]

and T_m is the maximum temperature inside the plasma.

Taking $T_m = 10$ eV $= 1.16 \times 10^5$ K (probably an overestimate for a fully ionised fibre) and $a = 62.5$ μm we find:

$$\tau_{k\perp}^{i} = 3.4 \times 10^{-13} \quad [s]$$

In equilibrium the temperature is proportional to the current squared. This means that there is almost an instantaneous response of the temperature to any variation in the current (since this results in a variation in the emitted intensity). If the emission is blackbody (which, if the fibre were fully ionised and a temperature of 10 eV, it would be) then the intensity of emitted radiation is proportional to the temperature (see later, section 4.4.4.) which is proportional to the current squared (from the Bennett equation). Thus for the observed modulation in intensity of a factor of ~ 1.5 − 2 the current has to vary by ~ 20 − 30% and over a time of ~ 30 ns. Such a modulation of current is not observed. Also note that the radial dependance of $\tau_{k\perp}^{i}$ is as the radius squared and again this is also not observed.

Thus neither model explains the observed behaviour of the intensity emitted from the centre of the fibre.

One other possible mechanism for heating the fibre internally is that of radiative heat conduction. In this case the energy is transported by the photons radiated from the plasma (Zel'dovich and Raizer (1966) p.652). This process is

non−linear since the photon radiation specific heat, c_{rad}, and hence the diffusivity of the photons ($\propto \ell_p c_{rad}$ where ℓ_p is the photon mean free path) is dependent on temperature ($c_{rad} = dU_p/dT$ where U_p is the radiation energy density $= 4\sigma T^4/c$; $\therefore c_{rad} \propto T^3$).

With the onset of a large temperature (> few eV) at the fibre surface a thermal wave is launched into the solid. The energy will be propagated faster compared to the normal (linear) heat conduction process since the speed of the photons in the fibre is greater than the local sound speed (which characterises linear heat conduction).

However, the transit time of the wave across the fibre is some function of the fibre radius, depending on exactly how the photon diffusivity varies with temperature. In general, the thermal wave slows down as it propagates in time (Zel'dovich and Raizer). One would then expect the transit time across the fibre to be shorter for the smaller diameter fibres than for the larger ones.

So this process still does not explain the observed behaviour of the internally emitted intensity.

(b) Shock heating

With the appearance and fast rise of the pinch current there will be a corresponding rapid rise in magnetic pressure and a shock will be driven into the solid fibre. The description of the interaction of the shock with the solid is complicated, with many factors having to be taken into account − for example, the change of state of the fibre, the transfer of energy between the shock and the solid etc. (see e.g. Zel'dovich and Raizer, 1966, p.685). Such analysis is beyond the scope of this thesis and we shall restrict ourselves to a few passing comments.

As regards the dependence of the shock radial transit time with the dimensions of the fibre then presumably the velocity of the shock front will be the same irrespective of the radius of the fibre (which is assumed to be at some constant temperature). The transit distance is just the radius of the fibre and so one might expect the shock transit time to scale linearly with the radius. Although one has to bear in mind any change of state of the fibre (e.g. solid to liquid) the initial shock front will not be affected by this. The above scaling, however, is not observed. Some experimental studies have been made on the interaction of shocks (driven by explosives) with SiO_2 (e.g. Wackerle, 1962) but the results depend on the geometry and composition of the material used and it is not clear to what extent they apply to general situations.

(c) Other possible mechanisms

Two further possible mechanisms could be responsible for the emission observed from the core of the fibre. They are:

(i) fluorescence

(ii) scintillation.

The former arises when photoelectric absorption takes place. In this case, absorption of a photon results in the ejection of an electron from the n^{th} shell of the atom. The subsequent vacancy is filled by an electron from an outer shell. The energy can appear as a fluorescent photon or a radiationless Auger electron (see e.g. Dyson, 1973). We also note that this is an ionising process, with one or two electrons being liberated for every incident photon.

When a high energy electron passes through a material it will lose its energy through collisions. These collisions will take the atoms into an excited state form which they return to the ground state by emitting photons. When these photons are in the visible part of the energy spectrum then the process is termed scintillation. Certain materials also respond to photons in the XUV energy region which cause them (the atoms of the material) to scintillate.

There is considerable X−ray output from both the plasma and the electrodes (see Chapter 6). In fact, different phases in the time−resolved X−ray emission are observed and the timescale of these is approximately the same as the modulation period of the emitted intensity from within the fibre.

The internal emission from the fibre is consistent with there being scintillation of the internal core. Accompanying fluorescence would ionise the fibre to a certain extent, allowing current to diffuse into it but it is not clear whether this is responsible for the sudden increase in the intensity of emission at around the time of peak current. Although radiative heat conduction might not explain the early behaviour of the internally emitted fibre light, calculations using a one−dimensional MHD code suggest that it is responsible for the observed increase in the emission at around peak current − the code shows that there is a sudden increase in temperature at the centre of the fibre, due to the transport of radiation, at around peak current. The MHD model and its results are more fully discussed in section *7.3.1*, Chapter 7.

4.4.4. A Determination of T_e from Optical Photographs

Results from schlieren photography and holographic interferometry (Chapter 5) indicate that the plasma is optically thick. If this is the case then it is possible to determine the plasma temperature from the optical photographs discussed in this chapter. This analysis is presented below.

We refer to the schematic of the streak arrangement as shown previously in figure 4.1. The plasma is imaged onto the streak slit by an imaging lens. If the magnification of the optical system is m then the length of the pinch that is imaged onto the slit is w_s / m. The pinch diameter is φ_p and hence the projected surface area of this pinch element is $dA_p = (w_s / m)\, \varphi_p$. The solid angle subtended by the imaging lens at this pinch element is $d\Omega_p = \pi(\varphi_l / 2d)^2$ [str].

The plasma is assumed to be radiating as a blackbody in the optical region. Denote its specific spectral intensity by $I_p(\lambda)d\lambda$ [$Wm^{-2}str^{-1}$]. This radiation passes through a quartz window whose transmission is a function of the wavelength of the incident radiation: $W(\lambda)$. There is also some neutral density filtering at the entrance to the streak slit: the transmission of the filter is a function $F(\lambda)$. The functions $W(\lambda)$ and $F(\lambda)$ are shown in figure 4.9. Hence the power in the image at the slit is:

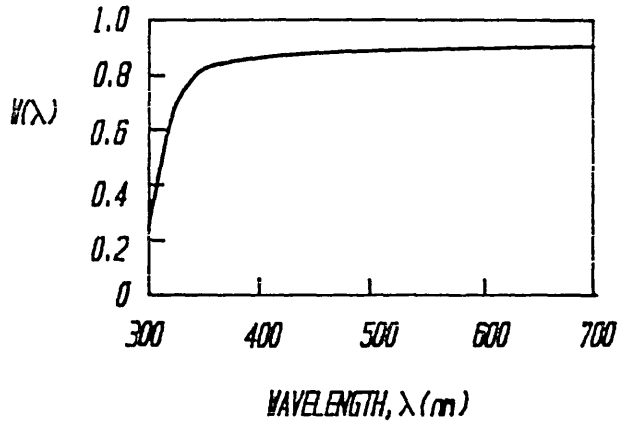
$$I_p(\lambda)W(\lambda)F(\lambda)d\Omega_p dA_p d\lambda \qquad [W]$$

The streak camera itself has a response which is dependent on the wavelength of the incident radiation. The camera was calibrated as follows: a blackbody source of known temperature was placed a known distance from a small calibrated aperture behind which the camera was placed. Calibrated filters were arranged behind aperture to pick out a known amount of power in a known spectral interval. The photocathode current was then measured as a function of the wavelength at the centre of each spectral interval. This was converted into a sensitivity given in units of mA/W. One then assumes that the intensity of the image on the phosphor is proportional to this sensitivity. Figure 4.10 is a graph of the spectral sensitivity of the camera versus wavelength.

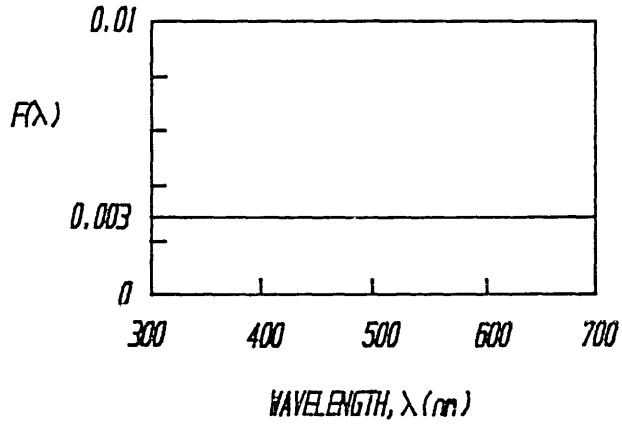
Thus the power in the image on the phosphor is

$$KI_p(\lambda)W(\lambda)F(\lambda)R(\lambda)d\Omega_p dA_p d\lambda \qquad [W]$$

where $R(\lambda)$ is the spectral response of the camera and K is the constant of proportionality.



(a)



(b)

Figure 4.9: Transmission of:
(a) quartz window, W(λ)
(b) neutral density filter, F(λ)

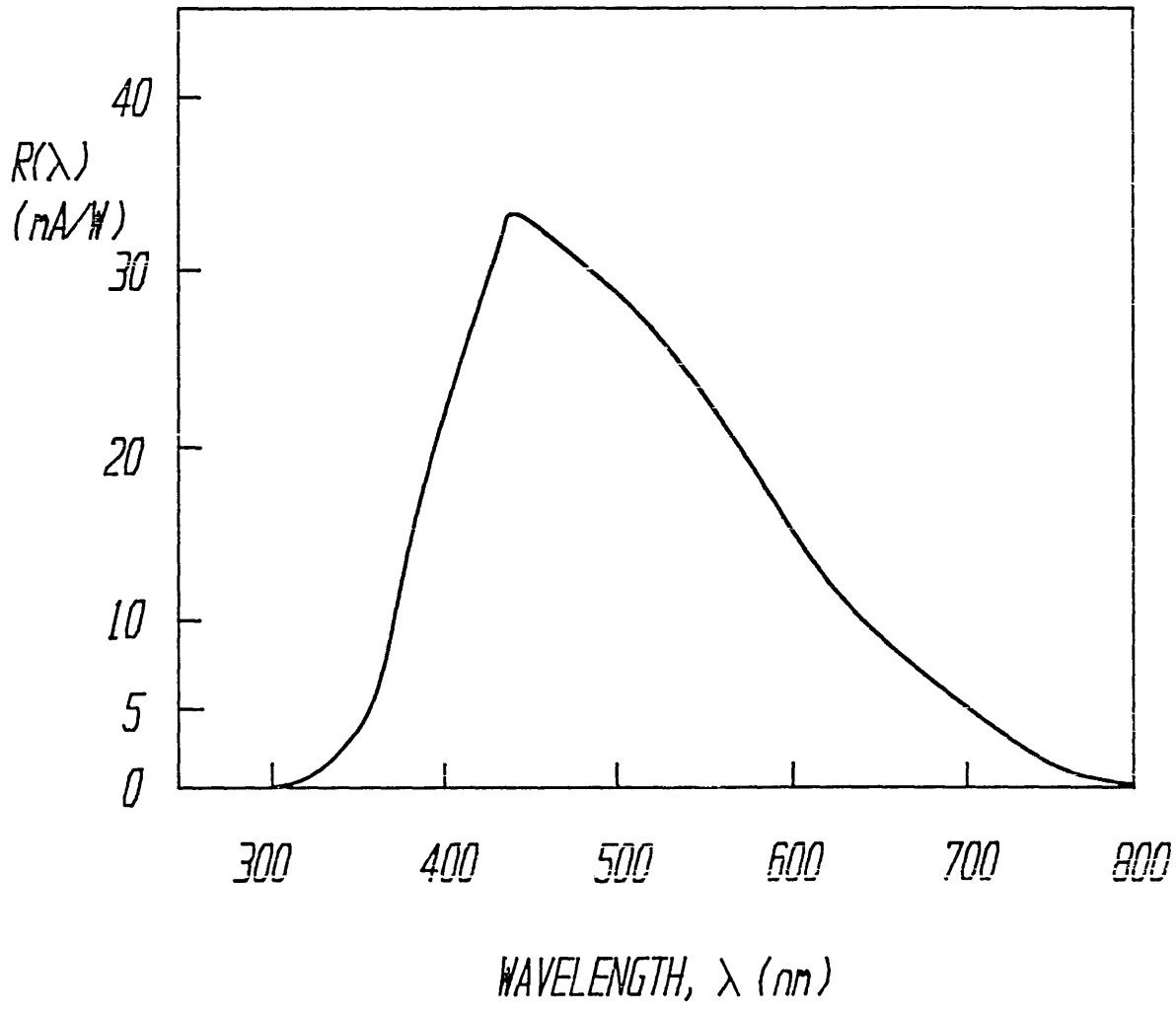


Figure 4.10: Spectral sensitivity of the streak camera

If one assumes that the plasma maintains a cylindrical profile during the time of interest then the area of the image is $(m\varphi_p)w_s$.

So the total intensity of the image of the plasma on the phosphor is:

$$I_i^{plasma} = \frac{Kd\Omega_p}{m^2}\int I_p(\lambda)W(\lambda)F(\lambda)R(\lambda)d\lambda \quad [Wm^{-2}] \tag{7}$$

since $dA_p/(m\varphi_p w_s) = 1/m^2$.

For blackbody radiation:

$$I_p(\lambda)d\lambda = \frac{2hc^2}{\lambda^5}(e^{hc/\lambda eT_e} - 1)^{-1}d\lambda \quad [Wm^{-2}str^{-1}] \tag{8}$$

If $hc/\lambda eT_e \ll 1$ (which for $\lambda = 6943$ Å, requires $T \gg 1.8$ eV) then:

$$I_p(\lambda) = (2ceT_e/\lambda^4)d\lambda \tag{9}$$

Therefore, from equation (7) we derive for the temperature:

$$T_e = I_i^{plasma}\frac{m^2}{(2\cdot ce)(d\Omega_p)K}\left\{\int W(\lambda)F(\lambda)R(\lambda)d\lambda/\lambda^4\right\}^{-1} \tag{10}$$

Taking $m = 5.5$, $d\Omega = 5.28 \times 10^{-2}$ str and evaluating the integral inside the brackets gives:

$$T_e = I_i^{plasma} \times \frac{1.78 \times 10^{-5}}{K} \quad [eV] \tag{11}$$

The constant K was determined by streaking a ruby laser pulse of known energy. Figure 4.11 is a diagram of the set-up.

The laser intensity is a function of both space and time *i.e.*

$$I_{laser} = I_Q(x,y,t) \quad [Wm^{-2}]$$

The Joule meter measures the total energy in the pulse:

$$E_{tot} = \int_t \left\{ \int_x \int_y I_Q(x,y,t)dxdy \right\} dt \quad [J] \tag{12}$$

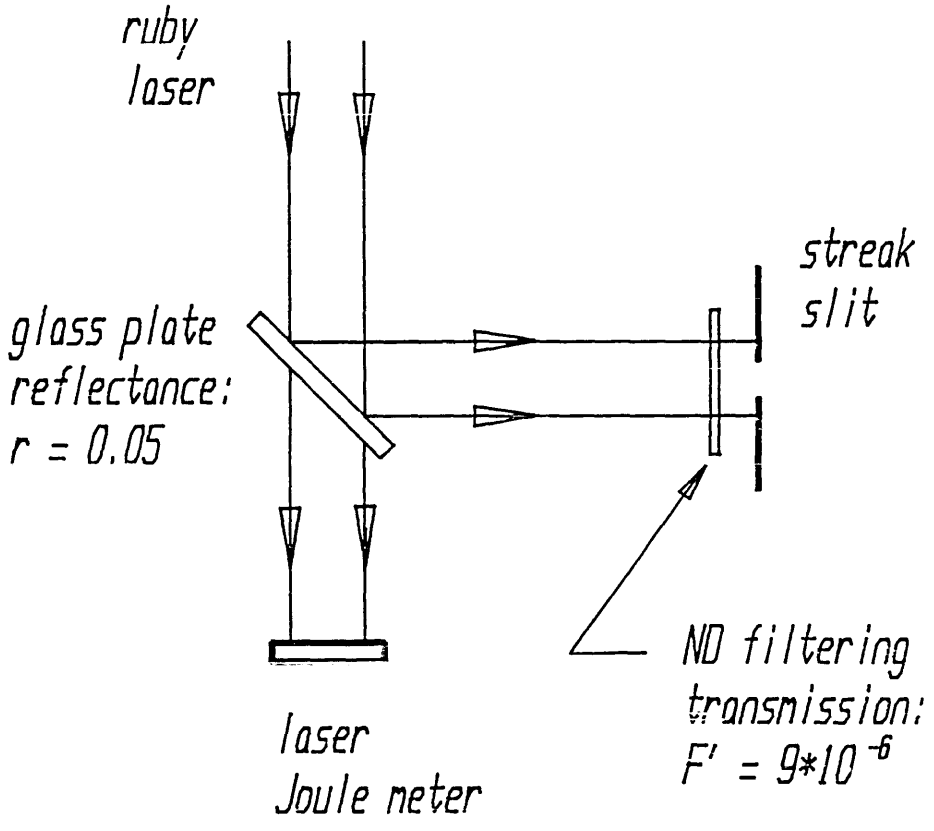


Figure 4.11: Set-up for determining the constant K

In this set−up the measured energy is a fraction $(1-r)$ of the input energy. Hence the energy entering the slit is:

$$E_s = \frac{rfF'}{1-r} E_m \qquad (13)$$

where E_m is the energy measured by the Joule meter and f is the fraction of the laser beam intercepted by the streak slit.

The intensity of the laser image is:

$$I_i^{laser} = I_s^{laser}\ KR(\lambda_Q) \qquad (14)$$

where I_s^{laser} is the laser input intensity at the streak slit and $R(\lambda_Q)$ is the camera response function at the ruby laser wavelength.

By expressing E_s as an integral of I_s^{laser} (which is proportional to $1/K$) one gets:

$$\frac{1}{K} = \left[\frac{rfF'}{1-r}\right] E_m R(\lambda_Q) \left\{ \int_t \int_x \int_y I_i^{laser}\ dxdydt \right\}^{-1} \qquad (15)$$

The integral of I_i^{laser} is carried out over the image of the laser (after compensation for the film response). The magnitude of I_i^{laser} obtained after digitising the data is only proportional to the real intensity but since T is derived by comparing two intensities (the plasma intensity to that of the laser) then this is of no consequence. Putting in the values for the coefficients (given in figure 4.11) in the above equation, we get:

$$1/K = 5.92 \times 10^3 \qquad \text{[mA/W]}$$

Hence, equation (3) becomes:

$$T_e = 1.05 \times 10^{-1} \times I_i^{plasma} \qquad \text{[eV]} \qquad (16)$$

where I_i^{plasma} is measured in the same units as I_i^{laser}.

The contributions to the error in determining the temperature come chiefly from determining the value of K which depends on measuring the energy of the laser and the fraction that is intercepted by the streak slit. This is about 6% and including the errors from m and $d\Omega$ the total error is ~ 10%.

Figure 4.12 shows a digitised scan of a plasma image as a function of time. The peak value of the intensity occurs at a time, $t=62$ ns after the start of current, and its value is *813*. Putting this into equation (4) we get for the temperature:

$$T_e = 85.8 \ eV$$

At earlier times the plasma intensity is lower (figure 4.12). Substituting the lower values for I_i^{plasma} we get:

$$T \simeq 30 \ eV$$

The smallest detectable blackbody temperature is determined by the level of the background film density of the image. This gives for the minimum temperature:

$$T_e^{min} \simeq 2.5 \ eV$$

At early times ($t < 10$ ns) if the radiation emitted by the plasma had been blackbody at a temperature lower than 2.5 eV then it would not have been detectable. However, if at early times the radiation is predominantly bremsstrahlung then one can calculate the electron number density needed for it to be detectable as follows:

The power in the image from bremsstrahlung radiation is

$$P_i^{brem} \propto \int R(\lambda) I_{ff}(\lambda) dV d\lambda \qquad (17)$$

where $R(\lambda)$ is the camera response function

dV is a plasma volume element

$I_{ff}(\lambda) = 1.92 \times 10^{-28} Z n_e^2 T_e^{-\frac{1}{2}} \lambda^{-2} e^{-\beta/\lambda}$ [J/cm^3/s/dλ]

λ is in Angstroms

$\beta = 12.39 \times 10^3 / kT.$

If the radiation is blackbody then the corresponding expression is

$$P_i^{bb} \propto \int R(\lambda) I_{bb}(\lambda) dA d\lambda \qquad (18)$$

By equating P_i^{brem} and P_i^{bb} one determines the required electron number density (for a given electron temperature) at which the detected bremsstrahlung

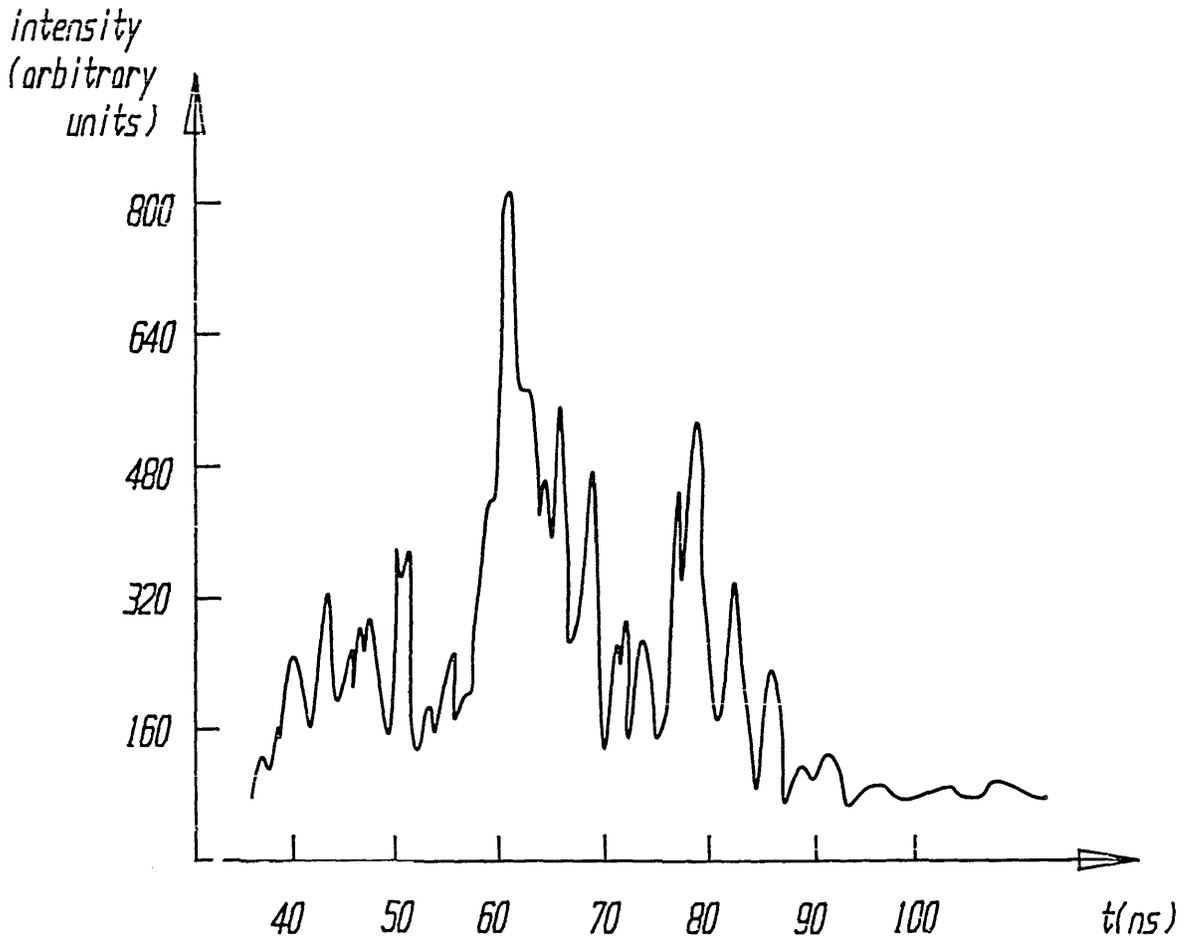


Figure 4.12: Microdensitometer scan of a typical plasma image

radiation is equal to the detected blackbody radiation.

At a temperature of *2.5* eV the necessary number density is:

$$n_e = 2.9 \times 10^{19} \qquad [\mathrm{cm}^{-3}]$$

Even at a temperature of *100* eV we find:

$$n_e = 1.0 \times 10^{19} \qquad [\mathrm{cm}^{-3}]$$

Holographic interferometry measurements show that there exists a low density coronal plasma surrounding a high density core plasma column (Chapter 5). The measured number density of the coronal plasma at early times ($t = 17$ ns, Chapter 5) is:

$$n_e^{meas} = 3.0 \times 10^{18} \quad [\mathrm{cm}^{-3}]$$

Thus not even bremsstrahlung radiation from the coronal plasma would have been observable in the experiment at early times. This is consistent with the observations (or rather non-observation of any light emission for $t < 15$ ns).

We shall now discuss the validity of assuming blackbody radiation in the above calculation. We shall see how the intensity of emission is related to the local plasma parameters and under what conditions this intensity will approach the blackbody limit.

4.4.5. Radiation from a Plasma

When a plasma is optically thin then radiation emitted in its interior can escape freely without interacting with the surrounding particles. The intensity of emission in a given spectral interval is then just the sum of the emission coefficients (that is the energy radiated by a unit volume of plasma per unit time per unit solid angle per spectral interval) along the line of sight.

When the plasma ceases to be thin and becomes optically thick then the intensity of emission will depend on how efficiently the radiation is transported within the plasma. It is no longer simply an integral of emissivity along the line of sight; furthermore, the effects of radiation trapping on the population levels within the plasma becomes important.

The equation of radiative transfer provides a description of the transport of

radiation within a plasma. It is written as (Griem, Lochte−Holtgreven):

$$\frac{dI_\nu(x)}{d\tau'(\nu,x)} = S_\nu(x) - I_\nu(x) \qquad (19)$$

where I_ν is the intensity per unit frequency

$d\tau' = \kappa'(\nu)d\ell$ is the element of optical depth

$\kappa'(\nu)$ is the absorption coefficient which defines the decrease in intensity due to absorption

$S_\nu = \epsilon_\nu/\kappa'(\nu)$ is the source function, being the ratio of emissivity to absorption.

In the limiting case of a homogeneous plasma with no incident radiation, then the solution of equation (19) is:

$$I_\nu(x_0) = S_\nu[1 - exp(-\tau'_0(\nu)] \qquad (20)$$

where $\tau'_0(\nu) = \kappa'(\nu)x_0$ is the optical depth of the plasma (at a frequency, ν)

x_0 defines the edge of the plasma.

In the two limiting cases, for optically thin plasmas:

$$\tau'_0(\nu) \ll 1: \qquad I_\nu(x_0) = \epsilon_\nu x_0 \qquad (21.a)$$

whilst for optically thick plasmas:

$$\tau'_0(\nu) \gg 1: \qquad I_\nu(x_0) = S_\nu \qquad (21.b)$$

So only in a homogeneous and optically thin plasma does the intensity represent the emission coefficient.

We are now interested to examine under what conditions the source function S_ν approaches the blackbody limit. In fact, S_ν is only equal to the blackbody Planck function in one situation: thermodynamic equilibrium (TE). For TE, Kirchoff's Law establishes a relation between ϵ_ν and $\kappa'(\nu)$. This states that

$$\epsilon_\nu = \kappa'(\nu)B_\nu(T) \qquad (22.a)$$

where $B_\nu(T) = (2h\nu^3/c^2)[exp(h\nu/kT) - 1]$ [W/m^2/str/dν] (22.b)

is the Planck blackbody function.

This follows from the fact that in TE, ϵ_ν and $\kappa'(\nu)$ only depend on the

atomic level populations (and atomic constants). Away from complete TE, detailed calculations of collisional and radiative rate processes are usually needed to the determine the source function (see Griem 1964, Richter, McWhirter).

However, in local thermodynamic equilibrium (LTE – which can be thought of as LTE with a diluted radiation field) and collision–dominated plasmas, if conditions are such that the optical depth is large compared to the typical plasma dimensions then the source function will approach the blackbody limit quite closely. If these conditions are fulfilled, then the radiation is being emitted from the surface. Even if the bulk plasma is homogeneous, there is the possibility that the observed radiation is coming from boundary layers which are inhomogeneous in which case the source function is not described by the Planck equation.

A detailed discussion of calculating source functions in non–LTE plasmas can be found in the texts by Griem (1964) and Zwicker. A detailed discussion of radiative transport is given by Zel'dovich and Raizer (1966). Opacity effects in the spectroscopic diagnosis of plasmas are also reviewed in an article by De Michelis and Mattioli (1981).

To summarise, it is important to determine the equilibrium state of the plasma since the source function and hence the emitted intensity are critically dependent on this. The last section will briefly discuss the plasma equilibrium states and which of these most aptly describes the fibre plasma.

4.4.6. The Plasma Equilibrium State

The basic models for describing the equilibrium state of a plasma (namely TE, LTE, coronal and collisional–radiative equilibrium) are discussed in detail by various authors (Griem, De Michelis and Mattioli, Bekefi). In our case it is of relevance to only examine LTE since this is the state in which S_ν is most likely to approach the Planck function.

In complete TE the plasma is homogeneous. The radiation field is blackbody and hence the optical depth in all directions and at all frequencies is large. However, for most plasmas radiation from within is free to escape to the surface and beyond. A state where the population distribution is described by the Boltzmann equation but where the radiation field is not blackbody is known as local thermodynamic equilibrium (LTE).

This state is collision dominated and for the model to be applicable the collisional and radiative population rates for a level n must satisfy the following conditions (Griem 1964, NRL Plasma Formulary 1986):

$$Y_{nm} \geq 10 A_{nm} \tag{23}$$

Additionally the electron density must satisfy:

$$n_e \geq 7 \times 10^{18} Z^7 n^{-8.5} (T/E_\infty^Z)^{\frac{1}{2}} \qquad [\mathrm{cm}^{-3}] \tag{24}$$

where Z is the charge on the ion and E_∞^Z is the ionisation energy of the ion.

The population distribution is described by the Saha equation:

$$\frac{n_e n_1(z)}{n_n(z-1)} = 6.0 \times 10^{21} \frac{g_1^Z}{g_n^{Z-1}} T_e^{3/2} \exp[-E_\infty^Z/T_e] \tag{25}$$

where $n_j(z')$ is the population of the j^{th} level of ion z'

$g_j^{z'}$ is the statistical weight of level j for ion z'.

We can use equation (24) to estimate whether the fibre plasma is in LTE or not. Table 4.2 lists E_∞^Z for the different ionisation stages for silicon with the corresponding electron densities needed for LTE to hold down to the level $n=2$ for two different temperatures (*10* eV and *30* eV). As one can see, for $Z > 2$ very large electron densities are needed to establish LTE. The condition for LTE in the ground state is even more stringent.

Table 4.2: *Electron densities needed for LTE to hold for n=2*

Z	E_∞^Z (eV)	n_e (cm^{-3}, 10 eV)	n_e (cm^{-3}, 30 eV)
1	8.22	2.1×10^{16}	3.7×10^{16}
2	13.77	2.0×10^{18}	3.6×10^{18}
3	21.09	2.9×10^{19}	5.0×10^{19}
4	62.56	1.2×10^{20}	2.1×10^{20}
5	80.40	5.4×10^{20}	9.3×10^{20}
6	93.30	1.8×10^{21}	3.1×10^{21}

In transient plasmas, for LTE to be achieved not only do conditions (23) and (24) have to be satisfied but the time required to establish such conditions has to be small compared to the timescale of the experiment. The time to establish an equilibrium is given by Griem (1964):

$$\tau^Z \approx \frac{1.1 \times 10^7 Z^3 n_a^{\,2}}{f_{21} n_e (n_a^Z + n_a^{Z-1})} \frac{E_2^{Z-1,a}}{Z^2 E_h} \left[\frac{kT}{Z^2 E_h}\right]^{\frac{1}{2}} \exp\left[\frac{E_2^{Z-1,a}}{kT}\right] \quad [s] \qquad (26)$$

where the units are c.g.s.

τ^Z as a function of Z and electron density for silicon and $T_e = 10$ eV is shown in Table 4.3.

Table 4.3: *Equilibration times to achieve LTE in transient plasmas*

Z	n_e (cm^{-3})	τ^Z (s)
1	2.1×10^{16}	3.2×10^{-9}
2	2.0×10^{18}	5.2×10^{-12}

So, only for densities $\geq 1 \times 10^{18}$ cm^{-3} is the equilibration time smaller than the timescale of the present experiment.

We have to estimate the optical depth of the plasma to determine whether it is optically thick or not. Zwicker gives the optical thickness for Bremsstrahlung radiation as:

$$\tau_0'(\nu) = CZ^2 c^2 G n_e n_i (kT_e)^{-3/2} \nu^{-2} \ell \qquad [c.g.s] \qquad (27)$$

where $C = 3.18 \times 10^{-47}$ (c.g.s units)

G is the Gaunt correction factor (see, e.g., Bekefi 1966).

Taking $n_i = n_e / Z_{eff}$ with $Z_{eff} = 3$, $n_e = 3 \times 10^{19}$ cm^{-3}, $\lambda = 4000$ Å, $T_e = 10$ eV and $\ell = 100$ μm we find:

$$\tau_0'(\nu) = 6.4 \times 10^{-6} \ll 1$$

So the plasma is optically thin to Bremsstrahlung over the optical region (300 nm $< \lambda <$ 700 nm).

The optical depth for Doppler broadened lines is given by (NRL Plasma Formulary, 1986):

$$\tau_{\ell}(\lambda) = 5.4 \times 10^{-9} (\mu / T_e)^{\frac{1}{2}} \lambda n_i \ell \qquad \text{[c.g.s]} \qquad (28)$$

where $\mu = m_i / m_p = 2\theta$ for silicon.

The main resonance transitions in the optical region are given by authors such as Allen (1955). The typical wavelengths are $\lambda \sim 300 - 600$ nm (for example: $Si(z=2)$, $3s4s-3s4p$, $\lambda = 4553$ Å; $Si(z=3)$, $4s-4p$, $\lambda = 4089$ Å).

Taking $T_e = 10$ eV, $\lambda = 4000$ Å and $\ell = 100$ μm we find that:

$$\tau_{\ell} \gg 1 \qquad \text{for} \qquad n_i \gg 2.8 \times 10^{14} \ cm^{-3}.$$

Post (1961) has reviewed the losses by impurity radiation from high temperature plasmas. He has found that the ratio of line radiation to hydrogenic bremsstrahlung is many orders of magnitude (~ 5) higher for temperatures below 1 keV. With line radiation being so dominant then if these lines are all optically thick then the radiation from the plasma (if it is in LTE) will tend towards blackbody radiation.

4.5. Conclusions

The optical photographs show that the fibre plasma is unstable. This instability is observed within 13 ns of the start of current flow and its characteristics (shape, wavelength and subsequent development) are consistent with it being an $m=0$ instability.

Axial motion of the instabilities is also observed. This motion is in both directions.

Estimates of the electron number density indicate that only a small surface layer of the fibre forms the early plasma. The fact that an $m=1$ instability is not seen, even though the instability is long wavelength (for such cases the $m=1$ growth rate is greater than that for the $m=0$ mode), confirms that the fibre is not fully ionised.

It has been shown that thermal conduction (both for a surface plasma and a fully ionised fibre) does not explain the behaviour of the intensity of the light emitted from the inside of the fibre. This emission, however, is consistent with the fibre core scintillating and fluorescing. These processes are closely related to the plasma X−ray emission. There is also a modulation of this X−ray emission in time (Chapter 6), the timescale of which is in close agreement with the observed modulation of the internal fibre emission; this is another strong indicator that the fibre core is indeed scintillating.

It is not clear whether this would then be responsible for the increase in the internal emission at around peak current. However, this increase in emission is consistent with a sudden peak in the temperature at the core of the fibre as a result of radiative heat conduction (section *7.3.1*, Chapter 7) − this is discussed in more detail in Chapter 7.

On the basis of evidence from laser diagnostics (Chapter 5) a method of estimating the electron temperature, based on blackbody radiation, has been discussed. It was found that the emission is consistent with a blackbody temperature of *10 − 30* eV. Similar observations have been made by Skowronek *et al* (1970), who measured the optical thickness of their plasma by measuring the ratio of incident to transmitted laser light. They found that their plasma column was optically thick, with $n_e \simeq 10^{21}$ cm^{-3} and $T_e \simeq 4$ eV and that it radiated as a blackbody over a large spectral region.

From the ensuing discussion about plasma radiation if the plasma is to radiate as a blackbody at a temperature $T_e = 10$ eV then it has to be in LTE, be optically thick and it also has to be homogeneous. To achieve the first condition the electron density must be a minimum of $\sim 3 \times 10^{18} - 10^{19}$ cm^{-3}. The equilibration time to achieve this is then much shorter than the timescale of the experiment. For the plasma to be homogeneous then the temperature has to be 'smoothed out' across the plasma. This is done by thermal conduction; the timescale is (section 4.4.3.):

$$\tau_{th} = 3.4 \times 10^{-13} \text{ [s]}$$

and again this is much shorter than the experimental timescale.

The results from the optical observations, especially from the internal fibre emission, indicate that the fibre is not fully ionised for quite some time (at least up to current maximum); it is probable that there exists a solid core around which is situated a dense ($n_e > 10^{19}$ cm^{-3}), cold ($T_e \simeq 10 - 30$ eV) plasma and

that all the fibre is not ionised until approximately the time of peak current. This does not preclude the existence of a less dense, hotter plasma around the cooler one since it has been shown that such a plasma would be transparent to the streak camera. The holographic interferometry measurements indeed show a dense plasma core surrounded by a low density, coronal plasma; these results are discussed in Chapter 5. The radiation from a low density, hot plasma plasma can be detected using X−ray diagnostics and this is discussed in Chapter 6.

CHAPTER FIVE

Laser Diagnostics

5.1. Introduction

Diagnosis of the plasma using probes is not feasible because of the high fields inside the load chamber plus the fact that the probes are liable to disturb the plasma during a measurement. However, probing the plasma with a suitable laser is a very elegant and non−intrusive method of determining electron density profiles, plasma stability and symmetry etc. without perturbing the plasma.

The classical schlieren technique depends on the fact that the refraction of light passing through a plasma is proportional to the density gradient. This can provide a qualitative picture of the density gradients in a plasma. The shadowgraph technique, on the other hand, gives an indication of the spatial variation of density gradients within a plasma. The technique used in the experiment contained features of both the above methods.

Holographic interferometry was used to investigate the electron distribution in the pinch. This is now a standard technique and is well documented (e.g. Jahoda and Siemon, 1972). It involves taking two sequential holograms on the same holographic emulsion − one exposure with the plasma present and the other, with no plasma, providing a reference. Upon reconstruction, two superimposed wavefronts are generated and the phase differences introduced between these by the plasma give rise to an interference pattern which is then recorded on a photographic film. This technique has a great advantage over conventional interferometry in that the interfering beams traverse the same path, thus dispensing with the need for high quality optics and critical alignment.

In this chapter, the electron number density profiles in the fibre plasma are calculated. One can therefore estimate to what extent the fibre is ionised. The profiles also allow one to determine whether the schlieren pictures were due to refraction or absorption of the laser. The latter section is accompanied by a further discussion of blackbody radiation; one is thus able to conclude whether the determination of the electron temperature from the optical photographs (Chapter 4) is accurate.

5.2. The Experimental Arrangement

Figure 5.1 is a schematic showing the arrangement for schlieren/streaked shadowgraph photography. The pinch was backlighted by a *7* ns ruby laser pulse which then passed through a *50%* beamsplitter and one beam was imaged onto the film plane whilst the other was imaged onto the streak camera slit. The magnification was *1.6*. A *3* mm aperture was included in the path of the former beam to reduce the intensity of transmitted plasma light; additionally, a ruby interference filter was used to filter out the plasma light. The aperture, however, eliminates from the image any rays that would be strongly refracted by the plasma and this introduced an element of the schlieren technique (to be more exact, it is an 'inverse' schlieren since it uses an aperture rather than a stop). A timing mark (as described in Chapter 4, section 4.2.) was added to the current trace thus identifying at what time each picture was taken.

The arrangement for holographic interferometry is shown in figure 5.2.a. The laser pulse was split so that *50%* traversed the pinch chamber and the remainder was directed onto the holographic film (*35 mm 10E75P3AH*, Agfa−Gevaert) by means of two ruby laser steering mirrors. Background reference fringes were introduced by rotating mirror M_1 through a small angle between exposures. The plasma was imaged onto the holographic film by a *20* cm, *f3.5* lens (the resulting magnification being *3.2*) − this imaging counteracts the refractive bending effects of the plasma due to transverse refractive index gradients which otherwise degrade the interference fringe pattern and the plasma image. The scene and reference beam paths were matched to within the coherence length of the laser. An additional lens was included in the reference beam − this made exact superposition of scene and reference beams easier and eased the requirement for spatial coherence.

The development procedure for the exposed holograms was as follows:

(a) the film was developed in a standard solution of Microphen (Ilford Products) for *4* minutes;

(b) it was then fixed for *4* minutes in a solution of Hypam (Ilford Products);

(c) finally, the film was bleached in a potassium ferricyanide solution and then washed in alcohol.

The holograms were reconstructed using a white light source (figure 5.2.b). A well exposed hologram usually produced about 3 strong diffracted orders; an *f2.5*, *305* mm lens focussed the first diffracted order and produced a reconstructed image of the plasma at the film plane of a Polaroid Land Camera. The images were all recorded on *5"×4" FP4* film (Ilford Products).

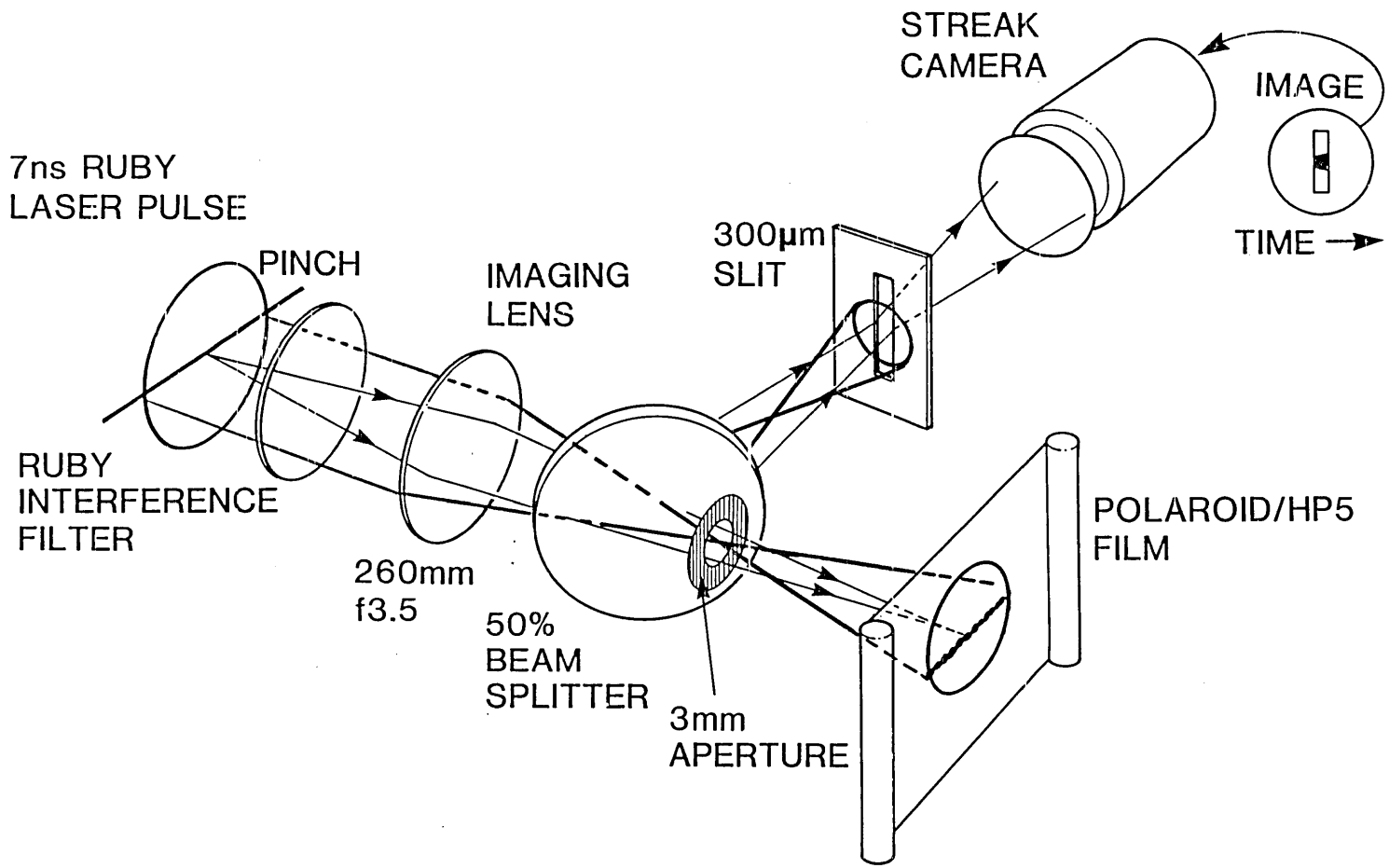


Figure 5.1: Set-up for schlieren and streaked shadowgraph photography

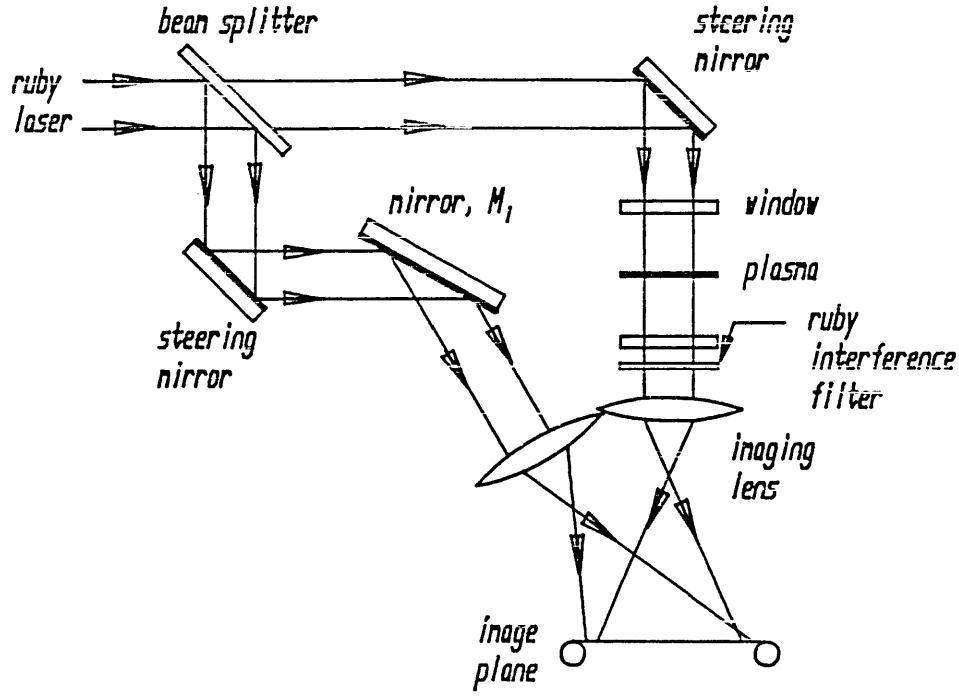


Figure 5.2.a: Set-up for holographic interferometry

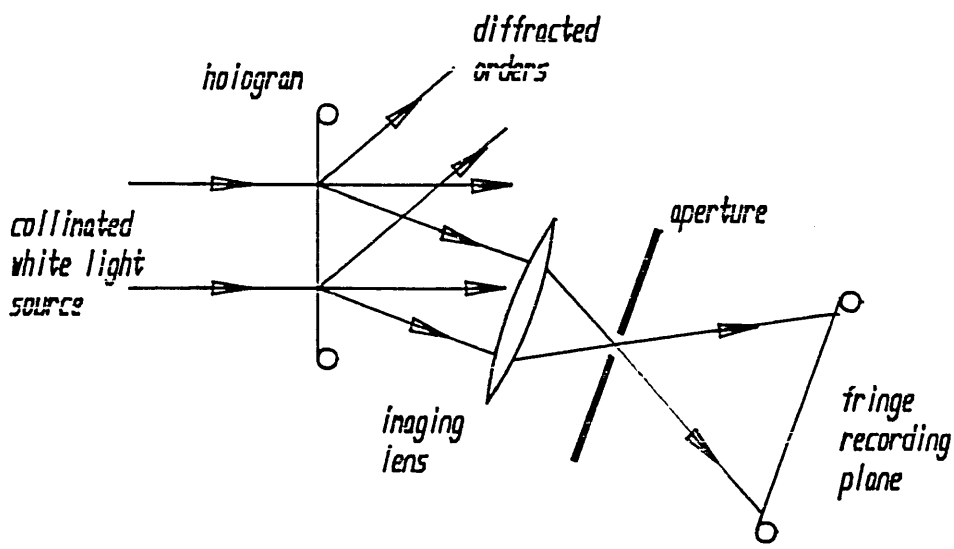


Figure 5.2.b: Reconstruction of the holograms

5.3. The Observations

5.3.1. Schlieren Photography

Figure 5.3 shows a sequence of schlieren photographs taken at different times during different discharges. All the initial fibre diameters were *125* μm. The photographs show that what appears to be an $m=0$ instability is well-developed within the first *20* ns of current flow. There are ~ *10* localised formations (instabilities) along the length of the fibre at this time. The typical diameter of the formations is ~ *1.7* mm, extending for ~ *600* μm in the axial direction. At the tip of the capillary (anode) there is a particularly large plasma formation. A well-defined central region is still visible; it does not appear to be of a uniform diameter along the axial direction – near the anode it is ~ *380* μm diameter, in the middle *500* μm whilst towards the cathode it is ~ *440* μm. Successive photographs show the local formations increasing in size with a velocity:

$$v_{exp} \simeq 4 \times 10^6 \qquad [\text{cm s}^{-1}]$$

This is in good agreement with the velocity of expansion as measured from optical streak and framing photography ($v_{exp} \simeq 5 \times 10^6$ cm s^{-1}).

It can be seen that most of the local formations have a disc-like appearance. This can be explained if one assumes that the instabilities are expanding radially and also moving axially along the fibre. Since the probing laser pulse has a FWHM of *7* ns and if one assumes that a movement of *50* μm is detectable, then any movement with a velocity of 0.5×10^6 cm s^{-1} or greater will be detectable and this will manifest itself as 'blurring' on the photograph. The velocities deduced from this 'blurring' are:

$$v_{exp} \simeq 4 \times 10^6 \qquad [\text{cm s}^{-1}]$$

and

$$v_{axial} \simeq 6 \times 10^6 \qquad [\text{cm s}^{-1}]$$

in good agreement with the optical observations (Chapter 4). Note also that the curvature of these 'discs' is in both axial directions. This implies that the instabilities are indeed moving in both directions along the pinch axis. Axial motion of instabilities (in exploding copper wires) has also been inferred from such a diagnostic technique by Aranchuk *et al* (1986).

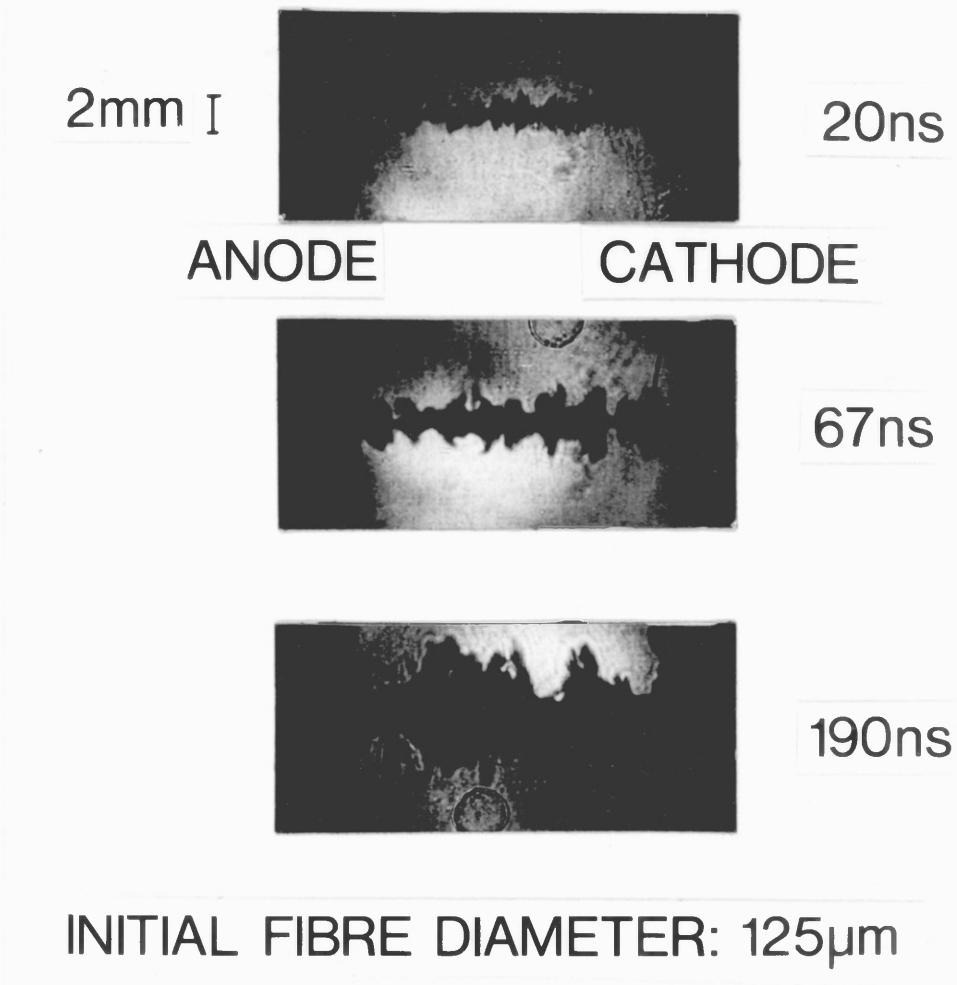
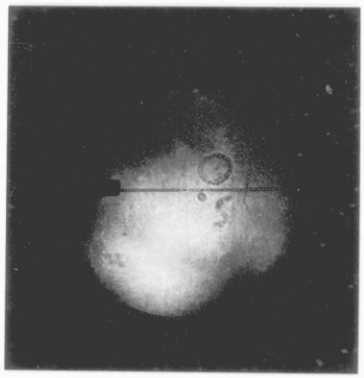


Figure 5.3: Sequence of schlieren photographs



mag^{n} = 1.6

Figure 5.4.a: Schlieren photograph of a reference (undisturbed) fibre

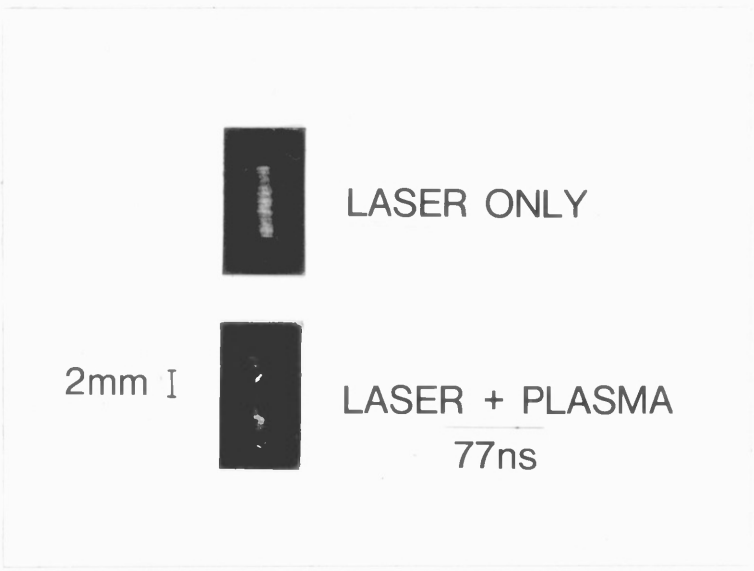


Figure 5.4.b: Streaked shadowgraph together with a streak of the laser

Figure 5.4.a is a photograph of the fibre backlighted by the ruby laser. No transmission is seen through the fibre. The fibre acts as a strong cylindrical lens and so, apart from a small central region, it will refract the laser light quite strongly. However a central region ought to allow transmission of the laser with little refraction. It seems that at the small magnification used ($m = 1.6$) the Polaroid film cannot resolve this central region. One thus cannot say conclusively that in the shadowgraphs the laser is being strongly absorbed by the plasma rather than being refracted out of the aperture.

Figure 5.4.b shows a typical streaked shadowgraph of the plasma. Also shown for comparison is a streak of the laser. In this particular photograph the laser has backlighted one of the instabilities – its diameter is $\simeq 1$ mm. As can be seen there is no transmission of the laser light through the plasma.

5.3.2. Holographic Interferometry

Figures 5.5 and 5.6 show a sequence of reconstructed holograms of different discharges taken at different times, together with a reference photograph of an undisturbed fibre. Notice that the fringes in this reference photograph are visible across the whole fibre diameter. The first photograph shows a central core (through which the laser is not transmitted) surrounded by a low density plasma (so inferred because of the small fringe shift). The diameter of the core is 250 μm and the plasma extends out to a radius of $\simeq 500$ μm (before $n_e \ell$ drops below the resolution of the recording system).

By performing an Abel inversion of the fringe data it is possible to recover the electron number density profile (see later, section *5.4.6.*) Figure 5.7 is the reconstructed electron density profile pertaining to figure 5.5.a. The electron number density at the edge of the core is:

$$n_e = 3.0 \times 10^{18} \qquad [\mathrm{cm}^{-3}]$$

At a radius of 500 μm this density has dropped to:

$$n_e = 5.0 \times 10^{16} \qquad [\mathrm{cm}^{-3}]$$

Figure 5.8 shows the reconstructed electron number density profile corresponding to figure 5.6.b at the different axial positions (marked z_1, z_2 etc.). These were derived assuming a uniform cylindrical symmetry and although the

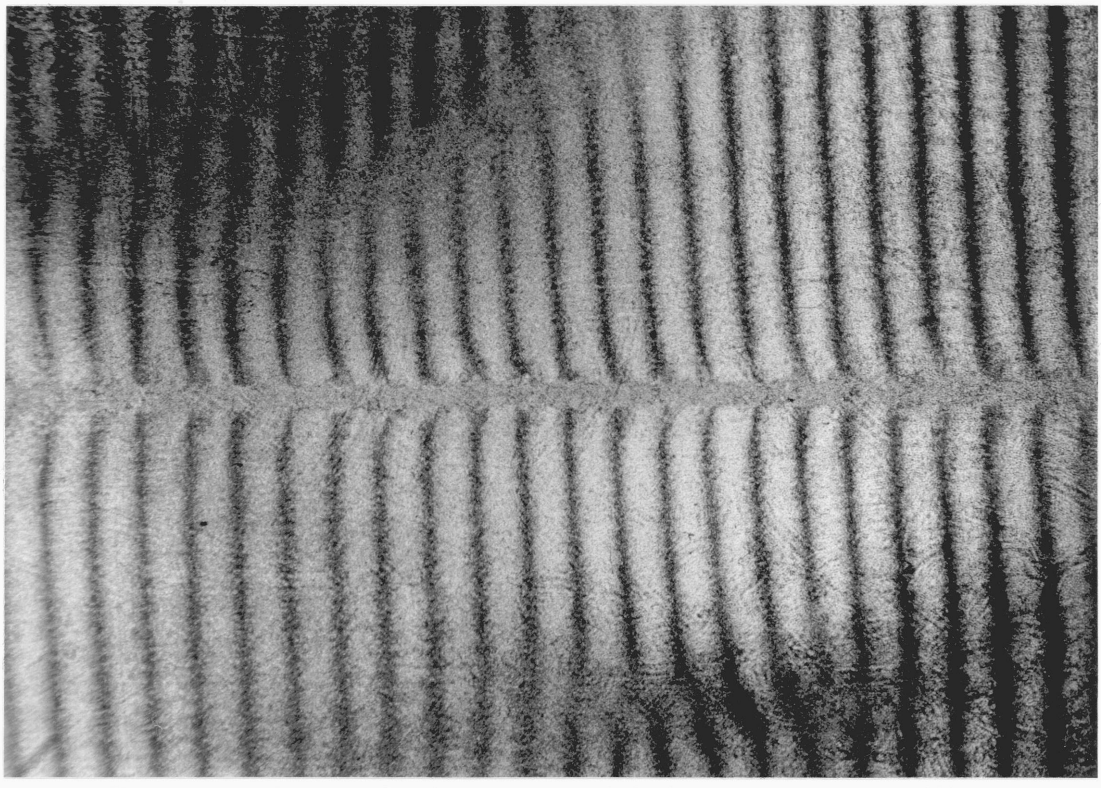


Figure 5.5.a: Reconstructed hologram at t = 17 ns

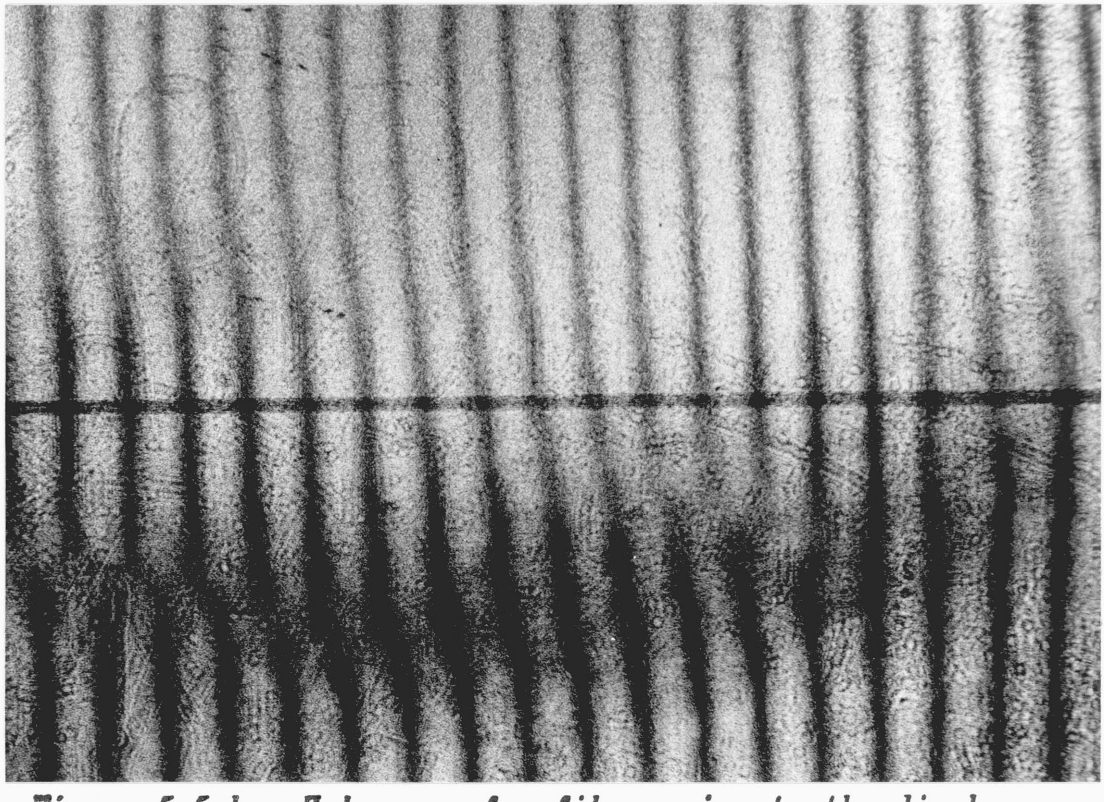


Figure 5.5.b: Hologram of a fibre prior to the discharge

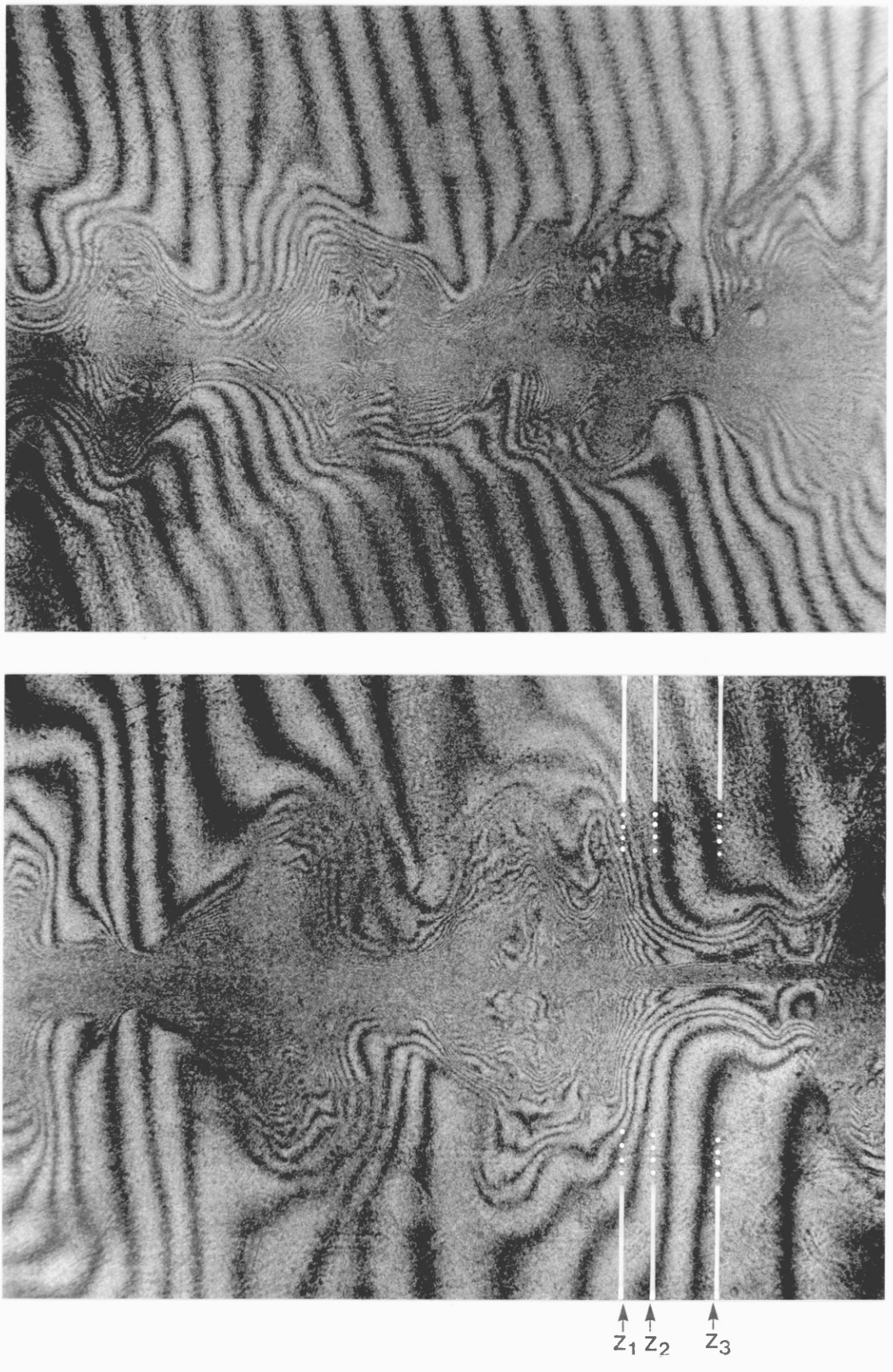


Figure 5.6: Reconstructed holograms at:
(a) t = 127 ns
(b) t = 147 ns

holograms do not show absolute symmetry an Abel inversion still provides a useful picture of the plasma state at this later stage.

In the unperturbed region (z_3) the electron density reaches a value of

$$n_e(z_3) \simeq 1.0 \times 10^{19} \qquad [\mathrm{cm}^{-3}]$$

whilst towards the centre of the instability (z_1) this value is

$$n_e(z_1) \simeq 2.0 \times 10^{19} \qquad [\mathrm{cm}^{-3}]$$

This shows that there is an increase in the number density as one goes from the necked region towards the instability.

In the hologram taken at $t=17$ ns (figure 5.5.a) there do not appear to be any instabilities present. However, other holograms taken at similar times do show perturbations along the fibre and the fringe pattern outside of the core region is identical to the one seen in figure 5.5.a. We shall thus assume that this hologram is typical of the evolution of the outer plasma at such early times.

At late times the reconstructed holograms quite clearly show local $m=0$ instabilities at an advanced stage in their development. All the pictures still show a central core in which no fringes are visible, in contrast to the reference photograph which does show the fringes going through the core region. There are also some local formations that are opaque to the ruby laser. The core region of the plasma is typically $\simeq 300$ μm throughout the recorded time history of the plasma; however, one interesting feature of the picture at $t=147$ ns is that in places the core region is only 170 μm in diameter.

At these late times there are large fringe shifts around the instabilities which mean that they are of a high density and indeed the Abel inversions show densities at the core edge of typically $1 - 2 \times 10^{19}$ cm^{-3} (a shift of one fringe over a distance of 200 μm implies a number density of $n_e \simeq 1.6 \times 10^{19}$ cm^{-3}). The instabilities are typically 1.2 mm in diameter, in agreement with the schlieren pictures and the optical photographs. There is still low density plasma extending out radially to about three times the spot size. Though the instability is well developed in the later stages ($t>100$ ns) there is still a high degree of radial symmetry of the plasma; this allows one to perform Abel inversions of the fringe data to deduce electron number density profiles to a reasonable degree of accuracy.

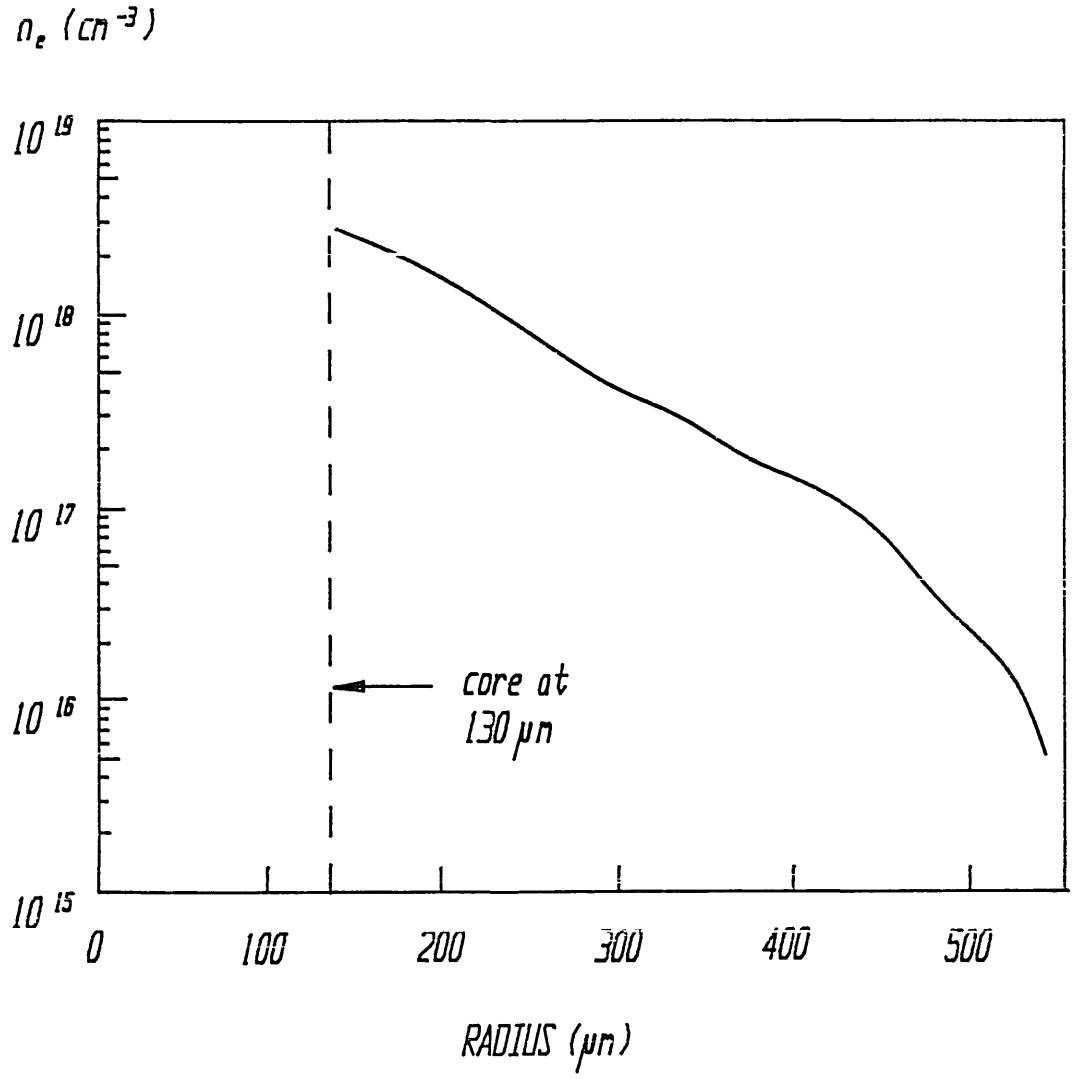


Figure 5.7: Electron number density profile at t = 17 ns

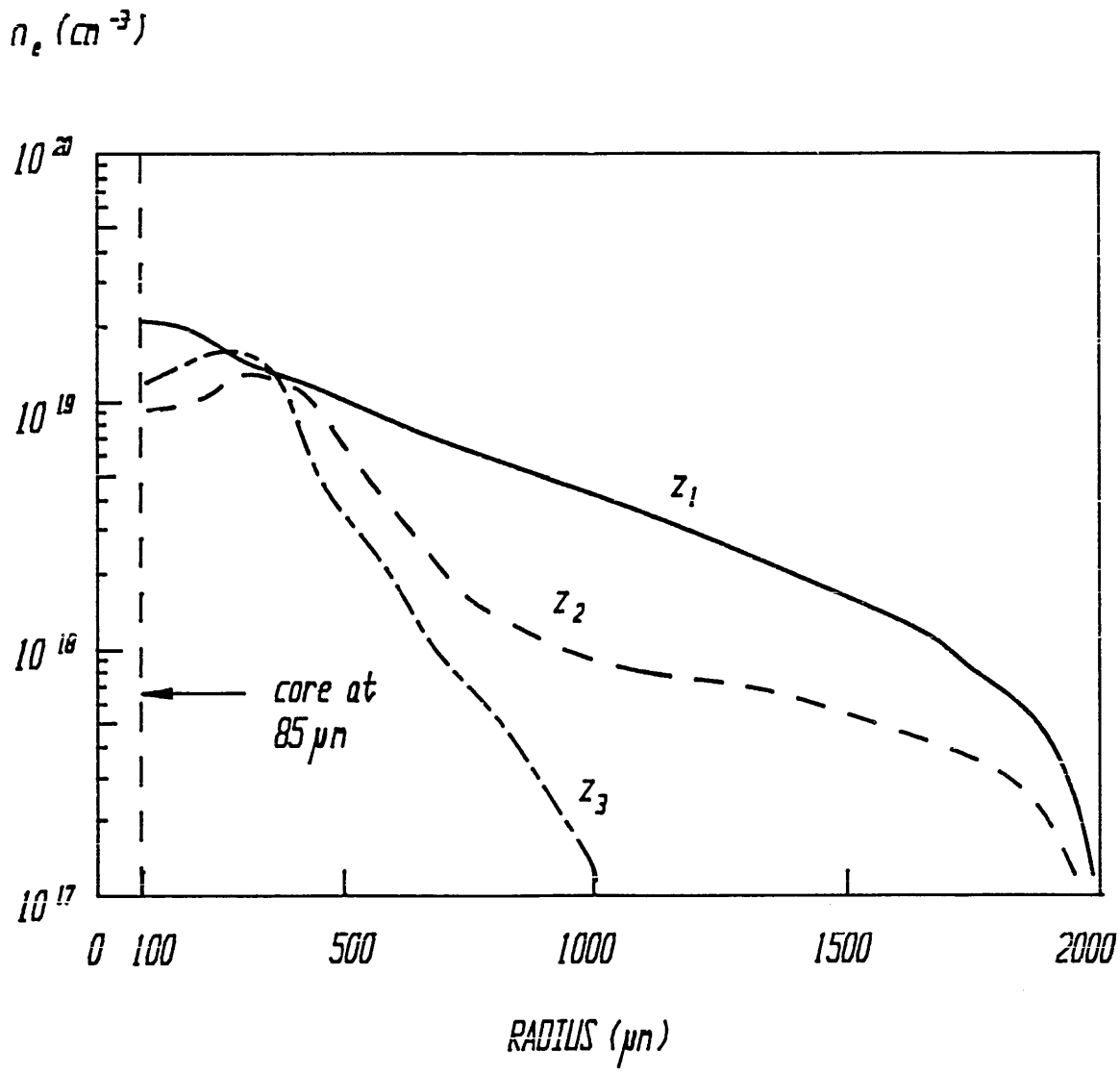


Figure 5.8: Electron number density profiles at t = 147 ns at axial positions z_1, z_2 and z_3

5.4. Discussion

In a plasma the refractive index μ is determined by the contribution of the electrons, ions and neutral particles. In the case of a partially ionised plasma the contribution to μ from neutrals and ions can be considerable especially in the optical region (Keilmann, 1972). However, in the infra-red region this contribution is very small for most laboratory plasmas.

The refractive index due to electrons is given by:

$$\mu_e = (1 - n_e/n_c)^{\frac{1}{2}} \qquad (1)$$

where n_e is the electron number density

n_c is the critical density at which radiation of wavelength λ is not transmitted.

The critical density is obtained by equating the plasma frequency to the frequency of the incident radiation. Since we are usually dealing with a laser of well defined wavelength then one has for n_c:

$$n_c = 1.11 \times 10^{13} \lambda^{-2} \qquad [\mathrm{cm}^{-3}] \qquad (2.a)$$

where λ is the laser wavelength (cm).

In the case of ruby, $\lambda = 6943$ Å and so the critical density is:

$$n_c = 2.31 \times 10^{21} \qquad [\mathrm{cm}^{-3}] \qquad (2.b)$$

This is the upper limit on the measureable electron density using a ruby laser.

One is usually measuring electron densities that are much smaller than the critical density. In this case equation (1) becomes:

$$\mu_e - 1 \simeq -n_e/2n_c \qquad (3.a)$$

Substituting for the critical density for the ruby wavelength gives:

$$\mu_e - 1 = -2.16 \times 10^{-22} n_e \qquad (3.b)$$

The corresponding expressions for the refractive index of neutrals and ions are given by the so-called Gladstone-Dale relation:

$$\mu - 1 = \sum_i K_i \rho_i \tag{4}$$

where K_i is the specific refractivity of the species i

ρ_i is the partial density of the species i

and all the contributions are summed over all existing species (see, for example, Alpher and White, 1958).

In the long wavelength region one can also write:

$$\mu_\infty - 1 = 2\pi n \bar{\alpha}_\infty \tag{5}$$

where the subscript implies long wavelength;

n is the number of particles per cm^3.

The mean polarizability, $\bar{\alpha}$, is given by:

$$\bar{\alpha} = \frac{e^2}{4\pi m_e} \sum_i \frac{f_i}{\nu_i^2 - \nu^2} \qquad [c.g.s] \tag{6}$$

where f_i is the atomic oscillator strength for transitions yielding ν_i.

Typical values for the strongest transitions for both silicon and oxygen ions can be found in Allen (1973). For $Z = 5$ we have for silicon $f_i \sim 1$ and $\nu_i = 1.2 \times 10^{16}\ s^{-1}$. Thus for silicon ions we have (typically):

$$\mu_{si} - 1 \simeq 8.7 \times 10^{-25} n_{si} \tag{7.a}$$

For oxygen $f_i \sim 1$ and $\nu_i = 2.9 \times 10^{15}\ s^{-1}$ ($Z = 5$) and hence:

$$\mu_O - 1 \simeq 1.5 \times 10^{-23} n_O \tag{7.b}$$

So the contribution from the electrons is about two orders of magnitude greater than the atoms or ions (for $Z_{eff} \sim 5$ there is an even greater difference since $n_i = n_e / Z_{eff}$); it is also of the opposite sign. We therefore ignore the ion and neutral contribution to the refractive index of the plasma and take equation (1) as the governing equation.

Finally, ray trajectories can be calculated using geometrical optics as long as the scale length, Δx, of the change in the refractive index, μ, is far greater than the wavelength (Born and Wolf, 1970):

$$|\partial\mu/\partial x| \ll \mu/\lambda \tag{8}$$

For electrons this condition becomes (using equation 3.a):

$$|\partial n_e/\partial x| \ll (2n_c - n_e)/\lambda \tag{9}$$

For $n_e \sim 10^{21}$ cm^{-3} we find:

$$\partial n_e/\partial x \ll 5.2 \times 10^{25} \quad [\text{cm}^{-4}]$$

If we take $\partial x = \Delta x = 100$ μm as the characteristic length, then:

$$\Delta n_e \ll 5.2 \times 10^{23} \quad [\text{cm}^{-3}]$$

which is satisfied in the experiment.

Thus, when analysing the schlieren photographs, one can use Bouger's formula (Born and Wolf, p. 123)

$$r\mu(r)\sin\gamma = constant \tag{10}$$

(where γ is the angle between the ray tangent and the radius vector) to describe the ray trajectory.

5.4.1. Schlieren/ Shadowgraph Measurements

The propagation of light rays through a plasma cylinder at right angles to its axis is discussed in numerous papers (Keilmann 1972, Dödel & Kunz 1975, Schmidt & Rückle 1978) and standard texts (e.g. Huddlestone and Leonard 1965, Lovberg and Griem 1971). In this section we shall use the results from these texts in order to estimate maximum electron number densities in the plasma and to try and estimate whether the density profiles are steep enough to cause refraction of the laser out of the schlieren aperture.

5.4.2. Estimate of the Electron Number Density

Refractive index gradients in the plasma column will cause light rays to be

deviated; since the plasma refractive index is less than one (equation (1)) then the rays will be deviated *away* from their original path. The angle through which they are deviated is a function of the density profile. The maximum of this deviation angle, α_{max}, is proportional to the maximum density in the plasma cylinder, $\hat{n}_e$ (Schmidt & Rückle, 1978):

$$\alpha_{max} = C_1 \hat{n}_e / n_c \qquad (11)$$

C_1 is proportional to the integral of the density profile along the ray's trajectory. α_{max} does not depend on the plasma dimensions but it is dependent (through C_1) on the density profile. In their paper, Schmidt and Rückle evaluate C_1 for a variety of normalised density profiles (see also Keilmann, 1972).

Figure 5.9.a is a schematic of the schlieren set−up, showing the beam deviation in the plasma. The maximum density that can be measured is defined by the diameter of the schlieren aperture, φ_s, since this defines the maximum schlieren angle, α_s:

$$\varphi_s / 2 = f\alpha_s \qquad (12)$$

where f is the focal length of the imaging lens.

Taking the experimental values given in figure 5.9.a we find:

$$\alpha_s = 7.5 \times 10^{-3} \qquad [\text{rad}]$$

Hence, from equation (11) the maximum detectable electron density is:

$$\hat{n}_e = 1.7 \times 10^{19} / C_1$$

Schmidt and Rückle give $C_1 = 1.00$ for the normalised density profile:

$$f(r) = 1 - 0.9(r/R)^2 \qquad (13)$$

where R is such that $n_e(R) = 0.1\hat{n}_e$ (figure 5.9.b, curve A). In this case:

$$\hat{n}_e = 1.7 \times 10^{19} \qquad [\text{cm}^{-3}]$$

This means that for the above electron density profile no laser light will be refracted out of the schlieren aperture if the maximum electron density is less than

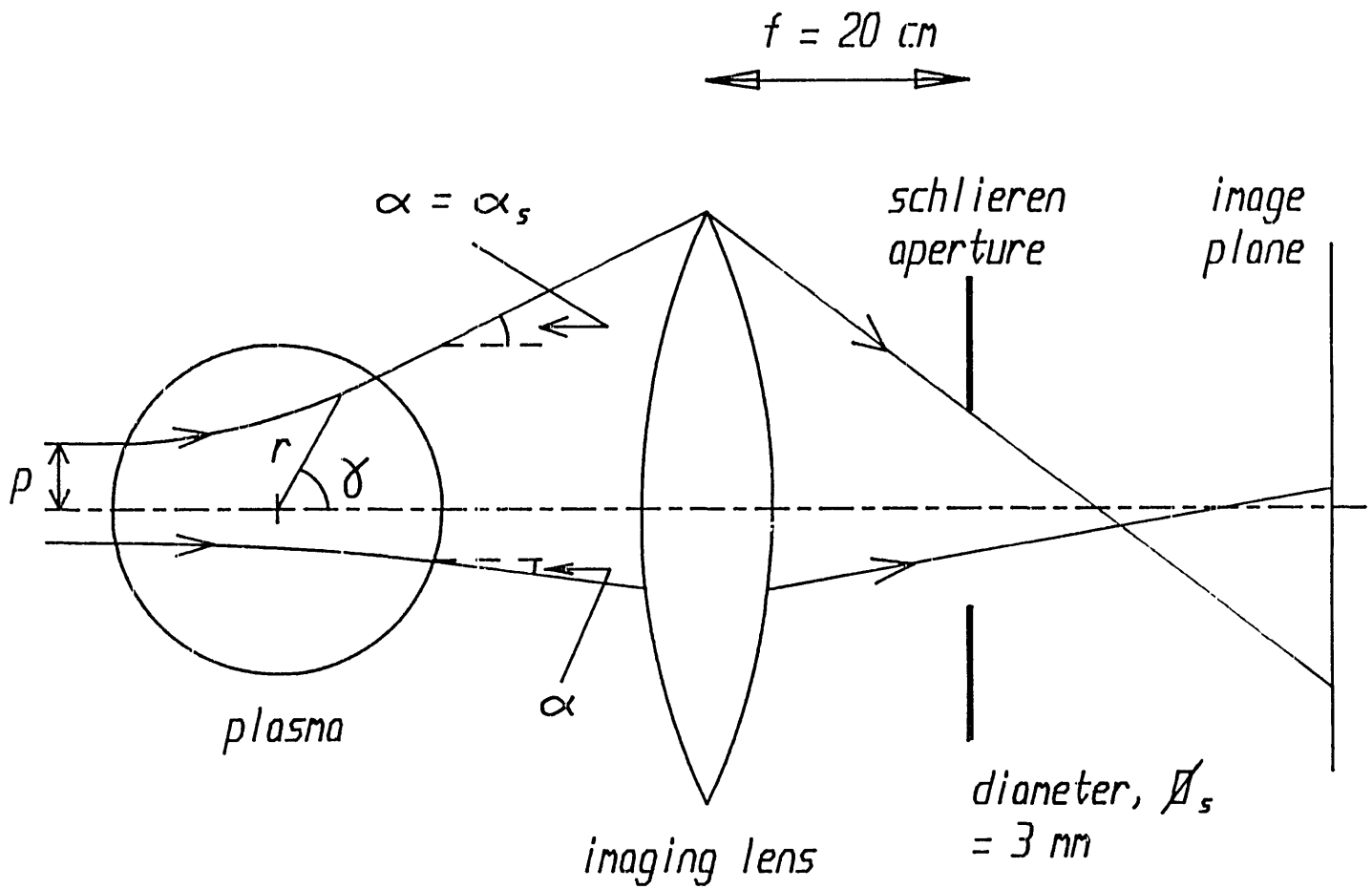


Figure 5.9.a: Schlieren set-up showing beam deviation in the plasma

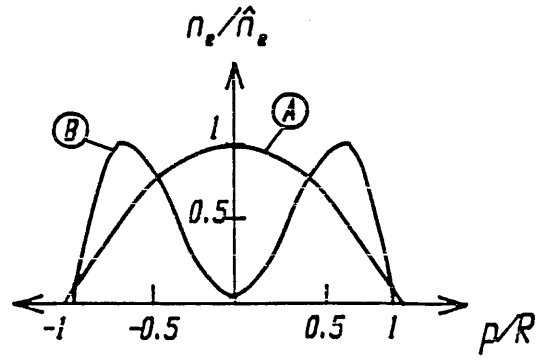


Figure 5.9.b: Normalised density profiles

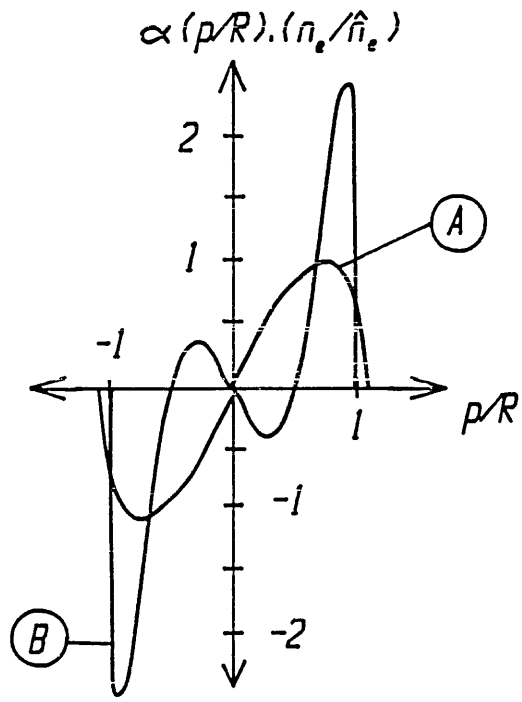


Figure 5.9.c: Deviation angle profiles for the density profiles in figure 5.9.b

the above figure.

As the electron density profile gets steeper at the plasma boundary (i.e. n_e peaks at the edge of the plasma column) the value of C_1 increases. For the profile depicted in figure 5.9.b (curve B), where the percentage dip in the elctron density at the centre is *96%*, the value of C_1 is *2.36*. Hence:

$$\hat{n}_e = 7.3 \times 10^{18} \qquad [\text{cm}^{-3}]$$

Figure 5.9.c shows the deviation angle as a function of normalised radius for the profiles discussed above. Note is that there is always a region close to the axis of the plasma column through which the light is only refracted by a very small amount and hence passes through the schlieren aperture, whilst along the axis itself there is no refraction at all.

5.4.3. Is the Laser Refracted or Absorbed?

We can also examine whether a ray passing through the low density outer plasma (as seen in the reconstructed holograms) will be refracted out of the schlieren aperture. As the ray passes through this plasma it always sees a component of the density gradient and so is continuously refracted. The amount of deviation is expressed through:

$$1/R = (1/\mu)\underline{\nabla}.(\mu\underline{\hat{n}}) \qquad (14)$$

where R is the radius of curvature of the deviation

$\underline{\hat{n}}$ is a unit vector perpendicular to the ray.

Since the experimental geometry is cylindrical, then the ray trajectory has to be described using cylindrical coordinates. The solution of equation (14) in such a geometry can be found in standard texts (Schmidt and Rückle, Keilmann, etc.). For the present purpose it is sufficient to treat the problem in planar geometry. Thus, if the refractive index gradient is $\partial\mu/\partial y$ in the y−direction and the ray is travelling in the x−direction then the angular deviation is:

$$\Theta_y = \int_0^L \frac{1}{\mu}\frac{\partial\mu}{\partial y}\, dx \qquad (15)$$

where L is the characteristic length which the ray traverses.

If we approximate the integral over dx as being equal to L, and substituting for μ and $\partial\mu/\partial y$ (and noting that $n_e/n_c \ll 1$) we get:

$$\Theta_y \simeq -\frac{1}{2n_c}\frac{\partial n_e}{\partial y} L \qquad (16)$$

The minus sign indicates that the refraction is in the opposite direction to the number density gradient.

Taking Θ_y = schlieren angle, $\alpha_s = 7.5 \times 10^{-3}$ rad and a scale length, $L=100$ μm we find:

$$\partial n_e/\partial y \simeq 3.5 \times 10^{21} \qquad [\mathrm{cm}^{-3}/\mathrm{cm}]$$

Since the measured density (from the reconstructed holograms) at the core edge is 3.0×10^{18} cm^{-3} it means that, for the outer plasma to cause the laser to be refracted out of the schlieren aperture, then the density must drop sharply (to essentially $< 10^{16}$ cm^{-3}) over a distance of 10 μm. This clearly not the case in the inferred profile (figure 5.5.a). Indeed, the profile is actually closely described by the normalised analytic function

$$f(r) = 1 - 0.9(r/R)^2$$

which, from computations in cylindrical geometry (Keilmann etc.), is not steep enough to cause refraction out of the aperture employed in the experiment.

5.4.4. The Streaked Shadowgraphs

All the schlieren photographs from early times onwards show no transmission of the laser beam through the plasma, but more importantly there is no transmission through its axis. This implies one of two things:

(a) density gradients transverse to the direction of propagation of the laser beam exist on axis in the fibre;

(b) the laser radiation is absorbed as it traverses the plasma.

Although the $m=0$ instability is azimuthally symmetric, in the fibre plasma these instabilities are seen to move axially and coalesce; in this case the symmetry will probably be destroyed. So situation (a) could certainly exist once the $m=0$ instability had fully developed in its late stages. However, at early times ($t \simeq 20$

ns) the perturbations are small and do show cylindrical symmetry; so the former situation is not the case. Thus situation (b) remains the only explanation for the schlieren photographs. Even if a large enough electron density to cause refraction has developed at such early times such a density will lead to significant absorption of the laser (see later, section *5.4.9.*).

However, one must remember that the photograph of the reference fibre shows that there is no transmission of the laser through the fibre. Although this is most probably due to the Polaroid film not being able to resolve the small central region which allows transmission, the possibility remains that if the fibre is not fully ionised and there is a solid core in the centre of the plasma then the laser will still not be seen at the centre of the schlieren photographs.

The streaked shadowgraphs also show no transmission of the laser through the plasma. In this instance a schlieren aperture was not used and so the exit window of the chamber becomes effectively that aperture. The schlieren angle defined by the exit window is :

$$\alpha_s = \varphi_w / 2u \qquad (17)$$

where φ_w is the window diameter and u is the distance from the fibre to the window.

In the experiment $\varphi_w = 70$ mm, $u = 220$ mm; thus:

$$\alpha_s = 57 \times 10^{-3} \qquad \text{[rad]}$$

This allows one to detect a maximum electron number density of about 1×10^{20} cm^{-3}, which is an order of magnitude greater than in the previous cases (with the schlieren aperture in place). Although the streaked pictures show an $m=0$ instability (and one could argue that situation (a) might be valid at this time) they also show part of the fibre core and again there is no transmission of the laser through that. So the streaked photographs seem to confirm that the laser is indeed being absorbed by the plasma.

5.4.5. Holographic Interferometry Measurements

Analysis of the reconstructed holograms yields quantitative electron number density profiles. In this section we look at how this information can be recovered from the reconstructed holograms by means of the inverse Abel transform. From the number density profiles one can estimate how much of the fibre has been

ionised and also discuss how the plasma might be evolving.

5.4.6. The Abel Transform and its Inverse

The quantity of primary interest in the interferometry of transparent media is the optical pathlength Φ of a ray through the medium. This is defined as:

$$\Phi = \int_{\ell} \mu d\ell \tag{18}$$

which is the path integral of the refractive index along the ray ($d\ell$ is an element of the path length of the traversing ray).

The effective change due to the plasma, in units of fringe spacing, F, is:

$$F = \int_{\ell} (\mu - 1)\frac{d\ell}{\lambda} \tag{19}$$

Figure 5.10 depicts an optical ray travelling in the x−direction through a radially symmetric plasma column (assuming no refraction).

Since the element of the ray path length, dx, is given by

$$dx = d(r^2 - y^2)^{\frac{1}{2}} = (r^2 - y^2)^{-\frac{1}{2}}\, rdr \tag{20}$$

then equation (19) becomes:

$$F(y)\lambda = 2\int_{r=y}^{R} \frac{rf(r)}{(r^2 - y^2)^{\frac{1}{2}}}\, dr \tag{21}$$

where $\mu - 1 = f(r)$ for a radially symmetric object.

In many cases phase objects decay smoothly to zero at large radii (i.e. there are no discontinuities). Hence equation (21) can be rewritten as:

$$F(y)\lambda = 2\int_{r=y}^{\infty} \frac{rf(r)}{(r^2 - y^2)^{\frac{1}{2}}}\, dr \tag{22}$$

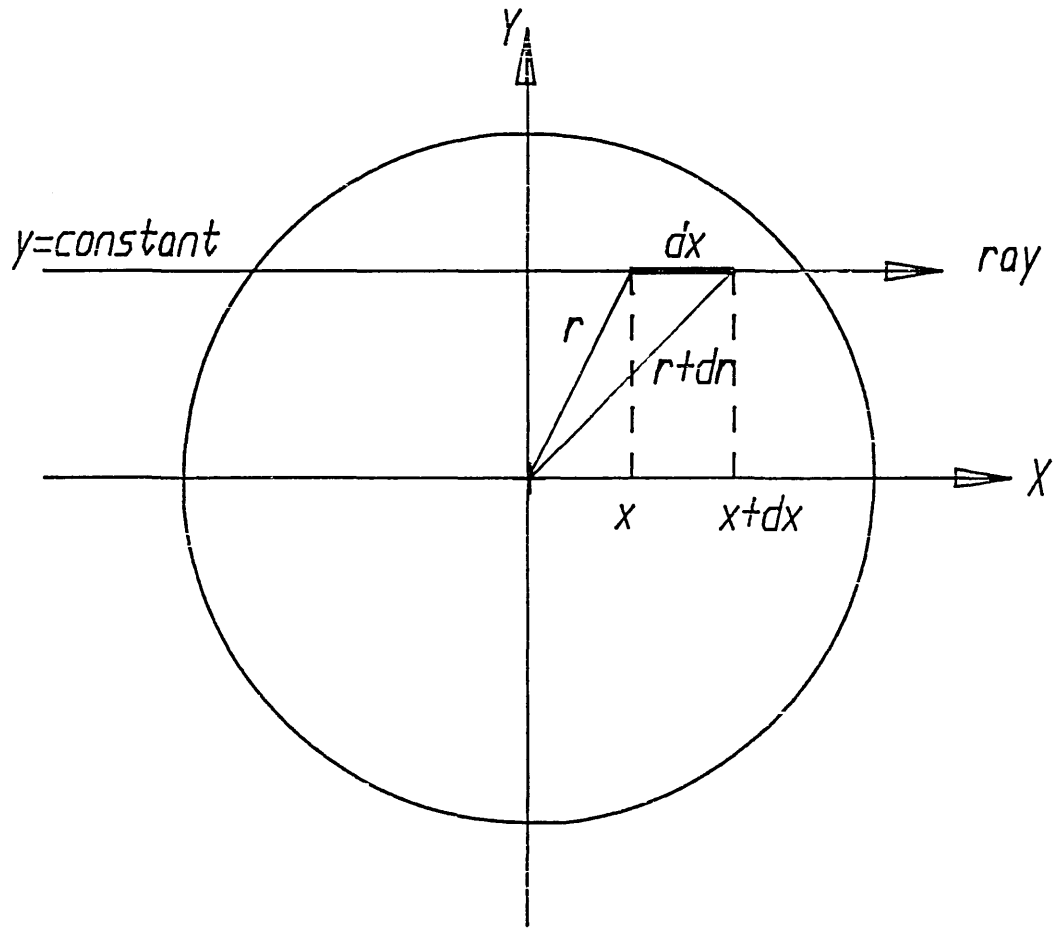


Figure 5.10: Geometry of a ray travelling through a radially symmetric plasma column (assuming no refraction)

The right hand side of equation (22) is known as the Abel transform of $f(r)$. To recover the function $f(r)$ one has to take the inverse of equation (22):

$$f(r) = -\frac{\lambda}{\pi}\int_{y=r}^{\infty}\frac{(dF/dy)}{(y^2 - r^2)^{\frac{1}{2}}}\,dy \qquad (23)$$

So the shift of fringes observed in the reconstructed hologram gives one information on the radial distribution of the electron density.

It has been found by computer simulation that (even for strong refraction) the errors due to refraction are quite small if equation (23) is used to invert data obtained by focussing on the centre plane containing the axis of symmetry (Vest, 1975).

A computer program was written to solve equation (23) numerically for the different fringe profiles obtained from reconstructed holograms (this is discussed in Appendix B). The integration was carried out from the radius of the central core (where no laser is transmitted) out to where the fringe shifts become negligible. This was the procedure used to obtain the electron number density profiles of figures 5.7 and 5.8.

5.4.7. Is the Fibre Fully Ionised?

By integrating the fringe shift over the whole area viewed, the total number of electrons responsible for the shift of fringes can be deduced (no assumption has to be made concerning the shape of the electron density profile – see e.g. Gatenby and Walker, 1979). This can be seen by combining equations (3.b) and (19) to give:

$$F = -K\int n_e d\ell \qquad (24)$$

where $K = 2.16 \times 10^{-22}/\lambda$.

Thus, integrating the fringe shift over the viewed area gives:

$$\iint F dx dy = -K\iint[\int n_e d\ell]dx dy = N_e^{tot} \qquad (25)$$

where N_e^{tot} is the total number of electrons.

For the profile in figure 5.7 one finds that:

$$N_e^{tot} = 4.0 \times 10^{15} \qquad \text{[electrons]}$$

This is the number of electrons responsible for the fringe pattern in the area of view of the hologram. Since the fringe pattern is independent (almost) of the position along the fibre (in this viewed area) we assume a uniform axial distribution of electrons. Thus the calculated electron line density is:

$$N_e = 2.0 \times 10^{17} \qquad [\mathrm{m}^{-1}]$$

The core region seen in the reconstructed holograms is larger than the initial fibre diameter. This means that part of this region, if not all of it, is dense plasma. Even though one cannot measure the number density of this plasma it is nevertheless interesting to estimate an average density in the core.

Assume that the Bennett equation applies within this core region. The temperature estimated at this time is *10* eV (Chapter 4). Taking a current of *40* kA and an effective Z of *2* we estimate an average line density of:

$$\bar{N} = 3.5 \times 10^{19} \qquad [\mathrm{m}^{-1}]$$

This is two orders of magnitude higher than that measured in the coronal plasma. The average density of the core can thus be estimated from:

$$\bar{n} = \bar{N} / \pi r^2 \qquad (26)$$

Using $r = 125$ μm (from figure 5.7) and the above value for $\bar{N}$ we find:

$$\bar{n} = 7.8 \times 10^{20} \qquad [\mathrm{cm}^{-3}]$$

This itself is two orders of magnitude smaller than the solid density and indicates that the fibre is not fully ionised.

It is also worthwhile to consider a simple picture of the fibre at early times and to estimate the amount of ionisation; take the hologram of figure 5.5.a with the reconstructed electron density profile of figure 5.7. If we take the best case that in the coronal plasma the number of ions is equal to the number of electrons then the total mass in this coronal plasma is:

$$m_p = N_i^{tot} \times m_i \qquad \text{[kg]} \qquad (27)$$

$$\therefore \quad m_p = 1.33 \times 10^{-10} \quad [\text{kg}]$$

The original mass of the fibre was:

$$m_o = 5.40 \times 10^{-7} \quad [\text{kg}]$$

(where the density of SiO_2 is $\rho = 2.20$ g/cc).

So only a small fraction ($\sim 2.5 \times 10^{-4}$) of the original fibre mass comprises the coronal plasma.

5.4.8. Instabilities, Refraction and Plasma Evolution

It has already been noted that the hologram in figure 5.5.a does not show any instabilities along its length. One then cannot comment on the schlieren pictures taken at the same time during the discharge. We thus see that at this late time the density of the plasma at the core edge is quite high. The instabilities themselves have an even higher density. At these high densities the laser would be refracted out of the schlieren aperture (if not absorbed). This is then consistent with the schlieren photographs.

However, the hologram in figure 5.6.b shows a region at the centre of the instability through which the laser is not transmitted and this can only be due to absorption of the laser and not refraction.

Also notice that within the general envelope of the high density perturbed region there appear to be two instabilities close together. This is unusual if one assumes that the $m=0$ instabilities are stationary during the discharge. However, if they actually move, then it is very possible for two of them to coalesce after a certain time and to appear in pairs. This behaviour is observed in the optical framing photographs.

One feature of the holograms at late times is that a very well-defined central core is present along the fibre length. The diameter of this core region is ~ 170 μm, which is less than the diameter observed in the hologram at $t=17$ ns. One might draw the following picture:

The initial stages of the plasma formation are a surface phenomenon, with only a small fraction of the fibre contributing to the plasma. In time, more and more of the fibre will be accreted into this plasma. This will be cold compared to the outer regions of the plasma which are being heated by the discharge current. Thus these outer layers expand rapidly compared to further inside the

plasma i.e. it looks as is if the outer layers are 'blown off'.

The additional presence of an $m=0$ instability means that mass is also transported from the necked regions of the plasma to the instabilities. Indeed, an increase in number density is observed in going from a necked region to a region of instability. So it is quite reasonable to expect to see, at late times, a core region that is smaller than at earlier times in the discharge.

It is tempting to say that the well-defined nature of the core indicates a residual unperturbed solid core within it. A simple analysis (as in the case of the hologram at $t=17$ ns) is not feasible because of the lack of data close to centre of the instabilities (and so one does not know how much mass they comprise). What the hologram does show is that a large fraction of the original fibre mass still resides in the core region and that the ablation of this mass is occurring even at late times.

In all the reconstructed holograms we see that the core is larger than the initial fibre diameter; this means that there is dense plasma in this core. One can estimate the lower value that this density might take. This is the density at which the laser is refracted out of the exit window of the pinch chamber. The schlieren angle defined by the exit window is

$$\alpha_s = 57 \times 10^{-3} \quad [\text{rad}]$$

Thus, from equation (9) the maximum density detectable (for $C_1 = 1$) is

$$\hat{n}_e = 3.1 \times 10^{20} \qquad [\text{cm}^{-3}]$$

This agrees well with the average density calculated earlier in the chapter. So although the number density within the core cannot be measured, the above calculations place a lower limit on the value that it must have.

5.4.9. A Further Discussion about Blackbodies

The conditions needed for the plasma to radiate as a blackbody were discussed in Chapter 4. An electron number density between $5 \times 10^{18} - 10^{19}$ cm^{-3} (at a temperature of less than ~ 30 eV) is needed for LTE to be established and for the plasma to be optically thick such that the Planck function is a valid description for the plasma radiation.

From the holographic interferometry measurements the plasma seen outside the

central core region is not dense enough to be optically thick or in LTE and so the radiation emitted by it is not blackbody.

However, there is evidence that the central core region does fulfil the necessary conditions. Firstly, at early times, the diameter of the luminous plasma as measured from the optical streak photographs (e.g. at $t=17$ ns, $\varphi \simeq 230$ μm) is approximately the same as the central core seen in the holographic interferograms ($\varphi \simeq 250$ μm at the same time). The central core has a minimum electron number density of $\sim 3 \times 10^{20}$ cm^{-3} and this is high enough for LTE to be valid at temperatures of ~ 10 eV.

Secondly, (if refraction is neglected) the absorption of the ruby laser places a lower limit on the electron density within the core region. The main process by which a laser is absorbed in a plasma is by inverse bremsstrahlung; the absorption coefficient for this process is given by the following expression (c.g.s. units, NRL Plasma Formulary, 1986):

$$\kappa = AZn_e^2 ln\Lambda T^{-3/2}\omega^{-2}(1 - \omega_p^2/\omega^2)^{\frac{1}{2}} \qquad (28)$$

where $A = 3.1 \times 10^{-7}$ [c.g.s]

$\omega_p^2 = n_e e^2/m_e\epsilon_0$ is the electron plasma frequency

ω is the angular frequency of the laser.

Putting in the experimental values and taking $\ell = 0.01$ cm (100 μm) we find that for $\kappa\ell \gg 1$ then the electron density must satisfy:

$$n_e \gg 5.0 \times 10^{19} \qquad [\text{cm}^{-3}]$$

Under these conditions the radiation from the plasma will certainly be blackbody.

5.5. *Conclusions*

The schlieren photographs taken of the fibre plasma confirm the fact that the $m=0$ instability is already well-developed within the first 17 ns of current flow. Subsequent photographs show that the instabilities move axially and merge together, as is observed in the optical photographs. However, even well after current peak a well-defined core region is still observed. This is shown very clearly in the holograms taken at these later times and indicates that a substantial amount of the original fibre mass still resides within the core.

The axial motion of the instabilities which was observed in the optical photographs is confirmed in both the schlieren photographs and the holograms, where the movement within the duration of the laser pulse gives the instabilities a 'disc−like' appearance. Since the curvature of some 'discs' is in the opposite direction to others, this implies that the movement is in both axial directions.

Measurements of the electron number density show that there is a dense plasma core surrounded by a low density coronal plasma and that this core persists even after peak current has been reached. The observed increase in the number density as one moves from a necked region of the plasma to an instability confirms the idea that there is axial plasma flow out of the necked regions and into the unstable ones. This ejection of plasma has also been observed in other experiments.

The results presented in this chapter show that it is a valid assumption that the plasma radiates as a blackbody in the optical region of the electromagnetic spectrum. The lack of transmission of the laser through a central core region of the plasma, especially through the axis, indicates that there must be high density plasma present in that region. This is true whether the reason for the lack of transmission is absorption of the laser beam or complete refraction of it out of the exit window of the load chamber. The minimum density that must be present in the core region is high enough for the plasma to radiate as a blackbody at the calculated temperature of $10 - 30$ eV. Thus, the calculation of the electron temperature based on observing the optical emission from the plasma is accurate.

CHAPTER SIX

X−ray Diagnostics

6.1. Introduction

High temperature plasmas ($T > 100$ eV) emit a substantial amount of energy in the form of X−rays. Such high temperature plasmas are of primary interest for fusion power generation. Measurements of the X−ray emission (spectra, intensities, time history and source size) yield information on the conditions (density, temperature, state of ionisation) within the plasma (see e.g. Nagel 1974, De Michelis and Mattioli 1981). Such measurements also characterise the plasma as an X−ray source for other possible applications (e.g. X−ray laser research, X−ray lithography etc.).

Various methods exist for diagnosing the X−ray emission from a plasma. X−ray spectroscopy ranges from using high resolution crystal spectrometers to estimate electron temperature (from line intensity ratios), electron density (from line widths) and the state of ionisation of the plasma, to lower resolution spectroscopy using absorbing K−edge or matched (Ross) filters in different wavelength regions to determine the electron temperature.

The amount of energy lost in the X−ray region can be measured using passive (e.g. X−ray film) or active (e.g. X−ray or PIN diodes) detectors. Temporal evolution of the X−ray emission can be followed with X−ray streak cameras or with a fast scintillator/optical streak camera arrangement (Challis, Ph.D. Thesis, 1986). The extent of the plasma volume emitting X−rays can be determined using Fresnel lenses or more simply using filters together with a pinhole to yield an X−ray image. The various instrumentation used for X−ray diagnostics of plasmas can be found in a review by Violet (1974).

In this thesis, X−ray pinhole photography together with the filtered PIN diode technique on the glass fibre Z−pinch is reported. The time−integrated photographs provide information about the spatial distribution of the plasma and an estimate of the energy of the emitted X−rays. The nature and cause of X−ray emission observed from the electrodes is also analysed and discussed. Time−resolved information about the plasma evolution is available from the filtered PIN diode measurements which also provide an estimate of the electron temperature in the plasma.

6.2. The Experimental Arrangement

6.2.1. The X-ray Pinhole Camera

The spatial extent of the X-ray emitting plasma is determined using a pinhole camera. Figure 6.1 shows the principle of the camera. The spatial resolution is limited by the pinhole. A point source at the object distance u will produce a uniform disc image at the image distance v. The diameter of this disc is:

$$d = w(1 + m) \tag{1}$$

where w is the pinhole diameter

m is the magnification $= v/u$.

The 'blurring' of this image is then:

$$d/D_i = (1 + 1/m)w/D_o \tag{2}$$

where $D_{i,o}$ are the image/object sizes.

Thus it is proportional to the pinhole size but decreases as m is made larger. The image size is related to the object size through:

$$D_i = mD_o + d \tag{3}$$

This allows one to compensate for the finite pinhole size when estimating the size of the object from the pinhole photographs.

Figure 6.2 is a schematic showing the X-ray pinhole arrangement. A filtered, double pinhole system was used. This yields some data on the energy of the emitted X-rays. The magnification of the camera was *0.3*. The pinholes were made from platinum and the different diameters used were *470* μm, *100* μm, *50* μm and *20* μm. The recording medium was Kodak DEF-392 X-ray film. This has a very low background fog level ($\simeq$ *0.09 - 0.15* ND - see Rockett *et al*, 1985) and is suitable for recording low flux images.

6.2.2. X-ray PIN Diodes

Figure 6.3 shows a schematic of the PIN diode arrangement. Up to four

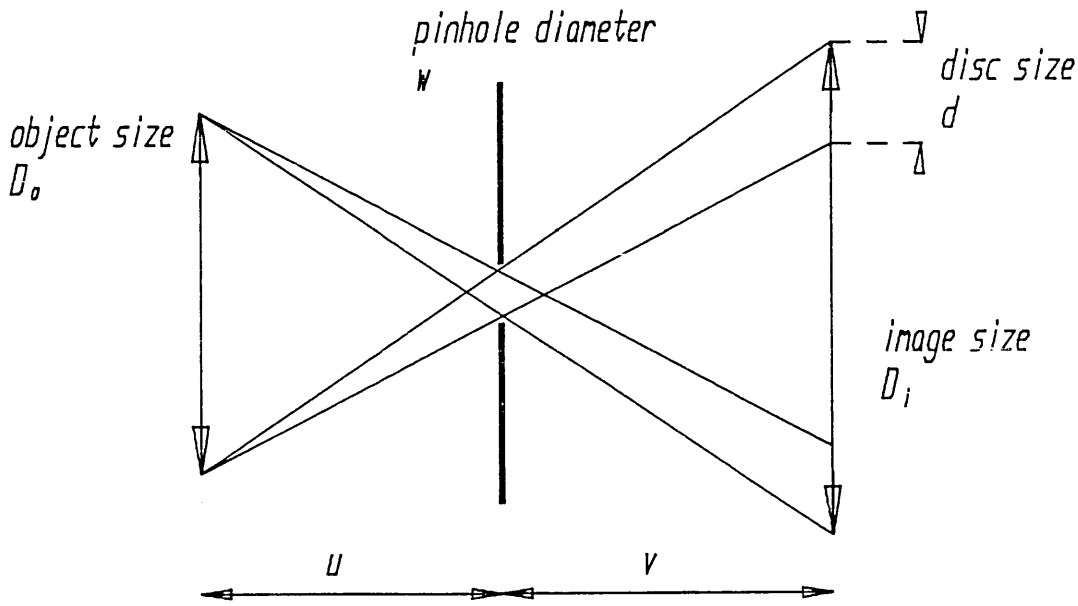


Figure 6.1: The pinhole camera

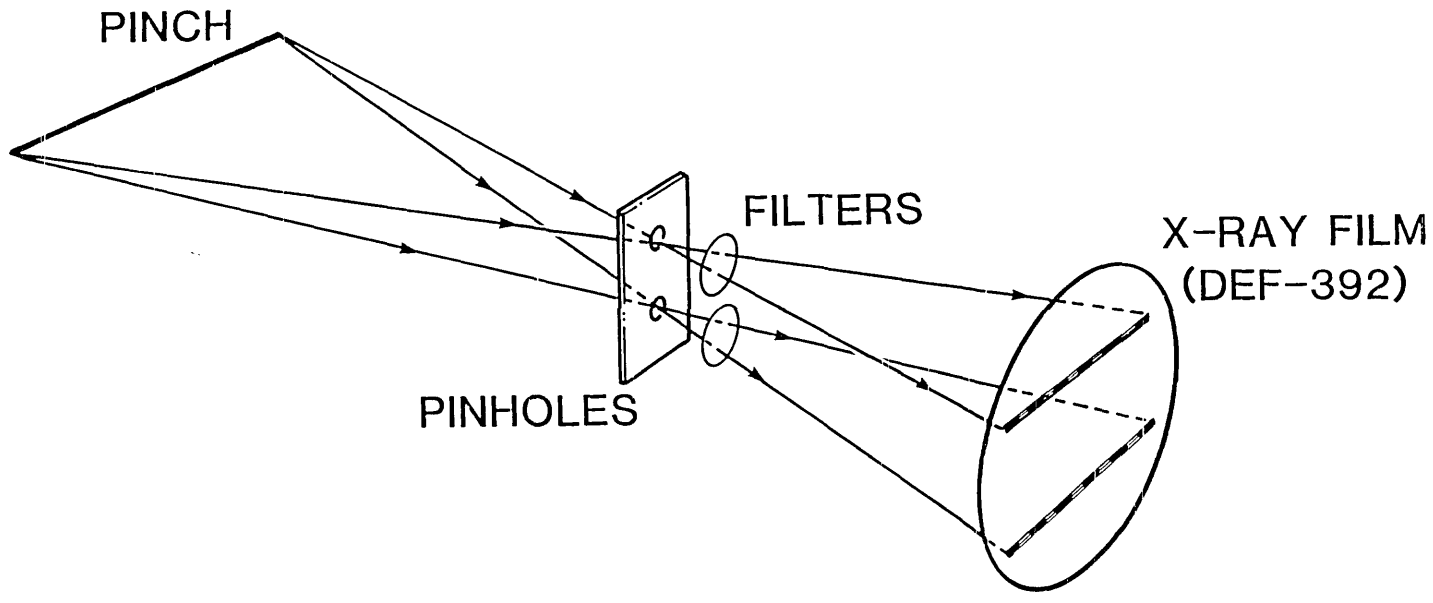


Figure 6.2: Schematic of the filtered pinhole arrangement

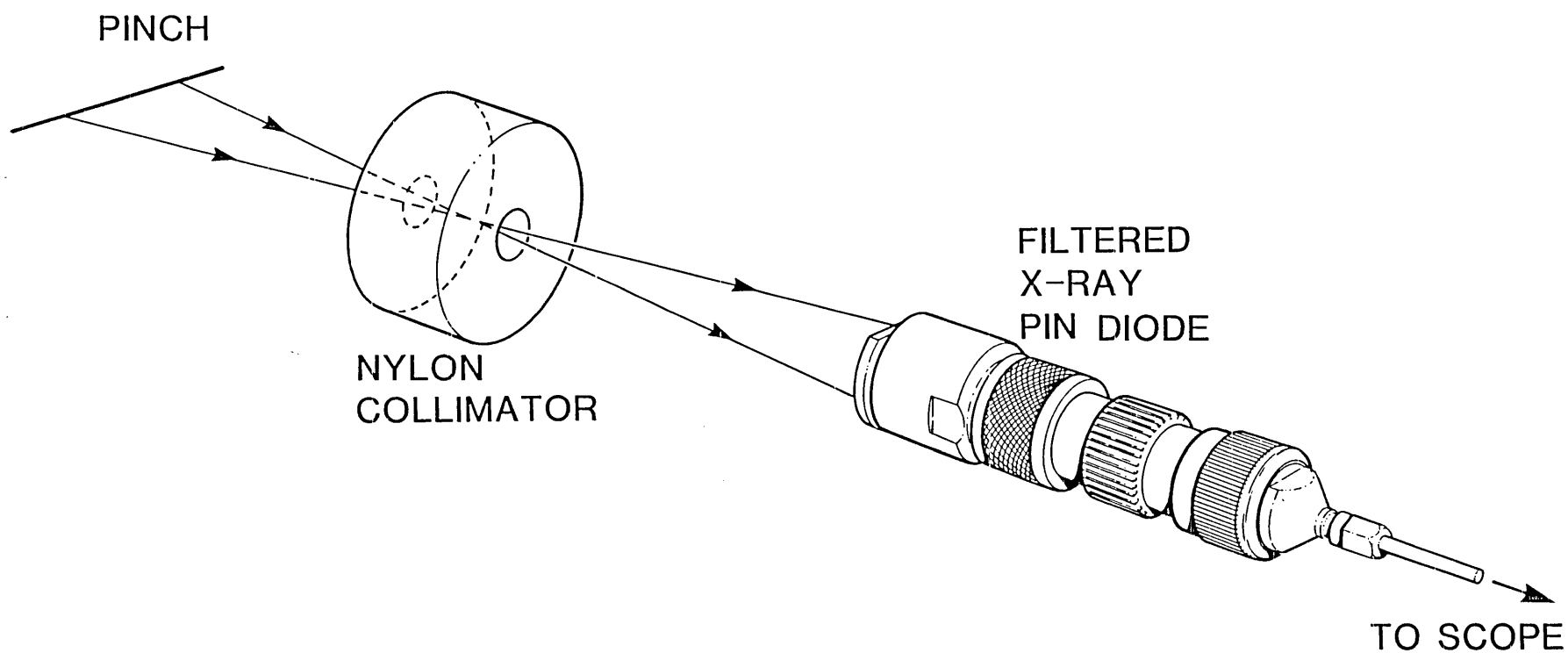


Figure 6.3: Schematic of the PIN diode arrangement

diodes, each with a different filter combination, were used to monitor the X−ray output of the plasma. The diodes used were silicon $p-i-n$ devices (Quantrad). They have a time resolution of ~ *1* ns − a detailed description of the operation of these devices is given by Deeney (Ph.D. Thesis, 1988).

The four diodes were filtered to look at the following:

(a) evolution of hard X−rays, $E > 10$ keV;

(b) existence and history of the silicon K−shell line emission and recombination continuum;

(c) radiation in the *1* − *2* keV range.

Nylon collimators, *35* mm thick, looking at *60* − *70%* of the fibre were used (see figure 6.3) to filter out the electrode X−rays in order to examine the plasma in isolation.

6.2.3. X−ray Film and Filters

Figure 6.4 shows the sensitivity of Kodak−DEF film as a function of incident photon energy. This is taken from published data of Rockett *et al* (1985). The sensitivity is measured as a ratio of photons/cm^2 per density unit needed to achieve a diffuse density of *0.1*, *1.0* and *2.0*. The DEF film itself is composed of a plastic substrate upon which X−ray sensitive material is deposited. For the purposes of calculating its transmission, the film can be treated as a layer of *205* μm mylar.

Figure 6.5 shows the transmission characteristics of the filters used to produce the image in figure 6.8.a.(i) (*3* μm aluminium). There is a decrease in transmission of two orders of magnitude at $\lambda \simeq 6$ Å ($E \simeq 2$ keV). The combination of the aluminium filter and the X−ray film layer allows an estimate of the energy of the photons to made.

The transmission characteristics of the filtering plus PIN diode response are shown in figure 6.6. The effect of the different thickness collimators is also shown. As can be seen the combination of Ti and Al allows one to monitor the appearance of the Si K−shell radiation which lies at $\lambda \sim 6.7$ Å. The mylar filter supplements these filters and an accurate picture is built up of the plasma emission. The Cu filtered PIN diode was used to monitor the presence of hard ($E \sim 10$ keV) X−rays.

Table 6.1 lists the relevant K−shell wavelengths and corresponding energies (see e.g. Kaye and Laby, 1986) for the main components of the electrodes (anode − stainless steel: Fe *75%*, Cr *15%*, Ni *10%*; cathode − brass: Cu, Zn) together

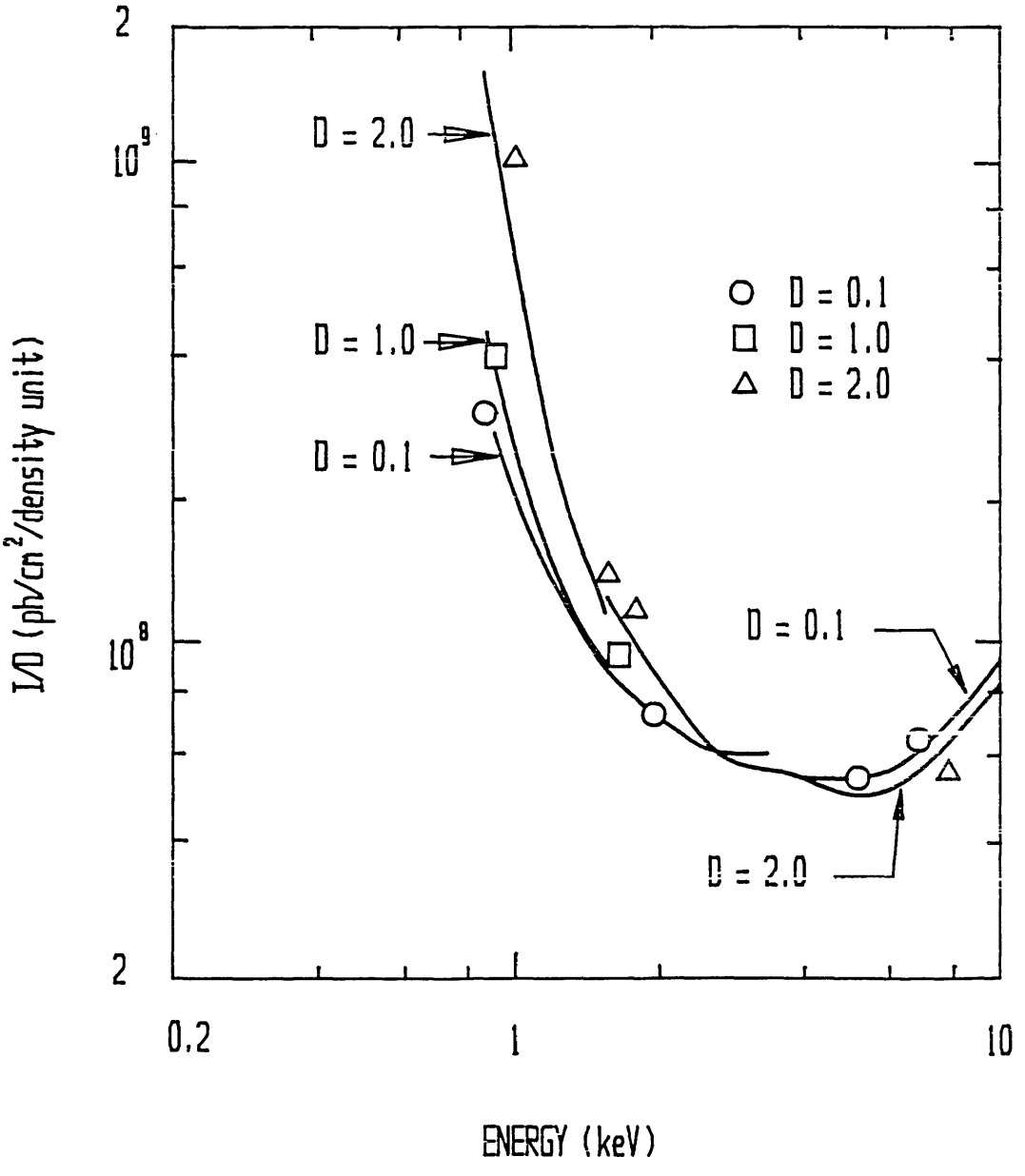


Figure 6.4: Sensitivity of Kodak DEF film

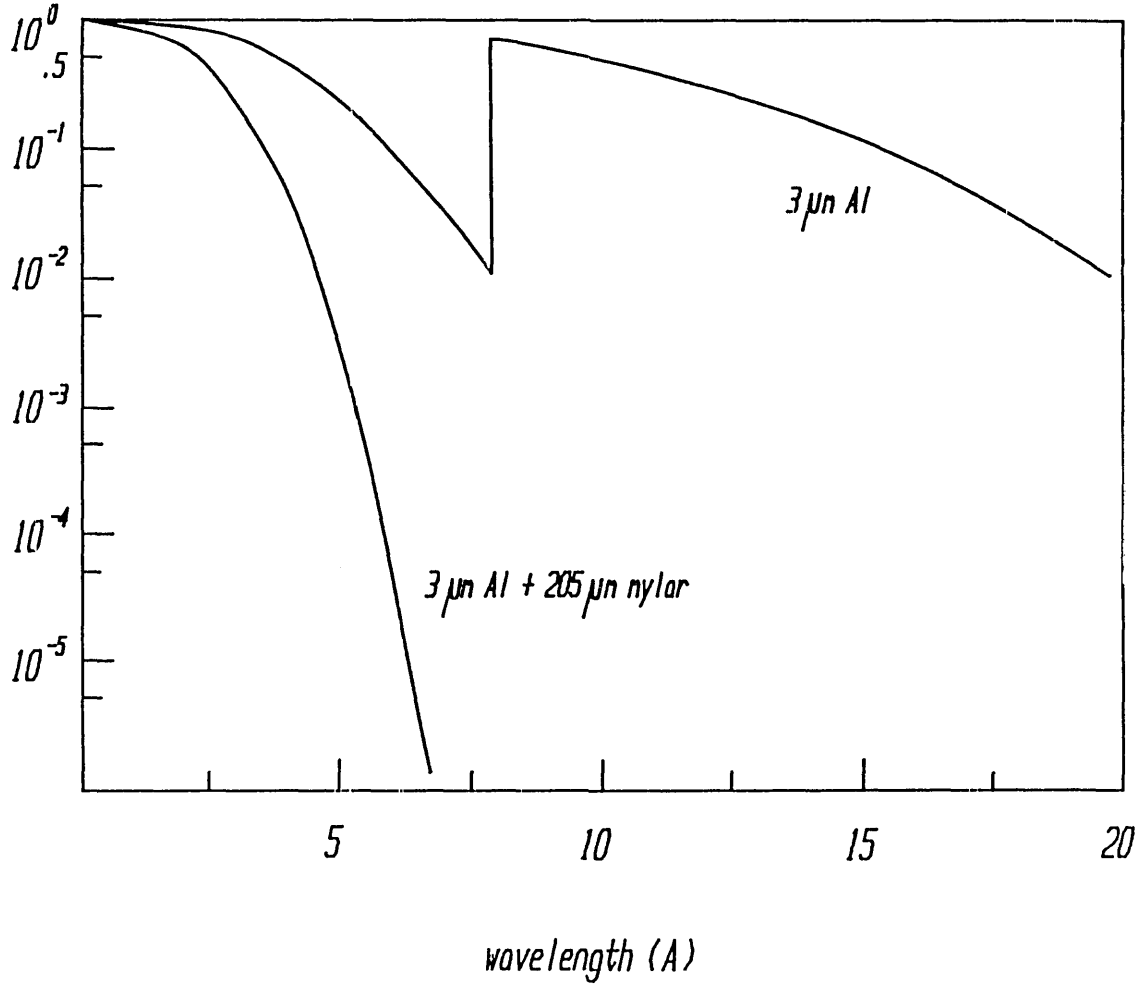


Figure 6.5: Transmission of 3 μm aluminium and the film layer

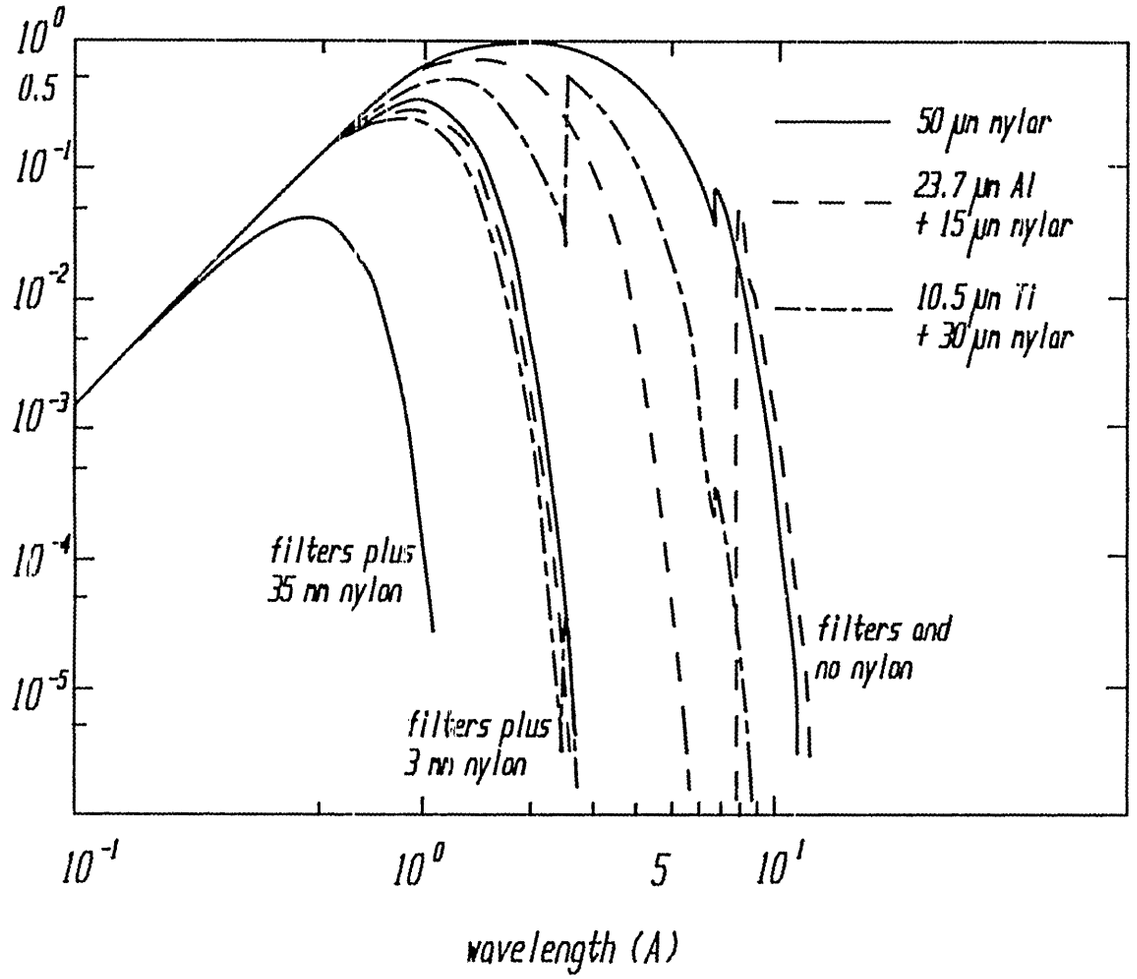


Figure 6.6: Filter transmissions incorporating PIN diode response

with the K−edge energies of the filters (Al, Ti and Cu). Also included is the K−edge of oxygen.

Table 6.1: *K−shell energies for the electrodes and filters*

element	*K−edge*		L_1 *−edge*	
	λ *(Å)*	*E (keV)*	λ *(Å)*	*E (keV)*
Al	7.93	1.56		
Ti	2.50	4.96	23.40	0.530
Si	6.73	1.84		
O	23.33	0.531		
Fe	1.74	7.12	14.65	0.846
Cr	2.07	5.99	17.86	0.694
Ni	1.49	8.32	12.20	1.02
Cu	1.38	8.98	11.17	1.11
Zn	1.28	9.68	10.26	1.21

The *35* mm nylon collimator effectively cuts off any radiation above ~ *1* Å (figure 6.6). This is just below the limit of the electrode K−shell energies. To be absolutely sure of eliminating such X−rays and fluorescence within the collimator it is advisable to put a high Z material behind the collimator.

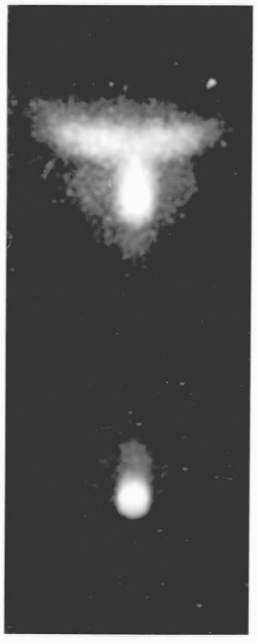
Meanwhile, Table 6.2 is a list of the important silicon lines in the wavelength region of interest (e.g. Scofield, 1985).

Table 6.2: *Important Silicon lines below 40 Å*

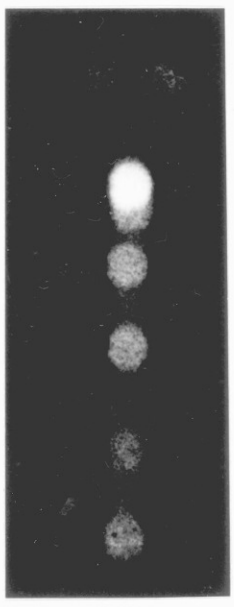
Silicon XIV	*ground state: 1s* $^2S_{1/2}$	
configuration	λ *(Å)*	*E (keV)*
1s−6p	4.770	2.597
1s−5p	4.831	2.565
1s−4p	4.947	2.505
1s−3p	5.217	2.375
1s−2p	6.182	2.004
2−7	20.21	0.613
2−6	20.88	0.593
2−5	22.09	0.561
2−4	24.74	0.501
2−3	33.39	0.371

6.3. The Observations

For all the X−ray measurements the initial fibre diameter was *125* μm. Initially, *470* μm diameter pinholes were used to look at the plasma. One pinhole was filtered with *2.5* μm kimfoil, the other with *2.5* μm kimfoil + *2.5* μm aluminised mylar (the aluminium thickness being *400* Å); a double film layer was used with the first layer acting as an additional *205* μm mylar filter for the second piece of film. Figure 6.7.a shows the resulting images. The first layer was totally overexposed and the images shown are those on the second layer. The anode is clearly seen and there are two intense regions, one at each electrode, with the



(a)



(b)

Figure 6.7: X-ray pinhole images using 470 μm pinholes

region at the anode being the more intense one. A fainter image of the fibre is also visible and this will be referred to as the core.

The filters were then changed to *3* μm aluminium for one pinhole and *11.85* μm aluminium for the other, still keeping the same diameter pinholes. Figure 6.7.b shows the result from the next discharge. The image from one pinhole was lost because of fogging. However, the other image shows a faint core with a number of bright localised regions along its length. There are six such regions being ~ *700* μm in diameter. The uniformity and appearance of these regions suggests that the image is pinhole limited. Also visible is the anode. This can also be seen on the second film layer. However, the localised bright regions are no longer visible hence the photons from these regions have been absorbed in the first layer. In contrast the core, though much fainter, is still imaged onto the second layer.

Keeping the same filter pair, *100* μm diameter pinholes were then introduced. Figure 6.8.a shows the resulting images. The images on the first film layer still show an axial structure but the localised regions are now much smaller in size (~ *150* μm in diameter). Again, no axial structure is seen on the second layer but a faint core, together with electrode emission, is visible.

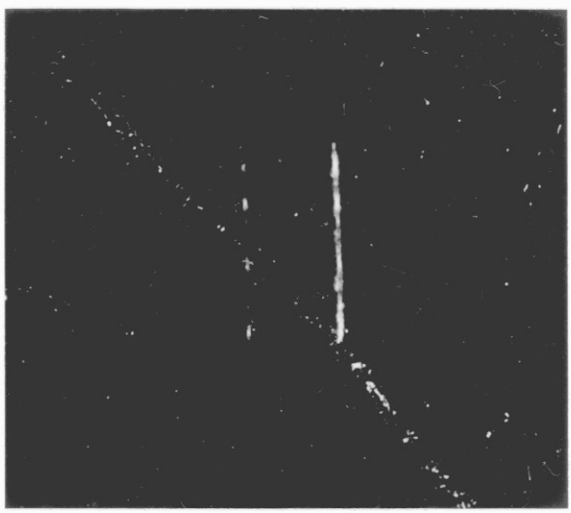
The above images were recorded on old (~ *3* years) DEF film and thus the background film density was high. Quoted figures for the increase in film density for Kodak−DEF are ~ *0.45* ND per *15* months (Rockett *et al*, 1985). Subsequent images were recorded on fresh DEF film.

A new pinhole pair was now employed − *50* μm and *20* μm diameter. The former pinhole was filtered by two layers of *2.5* μm aluminised mylar and the latter by only one layer of the same material. Now, there was not enough flux to expose a second layer of film. The resulting images are from one film layer only and are shown in figure 6.8.b. Axial structure is clearly evident. The image from the *20* μm pinhole shows four intense localised sources of X−rays (three of which might be composed of two or more smaller sources) and two less intense sources. These regions are slightly larger than the core, which is visible in both images. In the axial direction these sources measure about twice their radial size. It can also be seen that the image from the *50* μm pinhole shows intense emission from both edges of the core. During the time of this emission the plasma appears to be remarkably confined to a well−defined column, the diameter of which is ~ *450* μm.

Figure 6.9.a is a microdensitometer trace, taken axially, of the image shown in figure 6.8.b.(i). It can be seen that the intense, localised sources are in fact doublets − for example, the feature marked *A* (in figure 6.9.a) shows a double

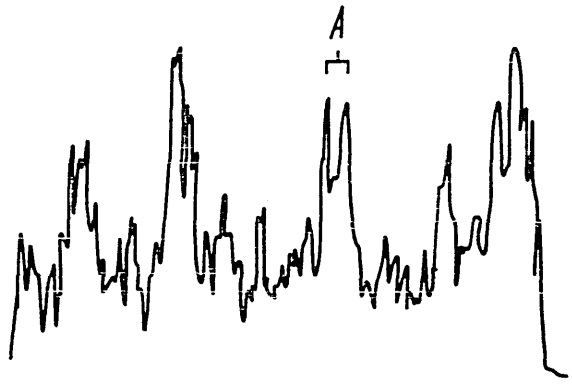


(a)

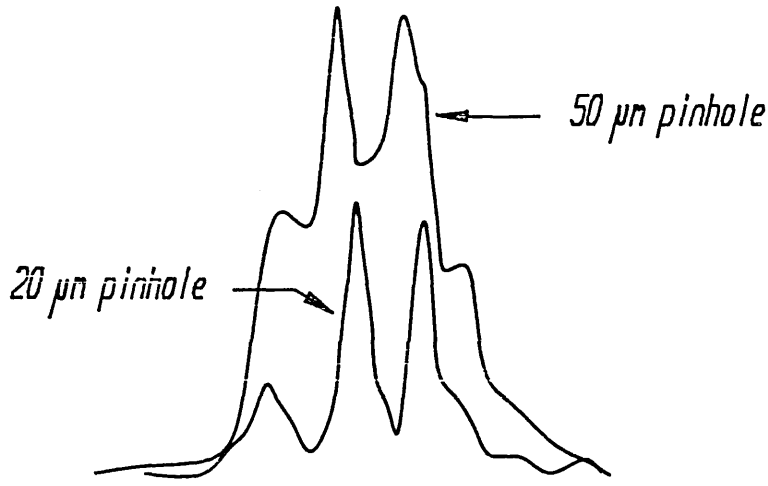


(b)

Figure 6.8: X-ray pinhole images using:
(a) 100 μm pinholes
(b) 50 & 20 μm pinholes



(a)



(b)

Figure 6.9: Microdensitometer scans of the image in figure 6.8.b
(a) axial scan
(b) radial scan

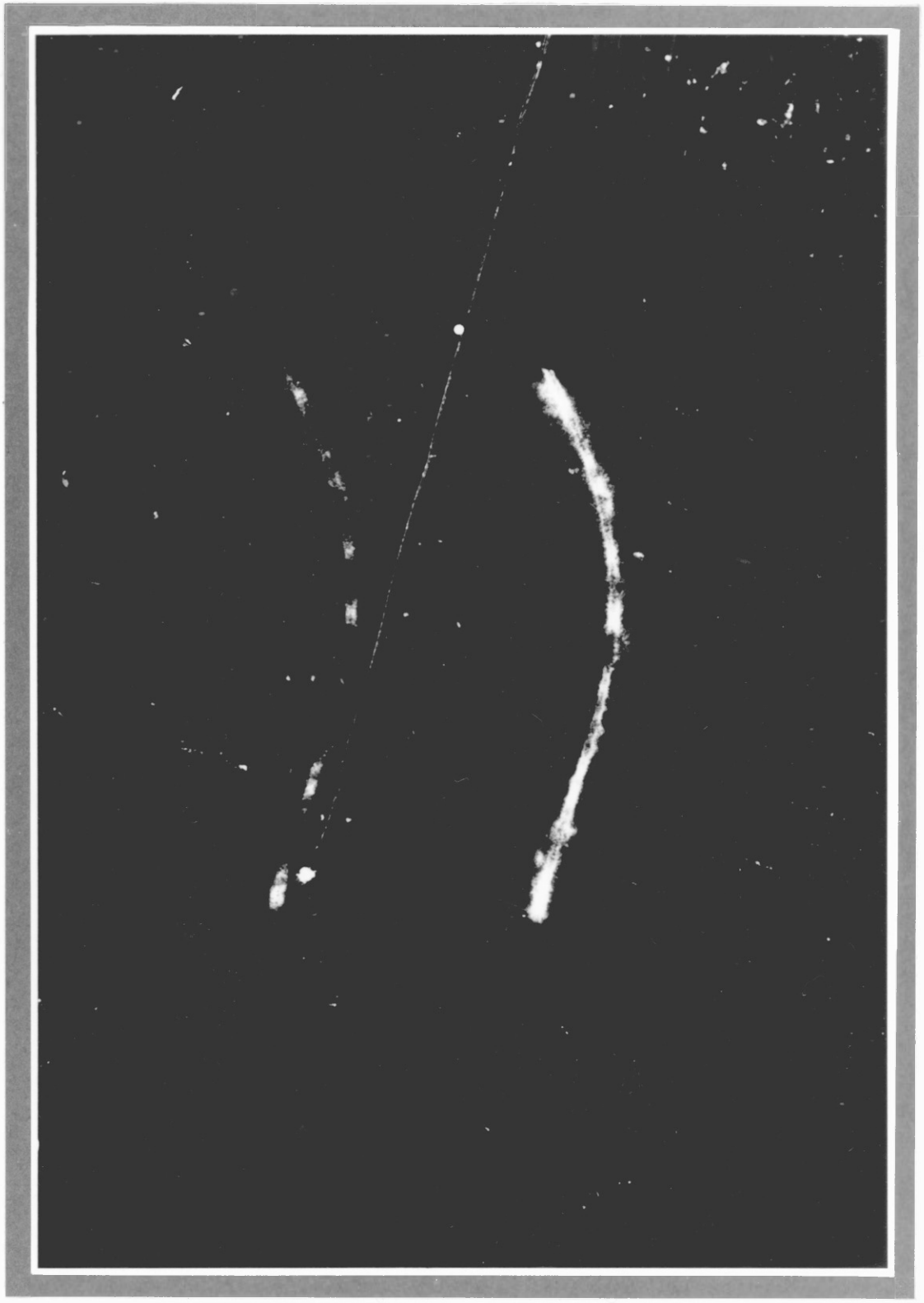


Figure 6.10: X-ray pinhole images of an initially curved fibre

peak; these peaks are separated by *500* μm whilst the whole feature is *1.55* mm in length. Radial microdensitometer traces are shown in figure 6.9.b – the top trace is taken through one of the localised sources whilst the bottom trace is taken through the core.

The typical diameter of the intense sources is

$$D_o \simeq 460 - 540 \quad [\mu m]$$

although some sources are ~ *650 – 730* μm in diameter. The measurements are taken at the base of the digitised traces and the finite pinhole size is taken into account (equation (3)). Typical half–widths of the traces are ~ *340* μm.

The diameter of the core is slightly smaller than that of the intense spots:

$$D_o^{core} \simeq 400 \quad [\mu m]$$

Figure 6.10 shows the X–ray images of an initially curved fibre, through the same pinhole/filter pair as in figure 6.8.b. In this shot there are seven intense sources and two less intense ones along the length of the fibre. Intense emission is seen along both edges of the fibre. The images also display the same curvature as the original fibre.

Figures 6.11 – 6.13 show typical PIN diode signals when viewing the plasma using no collimation, *3* mm and *35* mm thick nylon collimators respectively. In all the data, the X–rays are seen to appear between *0 – 8* ns after the start of current. The uncollimated signals show strong peaks in the emission early on in the discharge. At about $t=75$ ns the signals drop sharply but there is still a significant amount of emission after *100* ns, which decays quite slowly.

Using the *3* mm thick collimators, the data is similar to that with no collimation. The differences are that the signals are not quite as strong as before and the strong peaks are less evident. However, the signals with *35* mm thick collimation are very different from the preceeding ones. They are much lower in strength; there are no strong peaks at all, the signals peak much earlier and the decay is smooth with the long duration being clearly evident.

Figure 6.14 shows the ratios of the PIN signals for different conditions. It shows the ratios between matched filters for data using *3* mm and *35* mm thick collimators, together with one filter pair ratio for the case of no collimation.

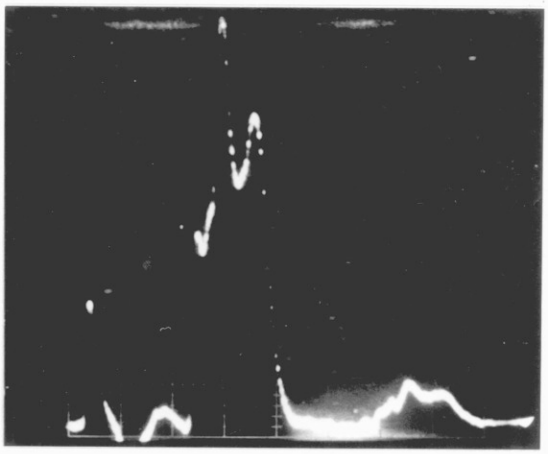


Figure 6.11: PIN diode signals - no collimation

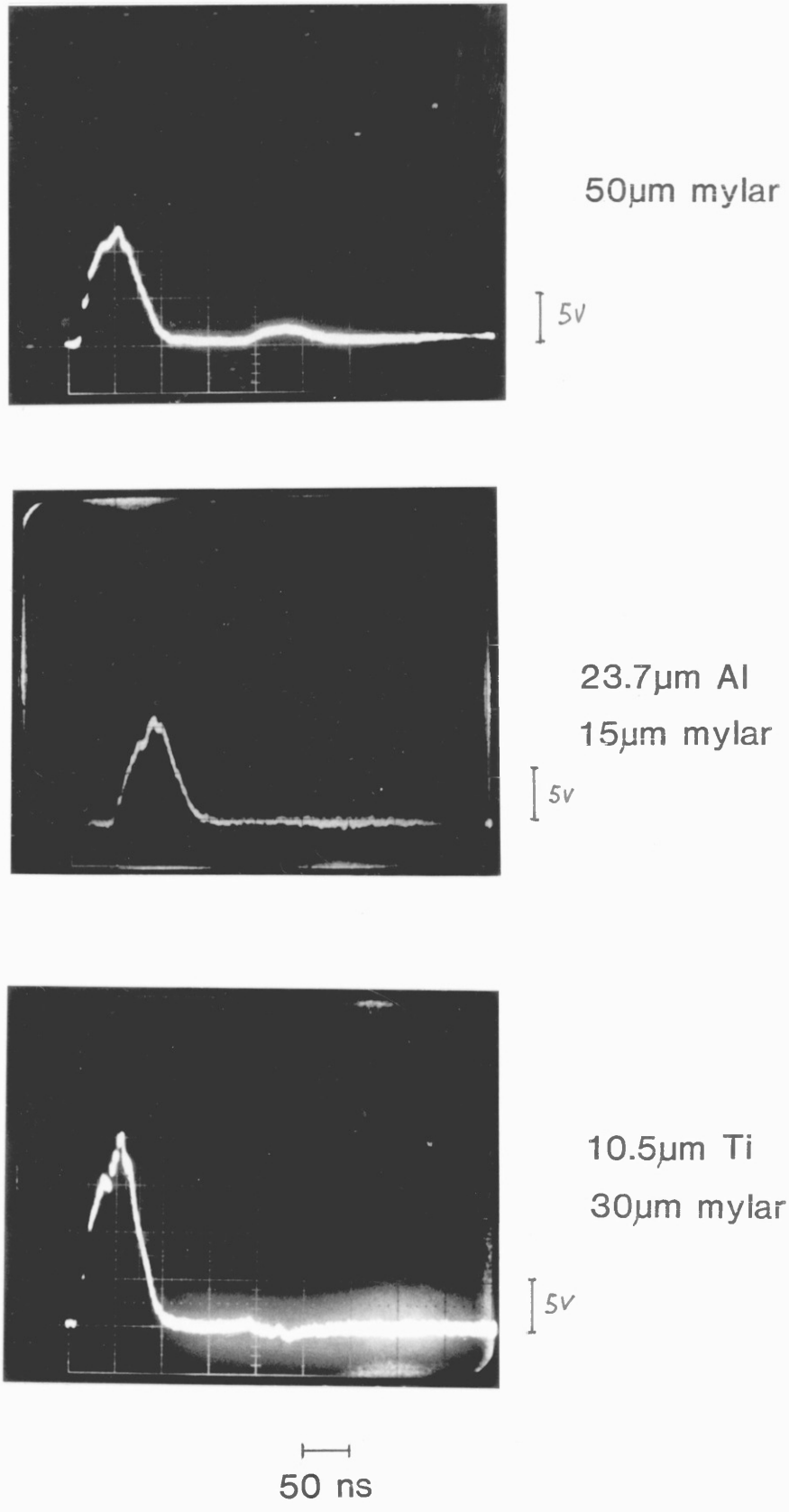


Figure 6.12: PIN diode signals - 3 mm collimation

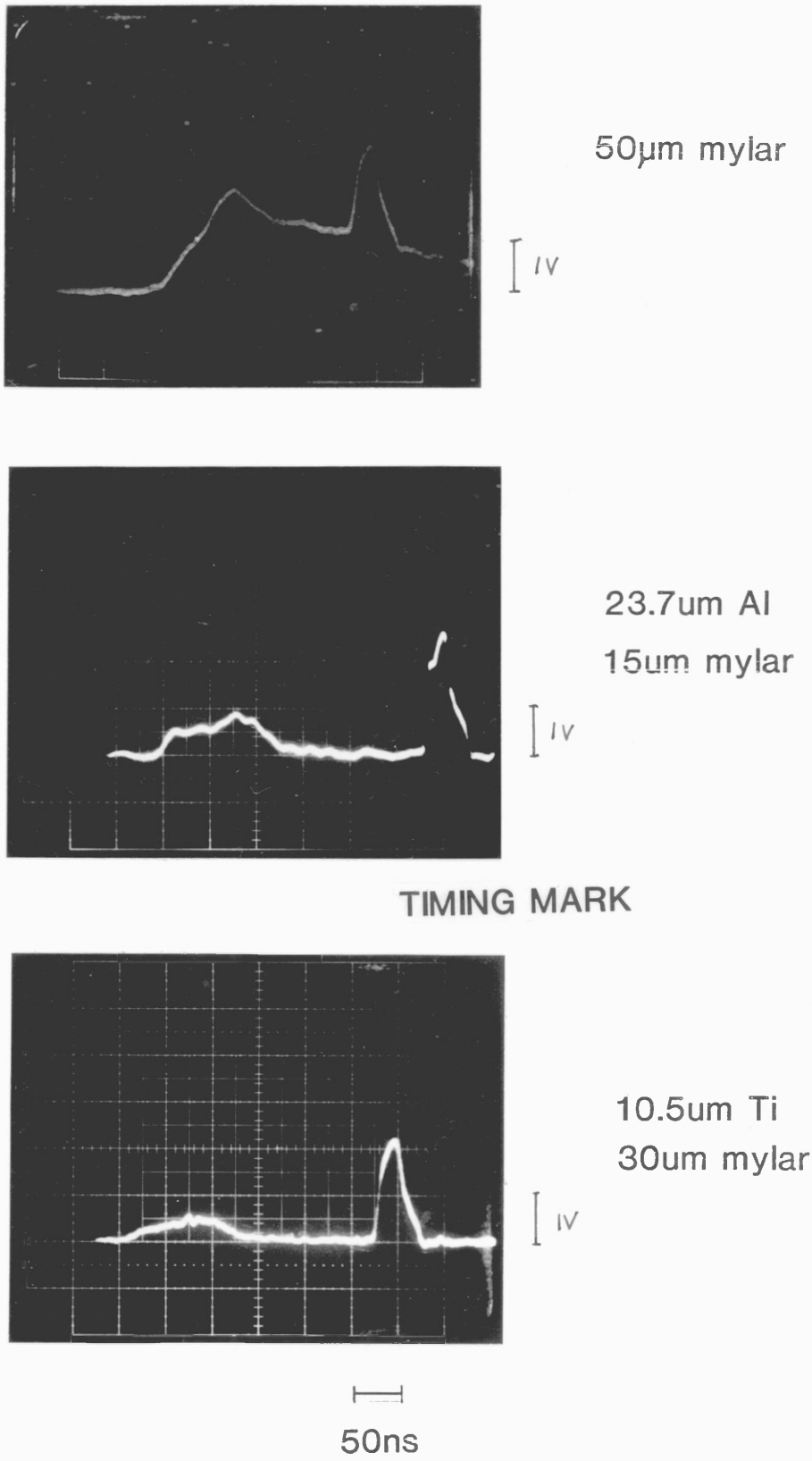


Figure 6.13: PIN diode signals - 35 mm collimation

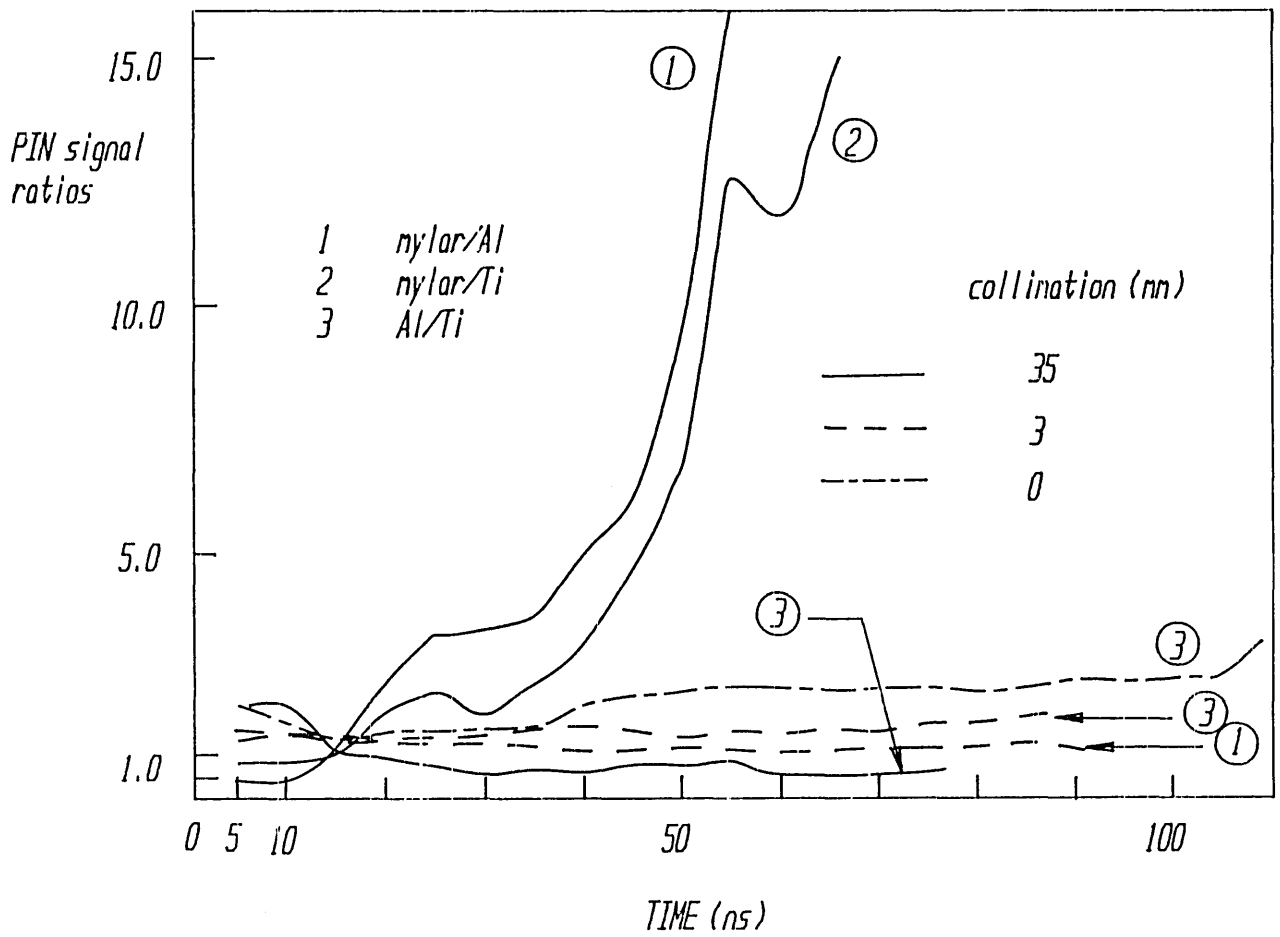


Figure 6.14: Ratios of differently collimated PIN diode signals

6.4. Discussion

From the pinhole photographs the spatial extent of the plasma and its emission profile can be obtained. Although the photographs are time−integrated one can still estimate the lifetime and temperature of the plasma. The electrode emission suggests the presence of an electron beam. This is also confirmed by the ratios of the PIN diode signals. These signals also provide information about the electron temperature in the plasma. A discussion and analysis of these points is presented below.

6.4.1. The Spatial Extent of the X−ray Emitting Plasma

The X−ray images show that the typical diameter of the core is $\simeq$ *400* μm whilst that of the localised sources is $\simeq$ *460 − 540* μm. The localised sources also appear in doublets, with each one being ~ *880* μm in length. How do these dimensions compare to what is observed in the optical photographs and the holograms?

The images are time−integrated and this has to be taken into account when comparing these dimensions with other observations. We know that the initial expansion of the plasma occurs with a velocity ~ 10^6 cm s^{-1}. If the X−rays originated from such expanding regions then the duration of the emission would be ~ *15* ns, starting approximately from when the discharge current starts to flow. This is not the case since the PIN diode signals show that there is emission for a long duration ($>$ *100* ns) rather than a short burst (see later, section *6.4.4.*). So the radiation is not emitted from these fast expanding regions.

The holograms of Chapter 5 clearly show that a narrow core (diameter, $\varphi \simeq$ *170* μm) exists through to late times ($t \simeq$ *150* ns). This core is surrounded by a low density, coronal plasma. The observed dimensions of the X−ray emitting plasma are consistent with the radiation coming from coronal plasma close to the core (within approximately *2* core diameters) where the electron number density is of the order *3 − 5* $\times$ 10^{18} cm^{-3}.

The bright, localised regions of plasma are slightly larger than the main core plasma. The spacing between them is about *1.1* mm which is the same as that of the instabilities observed in the optical photographs. This indicates that the two might be one and the same but the two diagnostics would have to be performed simultaneously to clearly establish this.

The doublet nature of the localised regions is interesting. Such a feature,

within the general envelope of an instability, is observed in the holograms at late times ($t \simeq 150$ ns). The typical dimensions of the envelope are ~ *1.7* mm radially and ~ *2.5* mm axially, which are larger than the size of the localised sources. Within this envelope there are two regions of approximate dimension *500* μm radially and *1* mm axially. This suggests that the doublet in the bright sources corresponds to the instability observed in the holograms. This would further suggest that the doublet feature is actually two separate regions moving towards each other rather than an appearance, in succession, of two short−lived sources.

6.4.2. The X−ray Emission Profile

Very much evident from the radial microdensitometer traces is the fact that the emission is peaked not on axis, but at the outer edge of the plasma. Since the fibre is cylindrically symmetric then the density distributions of the recorded images are Abel transforms of the object (*sic* plasma) emission intensity profile. One can thus, in principle, perform an inverse Abel transform of the digitised data (in a similar fashion to the inversion of the fringe data in Chapter 5) and recover the object profile. However, for our purposes, it is sufficient (and more straightforward) to perform Abel transforms of a number of given analytical profiles and match the transforms to the data.

Figure 6.15 shows two different normalised emission profiles together with their corresponding normalised Abel transforms. The first point to note is that any emission profile that is peaked on axis produces an image profile which is not only peaked on axis but also has a half−width that is smaller than that of the original object profile.

The distributions that peak off−axis were described analytically by a shifted Gaussian profile of the form

$$f(r) = exp[-(r-r_0)^2 / \sigma^2] \qquad (4)$$

Such profiles preserve the peak in emission on the outside of the object whilst filling in the central region. This type of profile matches the data very well. Also notice that the image is smaller in the radial direction than that predicted from simple geometry and that this amount depends on the width ($\propto \sigma$) of the object profile. This shift is a factor of ~ *0.27* of the half−width of the object profile. This increases the estimate of the diameter of the spots to:

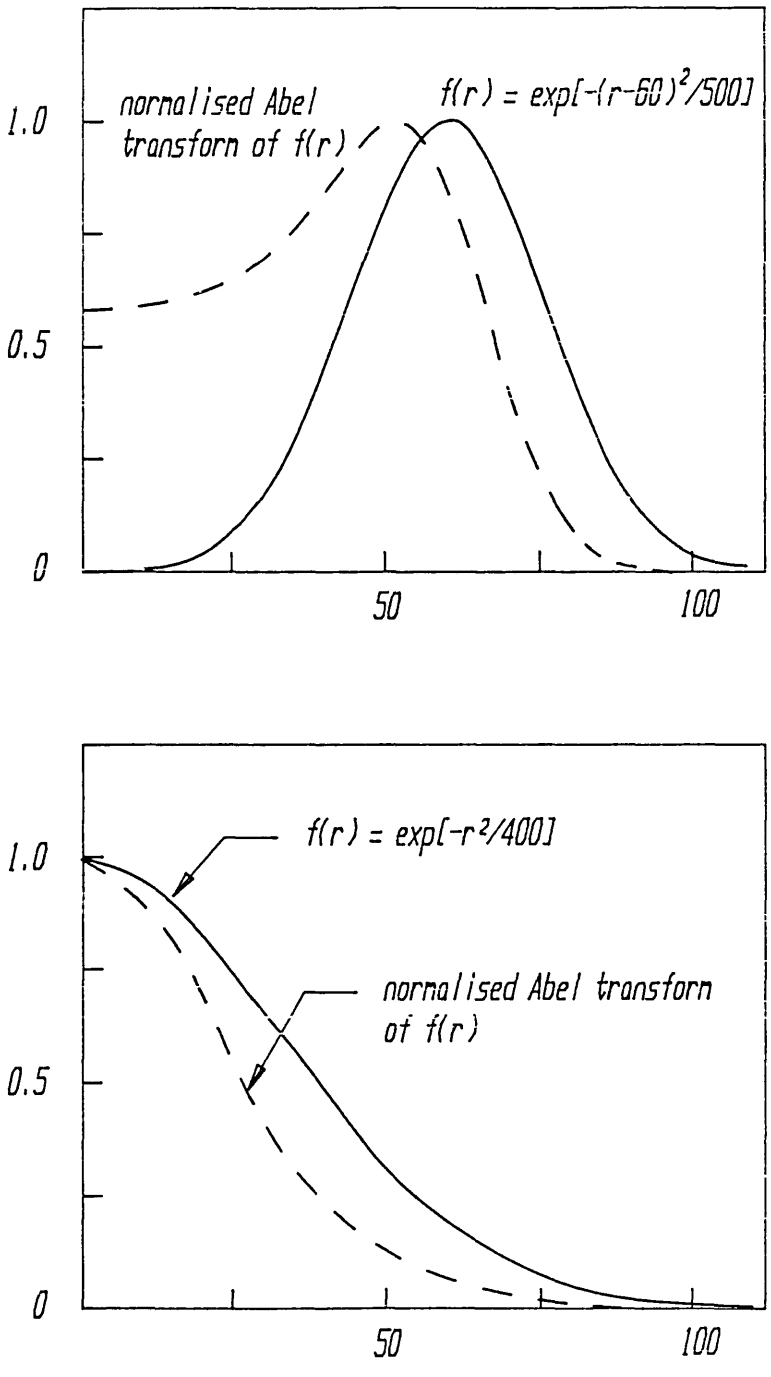


Figure 6.15: Emission profiles and their Abel transforms

$$D_o \simeq 500 - 580 \quad [\mu m]$$

i.e. ~ *10 − 15%* increase. This trend also applies to the core.

From the digitised scans one can also infer a half−width of the profile at the edge and its position with respect to the pinch axis. One finds that typically:

$$\sigma \simeq 47 \quad [\mu m]$$

Therefore, the Gaussian half−width, Δ, is:

$$\Delta = 2\sigma(ln2)^{\frac{1}{2}} \simeq 75 \quad [\mu m]$$

with the peak being centred at

$$r_p \simeq 150 \quad [\mu m]$$

We thus have an estimate of the volume of the emitting region and its radial position.

The general feature, then, of the core and spots is that the emission is peaked towards the outer edge of the plasma. From the holographic measurements it is known that the number density is strongly peaked in a central core region which is of a low temperature. In view of the type of filtering used in the experiment (looking at energies of the order of *1 − 2* keV) then if the X−rays are thermal in origin, then the temperature must be strongly peaked away from the axis, in the outer, low density plasma. If, on the other hand, the X−rays originate from e.g. an electron beam/solid or plasma interaction then a high kinetic plasma temperature is not necessary to explain the observed emission.

6.4.3. Modelling the Plasma X−ray Emission

To proceed with a quantitative analysis of the X−ray data, one needs to have a model for the plasma X−ray emission i.e. one wants to know the shape of the plasma X−ray spectrum. Thus, by comparing the measured data with the model, one is able to deduce quantities such as number density, lifetime of emission and temperature.

Two things are needed to model the X−ray emission:

(a) the processes by which the plasma radiates must be known;

(b) to calculate the contribution to the spectrum from each of these processes one needs to know the populations of different ion stages (and species) and the level populations within each ionisation stage, together with the corresponding ionisation and radiative rates.

These points are discussed in detail in works such as Griem (1964) and De Michelis and Mattioli (1981). A brief resumé of these points is presented below.

(a) Plasma Radiation

The spectral emission from the plasma consists of both continuum and line radiation. The continuum is a result of both free−free (bremsstrahlung) and free−bound (recombination) radiation. The spectral intensities for these two processes are given by the following expressions (De Michelis and Mattioli, 1981):

For free−free radiation

$$I_{ff}(\lambda) = \frac{1.53 \times 10^{-29}}{\lambda^2 \sqrt{T}} n_e^2 Z_{eff} g_{ff} \exp[-1.24\times10^4/\lambda T] \qquad (5)$$

$$[\mathrm{J\ s^{-1} cm^{-3}\ d\Omega^{-1} d\lambda^{-1}}]$$

where Z_{eff} is the effective ion charge

g_{ff} is the Gaunt factor for free−free radiation

λ is the wavelength (A)

n_e is the electron number density ($\mathrm{cm^{-3}}$)

T is the electron temperature (eV).

For free−bound radiation

$$I_{fb}(\lambda) = \frac{1.53 \times 10^{-29}}{\lambda^2 T^{3/2}} n_e \sum_{\alpha} \sum_{z} \xi \chi_{z-1}^{\alpha} n_z^{\alpha} \frac{Z^2}{(n_{0\alpha})^3} g_{fb}$$

$$\times \exp\left\{\frac{-1.24\times10^4/\lambda + \chi_{z-1}^{\alpha}}{T}\right\} \qquad (6)$$

$$[\mathrm{J\ s^{-1} cm^{-3}\ d\Omega^{-1} d\lambda^{-1}}]$$

where ξ is the number of places in the ground state

χ_z^{α} is the ionisation energy (eV) of species α and charge Z

$n_{0\alpha}$ is the principal quantum number of the ion ground state

g_{fb} is the Gaunt factor for free−bound radiation.

This is the expression for radiative recombination; we neglect three−body and dielectronic recombination since these are only important at very high densities.

Line radiation is due to bound−bound transitions within an ion. The emitted intensity of a transition from level $i \rightarrow j$ is given by:

$$I_{bb}(\lambda) = (A_{ij}/4\pi)n_i e E_{ij} \quad [\mathrm{J\ s^{-1} cm^{-3}/d\Omega}] \tag{7}$$

where A_{ij} is the radiative decay rate
for the spontaneous transition $i \rightarrow j$ ($\mathrm{s^{-1}}$)
n_i is the number density of ions in level i ($\mathrm{cm^{-3}}$)
E_{ij} is the energy of the transition (eV).

(b) The Ionisation Model

To calculate the charge−state distribution, one generally uses one of the following approximations: local thermodynamic equilibrium (LTE), coronal equilibrium or collisional−radiative equilibrium (CRE).

LTE has already been discussed in Chapter 4; in this model collisions determine the population levels and each process is balanced by its inverse. In LTE the population levels are in thermodynamic equilibrium whereas the radiation field is not (photons are free to escape). The charge−state distribution is determined by the Saha equation.

At high temperatures and at densities too low to satisfy the conditions for LTE, the coronal approximation is used. Here, excited levels are populated by collisions but, because of the low densities, the ions deexcite by radiation and not collisions. Thus collisional excitation is balanced by radiative deexcitation.

The coronal model is applicable when the following condition for the electron number density is satisfied (De Michelis and Mattioli, 1981):

$$n_e < 5.9 \times 10^{10} Z_n^6 \sqrt{T_e} \exp[0.1 Z_n^2 / T_e] \quad [\mathrm{cm^{-3}}, (\mathrm{ev})] \tag{8}$$

where Z_n is the nuclear charge of the species concerned.

The population distribution is described by:

$$n(z-1)/n(z) = \alpha_r / S(z-1) \tag{9}$$

where α_r is the radiative recombination rate

$S(z)$ is the collisional excitation rate for an ion of charge Z (see e.g. NRL Plasma Formulary, 1986).

When both collisional and radiative processes are important then one must take into account all the processes when determining the charge−state distributions. This is then the CRE model and is in general complicated due to the large number of processes that must be taken into account.

The x−ray pinhole images indicate that the observed radiation comes from the coronal plasma seen in the holograms, which has a density of 3×10^{18} cm^{-3}. The filters are looking at photons with energies in the *1* keV range, corresponding to a thermal temperature of > 100 eV. Equation (8) gives for silicon that for:

$$500 \text{ eV} < T_e < 2000 \text{ eV}$$

$$n_e < 1.0 \times 10^{19} \quad [\text{cm}^{-3}]$$

whilst at $T_e = 100$ eV, $n_e < 5.4 \times 10^{18}$ cm^{-3}. So we use the corona approximation to calculate the population distribution.

The plasma is treated as being solely composed of silicon − i.e. oxygen (from SiO_2) is omitted. This means that the average Z will be higher than if oxygen had been included (since the energy is shared amongst fewer atoms) and so the continuum will be stronger. In addition, only the hydrogen and helium−like, $n=1$ and $n=2$ levels are treated in modelling the line radiation.

A code developed by Dr. Peter Choi (Imperial College) was used to calculate the X−ray spectrum. The code calculates the number of photons radiated by the plasma in a given wavelength interval (the number of photons is given by $N = (\lambda / hc)I(\lambda)$ where $I(\lambda)$ is the spectral intensity) and folds in the X−ray detector response (either film or PIN diode), together with the appropriate filter transmission curve. This yields the dose, or the total number of photons, that the detector would measure for a given plasma temperature. The ratios of doses through different filters are then compared with the data thus allowing the temperature to estimated.

6.4.4. The Density and Lifetime of the X−ray Emitting Regions

From the intensity of the pinhole images one can estimate the duration of emission (for a given electron number density). Let us say that the plasma is

emitting N_e photons/sec/cm^3/str/Å. Thus the total number of photons detected by the pinhole camera is:

$$N_p = \int_\lambda N_e \tau \, dV d\Omega T_f(\lambda) d\lambda \tag{10}$$

where τ is the duration of the X−ray emission

dV is the volume of the emitting region

$d\Omega$ is the solid angle of the collecting system

$T_f(\lambda)$ is the transmission of the X−ray filter.

If the sensitivity of the film is S_λ (photons cm^{-2}/density unit) (which is a function of energy and is shown in figure 6.4) then the film exposure due to the impinging N_p photons is:

$$ND_{film} = \int_\lambda \frac{N_e \tau \, dV d\Omega T_f(\lambda)}{S_\lambda} \, d\lambda \tag{11}$$

The density measured on the X−ray film is:

$$ND_{meas} = \int\int ND(x,y) dx dy \tag{12}$$

where the integration is carried over the image region of the film.

Equating ND_{film} and ND_{meas} allows us to estimate the duration of emission, τ:

$$\tau = \frac{\left[\int\int ND(x,y) dx dy \right]}{\left\{ \int \frac{N_e T_f(\lambda)}{S_\lambda} \, d\lambda \right\}} \frac{1}{dV d\Omega} \tag{13}$$

The code calculates the quantity:

$$DOSE = 4\pi \int (N_e T_f(\lambda) / S_{0\lambda}) d\lambda \tag{14}$$

where N_e is made up from free−free and free−bound radiation and line radiation

$S_{0\lambda}$ is the normalised film sensitivity − this is normalised to the number of photons needed to produce an ND of 1 at $\lambda = 10$ Å i.e. the normalisation constant, $S^* = 10^8$ ph/cm^2.

Figure 6.16 shows the doses as a function of temperature through the filters pertaining to the images of figures 6.8.a.(i) and 6.8.b, respectively. The ratios are independent of the electron density. This is because the collisional and radiative rates are density dependent in the same manner.

Let us first examine the double film layer images of figure 6.8.a.(i). We observe that the bright sources visible on the first film layer are not visible on the second layer. The core, on the other hand, is less intense but it also shows through onto the second film layer.

From equations (13) and (14), the ratio of the film densities of the source to the core is:

$$R = ND_S / ND_C = (d_S \tau_S V_S) / (d_C \tau_C V_C) \tag{15}$$

where $d_{S/C}$ is the dose from the source/core

$\tau_{S/C}$ is the duration of emission

$V_{S/C}$ is the emitting volume.

The first film layer tells us that $R = R_1 > 1$. On the second film layer the spots cannot be seen; thus $R = R_2 = 1$. This tells us that the ratio of the emission times of source to core is:

$$\tau_S / \tau_C = (d_{C2} / d_{S2})(V_C / V_S) \tag{16}$$

where d_2 signifies the dose through the second film layer.

Substituting (16) into (15) gives:

$$R_1 = (d_{S1} d_{C2} / d_{C1} d_{S2}) > 1 \tag{17.a}$$

If we let $d_{S1} / d_{S2} = \alpha$ and $d_{C1} / d_{C2} = \beta$ then (17.a) becomes

$$\alpha > \beta \tag{17.b}$$

From figure 6.16, we see that the above condition can only be true if the temperature of the source regions is less than the temperature of the core.

To estimate τ, let us examine the image of figure 6.8.a from the *100* μm pinhole. The volume of the core region under consideration is:

$$V_C \simeq 2\pi r_p \Delta \ell$$

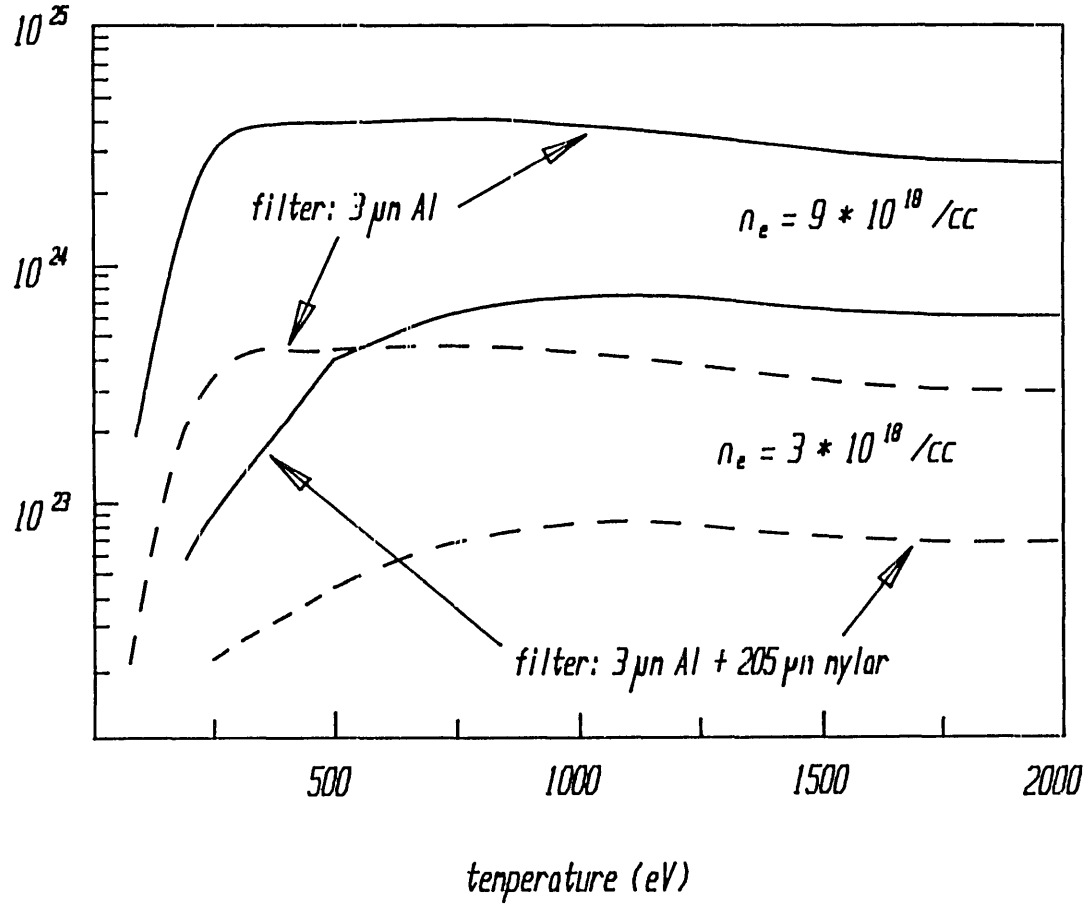


Figure 6.16: X-ray film dose (pertaining to figure 6.8) versus temperature

where r_p is the centre of the peak of the emission profile

Δ is the half-width of the profile

ℓ is the axial length of the core region.

If we consider a region $\Delta x = \Delta y = 200\ \mu m$ on the film then $\ell = 450\ \mu$m. Taking r_p and Δ from section *6.4.2.* we find for the volume:

$$V_c \simeq 3.2 \times 10^{-5} \quad [\text{cm}^{-3}]$$

The solid angle of the pinhole is

$$d\Omega = 1.45 \times 10^{-7} \quad [\text{str}]$$

An *ND* of $\simeq 1.24$ is measured over $\Delta x \Delta y = 4.0 \times 10^{-4}$ cm^2 and is approximately constant. Time-resolved measurements indicate that the plasma is emitting X-rays for at least *300* ns. So taking $\tau = 300$ ns, an electron number density of 3×10^{18} cm^{-3} and using figure 6.16 to determine the dose we estimate the temperature of the core to be:

$$T_c \simeq 300 - 800 \quad [\text{eV}]$$

The sources have a volume, $V_s \simeq 4.3 \times 10^{-5}$ cm^{-3} and the *ND* measured is $\simeq 2.56$. If we take the mean temperature of the core to be $\simeq 500$ eV then since the temperature of the spots is lower than that of the core, we assume $T_s \simeq 250$ eV. For a number density of 3×10^{18} cm^{-3} the emission time is:

$$\tau_s \simeq 790 \quad [\text{ns}]$$

This is much longer than the measured emissiontime and indicates that the density of the spots is higher. Taking $n_e \simeq 9 \times 10^{18}$ cm^{-3} we find for the emission time:

$$\tau \simeq 87 \quad [\text{ns}]$$

At the above density but at a temperature of $T_s \simeq 150$ eV, the emission time becomes $\tau \simeq 440$ ns.

We thus see that the core has a mean temperature of between $300 - 800$ eV and a density of 3×10^{18} cm^{-3} whilst the spots are cooler, with $T \simeq 200$ eV, but denser, $n_e \simeq 9 \times 10^{18}$ cm^{-3}. These temperatures are mean values and it is

probable that the core reaches a peak temperature of about *1* keV.

The source of error in these estimates, of course, comes from the facts that the model for the plasma emission, $N_e(\lambda, n_e, T_e)$, is not complete (the oxygen contribution is ignored) and that the images are time-integrated, which means that a time-dependent model for the plasma emission is required in order to make a detailed calculation. The figures, however, do at least provide rough estimates of the density and lifetime of both the localised sources and the core region; they are to be taken as being within an order of magnitude of the correct values.

6.4.5. The Electrode Emission and Electron Beams

Referring to figures 6.11 – 6.13 one can see that the difference between collimated and non-collimated signals is dramatic. From figure 6.13 we see that, apart from a difference in the individual PIN signal strengths, there is little difference between the behaviour of the uncollimated and *3* mm collimated signals. In contrast, the behaviour of the signals when viewed through *35* mm nylon is completely different. The collimators exclude any radiation coming from the electrodes; this means that the only significant contribution to the signals from the *35* mm collimated diodes is that from the plasma. The *3* mm collimated signals and the uncollimated data, on the other hand, are dominated by the emission from the electrodes.

Whereas in figure 6.14 the PIN ratios are constant up to ~ *90* ns into the discharge, with *35* mm collimation there is a steady increase in the ratios of mylar/Ti and mylar/Al after ~ *35* ns. This difference cannot be explained by a high temperature electrode plasma (the PIN ratios would not be altered as can be seen from figure 6.19). We also notice that since the collimators look at *60%* of the fibre then we might expect the ratio of uncollimated to *35* mm collimated signals to be $1/0.6 = 1.6$. The measured ratio is closer to *30* and this indicates that the electrode emission is different to that of the fibre. We assume that the electrode radiation is the result of an interaction between an electron beam and the electrode material. One can then see if the intense electrode emission seen in the pinhole photographs is consistent with this assumption.

We can calculate the total charge deposited at the electrodes as a result of a beam/target interaction. The calculation is similar to the previous method of estimating $n_e{}^2\tau$ for the plasma emission (see also Challis, Ph.D. Thesis, 1986). We thus have:

$$\int_x \int_y ND(x,y)dxdy = \int_\lambda \left[\frac{N_e}{4\pi}\right]\left[\frac{i_b\tau}{e}\right]\frac{d\Omega T_f(\lambda)}{S_\lambda}\, d\lambda \qquad (18)$$

where $N_e/4\pi$ is the number of photons emitted per incident electron into solid angle 4π

i_b is the electron beam current

τ is the duration of the beam

$d\Omega$ is the solid angle of the pinhole system

$T_f(\lambda)$ is the transmission of the pinhole filter

and the LHS is as before (section *6.4.3.*).

The contribution to N_e is made up of two parts: line radiation and continuum radiation. These processes are discussed below.

(a) line radiation

When electrons are incident on the electrodes they lose energy by collisions with the electrons in the electrode. These collisions are ionising and result in primarily K shell (and to a certain extent L shell) electrons being ejected if sufficient energy is available. This is termed 'direct' production of characteristic radiation. 'Indirect' production occurs when some of the continuous spectrum is absorbed by the material. This causes fluorescence and enhances the emitted characteristic radiation (see Dyson, 1973). A number of factors affect the overall intensity of the emitted characteristic radiation: the range of the electrons in the material, backscattering within the material, absorption of X−rays as they pass out of the material and the fluorescence yield.

Taking all this into account, Dyson gives an expression for the number of K−shell photons emitted per incident electron into solid angle 4π:

$$N_k/4\pi = \omega_k[K_1 Rk/A + K_2(Z-2)^2 Z][U_0 - 1]^{1.67} f(\chi) \qquad (19)$$

where $K_1 = 2.80 \times 10^3$

$K_2 = 4.27 \times 10^{-10}$

ω_k is the fluorescence yield

$U_0 = E_0/E_k$ is the ratio of incident energy to the K−shell energy

R is a factor taking into account backscattering

k is a constant depending on the element

A is the atomic weight of the electrode material

$f(\chi)$ is a factor taking into account the absorption of X−rays in the target

$\chi = (\mu/\rho)cosec\Theta$

μ/ρ is the mass absorption coefficient

Θ is the take−off angle with respect to the surface.

(b) continuum radiation

This arises from the acceleration of the electrons in the Coulomb field of the material ions. An expression for the intensity of the bremsstrahlung radiation has been derived by Kramers (1923) based on the electron scattering cross−section and the Thomas−Whiddington law, which describes the energy loss in the material (see Dyson, p.16):

$$I_\nu d\nu = kZ(E_0 - E_\nu)d\nu \qquad (20)$$

where Z is the atomic number

E_0 is the incident electron energy

E_ν is the energy of the emitted photon

k is a constant of proportionality.

We shall now examine the emission from the anode. The anode material is stainless steel which is 75% Fe and 15% Cr, 10% Ni. We thus take an average $Z \simeq 26$ and average $A \simeq 50$. The typical K−shell energy, E_k, is ~ 8 keV (see Table 6.1, section *6.2.3.*).

For energies $20 < E < 100$ keV the ratio of characteristic to continuous radiation is ~ $0.6 - 0.7$ and only varies slowly with atomic number. Since we are dealing with K−shell photons of energy ~ 8 keV then the filter transmission in this range is ~ 0.8. We thus approximate the integral over λ by:

$$\int(N_e/4\pi)T_f(\lambda)d\lambda \simeq 2 \times (N_k/4\pi) \qquad (21)$$

Under these conditions we have:

$R \simeq 0.8$, $\omega_k = 0.3$, $k \simeq 10^{-6}$, $f(\chi) \sim 0.8$, $d\Omega = 1.45 \times 10^{-7}$ str,
$dxdy = 0.4 \times 1 \times 10^{-2}$ cm^2, $S_{8keV} \simeq 7.0 \times 10^7$ ph cm^{-2}/ND
and we measure an ND of $\simeq 1$ (~ constant over $dxdy$).

We thus finally arrive at:

$$i_b\tau \simeq 1.34 \times 10^{-2}[(U_0 - 1)^{-1.67}] \qquad [\text{As}]$$

Figure 6.17 shows a plot of $i_b\tau$ as a function of U_0. We see that it depends weakly on the energy of the beam for $U_0 > 4$. In the region 30 keV $< E_0 < 60$ keV we can take the product $i_b\tau \simeq 10^{-3}$. If we take for the beam duration

$$\tau \sim 50 \qquad [\text{ns}]$$

then we find for the beam current

$$i_b \sim 20 \qquad [\text{kA}].$$

A lower estimate of the energy of the electron beam can be made from the ratios of the PIN diode signals with no collimation and 3 mm collimators. The continuum as a function of wavelength peaks at $\lambda = 1.5\lambda_0$ (where $\lambda_0(\text{A}) = 12.4/E_0(\text{keV})$ and E_0 is the beam energy). This peak must lie on the high energy side of the both the aluminium and titanium K−edges or else there would be a large difference in the aluminium ratios and the difference between the differntly collimated signals. Taking $\lambda \simeq 1$ A we find that:

$$E_0^{min} > 18 \text{ keV}$$

Referring to Table 6.1 (see earlier, section *6.2.3.*), we thus see that the ratios are consistent with the radiation coming from inner K−shell excitation. The cross−section for inner K−shell ionisation is given by (Dyson, 1973):

$$Q_k = (2\pi e^4 b/EE_k)\ln(4E/B) \qquad [\text{cm}^2, (\text{eV})] \qquad (22)$$

where $b \sim 0.7$

$B = [1.65 + 2.35\exp(1 - U)]E_k$

$U = E/E_k$.

Q_k peaks when $E \sim 3-4 \times E_k \simeq 30$ keV. An electron beam of an energy close to this value would then interact very efficiently with the electrode material to produce characteristic line radiation.

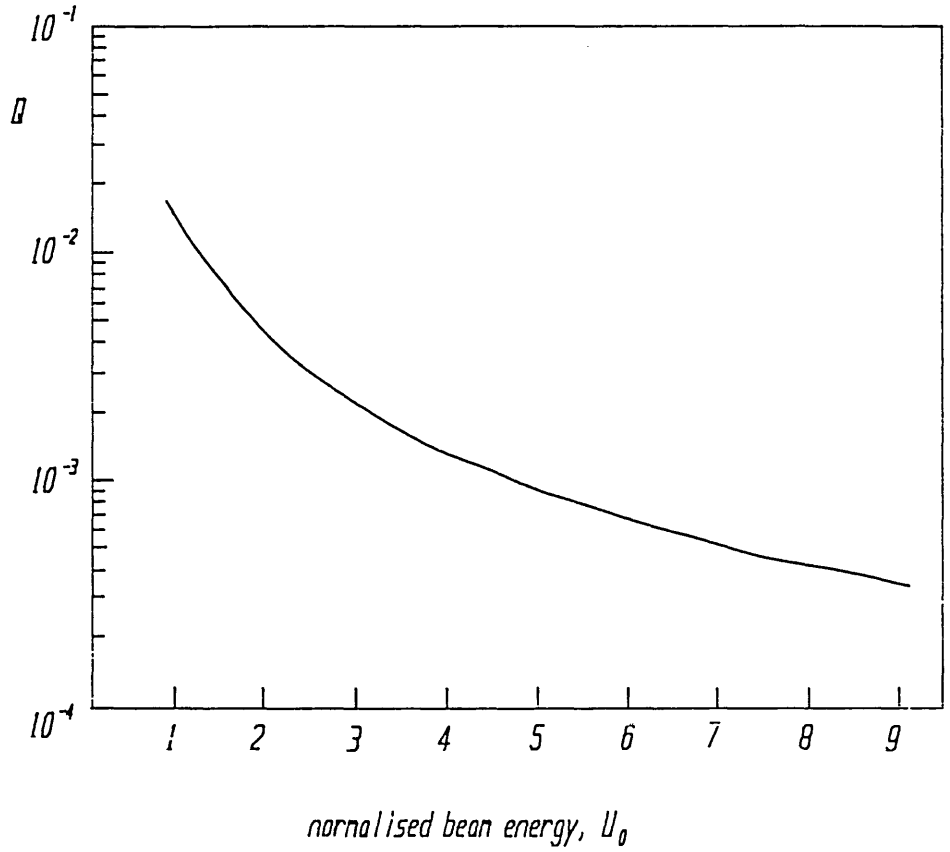


Figure 6.17: Charge delivered to anode as a function of beam energy

The PIN diode measurements show that the electrode X−rays are emitted within 8 ns of the start of current flow. It thus appears that the electron beam is produced in this time. This is tied up with the breakdown of the fibre which is discussed in Chapter 7, section *7.3.2*. The fibre is non−conducting and there are large inductive voltages at the cathode. Ultimately, breakdown will occur along the surface, creating (initially) a low density plasma. The external field will exceed the Dreicer field (1959) in this plasma leading to runaway electrons which then form the electron beam.

The long duration of this electrode emission indicates that the electron beam is present for at least the first *50* ns of the discharge. Since the emission drops sharply at ~ *70* ns this means that the beam has decreased in intensity and the observed X−ray emission is then a combination of fibre plasma emission and high *Z* electrode plasma emission. We notice that at late times ($t > 100$ ns) the strength of the signals from the *35* mm collimated and the uncollimated shots are approximately the same − this shows that at this late time the dominant source of the radiation is the fibre plasma.

6.4.6. Plasma X−rays

The filtered X−ray PIN diodes provide a time−resolved picture of the plasma X−ray emission and by a suitable choice of filters, give the evolution of the electron temperature in the plasma. By comparing the PIN diode data with the results from the ionisation model for the X−ray spectrum we can estimate the electron temperature throughout the discharge provided that the model is valid at the appropriate times.

Figure 6.18 is the calculated dose detected by the filtered PIN diodes for different plasma temperatures. In this case, the detected number of photons is converted to the charge generated by the PIN diode; so the dose is proportional to the output signal of the diode. Figure 6.19 shows the calculated ratios of doses for the filters used in the experiment. These are compared with the data of figure 6.14 to give an estimate of the electron temperature.

In the initial *10* − *15* ns we notice that the ratio $R_{mylar/Ti} \sim 1$ whilst $R_{Al/Ti} > 1$ and $R_{mylar/Al} < 1$. The calculated ratios never take such values. This indicates that the temperature is quite low (< 100 eV). In this case, the corona approximation is probably not valid which explains why the calculated ratios are not in agreement with the experimental observations.

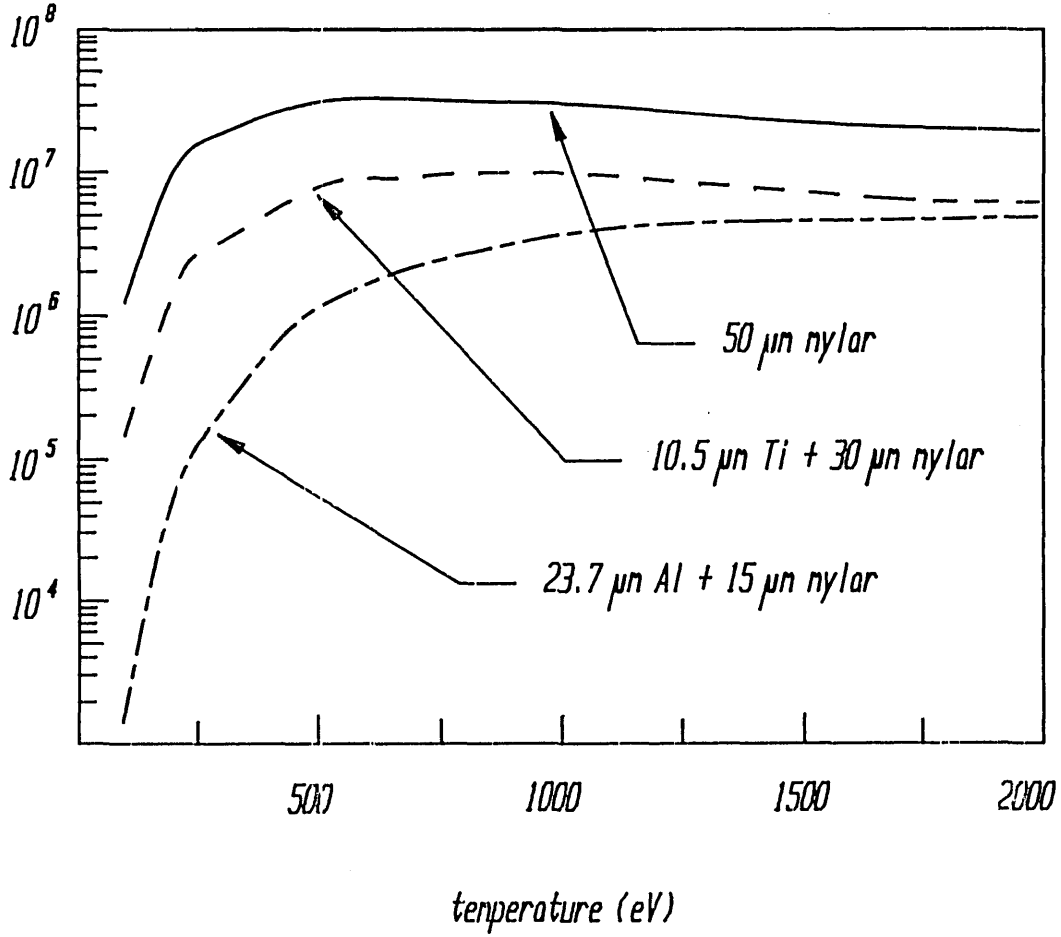


Figure 6.18: X-ray dose versus temperature for the filtered PIN diodes

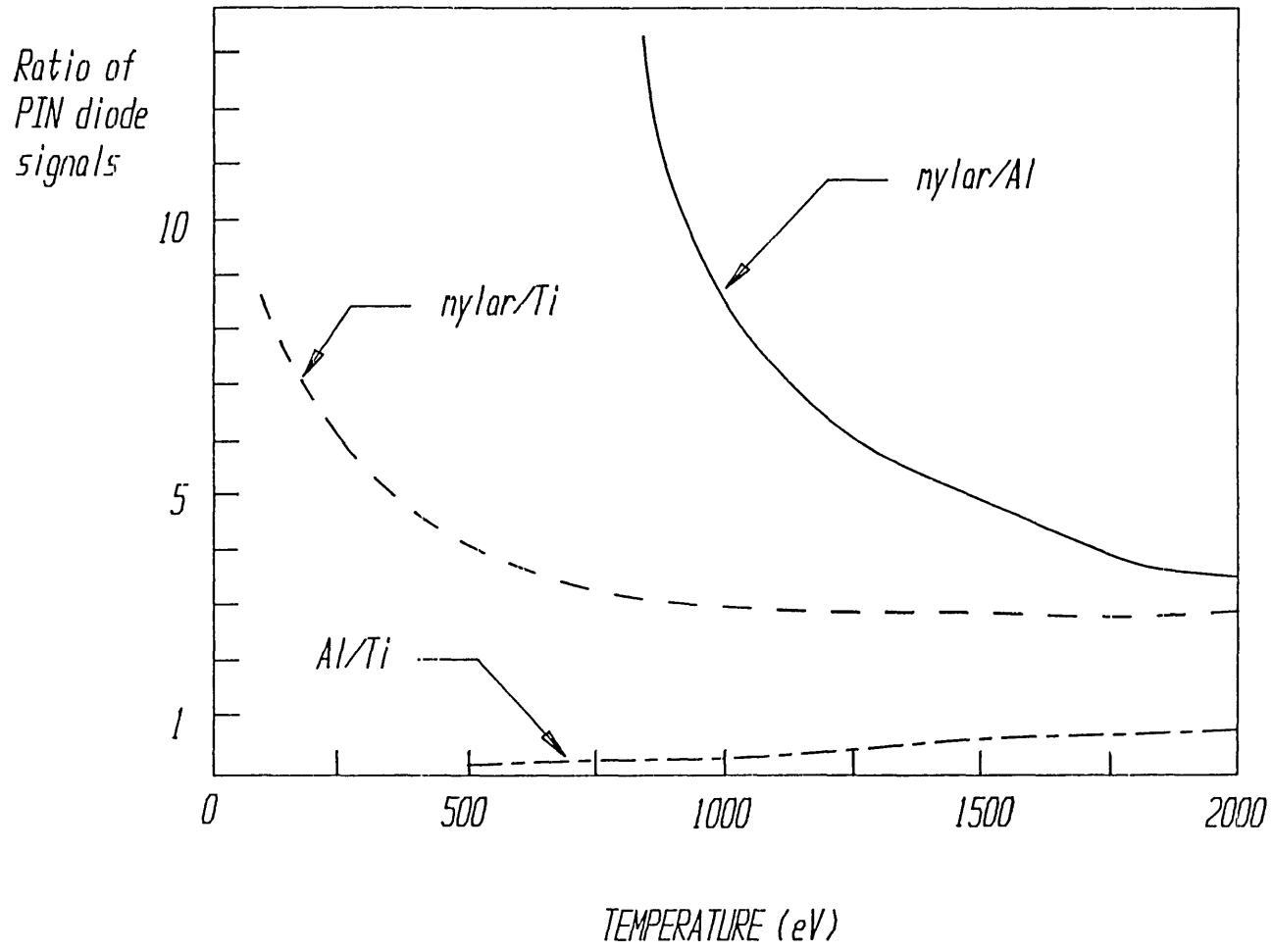


Figure 6.19: Ratios of the X-ray dose for the filtered PIN diodes

After ~ *15* ns, up to ~ *35* – *40* ns, we observe the ratios to be the following:

$$R_{mylar/Al} > 1,\ R_{Al/Ti} < 1 \text{ and } R_{mylar/Ti} < R_{mylar/Al}.$$

If the radiation is of thermal origin (rather than due to an electron beam/fibre interaction) then the temperature must now have increased considerably. The ratios in figure 6.19 indicate a peak temperature in the region of ~ *1* keV. Although the bright spots are also present, they are of a much lower temperature and their contribution to the ratios will be small (even though they are dense).

The signals (figure 6.13) are still rising up to this time. If the radiation is coming from a continuum then this means that the density must be increasing with little drop in temperature. Since the plasma is still expanding then this indicates that there is a continual ablation of the fibre. This is consistent with the picture of a surface plasma surrounding a solid fibre core.

At this time there is also an electron beam present. This could interact with the plasma and fibre giving rise to inner K–shell radiation. The combination of a beam/fibre interaction and continuum emission could then mean that the temperature less than *1* keV.

After *40* ns the ratios $R_{mylar/Al}$ and $R_{mylar/Ti}$ increase steadily although both the mylar and Al signals are decreasing. The Al/Ti ratio appears to be constant and < *1*. We know from previous diagnostics that the number density is increasing. Thus the temperature has to drop to explain the drop in the signal strength. However, since the mylar signal drops more slowly than the Al or Ti signals then there is still significant radiation around the Si K–edge and this means that the drop in the temperature is rather slow.

6.4.7. Can the Plasma be Hot?

Is it possible for the plasma to be heated to temperatures of ≃ *1* keV? The answer is 'yes' if the current density is high enough. In terms of the fibre plasma this would mean that most of the current would have to flow in the outer low density plasma (as seen in the holograms). Joule heating would be enough to heat the plasma to such temperatures even though the radiation losses are quite high.

The picture that emerges is that there exists a central core with a high density plasma at the surface, which radiates as a blackbody with a temperature of *10* – *30* eV whilst surrounding it is a hot, low density plasma. If this is correct

then it means that the low density, hot plasma is transparent in the optical streak photographs.

One can calculate whether, at a temperature of *1* keV, the bremsstrahlung radiation emitted in the wavelength range of the streak camera is comparable to the blackbody radiation in the same range. A similar calculation has already been made in Chapter 4 (to explain the lack of plasma emission in the first *15* ns of the discharge). By equating the power of free−free radiation detected by the camera to the detected blackbody power one estimates the electron number density necessary to achieve this.

Following the procedure in Chapter 4 (section *4.4.4*) and taking a blackbody temperature of *30* eV and for the low density plasma a temperature of *1* keV, gives:

$$n_e = 4.2 \times 10^{19} \qquad [\mathrm{cm}^{-3}]$$

This compares with the maximum observed density around the core of

$$n_e = 1.4 \times 10^{19} \qquad [\mathrm{cm}^{-3}]$$

measured in Chapter 5, at $t=147$ ns.

So a high enough density is never reached. Also, at 1.4×10^{19} cm^{-3}, the equivalent blackbody temperature for a plasma of the same dimension as the core is < 1 eV. This is less than the minimum detectable blackbody temperature ($=2.5$ eV) and so this low density, hot plasma will be transparent to the optical streak camera.

6.5. Conclusions

The analysis of the pinhole photographs shows that the emission is peaked towards the edge of the plasma. The intensity of emission from the core is consistent with the plasma temperature being ~ 500 eV (probably reaching a peak of $\simeq 1$ keV) and the density being $\sim 3 \times 10^{18}$ cm^{-3}. The bright spots are shown to be much colder ($\simeq 100 - 300$ eV) but denser.

The intense emission from the electrodes seen in the pinhole photographs is consistent with an electron beam/target interaction. The energy of the beam is typically around $20 - 30$ keV; the current is estimated at $\simeq 20$ kA and its duration is measured to be $\simeq 50$ ns. Such a beam is probably due to runaway

electrons as a result of the breakdown process by which the plasma is formed from the quartz fibre.

The time−resolved PIN diode measurements show that the plasma reaches a peak temperature of about *1* keV at around *40* ns into the discharge. The temperature subsequently drops, this being due to an increase in the number density as the result of further ablation of the solid fibre. This drop in temperature is quite slow and there is still significant radiation *300* ns after the start of the discharge.

CHAPTER SEVEN

Conclusions

7.1. Z−pinches and Pulsed Power

The Z−pinch was one of the first configurations to be experimented with in the search for CTR. Unfortunately, though the configuration is elegant and simple, the early Z−pinches were highly unstable. These typically low density (n_e ~ 10^{15} cm^{-3}) pinches were driven by low power devices (~ *100* MW) with low rates of rise of current (dI/dt ~ 10^{11} As^{-1}) and the experimental timescale determined by the drive (τ ~ *1* μs) was usually much longer than the MHD timescale (τ_{mhd} ~ *10* ns).

With the advent of pulsed power technology (Martin, AWRE), where high powers (~ *10* GW) could be switched to the load in a very short time (~ *50* ns), one now had a means of operating a new 'class' of Z−pinch: a high density, short duration pinch. The high densities (n_e > 10^{18} cm^{-3}) meant that a much shorter energy confinement time (< *100* ns) than before could now be used to satisfy the Lawson condition. This time was also matched by the pulsed nature of the new drive. The high power available would also be able to heat the pinch to thermonuclear temperatures and if disruptive instabilities could be avoided on these shorter timescales then the Z−pinch would achieve fusion conditions (Haines, 1982).

The work presented in this thesis was performed on two such new generation, high density Z−pinches: the gas−embedded Z−pinch and the fibre Z−pinch. This concluding chapter summarises the results from these experiments, discusses them in the context of current research and outlines areas for future work.

7.2. The Gas−embedded Z−pinch

The Z−pinch was initiated by focussing a ruby laser into a chamber filled with hydrogen (at *0.33*, *0.67* and *1.0* atm.). The discharge channel so formed was preheated by small current of ≃ *7* kA for ≃ *50* ns. The Z−pinch was then driven by a *3*Ω pulsed generator, giving a current of *150* kA with a *10−90%* risetime of *50* ns. An axial magnetic field probe was used to monitor the

occurrence of the $m=1$ instability (which, because of its helical nature, produces a B_z field). In addition, optical streak photography was performed (looking transversely to the plasma axis) to observe the dynamics of the pinch. The aim of the experiment was to investigate the stability of the pinch under conditions where finite ion Larmor radius effects were expected to be important.

There are three phases of the pinch evolution:

– the *preheat* phase, where the pinch expands whilst being heated by a small current prior to the main discharge;

– the *equilibrium* phase, where the main current heats the pinch under radial pressure balance;

– the *unstable* phase, where the equilibrium pinch is transformed into an expanding helical structure via an $m=1$ instability.

During the preheat, conditions are created such that the main current is able to heat the pinch under pressure balance. The characteristics of the preheating phase are identical to the low current experiment reported earlier (Favre–Dominguez, Ph.D. Thesis, 1985). The evolution of the initial discharge channel can thus be assumed to be the same in both experiments and has been described in Chapter 3.

When the main current is applied, the pinch is observed to be in radial equilibrium. The duration of this equilibrium increases as the initial filling pressure is increased. This is consistent with the scaling predicted by ideal MHD theory – i.e. since the MHD growth time scales as $1/v_{th}$ (where v_{th} is the ion thermal velocity) then as the number of particles is increased then the temperature reached (through Joule heating by the current) by the plasma is lower; thus the ion transit time across the plasma column is longer and so the instability growth time will be longer.

The results in this high current experiment are in contrast to those obtained in a similar but low current experiment (Favre–Dominguez). In this case the equilibrium time was observed to scale oppositely to that of ideal MHD. Coppins (1987) has suggested that the nature of the equilibrium is the result of the growth rate being a function of time – this then gives the instability the appearance of a sudden onset. If the initial perturbation is large then the onset of the instability happens very quickly after the start of the current. Thus in the low current experiment, if there is a larger initial perturbation at the higher pressures, then this would explain why the equilibrium time appears to scale oppositely to that predicted by ideal MHD.

The measurement of an axial magnetic field at the time of the onset of the instability confirms that the current flow is now helical. The consequent increase

in inductance is reflected in a momentary decrease in current at the time of the transition. This is consistent with the magnetic flux being conserved during the transition. It was also found that the current flow is always left−handed (when the generator provides 'negative' current). This cannot be due to an asymmetric current flow prior to the instability since the pinch geometry is radially symmetric. No satisfactory explanation exists for this phenomenon.

It has been shown that the conditions under which one might expect to observe enhanced stability due to finite ion Larmor radius effects are marginally fulfilled only at a pressure of *0.33* atm. The observed growth time of the instability in this case is less than twice the ideal MHD time, hardly meriting being called 'enhanced' stability. To achieve such conditions it is necessary to heat the pinch to high temperatures and this is limited by accretion of neutral particles into the plasma column.

7.3. The Fibre Z−pinch

The same generator used to drive the gas−embedded pinch was used to drive the fibre Z−pinch. The length of the fibre was *18* mm and a number of different fibre diameters was investigated (*20 − 125* μm). A variety of diagnostics was used to study the plasma; these included optical streak and framing photography, schlieren and holographic interferometry with a *7* ns ruby laser, time−integrated soft X−ray pinhole photography and time−resolved observations using filtered X−ray PIN diodes. All these diagnostics viewed the fibre transversely. Light generated internally within the fibre was monitored simultaneously with the optical streak observations.

The optical observations show that the plasma initially expands with a velocity $\simeq 10^6$ cm s^{-1} which increases to $\simeq 5 \times 10^6$ cm s^{-1} at around current maximum. However, the expansion is not reproducible. This is due to $m=0$ instabilities which are clearly seen in the framing and schlieren photographs. These instabilities develop within the first *13* ns of the discharge when the current is still rising. The spacing between the instabilities is typically about *1* mm and so they are of a long wavelength ($\lambda >$ the initial fibre radius, a). In the framing photographs it is evident that there is axial motion of the instabilities. This motion is in both axial directions and occurs with a velocity of about 5×10^6 cm s^{-1}. The instabilities also expand radially with a similar velocity. The distorted disc−like structure of the instabilities observed in the schlieren photographs is due to a combination of this axial and radial motion during the duration of the laser

pulse. The observed behaviour of the plasma is independent of the initial fibre diameter.

The holographic interferometry observations show that there is a coronal plasma surrounding a central region of dense plasma. The diameter of this central region is the same as that seen in the streak and schlieren photographs. No transmission of the laser radiation through this central core is observed. This is in contrast to a reference hologram taken of the fibre prior to the discharge which shows that the fringes are continuous across the fibre; this shows that there *is* transmission of the laser through the fibre. This indicates that the plasma is optically thick. Assuming that the plasma emits as a blackbody over the spectral range of the streak camera (*300 – 700* nm), an electron temperature of between *10 – 30* eV is deduced from the streak photographs. Estimates of the electron number density ($n_e > 10^{20}$ cm^{-3}) in this central core confirm that the plasma is optically thick and that the blackbody radiation law is applicable. On the other hand, the coronal plasma has a typical density of 3×10^{18} cm^{-3} at the edge of the core which drops to about 10^{17} cm^{-3} at a radius of about *7* times the initial fibre radius during the early part ($\approx$ *20* ns) of the discharge.

The internal emission in the fibre, seen in the streak photographs, occurs within *5* ns of the discharge initiation. There is modulation of the early emission with a period of between *15 – 30* ns. At around the time of current maximum there is a large increase in this emission. These observations are independent of the initial fibre diameter. Normal (linear) heat conduction is too slow a process to account for this emission whilst shock heating depends on the fibre radius. This emission is most probably due to scintillation of the fibre core. The modulation period of the early intensity is consistent with the observed modulation of the time–resolved X–ray PIN diode signals. Since high energy photons are present there will be some degree of fluorescence. This is an ionising process; this, together with perhaps impact ionisation of the fibre by an electron beam means that current is able to diffuse into the fibre but it is not clear whether this would account for the intense emission at current maximum. However, as the calculations from the one–dimensional MHD code have shown, this intense emission is consistent with the centre of the fibre being heated very quickly by the process of radiative heat conduction which occurs at around the time of peak current.

Time–integrated soft X–ray pinhole photographs show a plasma column with a radius four times larger than the initial fibre. The photographs also show a number of bright, localised sources along the length of the fibre; the separation and size of these sources is consistent with the characteristics of the instabilities

observed with the optical diagnostics. These sources are less hot ($T \simeq 200$ eV) than the main core plasma ($T \simeq 500$ eV) but are denser ($n_e \simeq 9 \times 10^{18}$ cm^{-3}) and it is this that accounts for the intensity of their emission.

Most strikingly, the photographs show that the intensity is peaked towards the surface of the column. This clearly indicates that the plasma is formed on the surface of the fibre and that at the time of maximum X−ray emission there exists a sizeable fraction of the fibre that is not ionised. This is consistent with the holographic observations, where the estimated line density is far less than the solid line density indicating incomplete ionisation of the fibre. Since the density profile of the coronal plasma is peaked at the edge of the core, whilst the emission profile peaks towards the edge this means that the temperature is very strongly peaked towards the edge of the plasma. This indicates that the current is flowing in the outer regions of the plasma and not through the bulk of the fibre.

The pinhole photographs also show intense emission from the anode (and somewhat less so from the cathode). X−ray PIN diodes viewing the same region indicate that this emission is dominated by inner K−shell emission from the electrode material. The most probable cause for this is an interaction of an electron beam with the electrode material. Assuming such a process, then a beam of 30 keV electrons carrying a current of about 20 kA, with a lifetime of 50 ns is calculated from the intensity of the observed emission in the pinhole photographs.

The filtered PIN diode signals show that the radiation from the plasma is dominated by K−shell emission. The temperature peaks at around *1* keV and is due to the current flowing mostly in the outer plasma. After current maximum, an increase in number density leads to a fall in temperature; this is, however, a slow process lasting for quite a few hundred nanoseconds after peak current is reached.

7.3.1. Simulation of the Fibre Experiment

Computer simulations of the experiment have been performed by Dr. Gene McCall (Los Alamos National Lab., private communication). The simulations were performed using a one−dimensional Lagrangian code (RAVEN) and included radiation transport. SESAME equations of state for fused silica were used. The thermal and electrical conductivities were calculated using the transport coefficients of Lee and More (1984).

A digitised current waveform from a typical shot was taken as the input to the code. The calculations were started by placing two low density zones

($\rho = 2 \times 10^{-5}$ g/cc, $\Delta r = 2.5$ μm) at the outside of the fibre, with their initial temperature being 0.2 eV. The fibre itself was 125 μm in diameter, 5 cm in length, with an initial temperature of 0.026 eV (300 K). Plots of the radius, electron temperature, density and average ion charge are shown in figures 7.1 – 7.4 as a function of time for two cases:

(a) no radiation transport

(b) radiation included.

One immediately notices that only the outside of the fibre expands rapidly. The different lines on the plots indicate the different zone boundaries. After 20 ns only the outer three zones (i.e. the outer 7.5 μm of the fibre) have expanded to any great extent; even after 75 ns the number of zones to have really expanded is only seven (17.5 μm).

From the plot of electron temperature against time for the two different cases (a) and (b), one can see that radiation is mainly responsible for the heating of the fibre. We shall concentrate on this case.

The plot of density versus time shows that most of the fibre is still at solid density. At early times (the first 20 ns or so) the outer zone has a density $\rho \sim 10^{-5}$ g/cc which together with an effective ion charge, $Z_{eff} \simeq 5$, means that the electron number density is

$$n_e \simeq 1.5 \times 10^{18} \qquad [\mathrm{cm}^{-3}]$$

The agreement with the observed electron density at the core edge of $n_e = 3.0 \times 10^{18}$ cm^{-3} is excellent (perhaps this is not so surprising since a density of $\rho = 2 \times 10^{-5}$ g/cc, and hence $n_e \leqslant 10^{18}$ cm^{-3}, was originally imposed on these outer zones).

The second zone, which at $t = 25$ ns has expanded to a radius of ~ 130 μm has a density $\rho \sim 8 \times 10^{-4}$ g/cc and hence a corresponding electron number density of:

$$n_e \simeq 1.2 \times 10^{20} \qquad [\mathrm{cm}^{-3}]$$

which agrees well with the minimum density of the plasma ($\approx 3 \times 10^{20}$ cm^{-3}).

Figure 7.2 shows the temporal evolution of the electron temperature of the fibre plasma. The temperature reaches a value of ~ 14 eV at early times and this agrees well with the blackbody calculation presented in Chapter 4. One can see from the density plots in figure 7.3 that the core plasma is certainly dense enough to satisfy the criteria for LTE to hold.

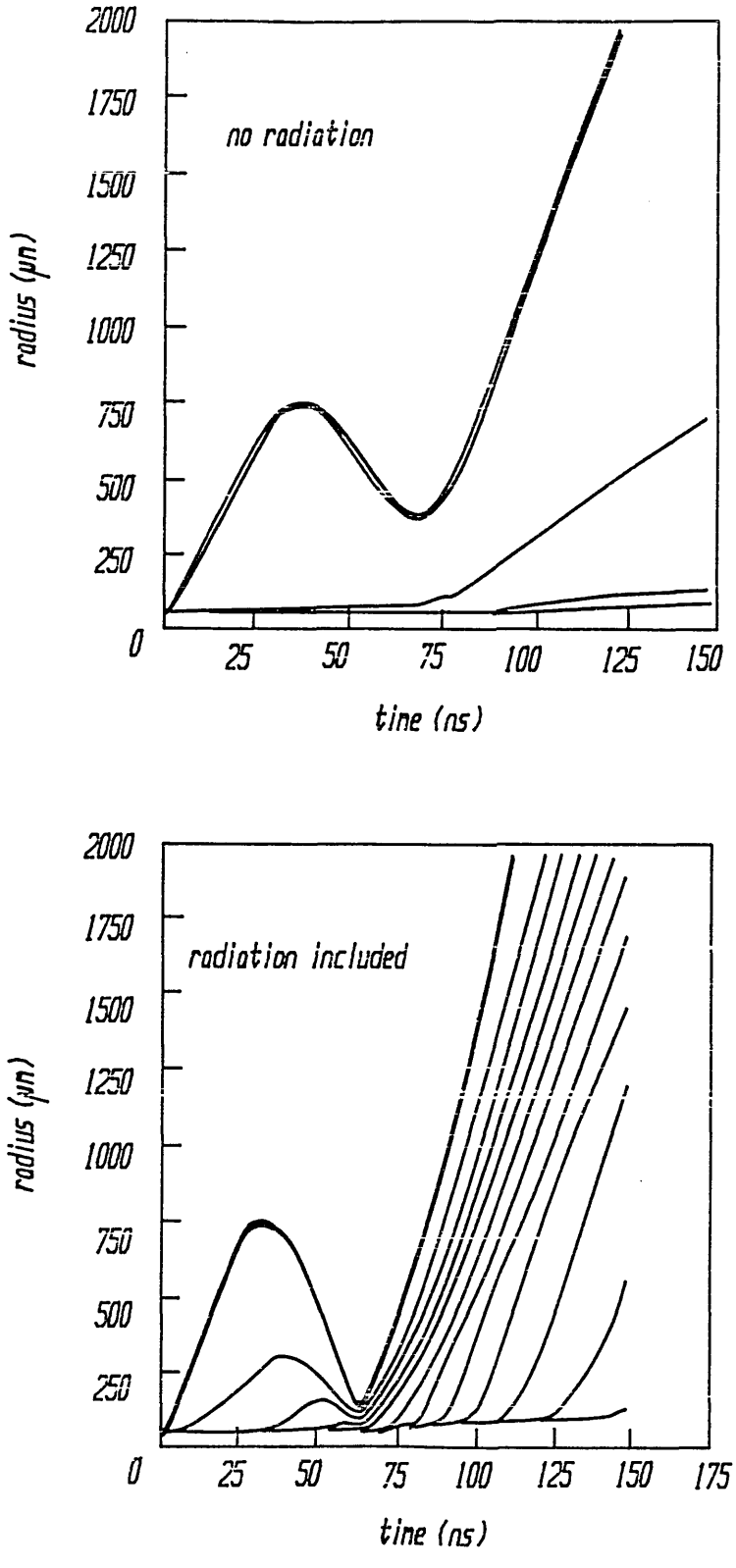


Figure 7.1: Plasma radius

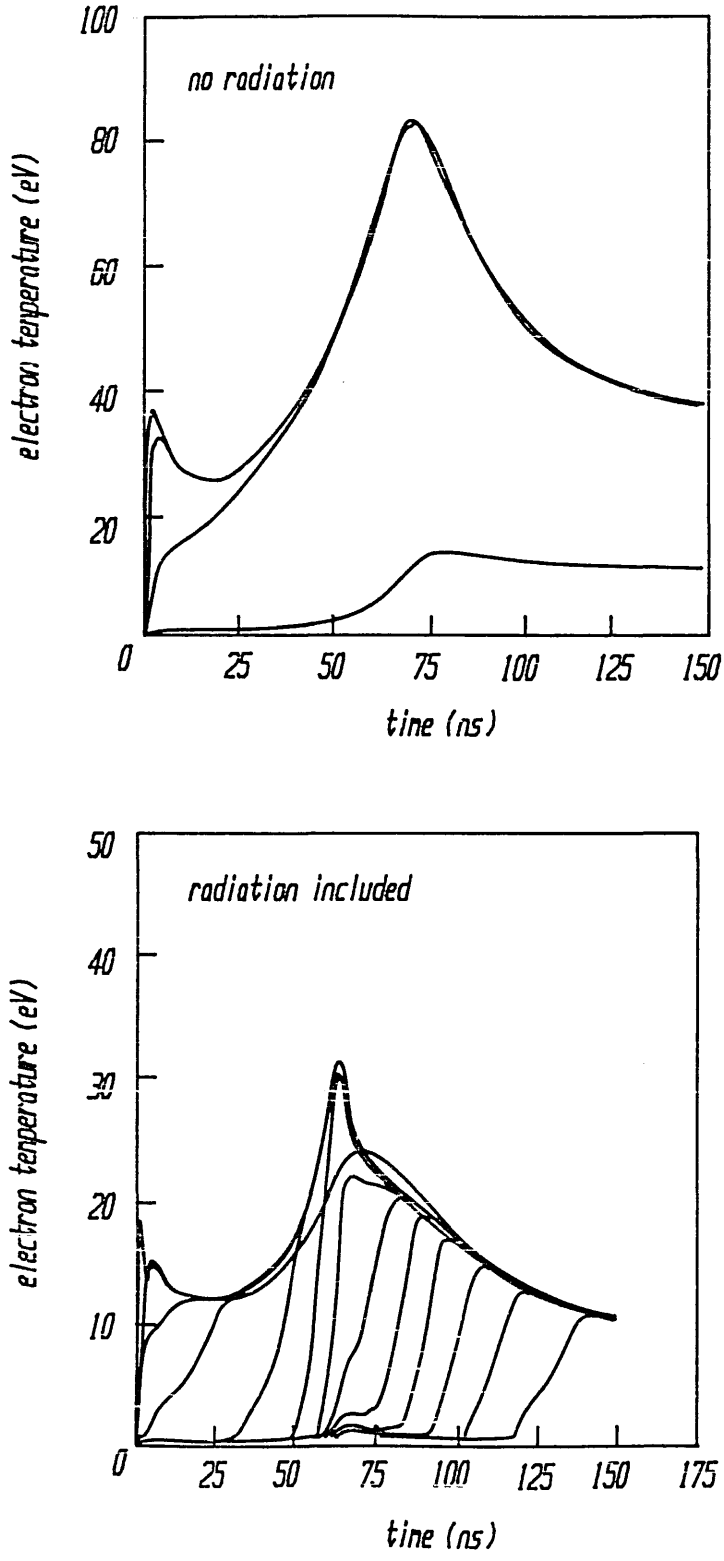


Figure 7.2: Electron temperature

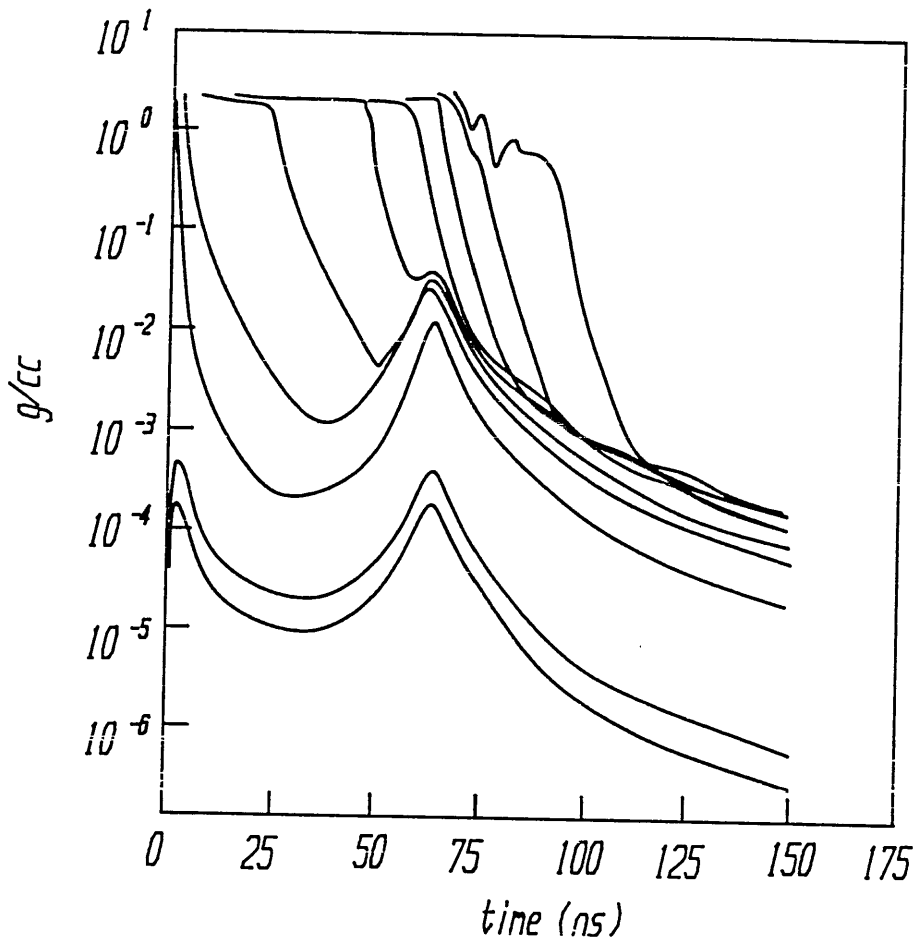


Figure 7.3: Mass density

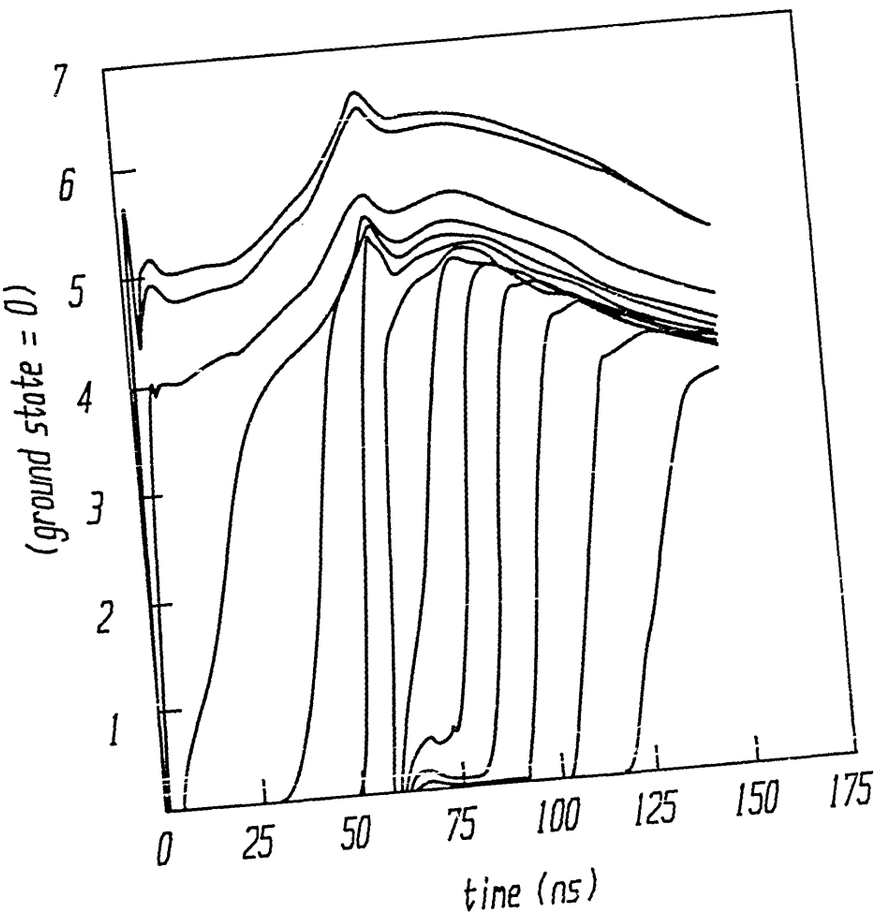


Figure 7.4: Average ion charge

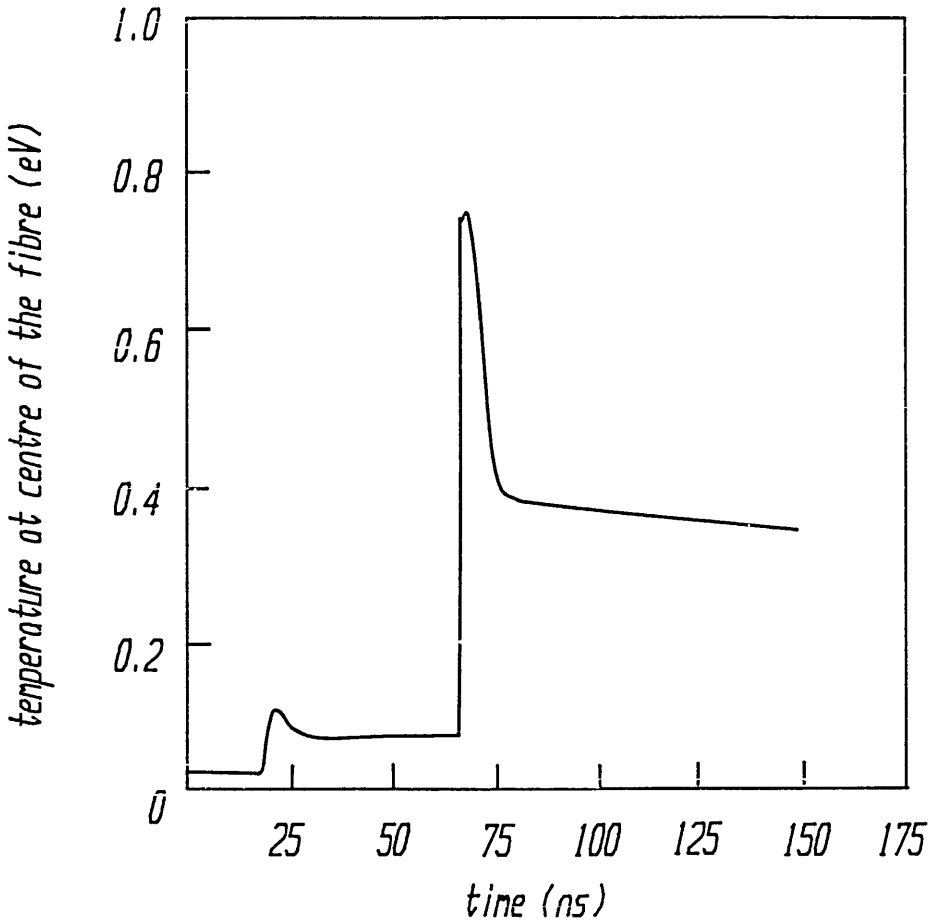


Figure 7.5: Heating of the centre of the fibre

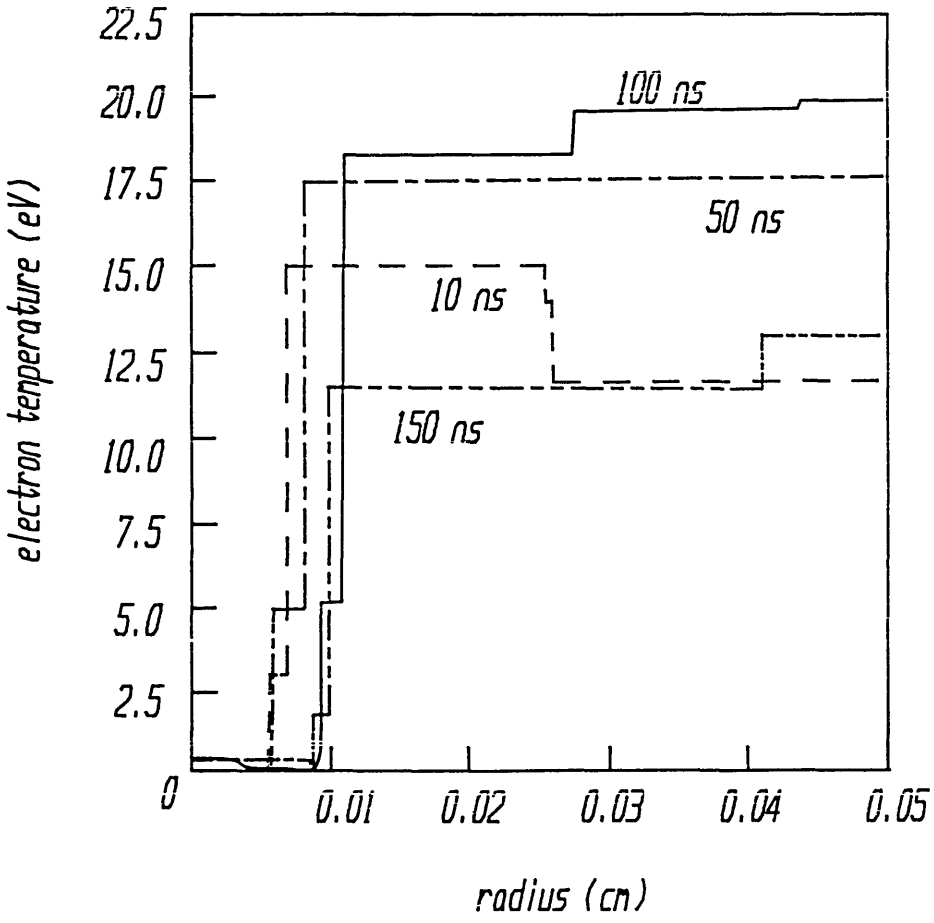


Figure 7.6: Radial electron temperature profile at different times

Figure 7.5 shows how the centre of the fibre is heated during the discharge. Figure 7.6 shows the electron temperatures as a function of radius at different times. The centre of the fibre is really heated very little with the greatest temperature ($\simeq 0.75$ eV) occurring at around current maximum (at a time $t \simeq 70$ ns). The outer zones of the plasma are the ones that are heated the most; a peak temperature of ~ 30 eV is reached about 60 ns into the discharge which again agrees remarkably well with the blackbody measurements presented in Chapter 4.

Some features predicted by the model are not observed in the experiment. Firstly, the code shows that the outer zones of the plasma are compressed at $t \simeq 35$ ns. From the code the outer zone initially expands with a velocity

$$v_{exp} \simeq 3 \times 10^6 \quad [\text{cm s}^{-1}]$$

whilst the second zone (at $t = 20$ ns) is expanding with a velocity

$$v_{exp} \simeq 8 \times 10^5 \quad [\text{cm s}^{-1}]$$

This increases to a maximum of $\sim 4 \times 10^6$ cm s^{-1} at $t = 30$ ns.

After the pinching these zones 'bounce' and then expand with typical velocities of $3 - 4 \times 10^6$ cm s^{-1}. All this is in contrast to the observed behaviour. The initial observed expansion is

$$v_{exp} \simeq 0.7 - 0.9 \times 10^6 \quad [\text{cm s}^{-1}]$$

whilst at $t = 55$ ns the pinch expands more rapidly:

$$v_{exp} \simeq 3 - 4 \times 10^6 \quad [\text{cm s}^{-1}]$$

Although the initial expansion of the second zone in the model is in good agreement with observations, as are the later velocities, the later expansion (after bouncing) occurs at later times than is observed experimentally. That the bouncing of the plasma is not observed in the experiment can be explained quite simply. The outer zones (which are the ones that bounce) are of a low density ($n_e \simeq 10^{18}$ cm^{-3}); the radiation from these regions would not be observed by the streak camera for the same reasons that the early part of the discharge was not observed (Chapter 4).

If the expansion is proceeding at the ion sound velocity then the temperature is given by:

$$T_e = (1.02 \times 10^{-6}\ c_s)^2(\mu/\gamma Z) \quad [\text{eV}]$$

where c_s is the ion sound velocity (cm s^{-1})

$\mu = m_i/m_p$

γ is the ratio of specific heats

Z is the effective charge.

Taking an early velocity, $c_s = 3 \times 10^6$ cm s^{-1}, $\mu = 20$, $\gamma = 5/3$, $Z = 5$ we get:

$$T_e = 23 \quad [\text{eV}]$$

This is slightly higher than the temperature calculated in the code but it is in good agreement.

One would also like to calculate the Bennett temperature and compare it with the above estimate. For this, one needs to know the line density and this is not easy to estimate from the plots as only the first three zones are clearly seen at early times. A lower estimate, taken by assuming that at $t = 20$ ns only the outer three zones contribute to the line density, is:

$$N_e \simeq 10^{19} \quad [\text{m}^{-1}]$$

This gives a Bennett temperature (with $I = 40$ kA) of:

$$T_e \simeq 38 \quad [\text{eV}]$$

This is again higher than the temperature presented in the computational plots, though the error could quite easily lie in an underestimation of the line density. Also notice that the line density is far from the solid density, again confirming that the fibre is far from being fully ionised in the early stages of the pinch formation.

We can use the equation relating the required dI/dt (for heating under pressure balance) to the line density and plasma temperature, to see if under the present conditions an expansion is expected. We have from Chapter 1:

$$dI/dt = 3.88 \times 10^{-3}\ N^{\frac{1}{2}}/(a^2 T_e) \quad [\text{As}^{-1}]$$

At $t = 20$ ns, $a = 575$ μm, $T_e = 38$ eV, $N = 10^{19}$ m^{-1}. Thus:

$$dI/dt \simeq 9.8 \times 10^{11} \qquad [\mathrm{As}^{-1}]$$

This is less than the measured dI/dt ($\sim 3 \times 10^{12}$ As^{-1}) and thus no expansion ought to be seen. However, if the line density had been underestimated, by say a factor of two, then the required dI/dt would be:

$$dI/dt \simeq 2.8 \times 10^{12} \qquad [\mathrm{As}^{-1}]$$

and in this case the plasma could well expand.

To understand how the fibre is heated we refer to figure 7.5 which shows the temperature at the centre of the fibre as a function of time. This peaks at $\simeq 0.8$ eV after a time $t = 70$ ns (at around current peak) and there is a smaller peak of $\simeq 0.1$ eV at $t = 20$ ns. It is not clear whether there is a correlation between this 'modulation' of the temperature and the modulation of the intensity of the observed internal fibre emission. The period of modulation is of the same order as the experimental observations; what is needed is for different diameter fibres to be modelled and to observe how the centre is heated in such cases.

We can estimate if the temperature at the fibre core (assuming it to be blackbody) can account for the intensity of the internally emitted light from the fibre. Since blackbody radiation is assumed then the internal fibre light is being emitted over an area πr_c^2, where r_c is the fibre core radius (4 μm). Only about 20% of this light will actually reach the streak slit. Then the intensity of the final image is:

$$I_f = K \int \frac{2ceT_e}{\lambda^4} \, 2\pi(\pi r_c^2)(0.2) d\Omega R(\lambda) d\lambda$$

following the procedure in Chapter 4 (and using the same notation).

Evaluating the integral we get:

$$T_e \simeq 2.4 \times 10^{-5} I_f \qquad [\mathrm{eV}]$$

where I_f is measured in the same units as I^i in Chapter 4.

Thus, to observe a temperature of $0.2 - 0.8$ eV requires a measured intensity of:

$$I_f \simeq 0.8 - 3.4 \times 10^4$$

The minimum measured intensity was:

$$I_f^{meas} \simeq 6 \times 10^3$$

Thus a temperature of 0.8 eV would certainly have been observable and this can account for the large increase in the intensity of the internal emission close to peak current. It is doubtful whether the earlier radiation at a temperature of $\simeq 0.2$ eV would have been observed and scintillation of the inner core remains the obvious explanation.

To summarise, the experiment can be modelled using a one-dimensional MHD model. The behaviour of the plasma predicted by the model is in good agreement with the experimental observations (e.g. the blackbody temperature, internal heating of the fibre core etc.). However, the model does not take into account the $m=0$ instability or any electron beam/plasma interaction. These processes give rise to localised phenomena (e.g. increased resistivity in the necked region of an instability, additional plasma heating due to the electron beam etc.) and a two-dimensional code is needed to incorporate these processes.

7.3.2. Initial Plasma Formation

The aim of the experiment was not to examine any specific stage of the fibre-plasma formation in detail but rather to investigate the general behaviour of such a plasma. Thus the initial plasma formation was not thoroughly investigated; yet, the internal emission from the fibre and the X-ray pinhole photographs have given an insight into these initial stages.

A preliminary review of the possible process of breakdown in the quartz fibre has been carried out by Malik (private communication). Here we give a brief summary of the possible processes responsible for the breakdown of the fibre.

According to Zenner (1934), breakdown occurs when the electrostatic field becomes sufficiently strong such that electrons are able to tunnel from the filled energy bands and so ionise the atoms of the insulator. The breakdown field, E_z, is given by (Franz, 1939):

$$E_z = 0.33 \times 10^6 \, (\Delta\varepsilon)^2 \qquad \text{[V/cm]}$$

where $\Delta\varepsilon$ is the energy band gap (eV).

Taking $\Delta\varepsilon \simeq 10$ eV we get $E_z \simeq 3 \times 10^7$ V/cm. The maximum applied field in the experiment is $E_a \simeq 250$ kV/cm. Even allowing for a magnification of this field (due to sharp edges etc.) of a factor of 2.5, the applied field, $E_a \simeq 650$ kV/cm, is still less than the required field E_z. Thus the breakdown in quartz does not occur due to this self−ionisation process.

Von Hippel (1938) has suggested that breakdown occurs due to electron avalanches through electron impact. This happens when the average electron gains more energy from the field, E_h, than it loses to the lattice. The equilibrium condition is:

$$(\partial\varepsilon/\partial t)_E = (\partial\varepsilon/\partial t)_{loss}$$

where $(\partial\varepsilon/\partial t)_E = eE_h\nu$

$(\partial\varepsilon/\partial t)_{loss} = hck\nu$

ν is the electron velocity

c is the acoustic velocity

k is the electron wave−vector

ν is the collision frequency.

One finds that for quartz:

$$E_h \simeq 10^8 \qquad \text{[V/cm]}$$

and again $E_a < E_h$. Thus this process does not explain the breakdown process in the fibre.

Finally, Shockley (1951) has attributed the breakdown in semiconductors to 'hot' electrons i.e. those in the tail of the electron distribution at higher energy levels in the presence of an external electrostatic field. In strong electric fields, the maximum energy of the 'hot' electrons is (Yamashita and Watanabe, 1954):

$$\hat{\varepsilon} = (E\lambda/2c)\sqrt{(kT/3m)} \qquad \text{[eV]}$$

where λ is the mean free path in the solid.

For quartz, one finds that $\hat{\varepsilon} \simeq 8$ eV. Although it is not definite, this avalanche process might produce the breakdown in the fibre.

In the absence of further experimental evidence of the breakdown phase, it is difficult to predict whether any of the above processes could lead to ionisation and breakdown of the fibre in the present experiment.

One point to note is that there will be a radial distribution of nuclei at the outer radius of the fibre because of the vapour pressure of the solid. The mean free path will be greatest in such regions whilst the refractive index will be reduced. So the speed of propagation of the electromagnetic field is greatest at the surface. This suggests that the breakdown is initiated at the surface of the fibre.

In addition, electrons emitted by the field at the cathode will cause impact ionisation and secondary electron emission at the surface leading to a surface breakdown. This is consistent with the observations of the internally emitted fibre light (which shows that current takes a long time to diffuse into the fibre) and also with the X−ray pinhole photographs, which show intense emission from the edge of the fibre suggesting a strong surface plasma.

7.4. Summary and Future Work

Although the fibre pinch experiment has characterised the general behaviour of the plasma, a lot of questions still remain to be answered. Firstly, the initial breakdown of the fibre has not been tho roughly investigated. This would require measuring the voltage across the pinch and the time delay between that and the start of current flow. The question of how quickly does the current penetrate the fibre could be investigated by perhaps coating the fibre with layers of different materials and looking at the characteristic X−ray spectrum of each as the current burns its way through. It could even be feasible to perform Faraday rotation measurements using the inside of the fibre to determine the current distribution. There is still no satisfactory explanation of the motion of the instabilities; one could try to correlate the instabilities with the localised sources seen in the pinhole photographs. If there is an electron beam present (as the evidence suggests) then there might be an interaction between it and these sources (as in a gas−puff − see Deeney, Ph.D. Thesis, 1988). Although these and other questions remain to be answered, the present experiment has provided an insight into the formation, dynamics and stability of a plasma produced from insulating fibres.

Recent theoretical studies (Haines 1988, Robson 1987) suggest that high densities and temperatures may be achieved in deuterium fibre pinches through the process of radiative collapse. A stationary equilibrium pinch can only carry one

current – the Pease–Braginskii current. Once this limit is exceeded then the pinch will start to radiate more energy than is being delivered to it; to maintain an equilibrium, the pinch will contract – this is known as radiative collapse and is a familiar process in the latter stages of dying stars.

The Pease–Braginskii current for a deuterium fibre is about *1.2* MA. Such currents are quite attainable with modern technology and there are already projects underway to examine this process. However, as the work in this thesis has shown, the problem of instabilities is always present. How to force current to flow through the whole fibre rather than its surface has yet to be answered. Some form of preionisation of the fibre might be necessary although it is not clear how this might be achieved. And yet, an $m=0$ instability might not be an unsavoury companion for Z–pinches; for if high densities and temperatures could be achieved in the necked regions of this instability and thermonuclear burn initiated, then this could lead to burn all along the pinch via a burn wave which propagates along the pinch axis (Vikhrev and Ivanov, 1985).

Z–pinches still remain a simple and attractive proposition for controlled nuclear fusion as well as having enormous potential for exotic things such as X–ray lasers. The field is beginning a most promising phase which should prove to be both interesting and fruitful.

APPENDIX A

Transmission Line Simulation

A.1. BERTHA – A Versatile Transmission Line Code

BERTHA can be used to simulate any electrical system that can be represented by a configuration of transmission line elements. It is a versatile code, capable of modelling, for example, magnetically insulated transmission lines, plasma opening switches, imploding plasma loads and discrete element electrical networks. The code works, in essence, by calculating the electrical behaviour of the system by repeatedly summing the reflected and transmitted waves at the ends of each element in the network. The original version of this code was written by W.H. Lupton (N.R.L.) and further improved by D.D. Hinshelwood (N.R.L./Jaycor). BERTHA was written in BASIC and the author subsequently wrote a version in FORTRAN.

A transmission line supports waves of voltage and current propagating in two directions. The sum of these two travelling waves determines the standing wave voltage and current which are physically measured. The instantaneous standing wave voltage, V and current, I at a given point are:

$$V = V_1 + V_2$$

$$I = (V_1 - V_2)/Z_0$$

where $V_{1,2}$ is the voltage of the wave travelling out/into the line;
Z_0 is the line impedance (see figure A.1).

A wave incident on an impedance discontinuity will be split into reflected and transmitted waves:

$$r = (Z_1 - Z_0)/(Z_1 + Z_0)$$

$$t = 2Z_1/(Z_1 + Z_0)$$

where $Z_{0,1}$ are the line/load impedances;
r,t are the reflection/transmission coefficients.

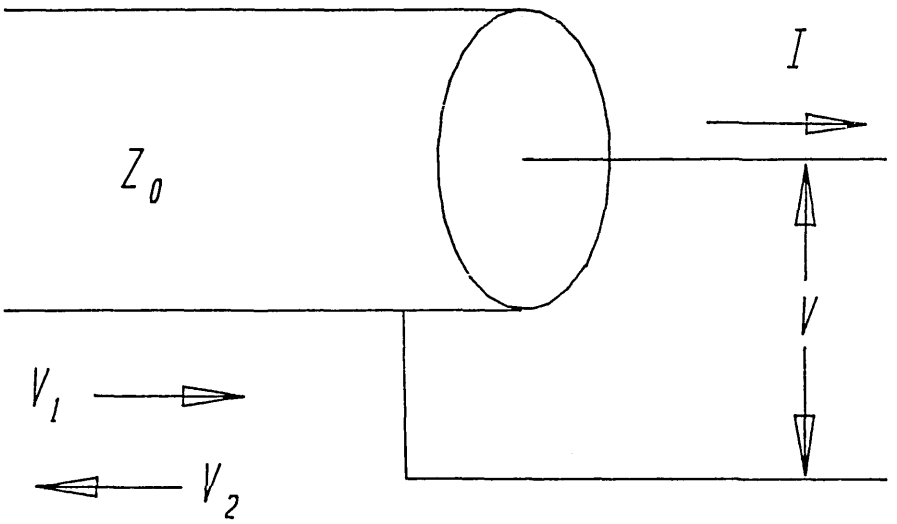


Figure A.1: Definition of the two travelling voltage waves

Reactive loads would appear to be more cumbersome to treat since the reflection depends on the time rate of change of the incident pulse. However, the problem can be simplified by noting that an inductor is actually a very short, high impedance transmission line element. The line impedance, Z, is related to the total lumped inductance, L by:

$$L = Z\tau$$

where τ is the one−way transit time of the element.

Likewise, a capacitor is a short, low impedance line element, with lumped capacitance C given by:

$$C = \tau / Z$$

The representation of reactive components by short line elements in effect replaces the differential equations involved with finite difference equations and the operations of integration and differentiation are replaced by simple arithmetic operations.

In fact, entire networks of passive lumped parameter elements may be replaced by transmission line element configurations. To predict the behaviour of these and and other systems it is only necessary to account for the waves running around the configuration.

A.2. Description of the Program

Rather than following particular waves around the circuit, the program keeps track of the instantaneous values of the two travelling voltage waves at the two ends of each line element:

V_1 is the the voltage wave incident on a junction from within an element;

V_2 is the wave leaving the junction, travelling into the element.

The wave V_2 is made up of the reflected portion of V_1 from the same line element plus the transmitted portion of V_1's from the other elements connected to the junction.

For a configuration of N elements there are $4N$ quantities which must be recalculated at each timestep. There are N pairs of equations describing the transit of waves within elements: the incident wave (into a junction) at an element end is the wave that left the opposite end of the same element at the

appropriate time in the past (determined by the element transit time). The remaining $2N$ equations describe the reflection and transmission of waves at the junctions. Figure A.2 shows an example of a transmission line configuration together with the relevant equations.

The first four equations are in a convenient form for programming; the last four can be put in a similar convenient form. The junctions handled by BERTHA join at most three element ends (figure A.3). Hence, the general expression for a wave leaving a junction (for example, junction element I – figure A.3) is:

$$V_2(I,t) = \alpha_{II}V_1(I,t) + \beta_{JI}V_1(J,t) + \beta_{KI}V_1(K,t)$$

where α_{II} is the reflection coefficient;

β_{JI}, β_{KI} are the transmission coefficients.

The values α_{II}, β_{JI}, β_{KI}, J and K are sufficient to specify the value of the reflected wave leaving an element end I – they are stored in an array $M(2N,5)$. The equations describing waves leaving junctions are now all in the form:

$$V_2(I,t) = M(I,1)*V_1(I,t) + M(I,2)*V_1(M(I,4),t) + M(I,3)*V_1(M(I,5),t)$$

The junction properties are stored in an array $J(N+1,4)$. The first entry is the junction type (of which there are six), the following two entries are the element ends comprising the junction and the last entry in J is either the third element end of a three element junction or the value of any resistance included in a two element junction. It is then straightforward to convert the array J to the array M for the purpose of calculating the voltages V_2.

Initial voltages and currents are just superpositions of two travelling waves, determined by:

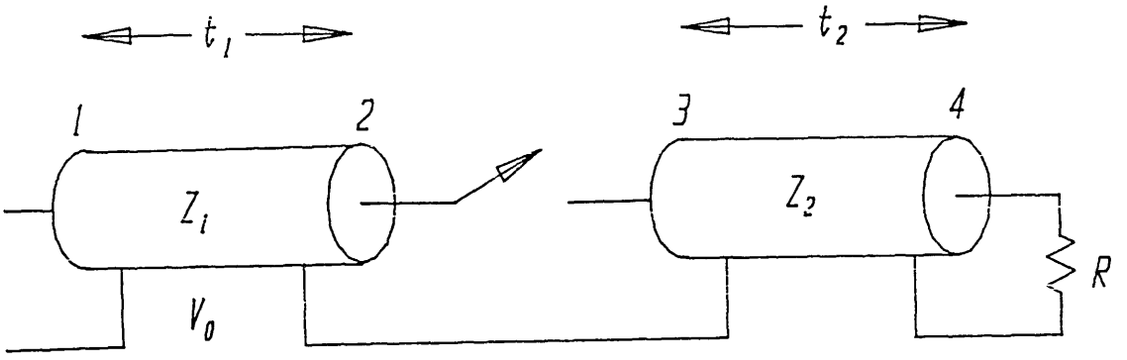
$$V_+ = (V_O + I_OZ)/2$$

$$V_- = (V_O - I_OZ)/2$$

At the start of execution, the array V_2 is backfilled to include these initial travelling waves.

Switches are represented by resistances whose values change from $0 \rightarrow \infty$ (or vice versa) at a preset time or voltage. They are simple to incorporate as switching just corresponds to a multiplication of the reflection coefficient by -1.

Inductive characteristics of a real switch can be modelled by adding a suitable



Element Z_1, initial voltage V_0 is discharged at t=0 into Z_2

$$V_1(1,t) = V_2(2,t-t_1)$$
$$V_1(2,t) = V_2(1,t-t_1)$$
$$V_1(3,t) = V_2(4,t-t_2)$$
$$V_1(4,t) = V_2(3,t-t_2)$$
$$V_2(1,t) = V_1(1,t)[\infty - Z_1]/[\infty + Z_1]$$
$$V_2(2,t) = V_1(2,t)[(Z_2-Z_1)/(Z_2+Z_1)] + V_1(3,t)[2Z_1/(Z_1+Z_2)]$$
$$V_2(3,t) = V_1(3,t)[(Z_1-Z_2)/(Z_1+Z_2)] + V(2,t)[2Z_2/(Z_1+Z_2)]$$
$$V_2(4,t) = V_1(4,t)[(R-Z_2)/(R+Z_2)]$$

Figure A.2: An example of a transmission line configuration

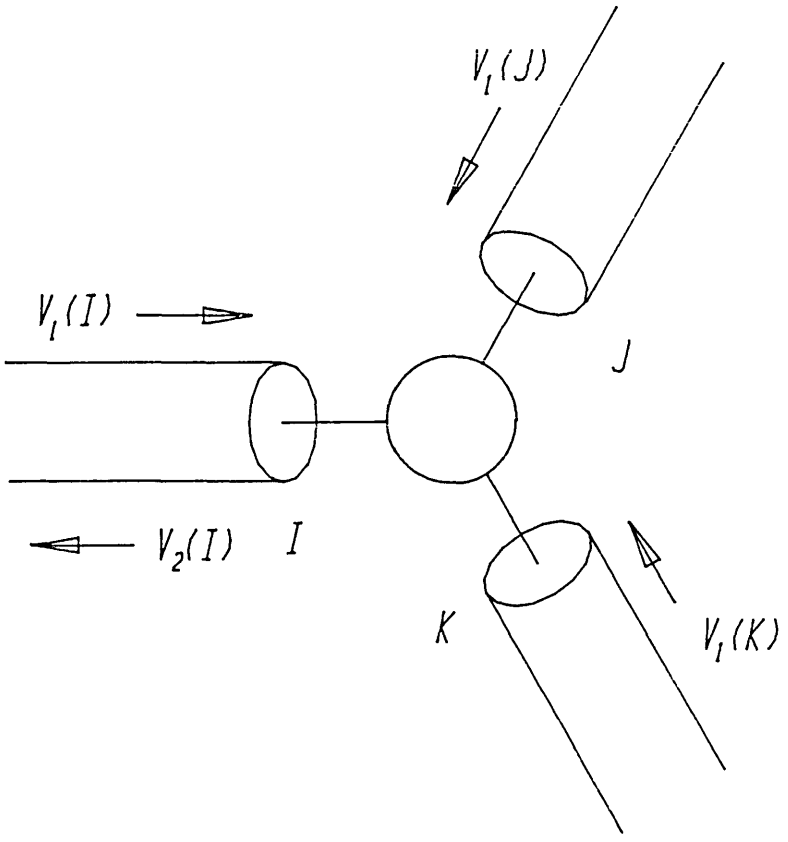


Figure A.3: A general three element junction

short line element. A more detailed description, such as resistive risetimes, requires variable resistances. All resistances may be varied during program execution by using external subroutines to which the time, voltage across and current through each resistance are supplied at each timestep.

The line element impedances may be varied in exactly the same fashion. When this is done, the values of the travelling wave voltages on that element must in general be changed to take into account the $I(dL/dt)$ and $V(dC/dt)$ terms. The change in element impedance is assumed to be instantaneous at each timestep, so no charge or magnetic flux can flow into the element during the change.

The charge, Q and flux, Φ are given by:

$$Q = CV = (\tau/Z)(V_1 + V_2)$$

$$\Phi = LI = \tau(V_1 - V_2)$$

where τ is the element transit time.

From charge and flux conservation, the new values of V_1 and V_2 are:

$$V_1' = [V_1(R_Z + 1) + V_2(R_Z - 1)]/2$$

$$V_2' = [V_2(R_Z + 1) + V_1(R_Z - 1)]/2$$

where $R_Z = Z'/Z$ (Z' is the new line impedqnce).

V_1 and V_2 must be corrected for each timestep of the element length. However, the correction is greatly simplified when modelling a changing lumped parameter element:

$$V_{1,2}' = V_{1,2} \qquad \text{for an inductor}$$

$$V_{1,2}' = V_{1,2}R_Z \qquad \text{for a capacitor.}$$

The memory requirements of BERTHA are reduced in two ways:

(a) at each timestep $V_1(t)$ is calculated from $V_2(t-\tau)$ (where τ is the one-way transit time in the element) and $V_2(t)$ is calculated from all of the V_1's entering the junction. Hence it is only necessary to know the value of V_1 for a single timestep. So V_1 is dimensioned $V_1(2N)$;

(b) it is never necessary to know the value of V_2 at a time further back in the past than the transit time of the longest element, $L0$. So V_2 is dimensioned

$V_2(2N,L0)$. The entries in V_2 are continually written over in a cyclical fashion.

The program's versatility comes from the fact that the configuration is alternatively considered to be a collection of separate elements and then a collection of separate junctions. This also makes the entry of data very easy. Figure A.4 is a schematic showing the main steps within the program.

There are two major limitations of the program. Firstly, BERTHA deals with idealised, one−dimensional transmisison line elements, supporting only TEM modes. Errors may result in modelling two−dimensional structures since the solutions will, in general, involve higher order TE and/or TM modes. At times it might be possible to simulate 2D effects by a suitable choice of configuration.

Secondly, the finite difference nature of this program can cause errors when the values of resistors and element impedances are functions of the electrical quantities. It may be that the solution diverges from the correct one or that numerical instabilities develop. In general, when resistances or impedances are varies, one has to check that the calculated solution does not change greatly when the run is repeated with a smaller timestep.

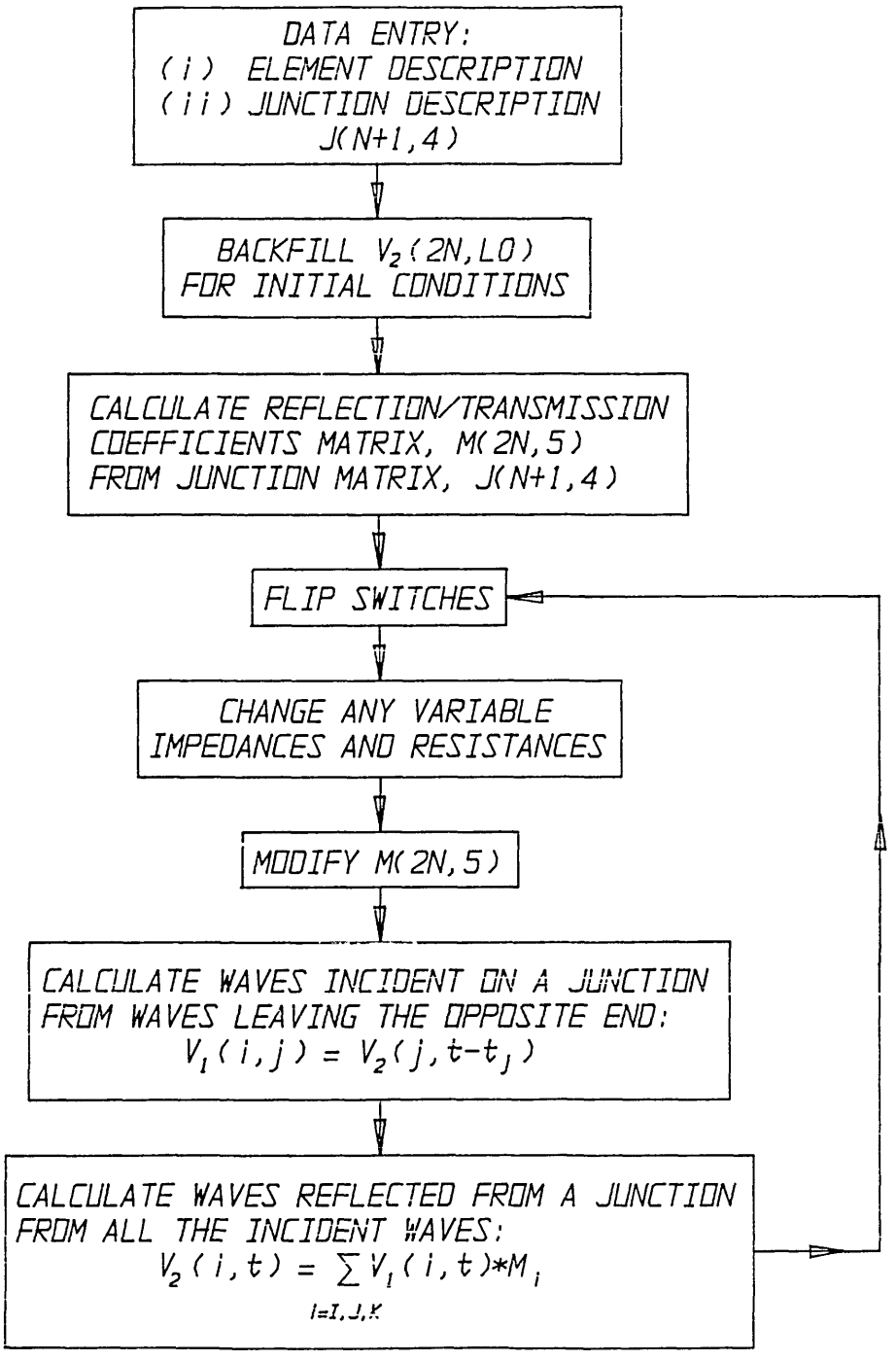


Figure A.4: Schematic of the general program

APPENDIX B

How to Determine Number Density Profiles

B.1. Holography and the Abel Transform

Optical emission or transmission is often used to obtain experimental measurements of radially symmetric sources (such as Z−pinch plasmas). The line−of−sight projection of the emission or transmission coefficients onto a one−dimensional axis can be used to determine the radial profile of the source.

The measured intensity, $I(y)$, is related to the emission coefficients, $\epsilon(r)$, via the Abel transform:

$$I(y) = 2 \int_{y}^{\infty} \frac{r\epsilon(r)}{(r^2 - y^2)^{\frac{1}{2}}} \, dr \qquad (1)$$

where y is the displacement of the intensity profile

r is the radial distance in the source.

The reconstruction of $\epsilon(r)$ from $I(y)$ is known as the inverse Abel transform, and is given by:

$$\epsilon(r) = -\frac{1}{\pi} \int_{r}^{\infty} \frac{(dI/dy)}{(y^2 - r^2)^{\frac{1}{2}}} \, dy \qquad (2)$$

In holography, the quantity of interest is not the intensity produced by the emission coefficients but rather the optical phase changes introduced by the plasma and the subsequent fringe pattern. In this case, we substitute $f(r)$ for $\epsilon(r)$ and $F(y)$ for $I(y)$, where:

$$f(r) = \mu - 1$$

is the plasma refactive index profile and $F(y)$ is the recorded fringe profile (in the units of fringe spacing). Thus, by measuring the the fringe profile in the reconstructed hologram, it is possible to recover the electron number density profile (through μ − see Chapter 5, section *5.4.*) by solving the inverse Abel transform.

B.2. Solution of the Inverse Abel Transform

Since the fringe profile, $F(y)$, is a data set consisting of a finite number of points then the simplest approach to solving the problem is to divide the circular plasma column into a finite number of shells, I, of thickness Δr; one then assumes that within each shell the function $f(r)$ is a constant. The laser is assumed to pass through the plasma column without deviation (there is invariably deviation, however, and thus errors are introduced – this will be discussed later).

The simplest way to approximate the derivative dF/dy is to interpolate the fringe data by assuming that $F(y)$ varies linearly with y^2 between each data point (see e.g. Vest,, 1975). Thus, in the shell $y_i \leqslant y \leqslant y_{i+1}$ we get:

$$\frac{dF}{dy} = 2\,\frac{(F_{i+1} - F_i)}{(y_{i+1}^2 - y_i^2)}\,y$$

The profile, f_i, in each shell is then:

$$f_i = -\frac{1}{\pi}\sum_{k=1}^{I-1} 2\,\frac{(F_{k+1} - F_k)}{(y_{i+1}^2 - y_i^2)}\int_{r_k}^{r_{k+1}} \frac{y\,dy}{(y^2 - r^2)^{\frac{1}{2}}}$$

The integral in the summation is equal to:

$$\Delta r\left[[(k+1)^2 - i^2]^{\frac{1}{2}} - (k^2 - i^2)^{\frac{1}{2}}\right]$$

whilst the denominator, in the approximation of the derivative, is:

$$y_{i+1}^2 - y_i^2 = (\Delta r)^2(2k + 1)$$

Thus, the numerical solution of equation (2) is:

$$f_i = -\frac{2}{\pi\Delta r}\sum_{k=i}^{I-1} B_{ki}(F_{k+1} - F_k) \qquad (3.a)$$

where:

$$B_{ki} = \frac{[(k+1)^2 - i^2]^{\frac{1}{2}} - (k^2 - i^2)^{\frac{1}{2}}}{(2k + 1)} \qquad (3.b)$$

This can now be solved trivially using a computer. The radial profile, $f(r)$, can also be recovered from the fringe data in a similar fashion by solving the

Abel transform (equation (1)) rather than its inverse. The method involves solving a set of coupled equations. In this case one needs to integrate from the outside of the cylinder towards the centre since $f(r)$ needs to be known at all points preceding the one being currently determined. By solving equation (2) directly, the procedure is much simplified.

B.3. Errors due to Refraction

In the above analysis, it was assumed that each ray travelled in a straight line as it traversed the plasma. However, due to refractive index gradients within the plasma, this will not be the case; the optical pathlength is thus altered not only because the deflected ray now travels a greater distance but because it also experiences a change in refractive index as it does so.

Let us first consider a simplified geometry where the ray travels in the $x-$direction and the refractive index gradient is in the $y-$direction. We consider only a linear variation of $\mu(y)$:

$$\mu(y) = \mu_0 + (d\mu/dy)(y - y_0) \tag{4}$$

The beam trajectory is given by (see Vest p.329, 1975):

$$y - y_0 = (1/2)(\mu'/\mu)x^2 \tag{5}$$

where $\mu' = d\mu/dy$ and only small gradients have been considered.

The optical pathlength through the plasma is given by:

$$\Delta = \int_{x=0}^{L} \mu(y)[1 + (dy/dx)^2]^{\frac{1}{2}} dx \tag{6}$$

where L is the size of the plasma.

Substituting into equation (6) from equations (4) and (5) gives:

$$\Delta = \mu_0 L[1 + (1/3)(\mu'/\mu_0)^2 L^2] \tag{7}$$

where terms less than $(\mu'/\mu_0)^2$ have been neglected.

The first term in equation (7) is that due to an undeflected ray; The second

term is that due to refraction.

With a lens in place, the interferogram is formed by imaging a plane $x=x_f$ (in the plasma) onto a screen. The expression relating the refractive index to the fringe profile, $F(y)$, is then given by (Vest, 1975):

$$\mu - \mu_0 = F(y)(\lambda / L) - \mu_0 L(\mu' / \mu_0)^2[(L/3) - (x_f/2)] \qquad (8)$$

Again, the first term on the RHS of equation (8) is as normal (see Chapter 5) whilst the second term is that due to refraction. As can be seen, by careful positioning of the imaging lens the error due to refraction can be eliminated.

If we consider the general case of a plasma with a non-uniform refractive index $\mu(x,y)$, then the trajectory of a light beam, $y = f(x)$, is determined by Fermat's principle:

$$\delta \int \mu(x, f(x))[1 + (df/dx)^2]^{\frac{1}{2}} dx \qquad (9)$$

i.e. the beam travels the shortest possible optical path.

This equation reduces to:

$$\frac{d^2y}{dx^2} = \frac{1}{\mu}\left[\frac{\partial \mu}{\partial y} - \frac{\partial \mu}{\partial x}\frac{dy}{dx}\right][1 + (dy/dx)^2] \qquad (10)$$

which describes the beam's trajectory through the plasma (see Matsumoto *et al.*, 1981).

The phase term is then given by:

$$\Phi = \frac{2\pi}{\lambda} \int_x \mu(x,y)[1 + (dy/dx)^2]^{\frac{1}{2}} dx \qquad (11)$$

In their paper, Matsumoto *et al.* solve this equation for various density profiles and calculate the errors involved, due to refraction. They find that even with a lens in place, it must be critically aligned and even then errors of 5% or more can be be introduced unless the fringe patterns close to the plasma are imaged.

B.4. Other Methods of Solving the Problem

Since completing this thesis, the author came upon two new methods for inverting Abel's integral equation. These achieve a far greater accuracy than the method outlined in section *B.2* and are to be preferred to it. Regrettably, the author did not have time to implement either of these methods which are now briefly outlined in this last section.

The first method is due to Moshe Deutsch and Israel Beniaminy (1982). It eliminates the need to differentiate any of the data and hence reduces the errors by an order of magnitude compared to the above method (since differentiation amplifies the random errors in the data).

We start with the Abel transform of the radially symmetric function, $f(r)$:

$$I(y) = 2 \int_y^1 \frac{r f(r)}{(r^2 - y^2)^{\frac{1}{2}}} \, dr \qquad (12)$$

where $I(y)$ is the measured intensity and the source radius is normalised to unity.

The inverse of equation (12) is:

$$f(r) = - \frac{1}{\pi} \int_r^1 \frac{I'(y)}{(y^2 - r^2)^{\frac{1}{2}}} \, dy \qquad (13)$$

where $I'(y) = dI(y)/dy$.

The standard procedure is to solve equation (13) numerically. This involves differentiation of the intensity data and errors in that can thus be greatly amplified.

Instead, we directly integrate equation (13) by parts, giving:

$$f(r) = - \frac{1}{\pi} \left\{ \left[\frac{I(y)}{(y^2 - r^2)^{\frac{1}{2}}} \right]_r^1 + \int_r^1 \frac{y I(y)}{(y^2 - r^2)^{3/2}} \, dy \right\} \qquad (14)$$

After evaluating the term in the square brackets we get:

$$f(r) = - \frac{1}{\pi} \left\{ \frac{[I(1) - I(r)]}{(1 - r^2)^{\frac{1}{2}}} + \int_r^1 \frac{y[I(y) - I(r)]}{(y^2 - r^2)^{3/2}} \right\} \qquad (15)$$

This is the derivative−free inversion formula. The singularity of the integrand at $y=r$ is integrable and can be taken care of numerically by a procedure which does not require the value of the integrand at the limits of integration (see e.g. Robinson, 1971). The above authors conclude that for any but the highest accuracy data, equation (15) yields *"significantly better results for f(r) than equation (13) even when fairly closely spaced I(y) data is available"*.

The second method formulates the Abel inversion in terms of transforms (Montgomery Smith *et al*, 1988). The noise in the data can be filtered in the frequency domain of the transform and the determination of the axis of symmetry can be done in a systematic rather than *ad hoc* fashion.

The essence of the method is as follows:

If the substitution $r = (x^2 + y^2)^{\frac{1}{2}}$ is made in equation (1), then $I(y)$ can be written as:

$$I(y) = \int_{-\infty}^{\infty} f([x^2 + y^2]^{\frac{1}{2}})dx \qquad (16)$$

The one−dimensional Fourier transform of equation (16) is:

$$F[\,I(y)\,] = \int_{-\infty}^{\infty}\int_{-\infty}^{\infty} f([x^2 + y^2]^{\frac{1}{2}})\exp(-i2\pi yq)dxdy \qquad (17)$$

If the variables of integration are now changed from Cartesian to polar coordinates, it can be shown that:

$$F[\,I(y)\,] = 2\pi\int_{0}^{\infty} rf(r)J_0(2\pi rq)dr \qquad (18)$$

where $J_0(...)$ is the zero−order Bessel function.

The right−hand side of equation (18) is the zero−order Hankel transform of $f(r)$, whose inverse is identical in form to the forward transform. The function $f(r)$ can thus be recovered by taking the inverse Hankel transform of the Fourier transform of the projected intensity, $I(y)$:

$$f(r) = 2\pi\int_{0}^{\infty} qJ_0(2\pi rq)\int_{-\infty}^{\infty} I(y)\exp(-i2\pi yq)dydq \qquad (19)$$

As can be seen, this technique avoids the singularity at the lower limit of integration. Also, after the Fourier transform of $I(y)$, filters can be applied to the frequency domain to reduce noise considerably and smooth the data in a known and systematic manner. However, the technique demands that the data be symmetric about the y−axis and one needs a procedure to determine the axis of symmetry of the data. These points are fully discussed in the paper by Montgomery Smith *et al* (1988).

REFERENCES

Aglitskii E.V., Antsiferov P.S. and Panin A.M.
Sov. J. Plasma Phys. 11(3), 159 (1985).

Alfven H. and Smars E.
Nature 188, 801 (1960).

Allen C.W. *'Astrophysical Quantities'* (Athlone Press, 1973).

Alpher R.A. and White D.R.
Phys. Fluids 2(2), 153 & 162 (1959).

Aranchuk L.E. *et al.*
Sov. J. Plasma Phys. 12(11), 765 (1986).

Bekefi G. *'Radiation Processes in Plasmas'* (J. Wiley, 1966).

Book D.L. *'N.R.L. Plasma Formulary', Publication 0084–4040* (1986).

Book D.L., Ott E. and Lampe M.
Phys. Fluids 19(12), 1982 (1976).

Born M. and Wolf E.
'Principles of Optics' (Pergamon Press, 1970).

Bowers E.A. and Haines M.G.
Phys. Fluids 14, 165 (1971).

Carslaw H.S. and Jaeger J.C.
'Conduction of heat in solids' (Oxford Univ. Press, 1959).

Challis C.D. *Ph.D. Thesis, Univ. Lond.* (1986).

Choi P. *Ph.D. Thesis, Univ. Lond.* (1983).

Coppins M. *Plasma Phys. and Contr. Fusion* 30, 201 (1988).

Coppins M., Chittenden and Culverwell I.D.
Internal Report DZP/P44.

Coppins M., Culverwell I.D. and Haines M.G.
Phys. Fluids 31(9), 2688 (1988).

Dangor A.E. *et al*
Proc. First Conf. on Dense Z–Pinches for Fusion
Alexandria, U.S.A. (1984).

Deeney C. *Ph.D. Thesis, Univ. Lond.* (1988).

De Michelis C. and Mattioli M.
Nuclear Fusion 21(6), 677 (1981).

Dodel G. and Kunz W.
Appl. Optics 14(7), 1601 (1975).

Dolan T.J. *'Fusion Research': Vol.I* (Pergamon Press, 1982).

Dreicer H. *Phys. Rev.* 115, 238 (1959).

Dyson N.A. *'X−rays in atomic and nuclear physics'* (Longman, 1973).

Ekdahl C.A. *Rev. Sci. Instr.* 51, 1645 (1980).

Fälthammer C.G.
Phys. Fluids 4(9), 1145.

Favre−Dominguez M.B.
Ph.D. Thesis, Univ. Lond. (1985).

Figura E.S., Choi P., Dangor A.E. and McCall G.H.
Bull. A.P.S. 32(9), 1757 (1987).

Franz W. *Zeits. f. Physik* 113, 607 (1939).

Freidberg J.P.
Rev. Mod. Phys. 54, 801 (1982).

Garanin S.F. and Chernyshev Yu.D.
Sov. J. Plasma Phys. 13(8), 562 (1987).

Gatenby P.V. and Walker A.C.
UKAEA Report: CLM−R192, Culham Laboratories (1979).

Goldsmith A., Waterman T.E. and Hirschhorn H.J.
'Handbook of thermo−physical properties of solid materials', Vol. III: Ceramics VII−C−6 (Macmillan, 1961).

Griem H.R. *'Plasma Spectroscopy'* (McGraw−Hill, 1964).

Grover F.W. *'Inductance Calculations, Working Formulas and Tables'* (Dover Publications, 1946).

Haines M.G. *Phys. Soc. Lond. Proc.* 76, 250 (1960).
J. Phys. D: Appl. Phys. 11, 1709 (1978).
Phil. Trans. R. Soc. Lond. A300, 649 (1981).
Physica Scripta Vol. T2/ 2, 380 (1982).
'An analytic model of radiative collapse of a z−pinch' (1988 − to be published in *Plasma Phys. and Cont. Fusion*).

Hammel J.E., Scudder D.W. and Schlachter J.S.
Nucl. Instr. and Meth., 207 (1983).

Huddlestone R.H. and Leonard S.L.
'Plasma Diagnostic Techniques' (Academic Press, 1965).

Jahoda F.C. and Siemon R.E.
Los Alamos Report LA−5058−MS (UC−37) (1972).

Kadomtsev B.B.
'Reviews of Plasma Physics', Vol. 2, 153 (1966).

Kaye G.W.C. and Laby T.H.
'Tables of Physical and Chemical Constants' (Longman, 1986).

Keilmann F. *Plasma Phys.* 14, 111 (1972).

Kies W. and Sethian J.D.
'Transformation of solid state fibres into pinch plasma', Internal Report (1987).

Lawson J.D. *Proc. Phys. Soc.* B70, 6 (1957).

Lee Y.T. and More R.M.
Phys. Fluids 27(5), 1273 (1984).

Lochte–Holtgreven W.
'Plasma Diagnostics', (North–Holland, 1968).

Lovberg R.H. and Griem H.R.
'Methods of Experimental Physics', Vol. 9 Plasma Physics, Parts A & B (Academic Press, 1971).

Manheimer W.M., Lampe M. and Boris J.P.
Phys. Fluids 16, 1126 (1973).

Martin J.C. *'Nanosecond Pulse Techniques', AWRE Report, SSWA/JCM/704/49* (1970).

Matsumoto Y. *et al.*
J. Appl. Phys. 52(5), 3259 (1981).

McWhirter R.W.P.
'Plasma Diagnostic Techniques' (Huddlestone & Leonard, 1965).

Meierovich B.E.
Sov. J. Plasma Phys. 11(12), 831 (1985).

Montgomery Smith L., Keeper D.R. and Sudharsanan S.I.
J. Quant. Spectrosc. Radiat. Transfer 39(5), 367 (1988).

Moshe Deutsch and Israel Beniaminy
Appl. Phys. Lett. 41(1), 27 (1982).

Mosher D. *et al.*
Appl. Phys. Lett. 23(8), 429 (1973).
Annals of the New York Academy of Sciences 251, 632 (1975).

Nagel D.J. *'Advances in X–ray Analysis', Vol. 18* (Plenum Press, 1974).

Pease R.S. *Proc. Phys. Soc. B* 70, 11 (1957).

Post R.F. *Plasma Phys. (J. Nucl. Energy, Part C)* 3, 273 (1961).

Richter *'Plasma Diagnostics'* (Lochte–Holtgreven, 1968).

Robinson I.G. *Austral. Comp. J.* 3(3), 126 (1971).

Robson A.E. *'Radiative Collapse of a hydrogen z–pinch', NRL Internal Report* (1987).

Rockett P.D. *et al.*
Appl. Optics 24(12), 2532 (1985).

Roderick N.F. and Hussey T.W.
J. Appl. Phys. 56(5), 1387 (1984).

Rosenbluth M.N., Krall N.A. and Rostoker N.
Nucl. Fusion Suppl. Part 1, 143 (1962).

Schlachter J.S.
Ph.D. Thesis, Univ. California (1982).

Schmidt H. and Rückle B.
Appl. Optics 17(8), 1275 (1978).

Shockley W. *Bell System Tech. J.* (1951).

Scofield J.H. *'Energies of Hydrogen and Helium like Ions for Z's from 6 to 54', Lawrence Livermore Lab. Report, UCID−16848* (1975).

Scudder D.W. *A.P.S Meeting*, San Diego (1985).

Sethian J.D. *et al.*
IAEA 10th Conf. Plasma Phys. and Contr. Nucl. Fusion Research, IAEA−CN−44/D−IV−2 (1984).

Sethian J.D., Gerber K.A., DeSilva A.W. and Robson A.E.
Proc. First Conf. on Dense Z−Pinches for Fusion Alexandria, U.S.A. (1984).
Phys. Rev. Lett. (1987).

Skowronek M. *et al.*
Phys. Fluids 13(2), 378 (1970).

Spitzer L. *'Physics of Fully Ionised Gases'* (Interscience, 1956).

Stormberg H.P., Murayama S. and Watanabe Y.
J. Appl. Phys. 62(10), 4090 (1987).

Storr T.H. *'Mini−B, Design and Operation', AWRE Report, SSWA/THS/692/9* (1969).

Tayler R.J. *Proc. Phys. Soc.* B70, 31 (1957).

VanDevender J.P.
Ph.D. Thesis, Univ. Lond. (1974).

Vest C.M. *Appl. Optics* 14(7), 1601 (1975).
'Holographic Interferometry' (Wiley, 1979).

Vikhrev V.V. and Ivanov V.V.
Sov. Phys. Dokl. 30(6), 492 (1985).

Violet C.P. *'Advances in X−ray Analysis', Vol. 18* (Plenum Press, 1974).

Von Hippel A. *Phys. Rev.* 54, 1096 (1938).

Wackerle J. *J. Appl. Phys.* 33(3), 922 (1962).

Yamashita J. and Watanabe M.
Prog. Theor. Phys. 12(4), 443 (1954).

Zel'dovich Ya.B. and Raizer Yu.P.
'Physics of Shock Waves and High–Temperature Hydrodynamic Phenomena' (Academic Press, 1966).

Zenner C.M. *Proc. Roy. Soc.* 145, 523 (1934).

Ackowledgements

It has been a pleasure to work in the Plasma Physics Group at Imperial College and I would like to thank the following people for their part in making it so:

Professor Malcolm Haines, who accepted my application to join the group and who enabled me to start the work on the fibre Z-pinch by arranging a contract with the Centre for Fusion Studies at Imperial College;

My supervisor, Bucker Dangor, for his encouragement of my work;

Dr. John Sethian, of N.R.L., for his help in the B_z measurements on the gas-embedded experiment and various discussions in the Texas Lone Star;

Dr. Gene McCall, of L.A.N.L., for his enthusiasm and participation in the fibre experiment, especially coming in at weekends to help perform measurements before equipment was diverted elsewhere;

Dr. Peter Choi, for helping to build the Marx cage during my first months with the group and for discussions and advice, especially during the X-ray measurements on the fibre experiment;

Kaliq Malik, of the C.E.G.B., for discussions and calculations concerning the fibre breakdown;

Mr. Peter Baldock, for his help in matters mechanical and technical (especially for the circuit which triggered the laser), designing the capillary feed for the fibre experiment, stimulating discussions on all sorts of matters and for all the games of chess;

Mr. Steve Atkins, for getting his hands dirty in helping to clean and adjust the gas switch on innumerable occasions, for sorting out endless problems with electronics (especially with the laser), the lunchtime games of snooker and general conversations at coffee-time;

Mr. Jack Beckwith, for stories, making numerous items for the experiment and machining the fibre pinch chamber;

Mr. John Westlake, for more stories, help in aligning the laser on three occasions and for the calibration of the optical streak camera;

Mr. Maurice Pimm of the student's workshop, for explanations and advice on mechanical matters and for the use of the workshop tools;

Mr. Nick Jackson, for the photographs in this thesis, advice on all matters photographic and especially the twice-weekly games of squash;

Mr. Neal Powell, for drawings of the fibre-pinch chamber;

Miss Meilin Sancho, for reproducing all the illustrations in this thesis;

Dr. Jean-Max Buzzi and colleagues, at the Ecole Polytechnique, France for giving me the opportunity to experience life abroad and for allowing me time to finish this thesis whilst engaged in stimulating work on metallic vapour jets;

The Science and Engineering Research Council for providing funding for the gas-embedded experiment (Grant *GR/C47342*);

And last, but not least, my family and my fiancee Miss Anneli Constable, for constant support and encouragement throughout the duration of this work.